EBM Experimental Biology and Medicine

Volume 250 | Issue 3

# Experimental Biology and Medicine

Editor in Chief

**Nicola Conran**
University of Campinas, Brazil

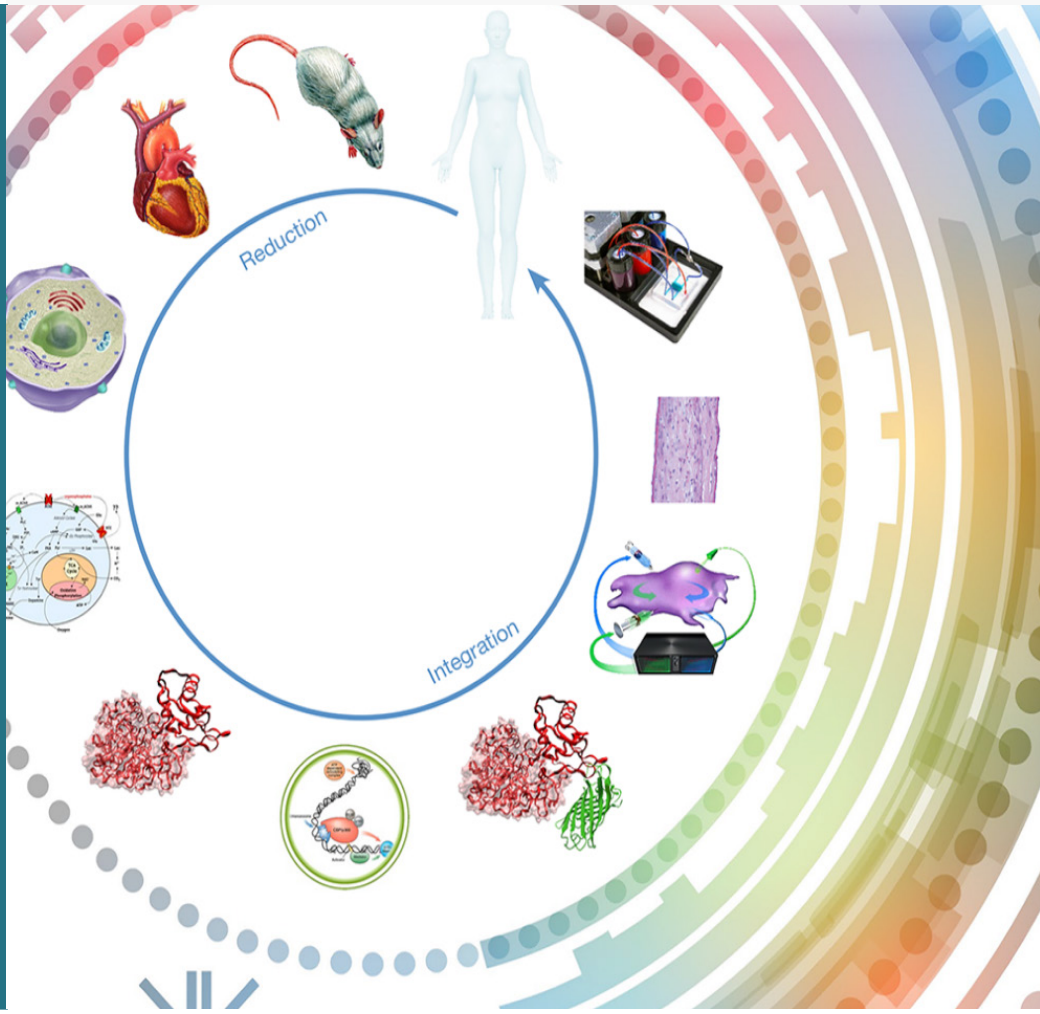


ISBN 978-2-8325-6281-9
DOI 10.3389/978-2-8325-6281-9

frontiers | Publishing Partnerships

# SEBM Executive Council



# Publication Committee



Society for Experimental Biology and Medicine
3220 N Street NW, #179
Washington DC 20007, USA
Executive Director – ed@sebm.org
Assistant to Editor-in-Chief – bzimmer@sebm.org

www.sebm.org

# Editorial Board

ISSN 1535-3699
ISBN 978-2-8325-6281-9
DOI 10.3389/978-2-8325-6281-9

EBM Experimental Biology and Medicine

2025 | Volume 250 | Issue 3 | ISSN 1535-3699

# Table of contents

## Artificial Intelligence/Machine Learning Applications to Biomedical Research

Original Research

07 MONet: cancer driver gene identification algorithm based on integrated analysis of multi-omics data and network models

Yingzan Ren, Tiantian Zhang, Jian Liu, Fubin Ma, Jiaxin Chen, Ponian Li, Guodong Xiao, Chuanqi Sun and Yusen Zhang

## Artificial Intelligence/Machine Learning Applications to Biomedical Research

Review

25 Artificial intelligence for children with attention deficit/hyperactivity disorder: a scoping review

Bo Sun, Fei Cai, Huiman Huang, Bo Li and Bing Wei

## Cell and Developmental Biology

Original Research

38 Coenzyme Q10 alleviates neurological deficits in a mouse model of intracerebral hemorrhage by reducing inflammation and apoptosis

Xiaoqing Yang, Yi Zhao, Sisi Yu, Lihui Chi and Yeyan Cai

## Clinical Trials

Highlight

Original Research

47 Clinical characteristics and prognosis of ALL in children with CDKN2A/B gene deletion

Yiyu Wang, Peijing Wu, Xiaoyan Mao, Nanjing Jiang, Yu Huang, Li Zhang, Li Liu and Xin Tian

## Genomics, Proteomics and Bioinformatics

Original Research

64 Whole blood transcriptome profile identifies motor neurone disease RNA biomarker signatures

Sulev Kõks, Karin Rallmann, Mari Muldmaa, Jack Price, Abigail L. Pfaff and Pille Taba

## Immunology/Microbiology/Virology

### Highlight

Review

79 Bone marrow immune cells and drug resistance in acute myeloid leukemia

Miao Zhang, You Yang, Jing Liu, Ling Guo, Qulian Guo and Wenjun Liu

## Translational Research

Original Research

96 The effects of major abdominal surgery on skeletal muscle mitochondrial respiration in relation to systemic redox status and cardiopulmonary fitness

Jia L. Stevens, Helen T. McKenna, Magdalena Minnion, Andrew J. Murray, Martin Feelisch and Daniel S. Martin

EBM Experimental Biology and Medicine

TYPE Original Research
PUBLISHED 04 February 2025
DOI 10.3389/ebm.2025.10399



OPEN ACCESS

*CORRESPONDENCE
Yusen Zhang,
zhangys@sdu.edu.cn

†These authors have contributed equally to this work

RECEIVED 06 October 2024
ACCEPTED 22 January 2025
PUBLISHED 04 February 2025

CITATION
Ren Y, Zhang T, Liu J, Ma F, Chen J, Li P, Xiao G, Sun C and Zhang Y (2025) MONet: cancer driver gene identification algorithm based on integrated analysis of multi-omics data and network models.
*Exp. Biol. Med.* 250:10399.
doi: 10.3389/ebm.2025.10399



# MONet: cancer driver gene identification algorithm based on integrated analysis of multi-omics data and network models

Yingzan Ren†, Tiantian Zhang†, Jian Liu, Fubin Ma, Jiaxin Chen, Ponian Li, Guodong Xiao, Chuanqi Sun and Yusen Zhang*

School of Mathematics and Statistics, Shandong University, Weihai, Shandong, China

## Abstract

Cancer progression is orchestrated by the accrual of mutations in driver genes, which endow malignant cells with a selective proliferative advantage. Identifying cancer driver genes is crucial for elucidating the molecular mechanisms of cancer, advancing targeted therapies, and uncovering novel biomarkers. Based on integrated analysis of Multi-Omics data and Network models, we present MONet, a novel cancer driver gene identification algorithm. Our method utilizes two graph neural network algorithms on protein-protein interaction (PPI) networks to extract feature vector representations for each gene. These feature vectors are subsequently concatenated and fed into a multi-layer perceptron model (MLP) to perform semi-supervised identification of cancer driver genes. For each mutated gene, MONet assigns the probability of being potential driver, with genes identified in at least two PPI networks selected as candidate driver genes. When applied to pan-cancer datasets, MONet demonstrated robustness across various PPI networks, outperforming baseline models in terms of both the area under the receiver operating characteristic curve and the area under the precision-recall curve. Notably, MONet identified 37 novel driver genes that were missed by other methods, including 29 genes such as APOBEC2, GDNF, and PRELP, which are corroborated by existing literature, underscoring their critical roles in cancer development and progression. Through the MONet framework, we successfully identified known and novel candidate cancer driver genes, providing biologically meaningful insights into cancer mechanisms.

KEYWORDS

**pan-cancer, driver genes, multi-omics data, graph convolutional network, graph attention network**

## Impact statement

The mechanisms underlying cancer development are complex, and identifying cancer driver genes is crucial for cancer diagnosis and personalized treatment. Therefore, we have developed a novel cancer driver gene identification algorithm called MONet, based on the comprehensive analysis of multi-omics data and network models. Our results demonstrate that MONet identifies a substantial number of confirmed and potential cancer driver genes with superior performance and reveals new driver genes that other methods have missed. Conducting biomedical experimental research on the new driver genes discovered by MONet can aid precision medicine and provide better treatment options for cancer patients.

## Introduction

The progression of cancer is driven by mutations in specific genes, known as cancer driver genes, that confer growth advantages to malignant cells [1–3]. Identifying these driver genes is crucial for disease diagnosis and personalized treatment, making it a primary objective of cancer genomics research [4–6]. Large-scale collaborative efforts such as The Cancer Genome Atlas (TCGA) [7] and the International Cancer Genome Consortium (ICGC) [8] have amassed unprecedented datasets, furnishing comprehensive resources for cancer driver gene discovery. Over the past decade, researchers have developed a multitude of computational methods to identify potential cancer driver genes, often grounded in experimental hypotheses. For instance, frequency-based methods typically assume that driver genes exhibit recurrent mutations at a higher frequency than non-driver genes [9–11]. In contrast, network-based methods hypothesize that cancer results from alterations in multiple genes that interact closely and play key roles in cancer-related biological pathways, rather than single-gene alterations [12]. These complementary approaches have collectively enriched our understanding of the complex and multifactorial nature of cancer. Computational methods based on gene mutation frequency have been widely applied to identify cancer driver genes. For example, Dees ND et al. developed MuSiC [9], an integrated mutation analysis tool that combines standardized sequence-based data with clinical data to infer relationships between mutations, affected genes, and pathways. This allows researchers to prioritize driver genes and distinguish significant driver mutations from passenger mutations. Tamborero D et al. proposed OncodriveCLUST [11], which uses silent mutations in coding regions as a background mutation model to identify genes with mutation frequencies significantly exceeding the background rate in specific protein regions. Lawrence MS et al. proposed the MutSigCV [10] algorithm, which is based on the mutation frequency and lineage of specific patients. This algorithm uses a background mutation model that incorporates gene expression and replication timing information to adjust for variations, thereby calculating the background mutation rate of specific genes to improve the accuracy of identifying cancer-related genes.

In recent years, through network analysis, researchers can identify cancer driver genes, a process that is vital for understanding the mechanisms and progression of cancer [13]. Representative algorithms for driver gene identification based on pathway and network analysis include the following. Leiserson MD et al. proposed the HotNet2 [14] algorithm, which is designed to identify mutated subnetworks within gene interaction networks. HotNet2 considers the weights of mutations within single protein networks, enhancing its ability to identify and understand key roles within mutated subnetworks. Cho A et al. introduced the MUFFINN [15] algorithm, which integrates mutation information of individual genes with that of neighboring genes in functional networks to identify driver genes. Colaprico A et al. developed the Moonlight [16] algorithm, designed to identify cancer driver genes that act as dual-role players within the transcriptome network.

In current cancer research, methods that integrate multi-omics data and biological network analysis are widely used for cancer driver gene identification. These methods not only enhance our understanding of cancer development mechanisms but also provide new strategies and approaches for personalized treatment. Therefore, combining multi-omics data integration with biological network analysis is becoming an inevitable trend in exploring cancer complexity. EMOGI [17] is an interpretable machine learning method based on graph convolutional networks (GCN) that integrates genomics, epigenomics, and transcriptomics data as gene features and combines them with PPI networks to learn more abstract gene features. MTGCN [18] is a multi-task learning framework based on GCN that optimizes both node classification and edge link prediction tasks by learning node embedding features. These methods have shown promising results, confirming the effectiveness of combining multi-omics data with network models for cancer driver gene identification.

Nevertheless, despite the efficacy of graph neural network-based methods, their predictive performance in cancer driver gene identification can be limited by the inherent complexity of biological networks. To address this, we propose MONet, which integrates both graph convolutional networks and graph attention networks to enhance the representational power of gene features through the concatenation of feature vectors. Additionally, we selected six independent PPI networks for model training, ensuring that the predicted candidate driver genes are comprehensive and accurate. Through MONet, we identified 376 candidate driver genes, 184 of which are known

driver genes recorded by multiple benchmarks. Among remaining 192 predicted genes, most of them are supported by other datasets or corroborative studies, highlighting the potential of MONet in cancer driver gene identification.

# Materials and methods

## Multi-omics data and PPI networks

We utilized the same multi-omics data and PPI networks as EMOGI to predict cancer driver genes. For the sake of completeness, we briefly introduce these data.

Our method employed four types of multi-omics data: somatic mutation (SM), copy number variation (CNV), gene expression (GE), and DNA methylation (DNAm). We integrated these four types of multi-omics data from 16 cancer types: BLCA, BRCA, CESC, COAD, ESCA, HNSC, KIRC, KIRP, LIHC, LUAD, LUSC, PRAD, READ, STAD, THCA, and UCEC. After normalizing these datasets, we concatenated them to form a feature matrix, where rows represent genes and columns represent features.

We collected protein-protein interactions from CPDB [19], STRING-db [20], MultinetI [21], IRefIndex [22], and PCNet [23]. Depending on the network, we only considered high-confidence interactions. For CPDB, interactions with a score higher than 0.5 are retained. For STRING-db, interactions with a score higher than 0.85 are kept. Multinet and the older version of IRefIndex (v.9.0) were collected from the HotNet2 GitHub repository. For the newer version of IRefIndex (v.15.0), only interactions between human proteins were considered. PCNet was used without further processing and serves as a consensus network.

## Benchmark datasets

In the absence of a recognized "gold standard" dataset containing both positive and negative driver gene annotations, it is challenging to accurately assess the performance of previous prediction tools [24, 25]. To comprehensively evaluate our method, we utilized three commonly used datasets as benchmark datasets, and their union was used as the source of positive samples. For ease of comparison, the datasets were used in the same versions as EMOGI. These datasets include CGC [6], NCG [26], and DigSEE [27]. The CGC database manually curates a list of 723 common genes causally implicated in cancer. The NCG database contains a curated list of expert-selected and candidate cancer genes, with the included genes being proven or predicted to be drivers of cancer. In the selection of positive samples, only confirmed cancer driver genes were used. DigSEE was employed to search for genes related to cancer in the PubMed database, restricted to the 16 cancer types, and a set of 85 highly confident cancer genes was identified using DNA methylation and gene expression as evidence.

Negative samples represent genes least likely to be associated with cancer. To generate a list of negative samples, potential cancer-related genes were recursively removed from all genes, including those present in the NCG database, genes related to cancer pathways in the KEGG [28]database, genes in the OMIM [29] disease database, genes predicted to be cancer-related in MutSigdb [30], and genes whose expression is correlated with cancer genes [31].

Since the proposed algorithm is trained using different PPI networks, only positive and negative samples contained within the underlying PPI networks were used for training. Table 1 presents the total number of genes included in the PPI networks used, along with the counts of positive samples, negative samples, and unlabeled genes.

TABLE 1 The total number of genes included in the PPI networks, along with the counts of positive samples, negative samples, and unlabeled genes.

| PPI | Number | Positive | Negative | Unlabeled |
|---|---|---|---|---|
| CPDB | 13,627 | 796 | 2,187 | 10,644 |
| STRING | 13,179 | 783 | 2,415 | 9,981 |
| Multinet | 14,398 | 790 | 3,709 | 9,899 |
| IRefIndex | 17,013 | 836 | 4,056 | 12,121 |
| IRefIndex (2015) | 12,129 | 785 | 1,971 | 9,373 |
| PCNet | 19,781 | 859 | 3,921 | 15,001 |

## Overview of MONet

Figure 1 illustrates the main workflow of MONet. Firstly, the graph structure constructed from the PPI network is fed into two graph neural network algorithms, GCN and GAT, to learn the feature vector representations of each gene, resulting in two feature matrices: the GCN-Feature matrix and the GAT-Feature matrix. Next, the feature vectors obtained from the two matrices are concatenated together gene-wise, forming a new feature vector for each gene, termed as the Graph Enhanced feature. Subsequently, the new feature vectors are inputted into a multilayer perceptron (MLP) model to perform semi-supervised cancer driver gene identification tasks, comprehensively learning the node features. This process yields the probability of each gene being predicted as a cancer driver gene, and genes are ranked based on these probabilities. Finally, the top 300 candidate genes from each of the six PPI networks are

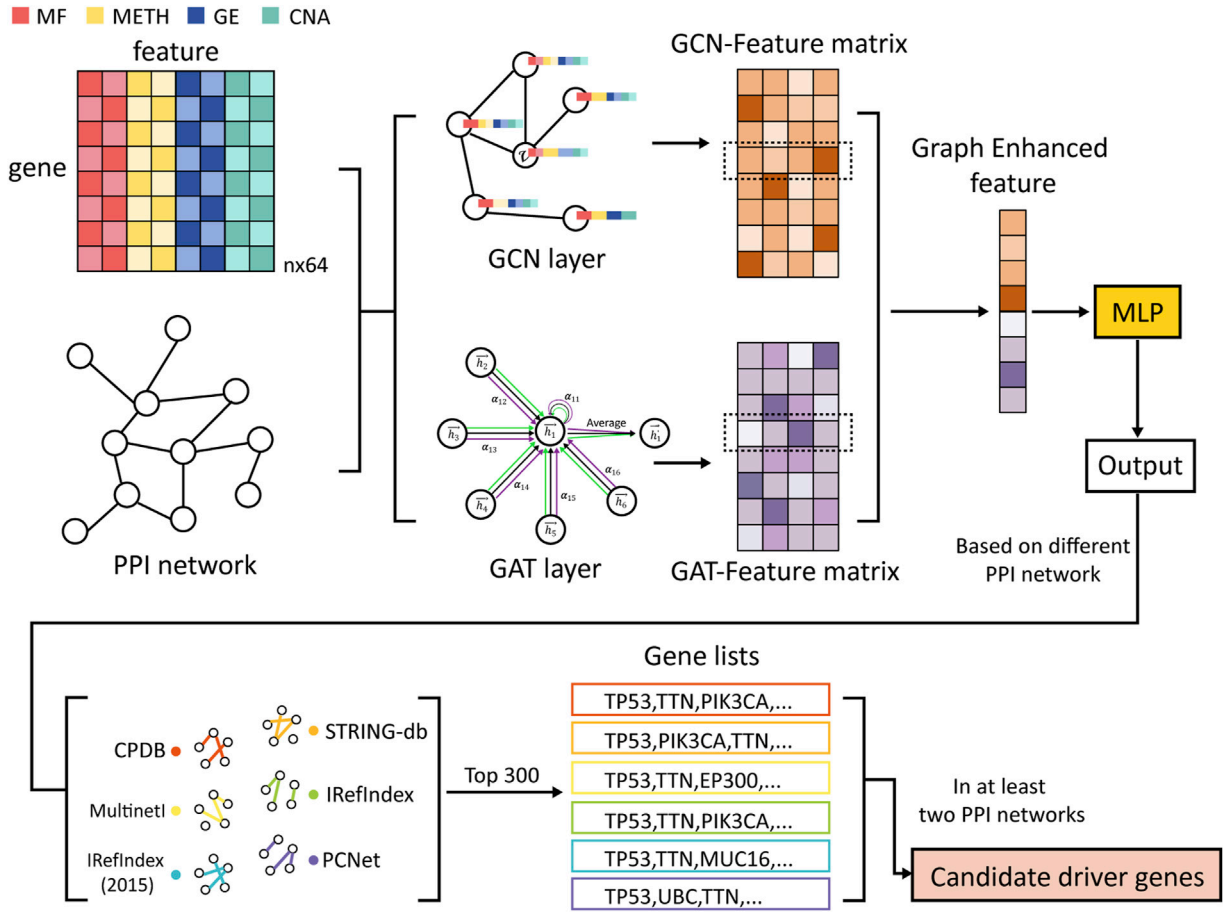


FIGURE 1
Overview of MONet. First, the graph structures of the PPI networks are learned using GCN and GAT to obtain feature vector representations for each gene. Then, these feature vectors from the two matrices are concatenated together to form a new feature vector. Subsequently, the new feature vectors are input into an MLP for the driver gene identification task. Finally, the top 300 candidate genes are selected from each of the 6 PPI networks, and genes appearing in at least two networks are designated as candidate driver genes. The multi-omics data include Mutation Features (MF), DNA Methylation Features (METH), Gene Expression Features (GE), and Copy Number Alteration Features (CNA).

selected, and genes that appear in at least two networks are considered as candidate driver genes.

## GCN layer and GAT layer

GCN algorithm can preserve the structural information of the graph. Therefore, we first use the GCN algorithm on the graph structure constructed from the PPI network to learn the feature vector representation of each gene.

GCN learns node features through the following steps. First, the initial graph structure data $G = (V, E)$ is mapped to a new space $f^G \rightarrow f^*$. Taking a single-layer forward propagation graph convolutional neural network as an example, the feature of the $i$-th layer neural network is represented by $w_i$. When computing the nodes $v_i$ in the graph, the output $H^{l+1}$ of each layer of the network can be represented by a nonlinear function $f(\bullet, \bullet)$ as $H^{l+1} = f(H^l, A)$, where $A$ is the adjacency matrix. The graph convolutional neural network structure is realized through a nonlinear activation function $\sigma(\bullet)$, and its layer-wise propagation rule is given in Equation 1.

$$f\left(H^{l+1}, A\right) = \sigma\left(\tilde{D}^{-\frac{1}{2}}\tilde{A}\tilde{D}^{-\frac{1}{2}}H^l W^l\right) \quad (1)$$

where $\tilde{A} = A + I$ represents the adjacency matrix of graph $G$, $I$ represents the identity matrix, $\tilde{D} = \sum \tilde{A}_{ij}$ represents the degree matrix of the adjacency matrix $\tilde{A}$, and $W^l$ represents the weight matrix of the convolutional neural network at layer $l$.

The GCN algorithm relies on two input matrices: the adjacency matrix of the network and the feature matrix composed of the features of each node. This allows GCN to preserve the structural information of the graph, fully exploiting the latent information in the PPI network, thereby enhancing the classification performance for genes.

However, during the learning process, GCN assigns equal importance to all nodes within the same neighborhood. In practical applications, we need an algorithm that can more intelligently discern the importance of neighboring nodes, which is where GAT excels.

In MONet, we used the GAT method with integrated multi-head attention mechanism. In GAT, for a single graph attention layer, the input consists of a set of node features: $h = \left\{\overrightarrow{h_1}, \overrightarrow{h_2}, ..., \overrightarrow{h_N}\right\}, \overrightarrow{h_i} \in \mathbb{R}^F$, where $N$ is the number of nodes and $F$ represents the dimensionality of each node's feature vector. This layer generates a new set of node features (with feature dimension $F$'): $h' = \left\{\overrightarrow{h_1'}, \overrightarrow{h_2'}, ..., \overrightarrow{h_N'}\right\}, \overrightarrow{h_i'} \in \mathbb{R}^{F'}$. The attention layer propagation mechanism employed in this study is based on Equations 2–5.

$$e_{ij} = a\left(W\overrightarrow{h_i}, W\overrightarrow{h_j}\right) \tag{2}$$

$$e_{ij} = LeakyReLU\left(\vec{a}^{T}\left[W\overrightarrow{h_i} \parallel W\overrightarrow{h_j}\right]\right) \tag{3}$$

$$\alpha_{ij} = softmax_j\left(e_{ij}\right) = \frac{exp\left(e_{ij}\right)}{\sum_{k\in N_i} exp\left(e_{ik}\right)} \tag{4}$$

$$\overrightarrow{h_i'} = \sigma\left(\frac{1}{K}\sum_{K=1}^{K}\sum_{j\in N_i}\alpha_{ij}^{k}W^{k}\overrightarrow{h_j}\right) \tag{5}$$

where $e_{ij}$ represents the importance of node $j$ to node $i$, $W$ and $\vec{a}$ are trainable parameters, $K$ represents the number of attention heads, and $\parallel$ denotes the concatenation operation.

Enhancing the GAT method through the integration of the multi-head attention mechanism brings several significant advantages. Firstly, introducing multiple attention heads allows for parallel processing of different aspects of the graph, thus improving computational efficiency. Each head focuses on learning different features, achieving a comprehensive representation of the graph's complex structure. Additionally, the multi-head mechanism enhances the model's robustness and generalization ability by integrating diverse attention distributions. Even in the presence of noise or errors in individual heads, collective insights from multiple heads ensure the model's resilience. Lastly, and most importantly, introducing multi-head attention mechanism can enhance the expressive power of the attention layers.

## Enhanced feature

By applying both the GCN layer and the GAT layer, the original gene feature vectors are transformed, resulting in two new feature matrices: the GCN-Feature matrix and the GAT-Feature matrix, where the rows represent genes and the columns represent new features. To fully leverage the gene feature vector representations learned by GCN and GAT, MONet innovatively concatenates these learned feature vectors into a single new feature vector, thereby enhancing the gene features. This new feature vector is termed the Graph Enhanced feature.

GCN and GAT are two distinct types of graph neural network algorithms, each employing different methods for information aggregation. GCN aggregates information from neighboring nodes based on the graph's Laplacian spectrum (or adjacency matrix), making it well-suited for capturing global structural features of the graph, particularly excelling in learning global relationships based on the graph topology. In contrast, GAT utilizes a self-attention mechanism to dynamically assign weights to each neighboring node, enabling it to flexibly capture the importance of local neighbors and highlight critical interactions between nodes. Therefore, GCN focuses more on learning global structures, while GAT emphasizes the importance of local interactions between nodes. By concatenating the feature vectors learned by both algorithms, the Graph Enhanced feature integrates the strengths of both methods, providing a more comprehensive description of gene characteristics. Our subsequent comparisons reveal that the feature vectors learned by GCN and GAT may possess complementary properties. By combining these features, we can address the limitations of features learned by each algorithm individually, thereby enhancing the overall feature representation. MONet achieved better results compared to using GCN and GAT alone.

## Identification and screening of driver genes

MLP is an artificial neural network composed of multiple layers of perceptrons or neurons. Each layer is fully connected to the next. A basic perceptron model includes three components: input values, weights and biases, and an activation function. Each perceptron receives a set of inputs, multiplies these inputs by the corresponding weights, and then adds a bias. This result is passed through an activation function to produce an output value. The training of an MLP typically involves the backpropagation algorithm and gradient descent optimization. In MONet, the integrated gene feature vectors, referred to as Graph Enhanced features, are input into an MLP to perform a semi-supervised cancer driver gene identification task. This process fully learns the node features, ultimately producing a probability for each gene being a cancer driver gene. The genes are then ranked based on these probability values.

Selecting candidate driver genes that appear in multiple PPI networks helps to reduce the influence of randomness and noise from individual networks. Additionally, by screening across different networks and choosing genes with high occurrence frequency as candidate driver genes, the consistency and reproducibility of the results are increased, thereby enhancing the credibility of the study. Consequently, we applied the MONet to the graph structures constructed from the six PPI networks

used in this study, resulting in six sets of gene rankings. We selected the top 300 genes from each ranking as candidate genes and included those that appeared in at least two sets as candidate driver genes for further analysis.

# Results

## Evaluation metrics

We evaluated the performance of MONet using common evaluation metrics, including accuracy, the area under the receiver operating characteristic curve (AUROC), the area under the precision-recall curve (AUPR), the F1 Score, and the Matthews Correlation Coefficient (MCC). AUROC represents the area under the receiver operating characteristic (ROC) curve, which is an important indicator for measuring classification performance. By computing the true positive rate (TPR) and false positive rate (FPR) and generating the ROC curve, we calculated the area under it. The precision-recall (PR) curve illustrates the relationship between precision and recall at different thresholds, and the area under it represents the AUPR value. The F1 Score and MCC are particularly well-suited for imbalanced datasets. The F1 Score evaluates a model's ability to predict positive samples by combining precision and recall into a single metric. MCC provides a comprehensive assessment of a model's predictive performance by incorporating all elements of the confusion matrix, including true positives (TP), true negatives (TN), false positives (FP), and false negatives (FN). These evaluation metrics comprehensively assess the classification performance and predictive capability of the model. Several indicators are introduced below.

$$Accuracy = \frac{TP + TN}{TP + FP + TN + FN} \tag{6}$$

ROC curve according to the following equation:

$$\begin{cases} TPR = \dfrac{TP}{TP + FN} \\ FPR = \dfrac{FP}{TP + FP} \end{cases} \tag{7}$$

PR curve according to the following equation:

$$\begin{cases} Precision = \dfrac{TP}{TP + FP} \\ Recall = \dfrac{TP}{TP + FN} \end{cases} \tag{8}$$

$$F1\,Score = 2 \cdot \frac{Precision \cdot Recall}{Precision + Recall} \tag{9}$$

$$MCC = \frac{TP \cdot TN - FP \cdot FN}{\sqrt{(TP + FP)(TP + FN)(TN + FP)(TN + FN)}} \tag{10}$$

where True Negative (TN), True Positive (TP), False Negative (FN), and False Positive (FP), respectively, are in Equations 6–10.

## Model training

In this study, we used a binary cross-entropy loss function $L = -(cylog\sigma(x) + (1 - y)log(1 - \sigma(x)))$. Due to the imbalance between positive and negative samples in the training data, we applied a weight $c$ to the positive samples in the loss function. For instance, in the CPDB network, there are 796 positive samples and 2,187 negative samples. Since the negative samples are approximately three times the number of positive samples, we assigned a weight of 3 to the positive samples in the loss function (c = 3). When training MONet, we first divided the labeled samples, i.e., the total of positive and negative samples, into 75% for the training set and 25% for the test set. We employed ten-fold cross-validation to train the model and calculated the average results of the test sets from the ten folds to evaluate the model's performance.

For the graph structure constructed from the CPDB network, after tuning the parameters, we found that in GCN, the number of hidden layers is 2, with dimensions of 300 and 100, respectively. The dimension of the GCN output layer is set to 16. In GAT, there is one hidden layer with a dimension of 100, incorporating a multi-head attention mechanism, with 5 heads in the hidden layer and 1 head in the output layer. The output layer of the GAT has a dimension of 16. We concatenated the output vectors from GCN and GAT to form a 32-dimensional vector, which was then fed into an MLP. The MLP has one hidden layer with a dimension of 16. Finally, the MLP outputs the probability that each node is predicted to be positive, which corresponds to the probability of each gene being a cancer driver gene. We ranked the genes based on these probability values to identify candidate cancer driver genes. During training, we used the Adam optimizer with a learning rate of 0.001, a weight decay rate of 0.0005, and a dropout rate of 0.5. We set the epochs to 2000 and used the validation set loss as the criterion for early stopping.

## Performance on PPI network

To demonstrate the necessity of using multiple PPI networks, we conducted tests with varying numbers of PPI networks. The results showed that when using a single PPI network, only a small proportion of the top 300 genes predicted by MONet were confirmed as known driver genes in the reference dataset. Moreover, the performance varied significantly across different networks, with the proportion of known driver genes reaching 38.7% for IRefIndex but 50.3% for STRING (Figure 2A), indicating suboptimal overall performance. When multiple PPI networks were used, and genes appearing in at least two networks were selected as candidate driver genes, the proportion of known driver genes identified was higher than that achieved with a single network (Supplementary File S1). This demonstrates that integrating multiple networks is more advantageous for identifying driver genes.

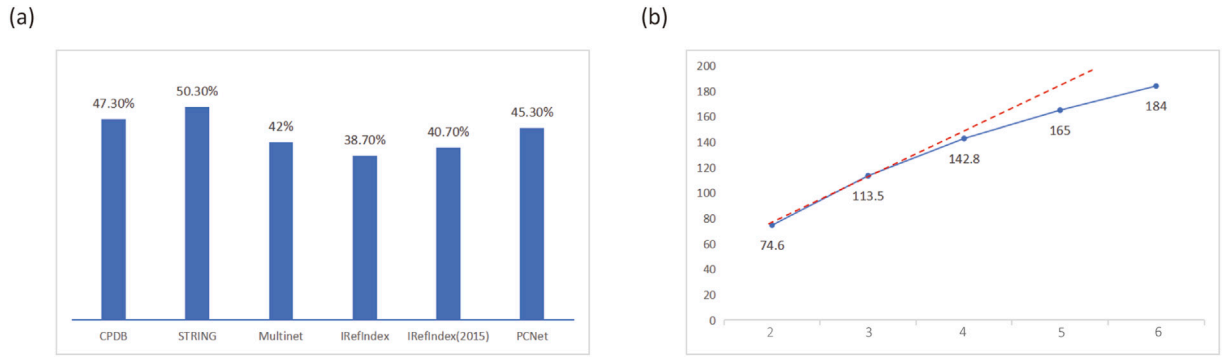


FIGURE 2
Impact of different PPI networks on MONet performance. **(A)** Proportion of known driver genes among the predicted driver genes identified using a single PPI network. **(B)** Trend in the number of known driver genes identified when using 2–6 PPI networks, with the results for 2–5 networks represented as the average.

TABLE 2 Performance of MONet on each PPI network. ACC, AUROC, AUPR, F1 score, and MCC values across six PPI networks.

| PPI | ACC | AUROC | AUPR | F1 score | MCC |
|---|---|---|---|---|---|
| CPDB | 0.7909 | 0.8864 | 0.7781 | 0.6750 | 0.5445 |
| STRING | 0.8125 | 0.9119 | 0.8069 | 0.6862 | 0.5774 |
| Multinet | 0.8622 | 0.9360 | 0.7825 | 0.6830 | 0.6172 |
| IRefIndex | 0.8618 | 0.9053 | 0.7076 | 0.6258 | 0.5432 |
| IRefIndex (2015) | 0.8058 | 0.8805 | 0.7525 | 0.7035 | 0.5740 |
| PCNet | 0.9067 | 0.9379 | 0.7700 | 0.6942 | 0.6456 |

Figure 2B shows the trend in the number of known driver genes identified by MONet when using 2–6 PPI networks, with results for 2–5 networks represented as averages. It can be observed that as the number of PPI networks increased, the number of identified known driver genes also grew. This may be attributed to the inclusion of additional protein-protein interaction pathways from newly added networks, which are potentially associated with driver gene functionality. However, the growth rate gradually diminished, suggesting that increasing the number of PPI networks does not always lead to continuous performance improvement. Since MONet's performance is highly dependent on the quality of PPI networks, it is significantly influenced by the accuracy and reliability of the network data. With the ongoing advancements in medical experiments, the diversity and quantity of PPI networks are continuously expanding. Given MONet's strong performance, we believe it can be applied to a broader range of PPI network structures, providing robust support for driver gene research.

To evaluate the capability of the proposed MONet method in predicting cancer driver genes, we employ five performance metrics: accuracy (ACC), AUROC, AUPR, F1 Score and MCC. In our study, we train MONet method on six different PPI networks and evaluate its performance on each network. By training and evaluating on multiple networks, we can comprehensively understand MONet's generalization ability and robustness. The performance metrics for MONet on each PPI network are summarized in Table 2. These metrics will help us thoroughly assess MONet's effectiveness in predicting cancer driver genes and provide a critical reference for further experimental results.

Observing the table, it can be seen that on CPDB, MONet performs well in terms of AUROC (0.8864) and AUPR (0.7781), though its ACC (0.7909) is slightly lower compared to other networks. On STRING, MONet demonstrates robust performance, particularly excelling in AUPR (0.8069) and achieving high AUROC (0.9119) and ACC (0.8125) values. Its F1 Score (0.6862) and MCC (0.5774) reflect good alignment between predictions and true labels. On Multinet, MONet achieves exceptional performance, with one of the highest AUROC (0.9360) values and strong AUPR (0.7825). The F1 Score (0.6830) and MCC (0.6172) highlight its ability to make balanced predictions. IRefIndex and IRefIndex (2015) show relatively better performance in AUPR compared to other metrics. PCNet emerges as the top-performing network, with the highest ACC (0.9067), AUROC (0.9379), and MCC (0.6456), along with a strong F1 Score (0.6942), reflecting its robust and balanced predictions. Overall, our MONet algorithm performs well on all six PPI networks.

## Ablation experiment

MONet employed multi-omics data for predicting driver genes. To examine whether the inclusion of multi-omics features improves model performance, we conducted ablation experiments. Specifically, we individually inputted single omics

TABLE 3 The performance comparison of MONet and its variants in driver gene prediction. The multi-omics features include Mutation Features (MF), DNA Methylation Features (METH), Gene Expression Features (GE), and Copy Number Alteration Features (CNA).

| Features | ACC | AUROC | AUPR |
|---|---|---|---|
| MF | 0.7708 | 0.8601 | 0.7497 |
| METH | 0.7547 | 0.8563 | 0.7242 |
| GE | 0.7480 | 0.8711 | 0.7351 |
| CNA | 0.7145 | 0.8055 | 0.6438 |
| MF + METH | 0.7855 | 0.8790 | 0.7689 |
| MF + GE | 0.7373 | 0.8300 | 0.6767 |
| MF + CNA | 0.7601 | 0.8639 | 0.7546 |
| METH + GE | 0.7761 | 0.8774 | 0.7430 |
| METH + CNA | 0.7399 | 0.8476 | 0.7098 |
| GE + CNA | 0.7668 | 0.8697 | 0.7399 |
| MF + METH + GE | 0.7601 | 0.8666 | 0.7352 |
| MF + METH + CNA | 0.7480 | 0.8717 | 0.7610 |
| MF + GE + CNA | 0.7413 | 0.8683 | 0.7537 |
| METH + GE + CNA | 0.7688 | 0.8714 | 0.7453 |
| Multi-omics | 0.7909 | 0.8864 | 0.7781 |

type features (namely, Mutation Features (MF), DNA Methylation Features (METH), Gene Expression Features (GE), and Copy Number Alteration Features (CNA)) into the model, as well as combined features of two omics types (namely, MF + METH, MF + GE, MF + CNA, METH + GE, METH + CNA, GE + CNA), combined features of three omics types (namely, MF + METH + GE, MF + METH + CNA, MF + GE + CNA, METH + GE + CNA), and all omics type features. The experimental results are presented in Table 3.

Table 3 displays the performance comparison of MONet and its variants in pan-cancer driver gene prediction. Firstly, we observed that when various omics features were individually applied to the model, multi-omics exhibited the best model performance. Specifically, the combination of multi-omics features achieved the highest scores in terms of ACC, AUROC, and AUPR, with values of 0.7909, 0.8864, and 0.7781, respectively. This indicates that integrating multiple omics data can better predict genes and improve model performance. Next, we further compared the performance of single omics features. Among single omics features, GE performed the best in terms of AUROC, reaching 0.8711, while CNA performed the worst in terms of ACC and AUPR, with values of 0.7145 and 0.8055, respectively. This may reflect the importance of gene expression data in gene prediction, and the relatively weaker predictive ability of copy number alteration features compared to other omics data. Subsequently, we analyzed the combination effects of various omics type features. We observed that the MF + METH combination exhibited the best comprehensive performance in terms of ACC, AUROC, and AUPR, with values of 0.7855, 0.8790, and 0.7689, respectively. However, the MF + METH + CNA combination achieved the highest score in terms of AUPR, reaching 0.7610, indicating that adding copy number alteration features can improve the performance of gene prediction models in certain scenarios.

Overall, integrating multiple omics data can significantly improve the performance of gene prediction models, and the combination of different omics features may have varying degrees of impact on model performance.

## Comparison with other methods

To further evaluate the performance of MONet, we selected four evaluation metrics, AUROC, AUPR, F1 Score and MCC. For comparison, we chose four other algorithms to compare their performance with MONet, including the EMOGI, MTGCN, GCN, and GAT. The EMOGI and MTGCN method are both graph neural network algorithms based on the integration of multi-omics data, where EMOGI is based on GCN and predicts cancer driver genes using multi-omics data, while MTGCN, also based on GCN, is a multitask learning framework that simultaneously optimizes node prediction and link prediction tasks. The GCN and GAT algorithms apply the integrated multi-omics data to GCN and GAT models, respectively, as in our study. Using the experimental data from our study, we applied the five algorithms to the CPDB network, and for the other four algorithms, we followed the default parameter settings of their original algorithms. For the results obtained with different algorithms, we plotted ROC curves (Figure 3A) and PR curves (Figure 3B) to compare their AUROC and AUPR values. Additionally, bar charts were created to visualize the F1 Score (Figure 3C) and MCC (Figure 3D) of the different methods.

Observing Figure 3, we find that MONet outperforms the other four baseline methods on the CPDB network. The AUROC of MONet reaches 0.8864, which is 0.0243 higher than the relatively effective MTGCN algorithm and 0.0315 higher than the least effective GCN. Comparing the area under the PR curves, the advantage of MONet becomes more prominent, reaching 0.7781, surpassing the other four algorithms. MONet outperforms other algorithms in terms of F1 Score (0.675) and MCC (0.5445), demonstrating its superior ability to balance precision and recall as well as to handle data imbalance effectively. Compared to other methods, MONet exhibits more balanced overall performance, making it a reliable and effective tool for cancer driver gene identification. Furthermore, comparing MONet, GCN, and GAT, it is evident that MONet significantly outperforms GCN and GAT. This improvement stems from the complementary nature of the

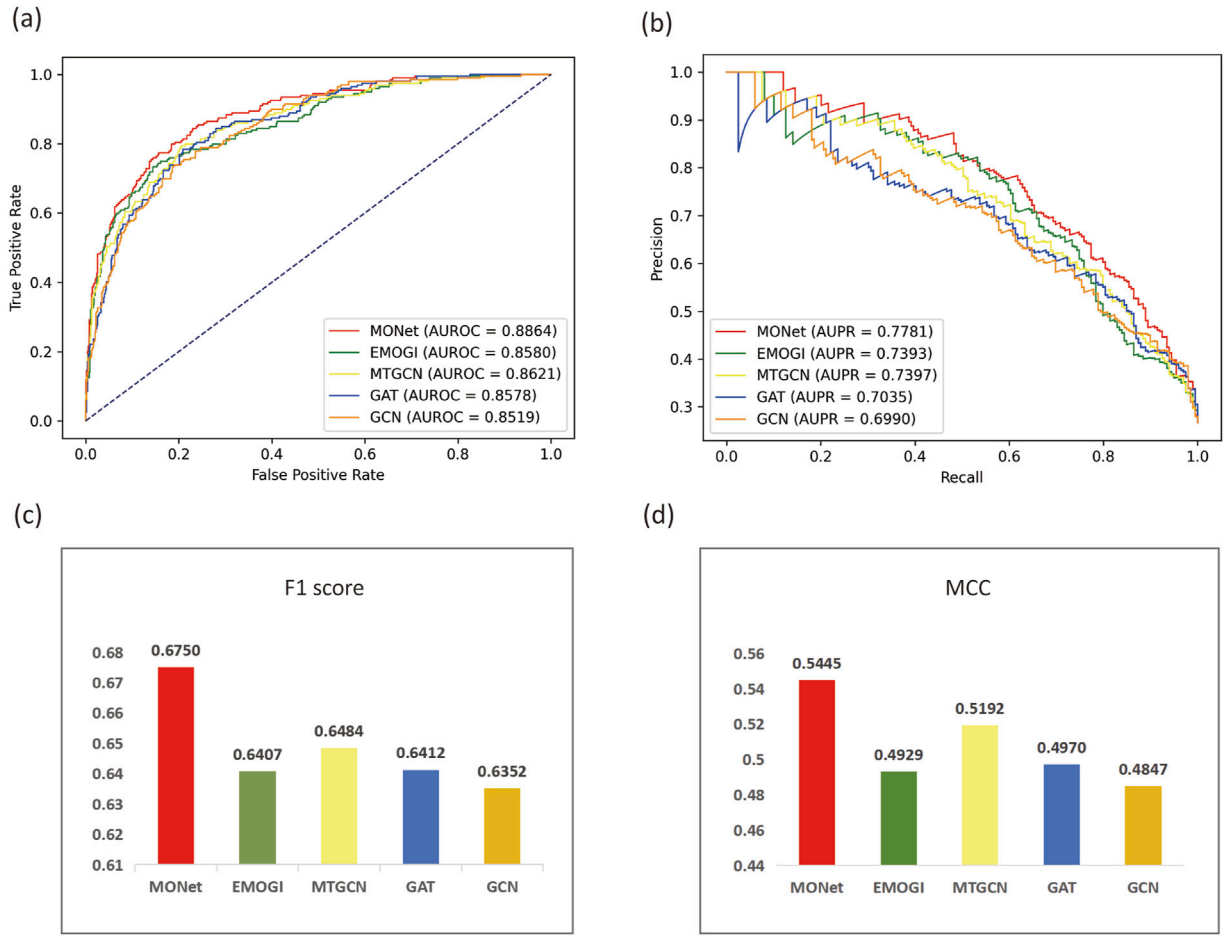


FIGURE 3
Comparison of MONet with other methods. **(A)** ROC curves and AUROC values of MONet, EMOGI, MTGCN, GAT, and GCN. **(B)** PR curves and AUPR values of MONet, EMOGI, MTGCN, GAT, and GCN. **(C)** F1 Scores of MONet, EMOGI, MTGCN, GAT, and GCN. **(D)** MCC values of MONet, EMOGI, MTGCN, GAT, and GCN.

new features derived from MONet's concatenation, which effectively integrates the global graph information captured by GCN with the local neighborhood relationships emphasized by GAT. This finding also validates the effectiveness of the ensemble approach in the task of pan-cancer driver gene prediction.

## Identifying novel cancer driver genes

### Database comparison

The identification of cancer driver genes is crucial for elucidating the mechanisms of tumorigenesis and cancer progression. Here, we present the capability of MONet in identifying novel cancer driver genes. Among the 376 candidate cancer driver genes identified by integrating six PPI networks, 184 genes were validated against benchmark datasets, accounting for approximately 49%. This indicates that MONet has a high predictive accuracy and that the selection of candidate driver genes is reasonable. In other words, these 184 genes are known cancer driver genes, while the remaining 192 genes are predicted cancer driver genes identified by MONet. Next, we compared the remaining 192 newly predicted cancer driver genes with three independent cancer gene sets, specifically from NCG, OncoKB [32], and ONGene [33], ensuring no overlap with the known cancer gene sets used for training MONet. Additionally, we analyzed the newly predicted cancer driver genes using CancerMine [34], a database that employs text mining and regular updates to collect information on driver factors, oncogenes, and tumor suppressors. The comparison results are illustrated in Figure 4A.

The study results indicate that among the remaining 192 newly predicted cancer driver genes, over 58% have at least one piece of evidence suggesting their potential as cancer

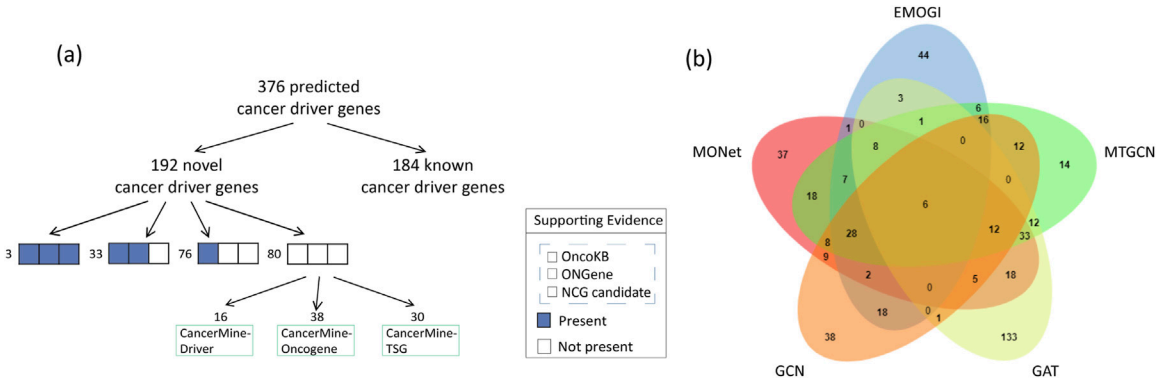


FIGURE 4
The analysis of cancer driver genes predicted by MONet. **(A)** Among the cancer driver genes predicted by MONet, 49% are already known cancer driver genes. For the newly predicted cancer driver genes, most have multiple sources of evidence supporting their potential as driver genes, including candidate cancer genes from NCG, manually curated cancer genes from OncoKB, and literature-curated cancer genes from ONGene. Specifically, 3 genes are supported by all three datasets, 33 genes are supported by two datasets, 76 genes are supported by one dataset, and 80 genes are newly identified by MONet. Based on the analysis from the CancerMine database, among these 80 newly identified genes, 61 genes are implicated in one or more aspects related to driver factors, oncogenes, or tumor suppressors. **(B)** Venn diagram showing the overlap between MONet and other methods. Thirty-seven genes were uniquely predicted by MONet.

driver genes. Specifically, 3 genes are supported by all three datasets (NCG, OncoKB, and ONGene), 33 genes are supported by two datasets, 76 genes are supported by one dataset, and the remaining 80 genes are considered new potential cancer driver genes. Analysis based on the CancerMine database shows that among these 80 new genes, 61 are implicated in one or more aspects related to driver factors, oncogenes, or tumor suppressors.

Ultimately, only 29 genes are not included in the four selected reference sets of candidate cancer driver genes. Overall, approximately 85% (163/192) of the newly predicted cancer driver genes have at least one piece of evidence supporting their potential as cancer driver genes.

## Comparative analysis

Similar to MONet, we applied EMOGI, MTGCN, GCN, and GAT to six PPI networks, selecting genes that ranked in the top 300 across at least two of the PPI networks for discussion. Our results revealed that MONet predicted 37 novel driver genes that did not overlap with those identified by other methods, demonstrating MONet's unique ability to uncover new driver genes missed by other approaches (Figure 4B). Among these novel driver genes, 29 have been supported by existing literature, indicating their association with cancer progression (Supplementary File S2). Among them, APOBEC2 may be associated with nucleotide alterations in cancer-related gene transcripts, potentially promoting carcinogenesis [35]. GDNF is considered a growth factor that plays a crucial role in the nervous system, affecting cell survival and differentiation. Evidence suggests that GDNF can promote the survival and spread of already occurring cancer cells in specific environments, such as the leptomeninges [36]. Furthermore, PRELP is linked to the onset, progression, and metastasis of colorectal cancer, suggesting it may act as a promoter in cancer progression and could be a potential therapeutic target or prognostic marker [37].

## KEGG and GO enrichment analysis

Using the R package clusterProfiler (v4.10.0) [38], we found that 181 KEGG pathways were significantly enriched ($p < 0.05$, $q < 0.05$) among the cancer driver genes identified by MONet (Supplementary File S3). The top 30 most significant pathways are considered known or potentially related to cancer (Figure 5A). For instance, pathways such as proteoglycans in cancer (p.adjust = $2.04 \times 10^{-42}$), human papillomavirus infection (p.adjust = $3.66 \times 10^{-28}$), prostate cancer (p.adjust = $1.86 \times 10^{-25}$), breast cancer (p.adjust = $9.30 \times 10^{-24}$), and microRNAs in cancer (p.adjust = $2.49 \times 10^{-20}$) are well-known cancer pathways. Additionally, the PI3K-Akt signaling pathway (p.adjust = $3.89 \times 10^{-39}$) plays a crucial role in regulating cell growth, survival, and metastasis, making it an attractive therapeutic target in cancer due to the frequent deregulation of PI3K pathway signaling [39]. The MAPK signaling pathway (p.adjust = $1.88 \times 10^{-22}$) is significant in regulating cancer resistance and suggests that targeting this pathway could be a potential therapeutic strategy for cancer treatment [40].

Next, we mapped the 376 candidate driver genes identified by MONet to GO terms (Supplementary File S4), including biological processes (BP), cellular components (CC), and molecular functions (MF). Our charts display the top 30 GO terms (Figure 5B). Overall, these terms are associated with processes such as cell death, cell differentiation, cell

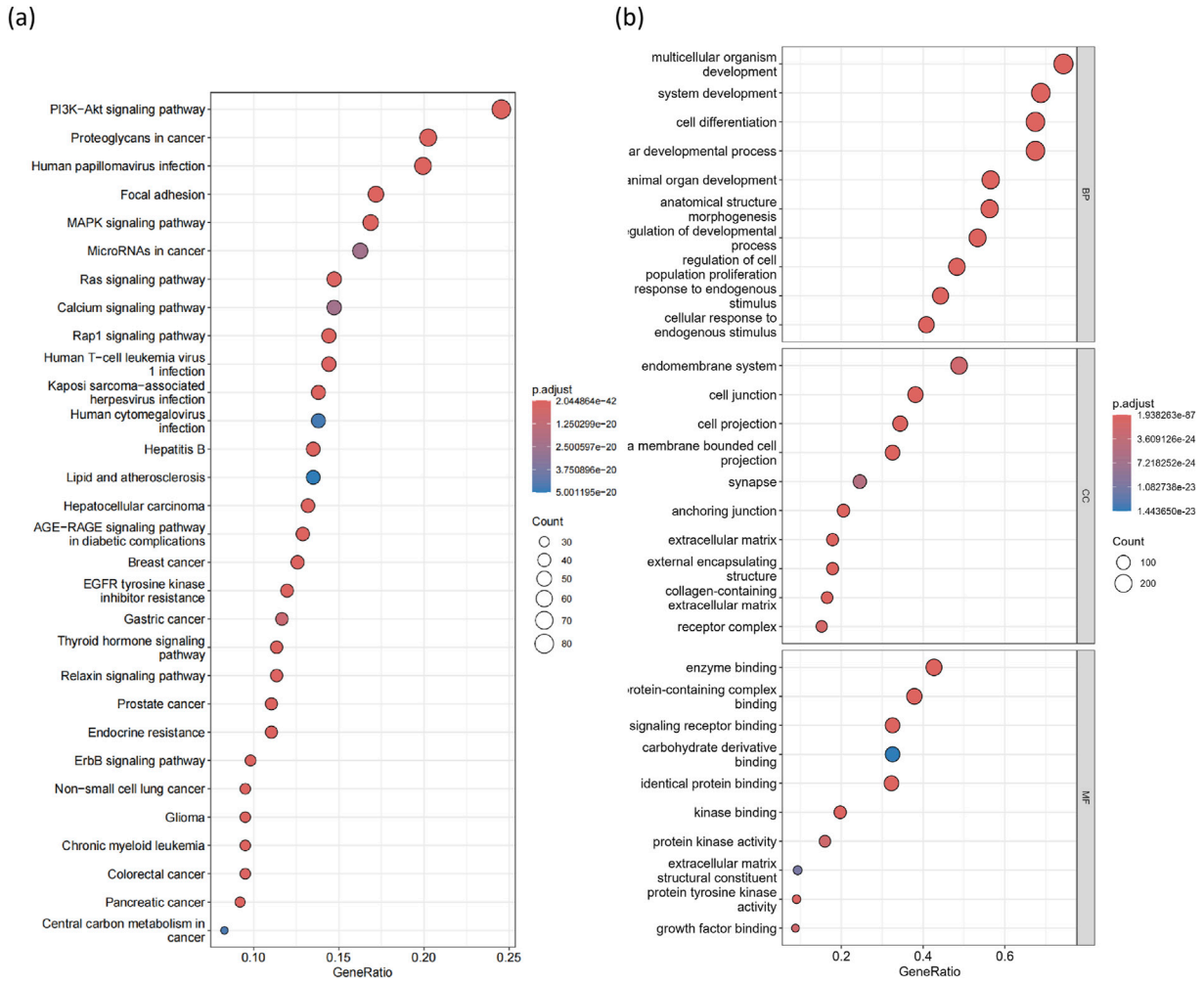


FIGURE 5
GO and KEGG enrichment analysis of 376 candidate driver genes. **(A)** Top 30 significantly enriched KEGG pathways. The horizontal axis represents the ratio of genes in each enriched KEGG pathway, and the vertical axis represents significantly enriched pathways. **(B)** Top 10 significantly enriched GO terms in biological processes (BP), cellular components (CC), and molecular functions (MF).

proliferation, cell activation, and immune system functions, all of which play critical roles in cancer development.

## Analysis of 29 newly predicted candidate driver genes

For the 29 candidate driver genes newly predicted by MONet, we conducted a search on the PubMed website[1] and found that 22 of these genes are closely related to the processes of cancer occurrence, development, and treatment. For instance, For example, LNX1 has been identified as a negative regulator of cancer stem-like cells (CSCs), playing a significant role in regulating the stemness of colorectal cancer cells [41]. Overexpression of SNW1 has been confirmed to be associated with poor prognosis in various types of cancers, with upregulation observed in a subset of prostate cancer samples [42]. COL4A4 is downregulated in lung adenocarcinoma and is associated with various tumor microenvironment (TME) parameters, immune therapy response, and drug resistance [43]. Previous reports have also indicated differential expression of COL4A4 in other tumors, correlating with prognosis, tumor stemness, immune checkpoint gene expression, and TME parameters. NID2, when demethylated or overexpressed in lung cancer cells, leads to decreased cell viability, proliferation, migration, and invasion, suggesting its role in promoting cancer development [44]. Silencing PTGER3 by siRNA in ovarian cancer cells is associated with

1 https://pubmed.ncbi.nlm.nih.gov/

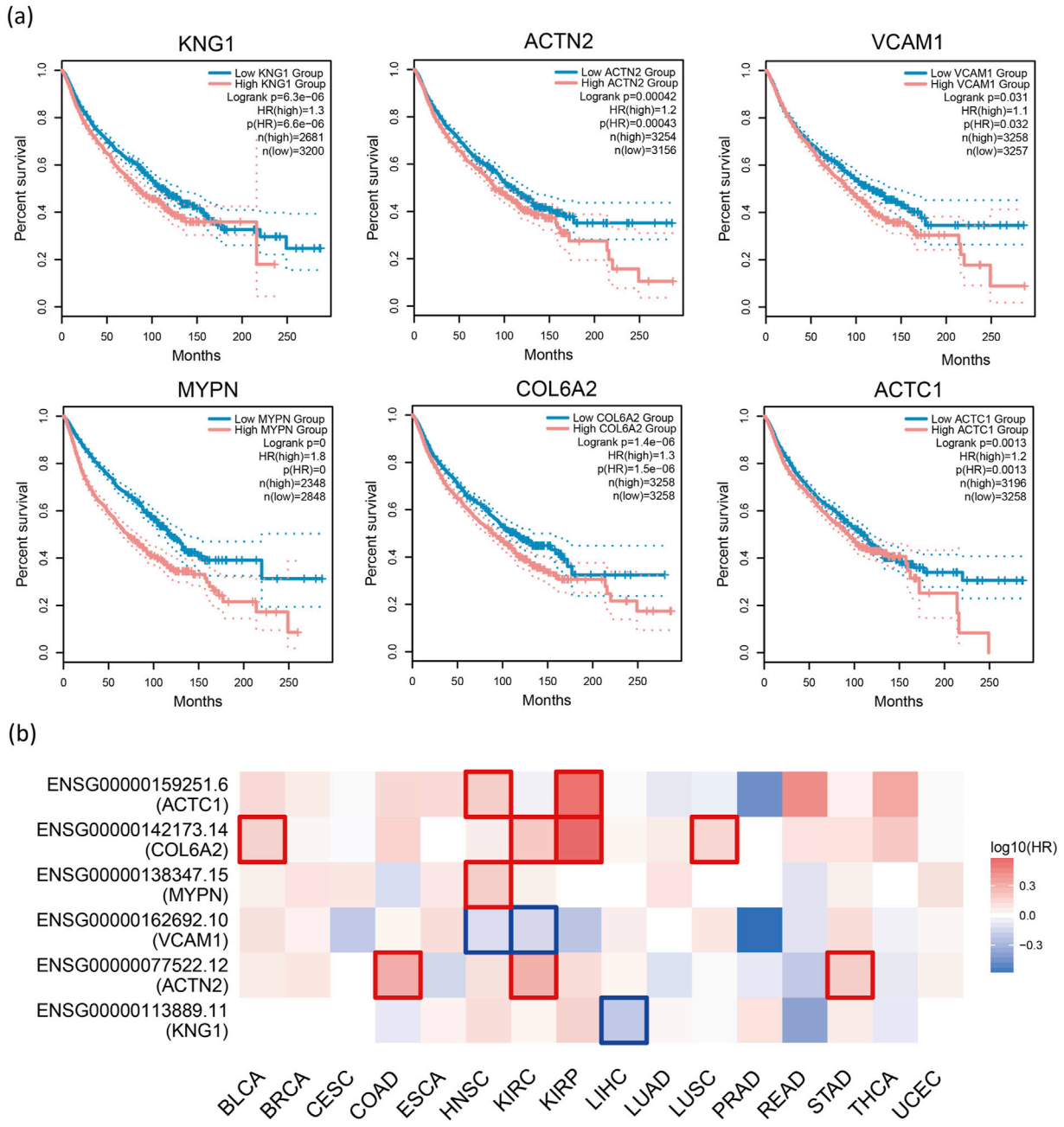


FIGURE 6
Survival analysis. **(A)** Survival analysis of 29 genes using GEPIA2 reveals that low expression of KNG1, ACTN2, VCAM1, MYDN, COL6A2, and ACTC1 is significantly associated with poor overall survival (OS), indicating that they are cancer risk factors ($P < 0.05$, HR > 1, group cutoff = median). **(B)** The heatmap displays the logarithmic scale (log10) of hazard ratios for different genes. Red and blue blocks represent higher and lower risks, respectively. Rectangles with borders indicate significant adverse and favorable outcomes in the prognostic analysis.

decreased cell growth, reduced invasiveness, cell cycle arrest, and increased apoptosis, indicating PTGER3 as a potential therapeutic target for chemotherapy-resistant ovarian cancer with high levels of expression of certain oncogenic proteins [45]. Additionally, genes like ACTA1 [46], COL4A3 [47], A2M [48], ADRB2 [49], MYOC [50], among others, are closely associated with cancer biomarkers, candidate prognostic factors, and therapeutic targets.

Gene Expression Profiling Interactive Analysis 2 (GEPIA2) [51] is an updated version of GEPIA used for analyzing RNA sequencing data. It includes expression data from 9,736 tumor samples and 8,575 normal samples obtained from The Cancer

Genome Atlas (TCGA) and the Genotype-Tissue Expression (GTEx) project. In this study, GEPIA2 was employed to conduct survival analysis on 29 candidate cancer driver genes, with cancer types limited to 16 pan-cancer datasets. The survival analysis using GEPIA2 revealed that low expression of six genes, namely KNG1, ACTN2, VCAM1, MYDN, COL6A2, and ACTC1, was significantly associated with poor overall survival (OS) and represented cancer risk factors ($P < 0.05$, $HR > 1$, group cutoff = median, (Figure 6A).

GEPIA2 conducts survival analysis based on gene or isoform expression levels. For a given list of cancer types, it provides a heatmap displaying survival analysis results for multiple cancer types. We restrict the six genes obtained just now to individual cancers and plot a heatmap to observe the relationship between these genes and the corresponding cancers (Figure 6B). Specifically, red squares indicate higher risk. We can observe that most gene blocks in the figure are red. Additionally, in certain cancers, high gene expression is associated with shorter survival time ($P < 0.05$, $HR > 1$), as indicated by the red-bordered blocks in the heatmap. We can observe many such squares in the figure. These findings suggest that these genes are likely associated with cancer. To explore the relevance of these genes to cancer, we conducted a literature search. Previous studies have indicated that the loss of ACTN1 inhibits cancer cell proliferation, invasion, and migration, while ACTN1 itself can promote tumor growth and metastasis [52]. COL6A2 has been identified as a central gene in risk prediction models for BLCA, with qRT-PCR results showing downregulation [53]. In KIRC, high expression of COL6A2 in patients correlates with poorer survival and may be associated with adverse outcomes and distant metastases [54]. COL6A2 has also been identified as one of the genes in classifiers distinguishing LUSC from other cancer types [55]. Based on these findings, we speculate that the aforementioned genes could serve as potential biomarkers for their corresponding cancers, aiding in auxiliary diagnosis and prognosis assessment, or could become candidate targets for targeted therapy, thus contributing to the development of new personalized treatment strategies.

## Analysis of gene-drug target associations

The improvement in cancer survival rates is primarily driven by advancements in early diagnosis and novel drug treatments [56]. Therefore, identifying the molecular targets of each drug and discovering new drug targets in cancer are crucial for enhancing cancer treatment efficacy.

The Drug-Gene Interaction Database (DGIdb v5.0.6, [2]) [57] integrates reported literature on drug-gene interactions and includes data from four sources: Gene Sources, Drug Sources, Interaction Sources, and Potentially Druggable Sources, comprising 47 databases. It provides information on the associations between genes and their known or potential drug interactions. DGIdb contains over 10,000 genes and 15,000 drugs involved in over 50,000 drug-gene interactions or belonging to one of 43 potentially druggable gene categories. Drugs targeting specific genes may be closely associated with the development and progression of cancer, and may even represent potential anticancer drugs.

In this study, we examined the newly predicted candidate driver genes using the DGIdb database. The data were limited to the NCIt database in Drug Sources and five databases in Interaction Sources (ChEMBL, CIViC, DTC, PharmGKB, TTD). Among the 29 newly predicted candidate driver genes, 19 were found to be associated with drugs in the DGIdb database, with 7 found in the NCIt database and 16 in the remaining five databases (Figure 7).

According to the literature supported by the DGIdb database, there is empirical evidence indicating the relevance of newly discovered genes to the occurrence, development, and treatment of cancer. For instance, van Huis-Tanja et al. conducted a clinical correlation study and found that specific genetic markers may influence the efficacy of oral 5-fluoropyrimidine prodrug capecitabine in treating metastatic colorectal cancer. In patients receiving single-agent capecitabine therapy, the rs4702484 variant located near the ADCY2 gene and the MTRR gene may be slightly associated with a decreased progression-free survival (PFS) in homozygous wild-type patients [58]. Additionally, the transferrin receptor TfR, which is upregulated in certain cancer cells, has emerged as a potential therapeutic target. A targeted drug against TfR is Transferrin Receptor-Targeted Anti-RRM2 siRNA CALAA-01 (NCI Thesaurus Code: C78450). It is a proprietary nanoparticle formulation targeted at the transferrin receptor, containing non-chemically modified small interfering RNA (siRNA) against the M2 subunit of ribonucleotide reductase (RRM2), with potential anti-tumor activity. This drug binds to and releases anti-RRM2 siRNA via the transferrin receptor (TfR), silencing RRM2 expression, thereby inhibiting the assembly of ribonucleotide reductase (RR) and resulting in cell proliferation suppression. Furthermore, a targeted drug for ACTC1, DEXAMETHASONE, is commonly used in cancer treatment to alleviate side effects induced by cancer therapy, control cancer-related inflammation and immune responses as part of cancer treatment. However, several clinical studies have found an association between the use of dexamethasone and a decrease in overall survival rate in patients. Preclinical studies in mouse glioma models have shown a reduction in tumor-infiltrating lymphocytes after dexamethasone treatment [59].

2 https://www.dgidb.org/

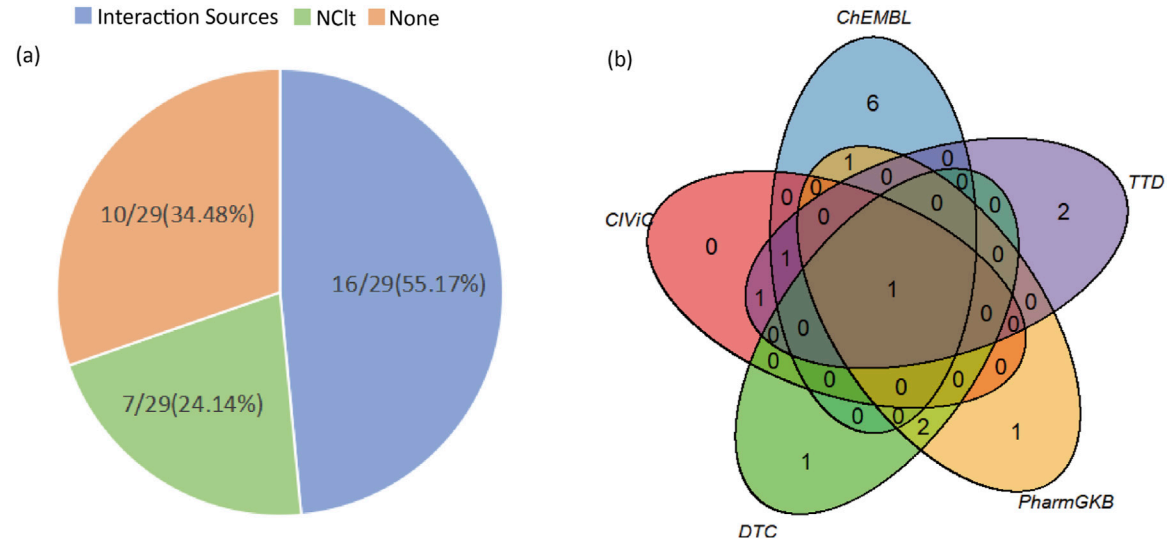


FIGURE 7
The results of the detection of candidate driver genes in the DGIdb database. **(A)** Left figure displays the number of candidate driver genes retrieved from the five databases within Interaction Sources, the NCIt database, and those not found in the DGIdb database, along with their proportions relative to the total number of candidate driver genes. **(B)** Right figure illustrates the overlap of candidate driver genes from the five databases within Interaction Sources (ChEMBL, CIViC, DTC, PharmGKB, TTD).

## Multi-omics feature analysis

To further validate the reliability of utilizing multi-omics features for identifying cancer driver genes, we systematically compared driver genes selected from the CGC database with neutral genes (NGs) obtained from DORGE [60] (3,417 genes in total). We evaluated each feature across different cancer types to assess whether there are significant differences between CGC and NGs genes.

Specifically, we extracted four types of features from multi-omics data and conducted a comparative analysis between CGC and NGs based on these features. To evaluate the distributional differences between the two groups of genes, we performed Wilcoxon rank-sum tests and calculated p-values for each feature to assess statistical significance. Typically, a p-value less than 0.05 is considered significant. Using the CPDB network as an example, we visualized the feature distributions between CGC and NGs through a heatmap (Figure 8A), box plots, scatter plots, and half-violin plots (Figure 8B). The analysis results for other networks are provided in the Supplementary Files S5-1, S5-2.

As shown in Figure 8, among the 64 features across 16 cancer types, the majority of features exhibit p-values below 0.05, indicating significant differences, with only six features failing to reach significance. This demonstrates that the selected four multi-omics features are effective in distinguishing CGC from NGs. Among them, the MF and METH features show significant differences across all 16 cancer types, whereas the GE feature fails to show significance in the PRAD cancer type, and the CNA feature does not achieve significance in CESC, KIRP, LUSC, READ, and THCA cancer types. These findings suggest that most features exhibit significant differences between CGC and NGs, implying that these features may hold potential biological relevance in the identification of cancer driver genes.

## Discussion

In this study, we introduced MONet, an integrated algorithm based on GCN and GAT, for the identification of cancer driver genes. MONet combines four pan-cancer omics data types (gene mutations, DNA methylation, gene expression, and copy number variations) with PPI networks to predict cancer driver genes. By integrating six PPI networks, MONet identified 376 candidate cancer driver genes. Among them, 184 were already known cancer driver genes, while most of the remaining 192 newly predicted cancer driver genes were supported by other datasets or research methods. Among the 192 newly predicted genes, we compared these genes with the driver genes identified by EMOGI, MTGCN, GAT, and GCN across the six PPI networks. Our analysis revealed that 37 genes were uniquely predicted by MONet. Notably, 29 genes, including APOBEC2, GDNF, and PRELP, have been confirmed by existing literature to be associated with cancer development and progression.

We observed that approximately 85% (163/192) of the newly predicted cancer driver genes were supported by evidence suggesting their potential as cancer driver genes.

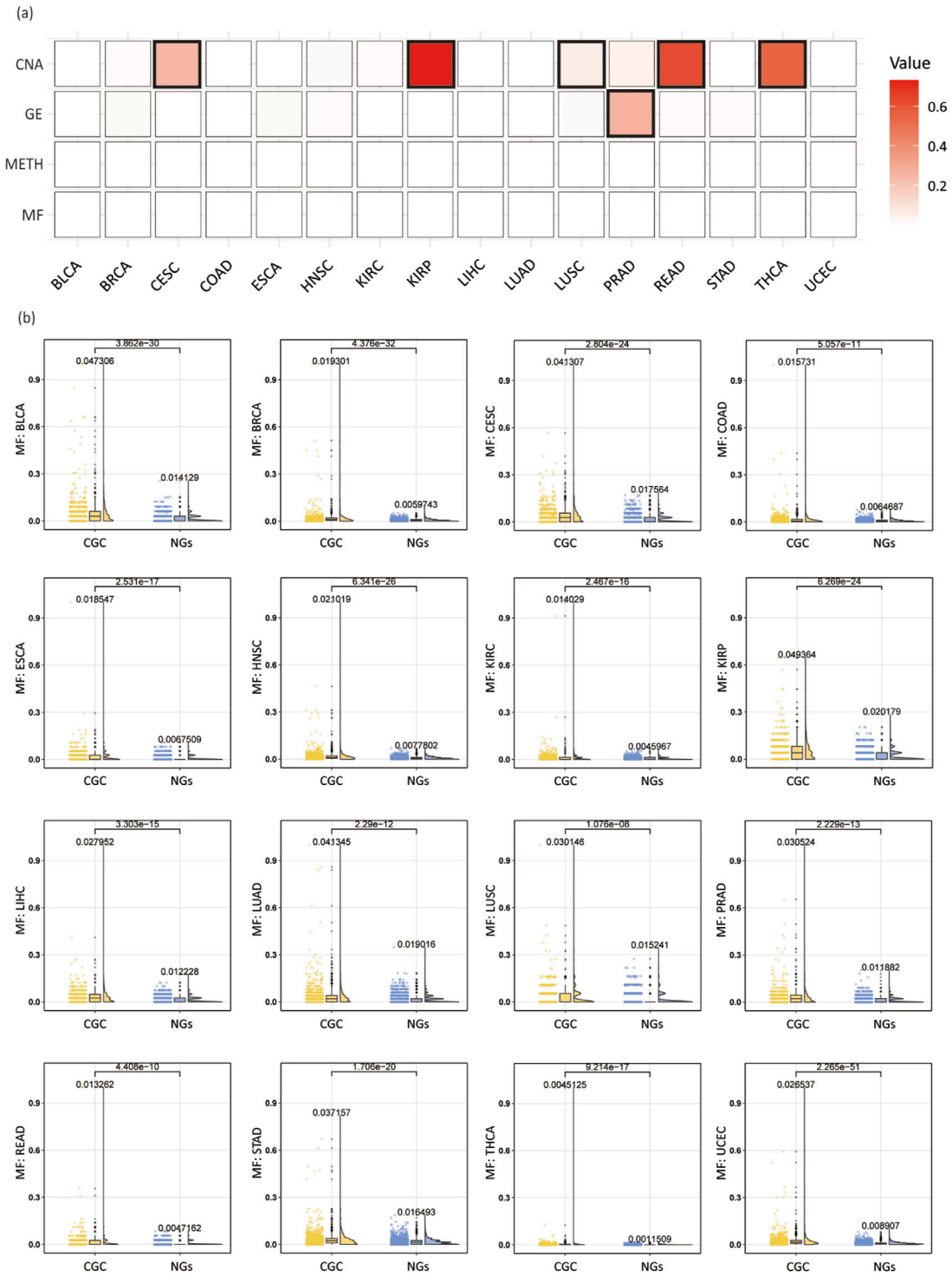


FIGURE 8
Analysis of multi-omics features in individual cancer types. **(A)** Wilcoxon rank-sum test p-values across 16 cancer types, with bold borders highlighting squares where the p-value is greater than 0.05. **(B)** Box plots, scatter plots, and half-violin plots for the MF feature across 16 cancer types. Each plot compares CGC and NGs, displaying the mean values for both groups and the p-values from the Wilcoxon rank-sum test.

The innovation of this study lies in the effective integration of GCN and GAT algorithms into a unified framework. The MONet model combines the complementary strengths of these two algorithms: GCN excels at capturing global graph structures, while GAT emphasizes the importance of local neighborhoods through its attention mechanism. By integrating multi-omics data with PPI networks to fully explore the potential information of multi-omics features and gene interactions, thereby improving the effectiveness of identifying cancer driver genes.

Results showed that the MONet model outperformed baseline models in terms of the area under the receiver operating characteristic (ROC) curve and the area under the precision-recall (PR) curve, demonstrating excellent performance and stability across different PPI networks. By conducting ablation experiments on the multi-omics data used by MONet, we verified that using multi-omics data can improve the prediction performance of driver genes. Additionally, we provided evidence support for newly predicted driver genes by comparing with existing driver gene databases, performing KEGG enrichment analysis and GO enrichment analysis, and consulting existing literature. For genes that could not be validated, we conducted survival analysis and drug target analysis to support their potential as cancer driver genes. Definitive evidence indicates the involvement of newly discovered genes to the occurrence, development, and treatment of cancer. We ultimately confirmed the reliability of the selected multi-omics data and can be used to explore and identify novel cancer driver genes, which provides a foundational assurance for our study.

Although this study has achieved significant results in identifying cancer driver genes, there is still room for improvement. For example, when constructing the graph structure based on PPI networks, we did not consider the issue of edge weights. Future research could incorporate edge weight information to develop more accurate cancer driver gene identification algorithms to further improve identification effectiveness. Our study demonstrates that increasing the number of PPI networks can enhance the performance of driver gene identification; however, the marginal benefits gradually diminish. Future research could focus on exploring optimal strategies for PPI network combinations to achieve a better balance between performance and resource utilization. Furthermore, as biotechnology advances, higher-quality PPI networks will further improve the reliability of driver gene identification, providing greater possibilities and opportunities for optimization in future studies.

## Author contributions

YZ was responsible for overseeing this project. YR and TZ proposed and designed the experiments and conducted all the benchmark analyses. YR, TZ, JL, and FM drafted the initial manuscript and discussed the design of the results. JC, PL, GX, and CS modified some details. All authors contributed to the article and approved the submitted version.

## Data availability

The original contributions presented in the study are included in the article/Supplementary Material, further inquiries can be directed to the corresponding author.

## Funding

The author(s) declare that financial support was received for the research, authorship, and/or publication of this article. This work was supported by the National Natural Science Foundation of China (61877064).

## Conflict of interest

The author(s) declared no potential conflicts of interest with respect to the research, authorship, and/or publication of this article.

## Generative AI statement

The author(s) declare that no Generative AI was used in the creation of this manuscript.

## Supplementary material

The Supplementary Material for this article can be found online at: https://www.ebm-journal.org/articles/10.3389/ebm.2025.10399/full#supplementary-material

## References

1. Martincorena I, Campbell PJ. Somatic mutation in cancer and normal cells. *Science* (2015) **349**:1483–9. doi:10.1126/science.aab4082

2. Stratton MR, Campbell PJ, Futreal PA. The cancer genome. *Nature* (2009) **458**: 719–24. doi:10.1038/nature07943

3. Vogelstein B, Papadopoulos N, Velculescu VE, Zhou S, Diaz LA, Jr, Kinzler KW. Cancer genome landscapes. *Science* (2013) **339**:1546–58. doi:10.1126/science.1235122

4. Tamborero D, Rubio-Perez C, Deu-Pons J, Schroeder MP, Vivancos A, Rovira A, et al. Cancer Genome Interpreter annotates the biological and clinical relevance of tumor alterations. *Genome Med* (2018) **10**:25. doi:10.1186/s13073-018-0531-8

5. Alexandrov LB, Nik-Zainal S, Wedge DC, Aparicio SA, Behjati S, Biankin AV, et al. Signatures of mutational processes in human cancer. *Nature* (2013) **500**: 415–21. doi:10.1038/nature12477

6. Sondka Z, Bamford S, Cole CG, Ward SA, Dunham I, Forbes SA. The COSMIC cancer gene census: describing genetic dysfunction across all human cancers. *Nat Rev Cancer* (2018) **18**:696–705. doi:10.1038/s41568-018-0060-1

7. The Cancer Genome Atlas Research Network. Integrated genomic analyses of ovarian carcinoma. *Nature* (2011) **474**:609–15. doi:10.1038/nature10166

8. The International Cancer Genome Consortium, Hudson TJ, Anderson W, Artez A, Barker AD, Bell C, Bernabe RR, et al. International network of cancer genome projects. *Nature* (2010) **464**:993–8. doi:10.1038/nature08987

9. Dees ND, Zhang Q, Kandoth C, Wendl MC, Schierding W, Koboldt DC, et al. MuSiC: identifying mutational significance in cancer genomes. *Genome Res* (2012) **22**:1589–98. doi:10.1101/gr.134635.111

10. Lawrence MS, Stojanov P, Polak P, Kryukov GV, Cibulskis K, Sivachenko A, et al. Mutational heterogeneity in cancer and the search for new cancer-associated genes. *Nature* (2013) **499**:214–8. doi:10.1038/nature12213

11. Tamborero D, Gonzalez-Perez A, Lopez-Bigas N. OncodriveCLUST: exploiting the positional clustering of somatic mutations to identify cancer genes. *Bioinformatics* (2013) **29**:2238–44. doi:10.1093/bioinformatics/btt395

12. Bashashati A, Haffari G, Ding J, Ha G, Lui K, Rosner J, et al. DriverNet: uncovering the impact of somatic driver mutations on transcriptional networks in cancer. *Genome Biol* (2012) **13**:R124. doi:10.1186/gb-2012-13-12-r124

13. Tan A, Huang H, Zhang P, Li S. Network-based cancer precision medicine: a new emerging paradigm. *Cancer Lett* (2019) **458**:39–45. doi:10.1016/j.canlet.2019.05.015

14. Leiserson MD, Vandin F, Wu HT, Dobson JR, Eldridge JV, Thomas JL, et al. Pan-cancer network analysis identifies combinations of rare somatic mutations across pathways and protein complexes. *Nat Genet* (2015) **47**:106–14. doi:10.1038/ng.3168

15. Cho A, Shim JE, Kim E, Supek F, Lehner B, Lee I. MUFFINN: cancer gene discovery via network analysis of somatic mutation data. *Genome Biol* (2016) **17**:129. doi:10.1186/s13059-016-0989-x

16. Colaprico A, Olsen C, Bailey MH, Odom GJ, Terkelsen T, Silva TC, et al. Interpreting pathways to discover cancer driver genes with Moonlight. *Nat Commun* (2020) **11**:69. doi:10.1038/s41467-019-13803-0

17. Schulte-Sasse R, Budach S, Hnisz D, Marsico AJNMI. Integration of multiomics data with graph convolutional networks to identify new cancer genes and their associated molecular mechanisms. *Nature Machine Intelligence Volume* (2021) **3**:513–526.

18. Peng W, Tang Q, Dai W, Chen T. Improving cancer driver gene identification using multi-task learning on graph convolutional network. *Brief Bioinform* (2022) **23**:bbab432. doi:10.1093/bib/bbab432

19. Kamburov A, Pentchev K, Galicka H, Wierling C, Lehrach H, Herwig R. ConsensusPathDB: toward a more complete picture of cell biology. *Nucleic Acids Res* (2011) **39**:D712–7. doi:10.1093/nar/gkq1156

20. Szklarczyk D, Gable AL, Lyon D, Junge A, Wyder S, Huerta-Cepas J, et al. STRING v11: protein-protein association networks with increased coverage, supporting functional discovery in genome-wide experimental datasets. *Nucleic Acids Res* (2019) **47**:D607–D613. doi:10.1093/nar/gky1131

21. Khurana E, Fu Y, Chen J, Gerstein M. Interpretation of genomic variants using a unified biological network approach. *Plos Comput Biol* (2013) **9**:e1002886. doi:10.1371/journal.pcbi.1002886

22. Razick S, Magklaras G, Donaldson IM. iRefIndex: a consolidated protein interaction database with provenance. *BMC Bioinformatics* (2008) **9**:405. doi:10.1186/1471-2105-9-405

23. Huang JK, Carlin DE, Yu MK, Zhang W, Kreisberg JF, Tamayo P, et al. Systematic evaluation of molecular networks for discovery of disease genes. *Cell Syst* (2018) **6**:484–95.e5. doi:10.1016/j.cels.2018.03.001

24. Forbes SA, Beare D, Bindal N, Bamford S, Ward S, Cole CG, et al. COSMIC: high-resolution cancer genetics using the catalogue of somatic mutations in cancer. *Curr Protoc Hum Genet* (2016) **91**:10.11.1–10.11.37. doi:10.1002/cphg.21

25. Tokheim CJ, Papadopoulos N, Kinzler KW, Vogelstein B, Karchin R. Evaluating the evaluation of cancer driver genes. *Proc Natl Acad Sci U S A* (2016) **113**:14330–5. doi:10.1073/pnas.1616440113

26. Repana D, Nulsen J, Dressler L, Bortolomeazzi M, Venkata SK, Tourna A, et al. The Network of Cancer Genes (NCG): a comprehensive catalogue of known and candidate cancer genes from cancer sequencing screens. *Genome Biol* (2019) **20**(1):1. doi:10.1186/s13059-018-1612-0

27. Kim J, So S, Lee HJ, Park JC, Kim JJ, Lee H. DigSee: disease gene search engine with evidence sentences (version cancer). *Nucleic Acids Res* (2013) **41**:W510–7. doi:10.1093/nar/gkt531

28. Kanehisa M, Goto S. KEGG: kyoto encyclopedia of genes and genomes. *Nucleic Acids Res* (2000) **28**:27–30. doi:10.1093/nar/28.1.27

29. McKusick VA. Mendelian inheritance in man and its online version, OMIM. *The Am J Hum Genet* (2007) **80**:588–604. doi:10.1086/514346

30. Liberzon A, Birger C, Thorvaldsdottir H, Ghandi M, Mesirov JP, Tamayo P. The molecular signatures database hallmark gene set collection. *Cell Syst* (2015) **1**:417–25. doi:10.1016/j.cels.2015.12.004

31. Subramanian A, Tamayo P, Mootha VK, Mukherjee S, Ebert BL, Gillette MA, et al. Gene set enrichment analysis: a knowledge-based approach for interpreting genome-wide expression profiles. *Proc Natl Acad Sci U S A* (2005) **102**:15545–50. doi:10.1073/pnas.0506580102

32. Chakravarty D, Gao J, Phillips SM, Kundra R, Zhang H, Wang J, et al. OncoKB: a precision oncology knowledge base. *JCO Precision Oncol* (2017) **2017**:1–16. doi:10.1200/po.17.00011

33. Liu Y, Sun J, Zhao M. ONGene: a literature-based database for human oncogenes. *J Genet Genomics* (2017) **44**:119–21. doi:10.1016/j.jgg.2016.12.004

34. Lever J, Zhao EY, Grewal J, Jones MR, Jones SJM. CancerMine: a literature-mined resource for drivers, oncogenes and tumor suppressors in cancer. *Nat Methods* (2019) **16**:505–7. doi:10.1038/s41592-019-0422-y

35. Wei L, Wu X, Wang L, Chen L, Wu X, Song T, et al. Expression and prognostic value of APOBEC2 in gastric adenocarcinoma and its association with tumor-infiltrating immune cells. *BMC Cancer* (2024) **24**:15. doi:10.1186/s12885-023-11769-3

36. Whiteley AE, Ma D, Wang L, Yu SY, Yin C, Price TT, et al. Breast cancer exploits neural signaling pathways for bone-to-meninges metastasis. *Science* (2024) **384**:eadh5548. doi:10.1126/science.adh5548

37. Gui Y, Deng X, Li N, Zhao L. PRELP reduce cell stiffness and adhesion to promote the growth and metastasis of colorectal cancer cells by binding to integrin α5. *Exp Cel Res* (2024) **441**:114151. doi:10.1016/j.yexcr.2024.114151

38. Yu G, Wang LG, Han Y, He QY. clusterProfiler: an R package for comparing biological themes among gene clusters. *Omics : a J Integr Biol* (2012) **16**:284–7. doi:10.1089/omi.2011.0118

39. Sathe A, Nawroth R. Targeting the PI3K/AKT/mTOR pathway in bladder cancer. *Methods Mol Biol* (2018) **1655**:335–50. doi:10.1007/978-1-4939-7234-0_23

40. Jia Y, Zhou J, Luo X, Chen M, Chen Y, Wang J, et al. KLF4 overcomes tamoxifen resistance by suppressing MAPK signaling pathway and predicts good prognosis in breast cancer. *Cell Signal* (2018) **42**:165–75. doi:10.1016/j.cellsig.2017.09.025

41. Ma L, Wang L, Shan Y, Nafees M, Ihab E, Zhang R, et al. Suppression of cancer stemness by upregulating Ligand-of-Numb protein X1 in colorectal carcinoma. *PLoS One* (2017) **12**:e0188665. doi:10.1371/journal.pone.0188665

42. Höflmayer D, Willich C, Hube-Magg C, Simon R, Lang D, Neubauer E, et al. SNW1 is a prognostic biomarker in prostate cancer. *Diagn Pathol* (2019) **14**:33. doi:10.1186/s13000-019-0810-8

43. Zheng T, Zheng Z, Zhou H, Guo Y, Li S. The multifaceted roles of COL4A4 in lung adenocarcinoma: an integrated bioinformatics and experimental study. *Comput Biol Med* (2024) **170**:107896. doi:10.1016/j.compbiomed.2023.107896

44. Wang J, Zhao Y, Xu H, Ma J, Liang F, Zou Q, et al. Silencing NID2 by DNA hypermethylation promotes lung cancer. *Pathol Oncol Res* (2020) **26**:801–11. doi:10.1007/s12253-019-00609-0

45. Rodriguez-Aguayo C, Bayraktar E, Ivan C, Aslan B, Mai J, He G, et al. PTGER3 induces ovary tumorigenesis and confers resistance to cisplatin therapy through up-regulation Ras-MAPK/Erk-ETS1-ELK1/CFTR1 axis. *EBioMedicine* (2019) **40**:290–304. doi:10.1016/j.ebiom.2018.11.045

46. Suresh R, Diaz RJ. The remodelling of actin composition as a hallmark of cancer. *Translational Oncol* (2021) **14**:101051. doi:10.1016/j.tranon.2021.101051

47. Nie XC, Wang JP, Zhu W, Xu XY, Xing YN, Yu M, et al. COL4A3 expression correlates with pathogenesis, pathologic behaviors, and prognosis of gastric carcinomas. *Hum Pathol* (2013) **44**:77–86. doi:10.1016/j.humpath.2011.10.028

48. Fang K, Caixia H, Xiufen Z, Zijian G, Li L. Screening of a novel upregulated lncRNA, A2M-AS1, that promotes invasion and migration and signifies poor prognosis in breast cancer. *Biomed Research International* (2020) **2020**:9747826. doi:10.1155/2020/9747826

49. Kulik G. ADRB2-Targeting therapies for prostate cancer. *Cancers (Basel)* (2019) **11**:358. doi:10.3390/cancers11030358

50. Jia X, Lei H, Jiang X, Yi Y, Luo X, Li J, et al. Identification of crucial lncRNAs for luminal A breast cancer through RNA sequencing. *Int J Endocrinol* (2022) **2022**:1–14. doi:10.1155/2022/6577942

51. Tang Z, Kang B, Li C, Chen T, Zhang Z. GEPIA2: an enhanced web server for large-scale expression profiling and interactive analysis. *Nucleic Acids Res* (2019) **47**:W556–W560. doi:10.1093/nar/gkz430

52. Wang R, Gao Y, Zhang H. ACTN1 interacts with ITGA5 to promote cell proliferation, invasion and epithelial-mesenchymal transformation in head and

neck squamous cell carcinoma. *Iran J Basic Med Sci* (2023) **26**:200–7. doi:10.22038/IJBMS.2022.67056.14703

53. Wang Z, Tu L, Chen M, Tong S. Identification of a tumor microenvironment-related seven-gene signature for predicting prognosis in bladder cancer. *BMC Cancer* (2021) **21**:692. doi:10.1186/s12885-021-08447-7

54. Zhong T, Jiang Z, Wang X, Wang H, Song M, Chen W, et al. Key genes associated with prognosis and metastasis of clear cell renal cell carcinoma. *PeerJ* (2022) **10**:e12493. doi:10.7717/peerj.12493

55. Vachani A, Nebozhyn M, Singhal S, Alila L, Wakeam E, Muschel R, et al. A 10-gene classifier for distinguishing head and neck squamous cell carcinoma and lung squamous cell carcinoma. *Clin Cancer Res* (2007) **13**:2905–15. doi:10.1158/1078-0432.ccr-06-1670

56. Arroyo MM, Berral-Gonzalez A, Bueno-Fortes S, Alonso-Lopez D, Rivas JDL. Mining drug-target associations in cancer: analysis of gene expression and drug activity correlations. *Biomolecules* (2020) **10**:667. doi:10.3390/biom10050667

57. Cannon M, Stevenson J, Stahl K, Basu R, Coffman A, Kiwala S, et al. DGIdb 5.0: rebuilding the drug-gene interaction database for precision medicine and drug discovery platforms. *Nucleic Acids Res* (2024) **52**:D1227–D1235. doi:10.1093/nar/gkad1040

58. van Huis-Tanja LH, Ewing E, van der Straaten RJ, Swen JJ, Baak-Pablo RF, Punt CJ, et al. Clinical validation study of genetic markers for capecitabine efficacy in metastatic colorectal cancer patients. *Pharmacogenetics and genomics* (2015) **25**:279–88. doi:10.1097/fpc.0000000000000119

59. Upadhyayula PS, Higgins DM, Argenziano MG, Spinazzi EF, Wu CC, Canoll P, et al. The sledgehammer in precision medicine: dexamethasone and immunotherapeutic treatment of glioma. *Cancer Invest* (2022) **40**:554–66. doi:10.1080/07357907.2021.1944178

60. Lyu J, Li JJ, Su J, Peng F, Chen YE, Ge X, et al. DORGE: discovery of Oncogenes and tumoR suppressor genes using Genetic and Epigenetic features. *Sci Adv* (2020) **6**:eaba6784. doi:10.1126/sciadv.aba6784

EBM Experimental Biology and Medicine

TYPE Review
PUBLISHED 24 April 2025
DOI 10.3389/ebm.2025.10238



OPEN ACCESS

*CORRESPONDENCE
Bing Wei,
weibing7112@163.com

†These authors have contributed equally to this work

RECEIVED 12 May 2024
ACCEPTED 28 March 2025
PUBLISHED 24 April 2025

CITATION
Sun B, Cai F, Huang H, Li B and Wei B (2025) Artificial intelligence for children with attention deficit/hyperactivity disorder: a scoping review.
*Exp. Biol. Med.* 250:10238.
doi: 10.3389/ebm.2025.10238



# Artificial intelligence for children with attention deficit/hyperactivity disorder: a scoping review

Bo Sun[1,2†], Fei Cai[2†], Huiman Huang[2], Bo Li[2] and Bing Wei[1*]

[1]Department of Neonatology, General Hospital of Northern Theater Command, Shenyang, Liaoning, China, [2]Post-Graduate College, China Medical University, Shenyang, Liaoning, China

## Abstract

Attention deficit/hyperactivity disorder is a common neuropsychiatric disorder that affects around 5%–7% of children worldwide. Artificial intelligence provides advanced models and algorithms for better diagnosis, prediction and classification of attention deficit/hyperactivity disorder. This study aims to explore artificial intelligence models used for the prediction, early diagnosis and classification of attention deficit/hyperactivity disorder as reported in the literature. A scoping review was conducted and reported in line with the PRISMA-ScR (Preferred Reporting Items for Systematic Reviews and Meta-Analyses Extension for Scoping Reviews) guidelines. Out of the 1994 publications, 52 studies were included in the scoping review. The included articles reported the use of artificial intelligence for 3 different purposes. Of these included articles, artificial intelligence techniques were mostly used for the diagnosis of attention deficit/hyperactivity disorder (38/52, 79%). Magnetic resonance imaging (20/52, 38%) were the most frequently used data in the included articles. Most of the included articles used data sets with a size of <1,000 samples (28/52, 54%). Machine learning models were the most prominent branch of artificial intelligence used for attention deficit/hyperactivity disorder in the studies, and the support vector machine was the most used algorithm (34/52, 65%). The most commonly used validation in the studies was k-fold cross-validation (34/52, 65%). A higher level of accuracy (98.23%) was found in studies that used Convolutional Neural Networks algorithm. This review provides an overview of research on artificial intelligence models and algorithms for attention deficit/hyperactivity disorder, providing data for further research to support clinical decision-making in healthcare.

KEYWORDS

**artificial intelligence, attention deficit/hyperactivity disorder, machine learning, deep learning, review method**

## Impact statement

At present, artificial intelligence is a hot topic, but it still needs to be developed in the medical field, especially in pediatric clinical research. We believe that the researchability of artificial intelligence is sufficient. As we know, in the medical field, early diagnosis and identification of a certain clinical disease is crucial for clinical doctors, and the emergence of artificial intelligence is likely to bring tremendous assistance to clinical diagnosis and treatment work. In this study, we conducted scope evaluation according to the PRISMA-ScR guidelines, and mainly summarized AI models and algorithms for diagnosis, prediction, and classification of attention deficit/hyperactivity disorder. The hope is to provide clinical decisions that support future research in healthcare.

## Introduction

Attention-deficit/hyperactivity disorder (ADHD) is a neurodevelopmental disorder caused by the interaction of genetic and environmental factors that has a worldwide prevalence of 7.2% in children [1, 2]. ADHD is characterized by a persistent and impairing pattern of inattention and/or hyperactivity/impulsivity, about 60% of children with ADHD have symptoms that persist into adulthood [3], and 89% of ADHD patients are accompanied by mental illness, representing a significant public health problem [4]. Therefore, early diagnosis of ADHD is critical to enable early intervention and treatment.

At present, the diagnosis of ADHD mainly relies on the judgment of psychiatrists, based primarily on reports from parents and teachers, behavioral observations, and clinical interviews, which are sensitive to subjective biases [5, 6]. Existing studies have shown that ADHD is a highly heterogeneous disease involving multiple etiological and risk factors, with different clinical characteristics, development process and outcome, which brings diagnostic challenges to clinicians, and false positive diagnosis or misdiagnosis may occur in clinical practice [7, 8]. It has been shown that a significant association between disease and trait does not necessarily imply that it can be used for disease prediction. Neuroimaging plays a vital role in the study of brain function by visualizing the structure and activity of the brain, allowing researchers to understand how different brain regions are involved in various cognitive and behavioral processes [9]. The brains of children with ADHD are different in terms of structure and function, and these differences are also associated with neurocognitive performance. Structural magnetic resonance imaging (sMRI), functional MRI (fMRI), resting-state fMRI (rs-fMRI) and diffusion tensor imaging (DTI) were used to characterize the etiology and phenotype of ADHD from different dimensions [10]. Genome-wide association studies have also revealed several variants in ADHD [11, 12]. In addition, other studies have attempted to use electrocardiogram (ECG) signals [13], eye tracking [14], physiological signals, wearable device data [15], and exercise data to help diagnose ADHD.

Artificial intelligence (AI) is a technology with great potential in medicine, machine learning (ML) is a powerful tool for making critical decisions by analyzing large data sets such as social behavior patterns and various health conditions, deep learning (DL) is a branch of ML [16]. Many neurological diseases are identified based on subjective diagnostic criteria. Neuroimaging is a promising objective diagnostic tool. The task of ML is to model the relationship between features extracted from imaging data and individual labels in the data set, which can be used for new or invisible data sets. It creates broad prospects for disease diagnosis, prognosis and management in health care and enriches personalized medicine [17]. With the increasing popularity of AI models, AI technology has achieved satisfactory results in the diagnosis of brain-related diseases such as Alzheimer's disease, Parkinson's disease, autism spectrum disorder (ASD) [18], and ADHD is no exception. AI can assist in ADHD diagnosis, classification, prognosis, treatment prediction, and the development of new therapeutic drugs.

A large number of articles have been published on AI technologies for ADHD. Several reviews were conducted to summarize previous studies; however, they had the following limitations: First, they focused on studies of ADHD diagnosis with machine learning methods using MRI data [19]; Second, they focused on describing the efficacy of ML or DL models in the diagnosis, classification, or prediction of ADHD, without describing in detail the characteristics of the AI algorithms used [20]. The available literature lacks a review that provides an overview of the features of the AI algorithms used in ADHD. Thus, this review aims to explore the characteristics of AI models used for the diagnosis, prediction and classification to aid scientists advance research on this field.

## Materials and methods

### Overview

In this scoping review, we conducted a systematic literature search that reviewed research involving the use of AI for ADHD prediction, classification, and diagnosis. To ensure the transparency and reliability of this study, the literature search was conducted according to the Preferred Reporting Items for Systematic Review and Meta-Analysis Protocols Extension for Scoping Reviews (PRISMA-ScR) guidelines [21]. The protocols used in the scoping review are detailed in the following sections.

### Search strategy

#### Search sources

Two authors (Bo Sun and Fei Cai) conducted an independent search in February 2025 and screened abstracts and full texts,

which were finally checked by the corresponding author (Bing Wei). During this period, we searched four online databases, including MedRXiv, BioRXiv, PubMed, and Science Direct. The search focused on both medical and computer science databases.

### Search terms

We used the following items as keywords: ("artificial intelligence" OR "machine learning" OR "deep learning" OR "supervised learning" OR "unsupervised learning" OR "reinforcement learning") AND ("attention-deficit/hyperactivity disorder") AND (diagnosis* OR detect* OR predict* OR screen*). For more information on the exact search terms used to search each database, see Multimedia Supplementary Appendix S1.

## Eligibility criteria

The studies included in this review mainly concerned AI technologies for ADHD diagnosis and risk prediction. In other words, we focus on AI models related to ADHD diagnosis. The search was limited to original journal research articles in English. We excluded articles (i.e., literature reviews, dissertations) outlining AI approaches to ADHD as well as studies based purely on clinical trials and experimental studies. Inclusion criteria include: (1) AI technology; (2) the goal to diagnose or screen for ADHD; (3) participants are children only; (4) the data is publicly available. Exclusion criteria include: (1) inadequate details in terms of AI models; (2) same raw data; (3) inappropriate article types (e.g., case reports, reviews, papers, proposals, conference abstracts, editorials, generic manuscripts, and reviews).

## Study selection

Articles selected from each database were charted on Microsoft Excel. At the same time, we imported all the retrieved articles into the EndNote software, and the duplicate check function was used to remove duplicate studies. Titles and abstracts were carefully selected and screened, and articles were searched for full text reading if they met the inclusion criteria. Any disagreements were resolved through discussion among the investigators. To measure agreement between investigators, we calculated the Cohen kappa [22], where the screening result for title and abstract was 0.976, while the screening result for full text was 0.82. We documented the inter-investigator agreement matrix in Multimedia Supplementary Appendix S2.

## Data extraction

The investigators performed the data extraction process using a pre-designed standardized form (Multimedia Supplementary Appendix S3). The extracted data included: (1) author, country, and year; (2) the age, number and health status of the participants; (3) the source, setting, and availability of the data used by AI; (4) algorithms, types, and features of AI models; (5) outcomes of AI diagnosis of ADHD.

# Results

## Search results

We preliminarily identified 1994 articles using four open online databases: PubMed (n = 613), Science Direct (n = 666), BioRXiv (n = 542), and MedRxiv (n = 173). After that, we excluded 557 duplicate articles. Of the remaining studies, 1,195 articles were removed after title and abstract screening. In addition, 13 articles were not searchable, so 229 articles were included in the full-text screening. As shown in Figure 1, after reviewing the full text, we excluded 177 articles for a variety of reasons. A total of 52 articles met our inclusion criteria and were included in this scoping review.

## Main characteristics of the included articles

Characteristics of the included studies were shown in Table 1. All of the studies we included were published in peer-reviewed journals (52/52, 100%). Eligible studies were published between 2012 and 2025, mainly in China (16/52, 31%), followed by Korea (9/52, 17%). The number of participants mentioned in the included studies ranged from 10 to 238,696. Of these, 33 studies reported the proportion of female participants, ranging from 2% to 50%. Furthermore, 88% (46/52) of the included studies only recruited participants with ADHD, and 12% (6/52) of the studies included participants with other medical conditions. Multimedia Supplementary Appendix S4 showed the detailed characteristics of the included studies.

## Characteristics of AI techniques for ADHD

Of the included studies, 76.9% used only ML algorithms, 9.6% used only DL algorithms, and 13.5% applied ML including DL algorithms. In addition, we collated the AI models, algorithms, and methods used in the included ADHD studies. The most commonly used model was support vector machine (SVM, 34/52, 65%), followed by random forest (RF, 17/52,33%). In the 52 studies, AI algorithms were used for 3 different purposes. The most common purposes were early diagnosis (38/52,79%) and risk predictions (10/52, 14%; Table 2). Only 11 studies stated the programming languages used to develop the models, and they were R (5/52,

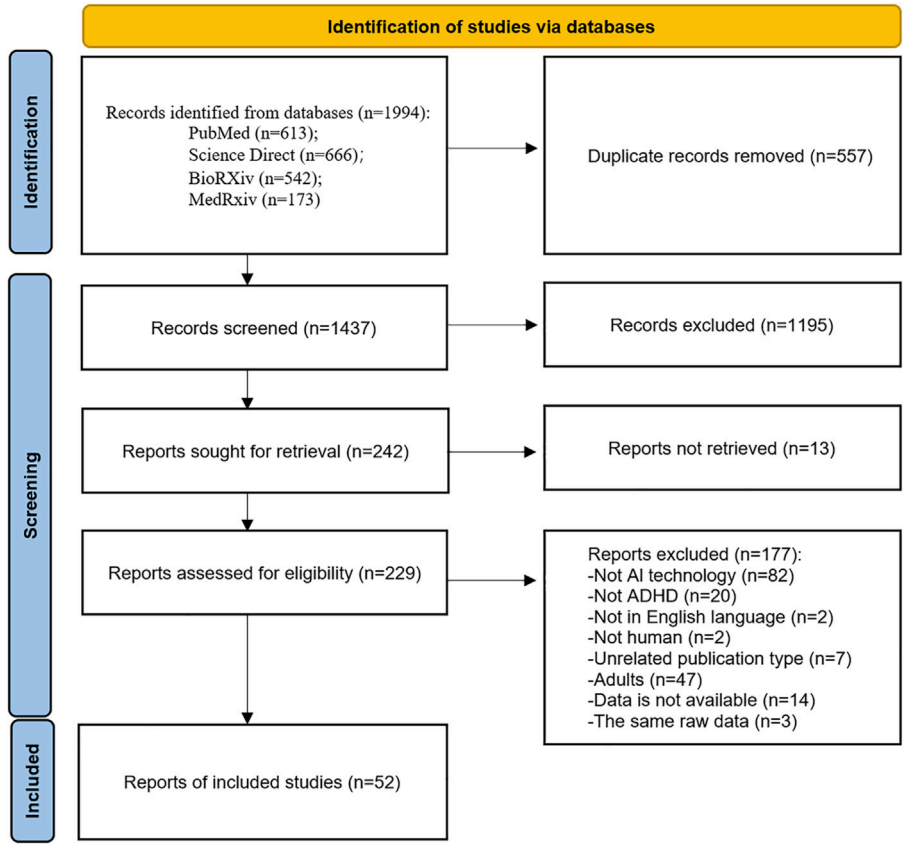


FIGURE 1
PRISMA-ScR flowchart of the study selection.

10%) and Python (6/52,12%). Multimedia Supplementary Appendix S5 showed the characteristics of the AI techniques used in each study.

Table 3 showed the different data categories used in the included studies: 38% of the studies (20/52) involved brain imaging, 25% (13/52) included demographic information, 19% (10/52) used electroencephalogram (EEG), and so on. 60% of the included studies used datasets from closed-source (i.e., data collected directly from databases of study participants or clinical settings) and 40% from open-source (i.e., publicly available databases). The numbers of features used to develop the models in the included studies ranged from 3 to 13,585,634. And 25 studies (48%) did not exceed 100 features in developing their model. We provided a detailed description of the number of features and data categories of the included studies in Multimedia Supplementary Appendix S6.

As shown in Table 4, the included studies used different validation techniques in the development of AI models, mainly of two. Among them, k-fold CV (34/52, 65%) is the more commonly used method. Only 13% of studies (7/52) mentioned confusion matrices, but all 52 studies mentioned performance metrics for AI models. According to statistics, the most commonly used performance measure was accuracy (ACC, 45/52, 87%). In Table 5, 8 studies reported the precision of AI algorithms, ranging from 80% to 95%, with an average of 92.53%; The area under the curve (AUC) in 26 studies ranged from 57.6% to 99.64%, with a mean of 83.77%; The mean ACC of the 45 studies was 83.06%, ranging from 53.2% to 98.23%; 35 studies reported specificities varying between 58.8% and 99.11%, with a mean of 84.08%; The F1-score valued in 11 studies ranged from 48.89% to 95%, with a mean of 85.21%. In addition, the sensitivity of the AI algorithms reported in 35 studies ranged from 33% to 98.24%, with an average of 74.67%.

# Discussion

## Principal findings

In this study, we explored the application of AI techniques in the early diagnosis, prediction, and classification of ADHD. We

TABLE 1 Characteristics of the included studies (n = 52).

| Characteristics | Studies n (%) | References |
|---|---|---|
| **Publication type** | | |
| Journal articles | 52 (100) | [12, 13, 15, 23–28], [29–71] |
| **Year of publication, n (%)** | | |
| 2025 | 1 (1.9) | [26] |
| 2024 | 9 (17.3) | [26, 63, 64, 66–71] |
| 2023 | 8 (15.4) | [35, 42, 47, 50] |
| 2022 | 7 (13.5) | [23, 27, 33, 39, 45, 60, 61] |
| 2021 | 4 (7.7) | [12, 13, 24, 38] |
| 2020 | 4 (7.7) | [25, 37, 44, 52] |
| 2012–2019 | 19 (36.5) | [28–32, 34, 36, 40–44, 48, 54–56, 58, 59, 62] |
| **Country of publication** | | |
| China | 16 (31) | [12, 24, 28, 29, 39, 46, 54, 59, 61, 64, 66, 68–71] |
| Korea | 9 (17) | [15, 25, 30, 47, 49, 50, 55, 58] |
| United States | 7 (13) | [23, 32, 38, 40, 41, 52, 57] |
| Canada | 2 (4) | [31, 43] |
| Germany | 2 (4) | [34, 60] |
| Spain | 3 (6) | [48, 56, 63] |
| Australia | 1 (2) | [53] |
| Denmark | 1 (2) | [67] |
| Iran | 1 (2) | [33] |
| Israel | 1 (2) | [37] |
| India | 1 (2) | [42] |
| Italy | 1 (2) | [62] |
| Japan | 1 (2) | [44] |
| Minnesota | 1 (2) | [36] |
| Singapore | 1 (2) | [13] |
| Sweden | 1 (2) | [27] |
| Turken | 1 (2) | [35] |
| Türkiye | 1 (2) | [51] |
| United Kingdom | 1 (2) | [45] |
| **Number of participants, n (%)** | | |
| <99 | 17 (33) | [25, 30, 34–36, 38, 47–49, 52, 56, 58, 62, 66, 69–71] |
| 100–999 | 28 (54) | [13, 15, 23, 26, 28, 29, 31, 33, 37, 39–44, 46, 50, 51, 54, 55, 59–61, 63–65, 67, 68] |
| >1,000 | 7 (13) | [12, 24, 27, 32, 45, 53, 57] |
| **Gender, range (%)** | | |
| Female | 2–50 | [12, 13, 15, 24, 28, 30, 31, 33, 35–40, 42, 44–47, 52, 55–60, 62–65, 67, 69, 70] |

(Continued on following page)

TABLE 1 (*Continued*) Characteristics of the included studies (n = 52).

| Characteristics | Studies n (%) | References |
|---|---|---|
| **Participants' health conditions, n (%)** | | |
| Only ADHD | 46 (88) | [12, 13, 15, 23–31, 34–39], [41–52, 54–60, 62–66, 68–71] |
| ADHD and OTHERS | 6 (12) | [32, 33, 40, 53, 61, 67] |

searched articles published from January 2012 to February 2025, and of the 1994 articles retrieved, 52 were eventually included in our scoping review. Over the past 4 years, an increasing number of studies have been published: 9 in 2024, 8 in 2023, 7 in 2022, and 4 in 2021. Tracing its causes, the digital innovation process has stimulated the increasing demand for telemedicine programs, and healthcare systems have increasingly relied on AI technology [72]. In the field of child and adolescent neuropsychiatry, the development and use of online platforms for collecting case histories, demographic, and behavioral information have been steadily increasing [73]. The increase in available data has provided new opportunities for cutting-edge methods such as ML and DL, which used high-dimensional data to build predictive models to capture non-linear relationships across multiple data sources, traditional statistical methods could not achieve [74]. The articles we included focused on AI being used for three purposes in ADHD: early diagnosis, classification, and prediction. None of the included articles were used for other purposes, such as treatment response prediction, prognosis, drug efficacy evaluation, and patient outcomes. Similar to the application of AI in other mental disease, China, the United States and South Korea (32/52, 61.54%) were the countries with largest number of studies related to the use of AI in ADHD.

The data available in the application of AI in ADHD could be roughly divided into the following seven categories: demographic characteristics (gender, age, race, ethnicity, parental education, etc.); parent/teacher report questionnaire; neurocognitive characteristics; brain imaging (fMRI, sMRI, DTI) [20]; genetic data; EEG; eye tracking. Among them, 20 studies included MRI. MRI has demonstrated the possible physiological basis of the disease and is a potential predictor. ML or DL techniques may help identify reliable features and use this as a classification or diagnostic predictor [23]. Zhou, Lin [24] constructed a multimodal ML framework combining Boruta-based feature selection and multi-core learning, integrating sMRI, fMRI and DTI data for early diagnosis of ADHD. Then they used SVM to distinguish ADHD from healthy children. AUC of the model for diagnosing ADHD was 69.8%, and the classification ACC was 64.3%. The reported ACC of existing ADHD classification models varied, with most ranging between 60 and 90% [75]. Despite the success of MRI-based ML models, it has been found that models that incorporated demographic characteristics and/or parent/teacher questionnaires reported higher ACC in classification or diagnosis. One study evaluated parent/teacher ratings of executive function (from BRIEF's Emergent Metacognition Composite score), behavioral/cognitive measures of executive function, measurements of cortical thickness in frontal subregions, and thickness and volume in the parietal cortex, two demographic characteristics (age and child sex), as well as a complete model with four categories. The results showed that the complete model with all the target features achieved a performance ACC of 0.994 in predicting ADHD diagnosis, with 0.926 derived from parent/teacher reports, which was considered critical in classifying ADHD [76]. ADHD was highly heritable (76% heritability) [77]. There was a study that combined multimodal MRI with candidate genetic data [25], including cortical morphology, diffusivity scalars, resting-state functional connectivity and polygenic risk score from norepinephrine, dopamine and glutamate genes. The integration of candidate single nucleotide polymorphism (SNP) data into the best model did not show a meaningful improvement in ACC. Existing studies of modeling using AI technique have all incorporated MRI diagnostic tools, in fact, it is important to acknowledge that neuroimaging data yields very little power [78]. There is still a need to focus on readily available behavioral/clinical data, including demographic information, subjective symptom ratings, and objective neuropsychological data. Integrated modeling approaches could facilitate the development of new approaches to ADHD classification and treatment. New types of data, such as eye tracking, could also be considered in the future in combination with clinical features.

Traditional ML and DL are two branches of AI. In this review, we investigated the characteristics of AI techniques present in the research. Most studies used ML, and the most commonly used algorithm was SVM (34, 65%), followed by RF (17, 33%). SVM by identifying the optimal hyperplane or by mapping nonlinear data into high-dimensional space using kernel functions to realize classification [79]. Its strength resides in its proficiency in managing small sample sizes, high-dimensional data, and nonlinear datasets efficiently, as exemplified when utilizing EEG to analyze ADHD [26]. Nevertheless, it is hindered by significant computational complexity and a heightened sensitivity to parameter adjustments. Conversely, Based on the voting mechanism of the integrated decision tree (DT), RF is good at processing large-scale multimodal data (such as when

TABLE 2 Types of AI techniques used for ADHD (n = 52 studies).

| Types | Studies n (%) | References |
|---|---|---|
| **AI type** | | |
| ML | 40 (76.9) | [13, 15, 23–26, 28–34, 36, 38, 39, 41–49, 52–56, 58, 60, 62–65, 67–70] |
| DL | 5 (9.6) | [35, 50, 51, 61, 66] |
| ML and DL | 7 (13.5) | [12, 27, 37, 40, 57, 61, 71] |
| **AI algorithms/models/methods** [a] | | |
| SVM | 34 (65) | [12, 13, 23, 24, 28–34, 39–46, 48, 49, 52, 54–60, 62, 63, 67, 68, 70] |
| RF | 17 (33) | [12, 15, 24, 27, 32, 33, 36–38, 40, 42, 45, 53, 63, 69–71] |
| DT | 10 (19) | [13, 31, 32, 38, 52, 53, 63, 68, 69, 71] |
| Gradient boosting | 7 (13) | [15, 26, 27, 33, 63, 69, 70] |
| K-nearest neighbors (KNN) | 7 (13) | [27, 31, 38, 42, 43, 45, 68–70] |
| AdaBoost | 6 (12) | [13, 27, 36, 63, 69, 70] |
| LR | 6 (12) | [27, 32, 38, 42, 43, 45] |
| Convolutional neural network (CNN) | 5 (10) | [12, 35, 51, 56, 59, 61] |
| Naive bayes (NB) | 5 (10) | [12, 35, 51, 59, 61, 63] |
| Extreme learning machine (ELM) | 3 (6) | [30, 54, 55] |
| Multi-layer perceptron (MLP) | 3 (6) | [45, 59, 63] |
| Neural network (NN) | 3 (6) | [37, 40, 63] |
| Deep-learning neural network (DNN) | 2 (4) | [27, 66] |
| Linear discriminant (LDA) | 2 (4) | [32, 47] |
| Multinomial regression (MR) | 2 (4) | [40] |
| Recurrent neural network (RNN) | 2 (4) | [50, 71] |
| Categorical lasso | 1 (2) | [32] |
| Classification and regression tree (CART) | 1 (2) | [70] |
| Elastic net regularization (EN) | 1 (2) | [58] |
| Partial least squares (PLS) | 1 (2) | [40] |
| **Purpose of AI algorithms** | | |
| Early diagnosis | 38 (79) | [15, 24, 25, 28–43, 47, 49–57, 59–62, 65–67, 70, 71] |
| Predicting | 10 (14) | [12, 23, 26, 27, 44, 45, 58, 63, 64, 68] |
| Classification | 4 (7) | [13, 46, 48, 69] |
| **Programming languages** [b] | | |
| Python | 6 (12) | [23, 26, 27, 32, 53, 64] |
| R | 5 (10) | [25, 39, 41, 44, 47] |

[a]Some studies used more than one model.
[b]Only 9 studies reported the programming languages used to develop the model.

applying multi-center imaging and clinical data fusion to characterize ADHD) [80], does not require feature selection and is robust, and RF is known for its ability to perform well in classification and regression tasks [81]. However, the high complexity of the model leads to weak interpretability, and overfitting may occur in extreme cases [82]. The application

TABLE 3 Features and categories of data used in the included articles (n = 52 studies).

| Features | Studies n (%) | References |
|---|---|---|
| **Data category** [a] | | |
| Brain imaging | 20 (38) | [23–25, 29–31, 33, 35, 37, 41–43, 46, 54–58, 65, 67] |
| Demographic information | 13 (25) | [28, 29, 37, 38, 41–45, 58, 60, 67] |
| EEG measurements | 10 (19) | [13, 26, 34, 39, 49, 51, 59, 61, 66, 71] |
| Parent/Teacher report questionnaire | 9 (17) | [32, 36, 45, 52, 53, 60, 63, 68, 71] |
| Neurocognitive features | 7 (13) | [36, 37, 44, 50, 52, 60, 62] |
| Eye tracking | 3 (6) | [48, 64, 66] |
| Genetic characteristics | 3 (6) | [12, 25, 58] |
| Behavioral data | 2 (4) | [69, 70] |
| Wearable data | 2 (4) | [15, 40] |
| Others | 3 (6) | [28, 47, 62] |
| **Number of features** | | |
| <99 | 25 (48) | [13, 15, 26, 27, 32–34, 36, 40, 43, 45, 46, 52, 58–60, 62–65, 67–71] |
| 100–999 | 10 (19) | [23, 29, 30, 38, 42, 47, 54, 56, 57, 66] |
| >1,000 | 9 (15) | [12, 24, 25, 31, 41, 49, 51, 53, 55] |
| Not reported | 8 (15) | [28, 35, 37, 39, 44, 48, 50] |
| **Type of data set source** | | |
| Closed | 31 (60) | [12, 13, 15, 23, 26, 34–40, 44, 49, 50, 52, 56–60, 62–71] |
| Open | 21 (40) | [24, 25, 27–33, 40–42, 44, 46–48, 51, 53–55, 61] |

[a]Many studies used more than one data category.

scenarios of the two in the field of ADHD are significantly different: SVM is suitable for accurate classification tasks with limited data but complex features, while RF is more suitable for mining potential patterns in large-scale data. The sample size of ADHD research data is limited, so SVM is more suitable. DT and logistic regression (LR) are rarely used because they are difficult to cope with the high dimensional, non-linear and heterogeneous characteristics of ADHD data [27].

In contrast, DL was used 12 times (23.1%). K-fold CV was used in 34 (34/52, 65%) studies for AI model testing. In the early days, ML was widely used for its simplicity and high efficiency, owing to its advantages over traditional analytical methods based on mass-univariate statistics, especially considering the inter-correction among regions [16]. DL is a particular subtype of ML which is based on deep neural networks (DNNs). In contrast to ML technology, which requires manual extraction of features during image segmentation, DL employs artificial neural networks (ANNS) that allow direct processing of raw data and are particularly useful in identifying complex patterns in high-dimensional fMRI data to maximize model performance for related tasks [83]. Although there are few DL studies, their results are better than those of ML. There are several issues to be noted, one is the limitation of data volume, due to cross-sample reliability/validity and sensitivity and specificity limitations, ADHD diagnosis is primarily based on parent/teacher reports, neuroimaging is not yet part of the routine diagnosis process of ADHD [84]. Most of the MRI data in the published studies come from public databases, such as ADHD-200, the Study of Cognitive Development in the Adolescent Brain (ABCD), and Autism Brain Imaging Data Exchange (ABIDE), which have limited sample size and limited reproducibility [6, 85], the amount of data that is available is still not enough to meet the needs of DL. Secondly, it is the lack of transparency in the learning and testing process of DL that has led them to be called black boxes, and the interpretability of medical algorithms may have become a prerequisite for clinical adoption [86].

A large amount of the studies reported in this paper employed CV methods (44,84.6%), especially k-fold CV. CV, which is one input dataset split into parts, some of which are used as training classifiers (training data), and the remainder is used for validation (test data), this method is relatively economical, and could deal with overfitting and generalization problems to a certain extent

TABLE 4 Validation approaches and performance measures (n = 52 studies).

| Validation and statistics | Studies n (%) | References |
|---|---|---|
| **Validation approach** [a] | | |
| K-fold CV | 34 (65) | [13, 24, 27–35, 37–39, 41–43, 45, 46, 48, 51, 53, 57–64, 68–71] |
| LOOCV | 10 (19) | [25, 26, 28, 47, 50, 52, 54, 56, 61, 62] |
| Not reported | 11 (21) | [12, 15, 23, 36, 40, 44, 49, 55, 65–67] |
| **Confusion matrix** | | |
| Reported | 7 (13) | [35, 36, 50, 51, 53, 61, 63] |
| Not reported | 45 (87) | [12, 13, 15, 23–34], [37–49, 52, 54–60, 62, 64–71] |
| **Performance measures** [b] | | |
| ACC | 45 (87) | [12, 13, 23–31, 33–43], [46–50, 52–54, 56–64, 66–71] |
| Sensitivity | 35 (67) | [12, 13, 15, 24, 26–29, 31, 33, 36–42, 44, 46, 47, 50–53, 55–57, 60–64, 67, 69, 71] |
| Specificity | 35 (67) | [12, 13, 15, 24, 26–29, 31, 33, 36–42, 44, 46, 47, 50–53, 55–57, 60–64, 67, 69, 70] |
| AUC | 26 (50) | [12, 15, 24, 25, 27, 29, 32, 35, 38, 40, 45, 46, 48, 49, 53, 54, 58–65, 69, 70] |
| F1-score | 11 (21) | [23, 26, 35, 45, 46, 50, 55, 61, 64, 68, 71] |
| Precision | 8 (15) | [26, 35, 45, 53, 55, 64, 68, 71] |
| Recall | 5 (10) | [35, 45, 55, 69, 71] |
| False-negative | 3 (6) | [36, 48, 50] |
| False-positive | 3 (6) | [36, 48, 50] |
| Negative predictive value | 3 (6) | [15, 27, 33] |
| Positive predictive value | 2 (4) | [15, 33] |
| Kappa | 1 (2) | [40] |
| J-statistic | 1 (2) | [46] |
| Positive predicted power | 1 (2) | [27] |
| True-negative | 1 (2.4) | [36] |
| True-positive | 1 (2.4) | [36] |

[a]Total number does not add up, as many studies used more than one validation method.
[b]Total number does not add up, as many studies used more than one performance measure.

[87]. However, due to the unbalanced nature of the number of features and the number of subjects in each study, as well as the high heterogeneity of the study sample, the generalization is still limited. Moreover, internal verification cannot guarantee the quality of ML model, it has no extrapolation [87]. Leave-one-out CV (LOOCV) is a special form of k-fold CV, which divides the data set into N subsets (N is the total number of samples). Only 1 sample is retained as the test set each time, and the remaining N-1 samples are repeated for N times. Finally, the average value of all test results is taken as the model evaluation index [28, 88]. This verification method can maximize the data utilization rate and is suitable for capturing the heterogeneity among ADHD individuals (such as the differences in neural markers of different subtypes). However, due to the high computational cost, it is not friendly to multi-modal high-dimensional data (such as fMRI), and can only be used for small data sets [28, 89]. AI requires large datasets to train models in order to avoid over-fitting and improve generalization. Only seven studies used datasets with more than 1,000 data points, and 21 studies used open datasets. In order to reflect the actual performance of the AI model in neuropsychiatric diseases, the model needed to be tested on multiple data sets to ensure its extrapolation [6]. AI models in future should be trained and validated in larger datasets [90]. DL has no advantage over ML in terms of classification and consumes more resources. However, the emergence of DL will further continue in the era of pediatric clinical studies because

TABLE 5 Overview of performance of AI models.

| Performance measures | Results (%), mean (range) |
|---|---|
| Precision | 92.53 (80–95) |
| AUC | 83.77 (57.6–99.64) |
| ACC | 83.06 (53.2–98.23) |
| Specificity | 84.08 (58.8–99.11) |
| F1-score | 85.21 (48.89–95) |
| Sensitivity | 74.67 (33–98.24) |

of its lesser reliance upon the existence of engineered features [91].

## Comparison with previous studies

So far, we had retrieved five reviews on the use of AI in ADHD. A summative review explored the complex interaction of multiple cognitive, genetic and biological factors related to ADHD underling the ML-based algorithm [5]. The authors reported the significance of ML models in ADHD research. Loh, Ooi [92] conducted a systematic review by following PRISMA guidelines and focused on the diagnostic value of AI-based, they identified existing diagnostic tools for ADHD that are commonly used: EEG, MRI, questionnaires, exercise data, performance tests, etc. From the perspective of each diagnostic tool, the most commonly used features were discussed. Pereira-Sanchez and Castellanos [93] provided a brief narrative review of recent AI studies using sMRI and fMRI in ADHD patients, focusing on meta-analyses, large analyses, and proposed novel multimodal approaches. Periyasamy, Vibashan [20] provided a literature review on the application of AI in ADHD. In studies focusing on the use of MRI data, the feature extraction, dimensionality reduction/feature selection, and classification techniques were compared. Taspinar and Ozkurt [19] reported a review focusing on the inclusion of studies using sMRI data. Our scoping review focused on the role of AI techniques in the diagnosis, classification, and prediction of ADHD, following PRISMA guidelines. Provide the purpose and characteristics of all AI technologies listed in the study by reviewing the data sources and platforms used by the AI model. Hopefully, our findings will contribute to further ADHD research.

## Limitations

This study had the following limitations. This review did not include articles related to the prognosis, treatment, and drug discovery of ADHD. The review was limited to journal articles written in English, while papers, review articles, conference abstracts, and review reports were excluded to reduce the complexity of the results. In fact, many research articles in the field of computers are published in full through conferences. In addition to popular public databases, half of the studies used private datasets, there was heterogeneity between studies in the methods and datasets used to generate assessment measures, such as the number of participants, data collection methods, and validation methods used. Finally, we only searched four commonly used databases, and there may have been omissions in some unsearched databases.

# Conclusion

This scoping review is undertaken to support the existing evidence on the role of AI techniques in ADHD. We summarized AI models and algorithms for prediction, early diagnosis, and classification. Research into the application of AI to ADHD is still in its infancy, but early attempts to study ADHD using AI have shown promising results. Translating research into clinical practice still has a long way to go, and more explainable AI research and public education initiatives are needed. We believe that this review will help the scientific community better understand the application of AI techniques in ADHD.

# Author contributions

Conceptualization, FC; methodology, BS; software, BS; validation, HH and BL; formal analysis, BS and FC; investigation, BW; resources, BW; data curation, HH and BL; writing – original draft preparation, BS and FC; writing – review and editing, BS, FC, HH, BL, and BW; visualization, FC; supervision, BW; project administration, BS. All authors contributed to the article and approved the submitted version.

# Funding

The author(s) declare that no financial support was received for the research and/or publication of this article.

# Conflict of interest

The author(s) declared no potential conflicts of interest with respect to the research, authorship, and/or publication of this article.

# Supplementary material

The Supplementary Material for this article can be found online at: https://www.ebm-journal.org/articles/10.3389/ebm.2025.10238/full#supplementary-material

# References


1. Riglin L, Leppert B, Langley K, Thapar AK, O'Donovan MC, Davey Smith G, et al. Investigating attention-deficit hyperactivity disorder and autism spectrum disorder traits in the general population: what happens in adult life? *J Child Psychol Psychiatry* (2021) **62**:449–57. doi:10.1111/jcpp.13297

2. Polanczyk GV, Salum GA, Sugaya LS, Caye A, Rohde LA. Annual research review: a meta-analysis of the worldwide prevalence of mental disorders in children and adolescents. *J Child Psychol Psychiatry* (2015) **56**:345–65. doi:10.1111/jcpp.12381

3. Sibley MH, Swanson JM, Arnold LE, Hechtman LT, Owens EB, Stehli A, et al. Defining ADHD symptom persistence in adulthood: optimizing sensitivity and specificity. *J Child Psychol Psychiatry* (2017) **58**:655–62. doi:10.1111/jcpp.12620

4. Mahone EM, Denckla MB. Attention-deficit/hyperactivity disorder: a historical neuropsychological perspective. *J Int Neuropsychological Soc* (2017) **23**:916–29. doi:10.1017/s1355617717000807

5. Cao M, Martin E, Li X. Machine learning in attention-deficit/hyperactivity disorder: new approaches toward understanding the neural mechanisms. *Transl Psychiatry* (2023) **13**:236. doi:10.1038/s41398-023-02536-w

6. Eslami T, Almuqhim F, Raiker JS, Saeed F. Machine learning methods for diagnosing autism spectrum disorder and attention- deficit/hyperactivity disorder using functional and structural MRI: a survey. *Front Neuroinform* (2020) **14**: 575999. doi:10.3389/fninf.2020.575999

7. Kessi M, Duan H, Xiong J, Chen B, He F, Yang L, et al. Attention-deficit/hyperactive disorder updates. *Front Mol Neurosci* (2022) **15**:925049. doi:10.3389/fnmol.2022.925049

8. Luo Y, Weibman D, Halperin JM, Li X. A review of heterogeneity in attention deficit/hyperactivity disorder (ADHD). *Front Hum Neurosci* (2019) **13**:42. doi:10.3389/fnhum.2019.00042

9. Elam JS, Glasser MF, Harms MP, Sotiropoulos SN, Andersson JLR, Burgess GC, et al. The human connectome project: a retrospective. *NeuroImage* (2021) **244**: 118543. doi:10.1016/j.neuroimage.2021.118543

10. Connaughton M, Whelan R, O'Hanlon E, McGrath J. White matter microstructure in children and adolescents with ADHD. *NeuroImage Clin* (2022) **33**:102957. doi:10.1016/j.nicl.2022.102957

11. Demontis D, Walters RK, Martin J, Mattheisen M, Als TD, Agerbo E, et al. Discovery of the first genome-wide significant risk loci for attention deficit/hyperactivity disorder. *Nat Genet* (2019) **51**:63–75. doi:10.1038/s41588-018-0269-7

12. Liu L, Feng X, Li H, Cheng Li S, Qian Q, Wang Y. Deep learning model reveals potential risk genes for ADHD, especially Ephrin receptor gene EPHA5. *Brief Bioinform* (2021) **22**:bbab207. doi:10.1093/bib/bbab207

13. Koh JEW, Ooi CP, Lim-Ashworth NS, Vicnesh J, Tor HT, Lih OS, et al. Automated classification of attention deficit hyperactivity disorder and conduct disorder using entropy features with ECG signals. *Comput Biol Med* (2022) **140**: 105120. doi:10.1016/j.compbiomed.2021.105120

14. Yoo JH, Kang C, Lim JS, Wang B, Choi CH, Hwang H, et al. Development of an innovative approach using portable eye tracking to assist ADHD screening: a machine learning study. *Front Psychiatry* (2024) **15**:1337595. doi:10.3389/fpsyt.2024.1337595

15. Kim WP, Kim HJ, Pack SP, Lim JH, Cho CH, Lee HJ. Machine learning-based prediction of attention-deficit/hyperactivity disorder and sleep problems with wearable data in children. *JAMA Netw Open* (2023) **6**:e233502. doi:10.1001/jamanetworkopen.2023.3502

16. Vieira S, Pinaya WH, Mechelli A. Using deep learning to investigate the neuroimaging correlates of psychiatric and neurological disorders: methods and applications. *Neurosci and Biobehavioral Rev* (2017) **74**:58–75. doi:10.1016/j.neubiorev.2017.01.002

17. Gaggioli A. Quality of experience in real and virtual environments: some suggestions for the development of positive technologies. *Stud Health Technol Inform* (2012) **181**:177–81. doi:10.3233/978-1-61499-121-2-177

18. Zhang Z, Li G, Xu Y, Tang X. Application of artificial intelligence in the MRI classification task of human brain neurological and psychiatric diseases: a scoping review. *Diagnostics (Basel, Switzerland)* (2021) **11**:1402. doi:10.3390/diagnostics11081402

19. Taspinar G, Ozkurt N. A review of ADHD detection studies with machine learning methods using rsfMRI data. *NMR Biomed* (2024) **37**:e5138. doi:10.1002/nbm.5138

20. Periyasamy R, Vibashan VS, Varghese GT, Aleem MA. Machine learning techniques for the diagnosis of attention-deficit/hyperactivity disorder from magnetic resonance imaging: a concise review. *Neurol India* (2021) **69**:1518–23. doi:10.4103/0028-3886.333520

21. Tricco AC, Lillie E, Zarin W, O'Brien KK, Colquhoun H, Levac D, et al. PRISMA extension for scoping reviews (PRISMA-ScR): checklist and explanation. *Ann Intern Med* (2018) **169**:467–73. doi:10.7326/m18-0850

22. Cumpston M, Li T, Page MJ, Chandler J, Welch VA, Higgins JP, et al. Updated guidance for trusted systematic reviews: a new edition of the Cochrane Handbook for Systematic Reviews of Interventions. *Cochrane Database Syst Rev* (2019) **10**: Ed000142. doi:10.1002/14651858.ED000142

23. Öztekin I, Garic D, Bayat M, Hernandez ML, Finlayson MA, Graziano PA, et al. Structural and diffusion-weighted brain imaging predictors of attention-deficit/hyperactivity disorder and its symptomology in very young (4- to 7-year-old) children. *Eur J Neurosci* (2022) **56**:6239–57. doi:10.1111/ejn.15842

24. Zhou X, Lin Q, Gui Y, Wang Z, Liu M, Lu H. Multimodal MR images-based diagnosis of early adolescent attention-deficit/hyperactivity disorder using multiple kernel learning. *Front Neurosci* (2021) **15**:710133. doi:10.3389/fnins.2021.710133

25. Yoo JH, Kim JI, Kim BN, Jeong B. Exploring characteristic features of attention-deficit/hyperactivity disorder: findings from multi-modal MRI and candidate genetic data. *Brain Imaging Behav* (2020) **14**:2132–47. doi:10.1007/s11682-019-00164-x

26. Kim JW, Kim BN, Kim JI, Yang CM, Kwon J. Electroencephalogram (EEG) based prediction of attention deficit hyperactivity disorder (ADHD) using machine learning. *Neuropsychiatr Dis Treat* (2025) **21**:271–9. doi:10.2147/ndt.s509094

27. Garcia-Argibay M, Zhang-James Y, Cortese S, Lichtenstein P, Larsson H, Faraone SV. Predicting childhood and adolescent attention-deficit/hyperactivity disorder onset: a nationwide deep learning approach. *Mol Psychiatry* (2023) **28**: 1232–9. doi:10.1038/s41380-022-01918-8

28. Wang XH, Jiao Y, Li L. Identifying individuals with attention deficit hyperactivity disorder based on temporal variability of dynamic functional connectivity. *Sci Rep* (2018) **8**:11789. doi:10.1038/s41598-018-30308-w

29. Tan L, Guo X, Ren S, Epstein JN, Lu LJ. A computational model for the automatic diagnosis of attention deficit hyperactivity disorder based on functional brain volume. *Front Comput Neurosci* (2017) **11**:75. doi:10.3389/fncom.2017.00075

30. Qureshi MN, Min B, Jo HJ, Lee B. Multiclass classification for the differential diagnosis on the ADHD subtypes using recursive feature elimination and hierarchical extreme learning machine: structural MRI study. *PLoS One* (2016) **11**:e0160697. doi:10.1371/journal.pone.0160697

31. Ghiassian S, Greiner R, Jin P, Brown MR. Using functional or structural magnetic resonance images and personal characteristic data to identify ADHD and autism. *PLoS One* (2016) **11**:e0166934. doi:10.1371/journal.pone.0166934

32. Duda M, Ma R, Haber N, Wall DP. Use of machine learning for behavioral distinction of autism and ADHD. *Transl Psychiatry* (2016) **6**:e732. doi:10.1038/tp.2015.221

33. Rezaei M, Zare H, Hakimdavoodi H, Nasseri S, Hebrani P. Classification of drug-naive children with attention-deficit/hyperactivity disorder from typical development controls using resting-state fMRI and graph theoretical approach. *Front Hum Neurosci* (2022) **16**:948706. doi:10.3389/fnhum.2022.948706

34. Muthuraman M, Moliadze V, Boecher L, Siemann J, Freitag CM, Groppa S, et al. Multimodal alterations of directed connectivity profiles in patients with attention-deficit/hyperactivity disorders. *Sci Rep* (2019) **9**:20028. doi:10.1038/s41598-019-56398-8

35. Uyulan C, Erguzel TT, Turk O, Farhad S, Metin B, Tarhan N. A class activation map-based interpretable transfer learning model for automated detection of ADHD from fMRI data. *Clin EEG Neurosci* (2023) **54**:151–9. doi:10.1177/15500594221122699

36. Heller MD, Roots K, Srivastava S, Schumann J, Srivastava J, Hale TS. A machine learning-based analysis of game data for attention deficit hyperactivity disorder assessment. *Games Health J* (2013) **2**:291–8. doi:10.1089/g4h.2013.0058

37. Slobodin O, Yahav I, Berger I. A machine-based prediction model of ADHD using CPT data. *Front Hum Neurosci* (2020) **14**:560021. doi:10.3389/fnhum.2020.560021

38. Das W, Khanna S. A robust machine learning based framework for the automated detection of ADHD using pupillometric biomarkers and time series analysis. *Sci Rep* (2021) **11**:16370. doi:10.1038/s41598-021-95673-5

39. Luo N, Luo X, Zheng S, Yao D, Zhao M, Cui Y, et al. Aberrant brain dynamics and spectral power in children with ADHD and its subtypes. *Eur Child Adolesc Psychiatry* (2023) **32**:2223–34. doi:10.1007/s00787-022-02068-6

40. Faedda GL, Ohashi K, Hernandez M, McGreenery CE, Grant MC, Baroni A, et al. Actigraph measures discriminate pediatric bipolar disorder from attention-deficit/hyperactivity disorder and typically developing controls. *J Child Psychol Psychiatry* (2016) **57**:706–16. doi:10.1111/jcpp.12520

41. Colby JB, Rudie JD, Brown JA, Douglas PK, Cohen MS, Shehzad Z. Insights into multimodal imaging classification of ADHD. *Front Syst Neurosci* (2012) **6**:59. doi:10.3389/fnsys.2012.00059

42. Lohani DC, Rana B. ADHD diagnosis using structural brain MRI and personal characteristic data with machine learning framework. *Psychiatry Res Neuroimaging* (2023) **334**:111689. doi:10.1016/j.pscychresns.2023.111689

43. Brown MR, Sidhu GS, Greiner R, Asgarian N, Bastani M, Silverstone PH, et al. ADHD-200 Global Competition: diagnosing ADHD using personal characteristic data can outperform resting state fMRI measurements. *Front Syst Neurosci* (2012) **6**: 69. doi:10.3389/fnsys.2012.00069

44. Yasumura A, Omori M, Fukuda A, Takahashi J, Yasumura Y, Nakagawa E, et al. Applied machine learning method to predict children with ADHD using prefrontal cortex activity: a multicenter study in Japan. *J Atten Disord* (2020) **24**: 2012–20. doi:10.1177/1087054717740632

45. Ter-Minassian L, Viani N, Wickersham A, Cross L, Stewart R, Velupillai S, et al. Assessing machine learning for fair prediction of ADHD in school pupils using a retrospective cohort study of linked education and healthcare data. *BMJ Open* (2022) **12**:e058058. doi:10.1136/bmjopen-2021-058058

46. Dai D, Wang J, Hua J, He H. Classification of ADHD children through multimodal magnetic resonance imaging. *Front Syst Neurosci* (2012) **6**:63. doi:10.3389/fnsys.2012.00063

47. Yang CM, Shin J, Kim JI, Lim YB, Park SH, Kim BN. Classifying children with ADHD based on prefrontal functional near-infrared spectroscopy using machine learning. *Clin Psychopharmacol Neurosci* (2023) **21**:693–700. doi:10.9758/cpn.22.1025

48. Varela Casal P, Lorena Esposito F, Morata Martínez I, Capdevila A, Solé Puig M, de la Osa N, et al. Clinical validation of eye vergence as an objective marker for diagnosis of ADHD in children. *J Atten Disord* (2019) **23**:599–614. doi:10.1177/1087054717749931

49. Abibullaev B, An J. Decision support algorithm for diagnosis of ADHD using electroencephalograms. *J Med Syst* (2012) **36**:2675–88. doi:10.1007/s10916-011-9742-x

50. Lee W, Lee S, Lee D, Jun K, Ahn DH, Kim MS. Deep learning-based ADHD and ADHD-RISK classification technology through the recognition of children's abnormal behaviors during the robot-led ADHD screening game. *Sensors (Basel)* (2022) **23**:278. doi:10.3390/s23010278

51. Esas MY, Latifoğlu F. Detection of ADHD from EEG signals using new hybrid decomposition and deep learning techniques. *J Neural Eng* (2023) **20**:036028. doi:10.1088/1741-2552/acc902

52. Bledsoe JC, Xiao C, Chaovalitwongse A, Mehta S, Grabowski TJ, Semrud-Clikeman M, et al. Diagnostic classification of ADHD versus control: support vector machine classification using brief neuropsychological assessment. *J Atten Disord* (2020) **24**:1547–56. doi:10.1177/1087054716649666

53. Haque UM, Kabir E, Khanam R. Early detection of paediatric and adolescent obsessive-compulsive, separation anxiety and attention deficit hyperactivity disorder using machine learning algorithms. *Health Inf Sci Syst* (2023) **11**:31. doi:10.1007/s13755-023-00232-z

54. Peng X, Lin P, Zhang T, Wang J. Extreme learning machine-based classification of ADHD using brain structural MRI data. *PLoS One* (2013) **8**: e79476. doi:10.1371/journal.pone.0079476

55. Qureshi MNI, Oh J, Min B, Jo HJ, Lee B. Multi-modal, multi-measure, and multi-class discrimination of ADHD with hierarchical feature extraction and extreme learning machine using structural and functional brain MRI. *Front Hum Neurosci* (2017) **11**:157. doi:10.3389/fnhum.2017.00157

56. O'Mahony N, Florentino-Liano B, Carballo JJ, Baca-García E, Rodríguez AA. Objective diagnosis of ADHD using IMUs. *Med Eng and Phys* (2014) **36**:922–6. doi:10.1016/j.medengphy.2014.02.023

57. Lin H, Haider SP, Kaltenhauser S, Mozayan A, Malhotra A, Constable RT, et al. Population level multimodal neuroimaging correlates of attention-deficit hyperactivity disorder among children. *Front Neurosci* (2023) **17**:1138670. doi:10.3389/fnins.2023.1138670

58. Kim JW, Sharma V, Ryan ND. Predicting methylphenidate response in ADHD using machine learning approaches. *Int J Neuropsychopharmacol* (2015) **18**: pyv052. doi:10.1093/ijnp/pyv052

59. Chen H, Song Y, Li X. Use of deep learning to detect personalized spatial-frequency abnormalities in EEGs of children with ADHD. *J Neural Eng* (2019) **16**: 066046. doi:10.1088/1741-2552/ab3a0a

60. Mikolas P, Vahid A, Bernardoni F, Süß M, Martini J, Beste C, et al. Training a machine learning classifier to identify ADHD based on real-world clinical data from medical records. *Sci Rep* (2022) **12**:12934. doi:10.1038/s41598-022-17126-x

61. Cheng Y, Han L, Wu L, Chen J, Sun H, Wen G, et al. Effect of first-line serplulimab vs placebo added to chemotherapy on survival in patients with extensive-stage small cell lung cancer: the ASTRUM-005 randomized clinical trial. *Jama* (2022) **328**:1223–32. doi:10.1001/jama.2022.16464

62. Crippa A, Salvatore C, Molteni E, Mauri M, Salandi A, Trabattoni S, et al. The utility of a computerized algorithm based on a multi-domain profile of measures for the diagnosis of attention deficit/hyperactivity disorder. *Front Psychiatry* (2017) **8**: 189. doi:10.3389/fpsyt.2017.00189

63. Navarro-Soria I, Rico-Juan JR, Juárez-Ruiz de Mier R, Lavigne-Cervan R. Prediction of attention deficit hyperactivity disorder based on explainable artificial intelligence. *Appl Neuropsychol Child* (2024) 1–14. doi:10.1080/21622965.2024.2336019

64. Liu Z, Li J, Zhang Y, Wu D, Huo Y, Yang J, et al. Auxiliary diagnosis of children with attention-deficit/hyperactivity disorder using eye-tracking and digital biomarkers: case-control study. *JMIR Mhealth Uhealth* (2024) **12**:e58927. doi:10.2196/58927

65. Chiang HL, Wu CS, Chen CL, Tseng WYI, Gau SS. Machine-learning-based feature selection to identify attention-deficit hyperactivity disorder using whole-brain white matter microstructure: a longitudinal study. *Asian J Psychiatry* (2024) **97**:104087. doi:10.1016/j.ajp.2024.104087

66. Zhang KF, Yeh SC, Hsiao-Kuang Wu E, Xu X, Tsai HJ, Chen CC. Fusion of multi-task neurophysiological data to enhance the detection of attention- deficit/hyperactivity disorder. *IEEE J Transl Eng Health Med* (2024) **12**:668–74. doi:10.1109/jtehm.2024.3435553

67. Blair RJR, Bashford-Largo J, Dominguez A, Dobbertin M, Blair KS, Bajaj S. Using machine learning to determine a functional classifier of reward responsiveness and its association with adolescent psychiatric symptomatology. *Psychol Med* (2024) **54**:4212–21. doi:10.1017/s003329172400240x

68. Wang G, Li W, Huang S, Chen Z. A prospective study of an early prediction model of attention deficit hyperactivity disorder based on artificial intelligence. *J Atten Disord* (2024) **28**:302–9. doi:10.1177/10870547231211360

69. Chiu YH, Lee YH, Wang SY, Ouyang CS, Wu RC, Yang RC, et al. Objective approach to diagnosing attention deficit hyperactivity disorder by using pixel subtraction and machine learning classification of outpatient consultation videos. *J Neurodevelopmental Disord* (2024) **16**:71. doi:10.1186/s11689-024-09588-z

70. Ouyang CS, Yang RC, Wu RC, Chiang CT, Chiu YH, Lin LC. Objective and automatic assessment approach for diagnosing attention-deficit/hyperactivity disorder based on skeleton detection and classification analysis in outpatient videos. *Child Adolesc Psychiatry Ment Health* (2024) **18**:60. doi:10.1186/s13034-024-00749-5

71. Chen IC, Chang CL, Chang MH, Ko LW. The utility of wearable electroencephalography combined with behavioral measures to establish a practical multi-domain model for facilitating the diagnosis of young children with attention-deficit/hyperactivity disorder. *J Neurodevelopmental Disord* (2024) **16**:62. doi:10.1186/s11689-024-09578-1

72. Perez DL, Biffi A, Camprodon JA, Caplan DN, Chemali Z, Kritzer MD, et al. Telemedicine in behavioral neurology-neuropsychiatry: opportunities and challenges catalyzed by COVID-19. *Cogn Behav Neurol* (2020) **33**:226–9. doi:10.1097/wnn.0000000000000239

73. Grazioli S, Crippa A, Rosi E, Candelieri A, Ceccarelli SB, Mauri M, et al. Exploring telediagnostic procedures in child neuropsychiatry: addressing ADHD diagnosis and autism symptoms through supervised machine learning. *Eur Child Adolesc Psychiatry* (2024) **33**:139–49. doi:10.1007/s00787-023-02145-4

74. Allesøe RL, Thompson WK, Bybjerg-Grauholm J, Hougaard DM, Nordentoft M, Werge T, et al. Deep learning for cross-diagnostic prediction of mental disorder diagnosis and prognosis using Danish nationwide register and genetic data. *JAMA psychiatry* (2023) **80**:146–55. doi:10.1001/jamapsychiatry.2022.4076

75. Quaak M, van de Mortel L, Thomas RM, van Wingen G. Deep learning applications for the classification of psychiatric disorders using neuroimaging data: systematic review and meta-analysis. *NeuroImage Clin* (2021) **30**:102584. doi:10.1016/j.nicl.2021.102584

76. Öztekin I, Finlayson MA, Graziano PA, Dick AS. Is there any incremental benefit to conducting neuroimaging and neurocognitive assessments in the diagnosis of ADHD in young children? A machine learning investigation. *Developmental Cogn Neurosci* (2021) **49**:100966. doi:10.1016/j.dcn.2021.100966

77. Faraone SV, Larsson H. Genetics of attention deficit hyperactivity disorder. *Mol Psychiatry* (2019) **24**:562–75. doi:10.1038/s41380-018-0070-0

78. Hoogman M, Bralten J, Hibar DP, Mennes M, Zwiers MP, Schweren LSJ, et al. Subcortical brain volume differences in participants with attention deficit hyperactivity disorder in children and adults: a cross-sectional mega-analysis. *The lancet Psychiatry* (2017) **4**:310–9. doi:10.1016/s2215-0366(17)30049-4

79. Barberis E, Khoso S, Sica A, Falasca M, Gennari A, Dondero F, et al. Precision medicine approaches with metabolomics and artificial intelligence. *Int J Mol Sci* (2022) **23**:11269. doi:10.3390/ijms231911269

80. Sharma CM, Chariar VM. Diagnosis of mental disorders using machine learning: literature review and bibliometric mapping from 2012 to 2023. *Heliyon* (2024) **10**:e32548. doi:10.1016/j.heliyon.2024.e32548

81. Hu J, Szymczak S. A review on longitudinal data analysis with random forest. *Brief Bioinform* (2023) **24**:bbad002. doi:10.1093/bib/bbad002

82. Roman-Naranjo P, Parra-Perez AM, Lopez-Escamez JA. A systematic review on machine learning approaches in the diagnosis and prognosis of rare genetic diseases. *J Biomed Inform* (2023) **143**:104429. doi:10.1016/j.jbi.2023.104429

83. Eitel F, Schulz MA, Seiler M, Walter H, Ritter K. Promises and pitfalls of deep neural networks in neuroimaging-based psychiatric research. *Exp Neurol* (2021) **339**:113608. doi:10.1016/j.expneurol.2021.113608

84. Takahashi N, Ishizuka K, Inada T. Peripheral biomarkers of attention-deficit hyperactivity disorder: current status and future perspective. *J Psychiatr Res* (2021) **137**:465–70. doi:10.1016/j.jpsychires.2021.03.012

85. Button KS, Ioannidis JP, Mokrysz C, Nosek BA, Flint J, Robinson ES, et al. Power failure: why small sample size undermines the reliability of neuroscience. *Nat Rev Neurosci* (2013) **14**:365–76. doi:10.1038/nrn3475

86. Lapuschkin S, Wäldchen S, Binder A, Montavon G, Samek W, Müller KR. Unmasking Clever Hans predictors and assessing what machines really learn. *Nat Commun* (2019) **10**:1096. doi:10.1038/s41467-019-08987-4

87. Ho SY, Phua K, Wong L, Bin Goh WW. Extensions of the external validation for checking learned model interpretability and generalizability. *Patterns (New York, NY)* (2020) **1**:100129. doi:10.1016/j.patter.2020.100129

88. Shao Z, Er MJ, Wang N. An efficient leave-one-out cross-validation-based extreme learning machine (ELOO-ELM) with minimal user intervention. *IEEE Trans Cybern* (2016) **46**:1939–51. doi:10.1109/tcyb.2015.2458177

89. Wang XH, Jiao Y, Li L. Diagnostic model for attention-deficit hyperactivity disorder based on interregional morphological connectivity. *Neurosci Lett* (2018) **685**:30–4. doi:10.1016/j.neulet.2018.07.029

90. Zhang-James Y, Helminen EC, Liu J, Busatto GF, Calvo A, Cercignani M, et al. Evidence for similar structural brain anomalies in youth and adult attention-deficit/hyperactivity disorder: a machine learning analysis. *Transl Psychiatry* (2021) **11**:82. doi:10.1038/s41398-021-01201-4

91. Sargolzaei S. Can deep learning hit a moving target? A scoping review of its role to study neurological disorders in children. *Front Comput Neurosci* (2021) **15**:670489. doi:10.3389/fncom.2021.670489

92. Loh HW, Ooi CP, Barua PD, Palmer EE, Molinari F, Acharya UR. Automated detection of ADHD: current trends and future perspective. *Comput Biol Med* (2022) **146**:105525. doi:10.1016/j.compbiomed.2022.105525

93. Pereira-Sanchez V, Castellanos FX. Neuroimaging in attention-deficit/hyperactivity disorder. *Curr Opin Psychiatry* (2021) **34**:105–11. doi:10.1097/yco.0000000000000669

EBM Experimental Biology and Medicine

TYPE Original Research
PUBLISHED 28 February 2025
DOI 10.3389/ebm.2025.10321



OPEN ACCESS

*CORRESPONDENCE
Yeyan Cai,
35689374@wmu.edu.cn

†These authors have contributed equally to this work and share first authorship

RECEIVED 19 July 2024
ACCEPTED 13 February 2025
PUBLISHED 28 February 2025

CITATION
Yang X, Zhao Y, Yu S, Chi L and Cai Y (2025) Coenzyme Q10 alleviates neurological deficits in a mouse model of intracerebral hemorrhage by reducing inflammation and apoptosis. *Exp. Biol. Med.* 250:10321. doi: 10.3389/ebm.2025.10321



# Coenzyme Q10 alleviates neurological deficits in a mouse model of intracerebral hemorrhage by reducing inflammation and apoptosis

Xiaoqing Yang[1†], Yi Zhao[2†], Sisi Yu[1], Lihui Chi[1] and Yeyan Cai[1*]

[1]Department of Neurosurgery, Ruian People's Hospital, The Third Affiliated Hospital of Wenzhou Medical University, Wenzhou, Zhejiang, China, [2]Department of Traditional Chinese Medicine, Ruian Tangxia People's Hospital, Wenzhou, Zhejiang, China

## Abstract

This research study was directed towards to assessing whether coenzyme Q10 (CoQ10) is linked to neuroprotection and induces anti-inflammatory and anti-neuronal death responses in an Intracerebral hemorrhage (ICH) mouse model via right caudate nucleus injection with collagenase VII. Autologous blood was injected into mice to induce ICH. We found that FoxM1 was upregulated in the ICH-injured animals. Moreover, CoQ10 treatment effectively ameliorated neurological deficits, mitigated cerebral edema, and minimized hematoma in model mice, demonstrating dose-dependent efficacy and promoting the functional recovery of the animals. ELISA and real-time PCR assays of pro-inflammatory cytokines indicated that CoQ10 was capable of alleviating neuroinflammation in ICH. In line with the part of CoQ10 in attenuating the inflammatory response, CoQ10 also suppressed cell apoptosis in the ICH-injured brain, which partly accounts for its neuroprotective effect. Furthermore, our analysis of different inflammatory pathways indicated that CoQ10 targeted the nuclear factor-kappa B signaling axis. Our findings suggest that CoQ10 protects against ICH by mitigating neuroinflammatory responses and preventing neuronal apoptosis, with the underlying mechanism possibly being connected with nuclear factor-kappa B pathway regulation. Therefore, CoQ10 holds significant potential as a therapeutic strategy for treating ICH.

KEYWORDS

**intracerebral hemorrhage, coenzyme Q10, autologous blood injection, inflammation, apoptosis**

## Impact statement

This study verified the function of CoQ10 in protecting against brain injury caused by ICH and that its neuroprotective effect is in part due to its inhibition of pro-inflammatory cytokine secretion and neuronal death. Moreover, CoQ10 was confirmed to suppress pro-inflammatory cytokine secretion by inhibiting p65 phosphorylation.

# Introduction

Intracerebral hemorrhage (ICH), including the rupture of cerebral blood vessel and blood leakage into the cerebral parenchyma [1, 2], takes up 10%–15% in stroke cases and exhibits a high incidence and mortality [3]. Cerebral impairment resulting from ICH occurs in two stages. The initial bleeding destroys the brain cell structure while the hematoma induces elevated intracranial pressure, thereby affecting blood circulation and causing brain herniation [4]. The second stage, which can be avoided, will continue for several hours or days [5, 6] and includes local inflammation [7], the generation of clotting components, and impairment of the perihematomal tissues (such as the blood–brain barrier) [8]. Some proofs indicate that secondary injury may be triggered by the generation of thrombin, hemoglobin, and iron [9–12]. Therefore, efficient treatment of hemorrhagic stroke-induced secondary impairments is warranted.

Ubiquinone, also known as CoQ10, is a kind of lipophilic, vitamin-like compound which plays a pivotal role in the mitochondrial electron transport system and contributing to ATP biosynthesis [13]. It is generally acknowledged that CoQ10 exhibits potent antioxidant effects and also enhances defensive effects of other antioxidative enzymes [14]. Aside from protecting neuronal cells via its antioxidative activity, CoQ10 has demonstrated the ability to improve brain-derived neurotrophic factor (BDNF) levels and enhance its signaling pathway in the brain, which accounts for its neuroprotective effects [15]. The effects of CoQ10 have been proven in numerous neurological diseases [16, 17]. Meanwhile, several reports have investigated the neuroprotective impacts of CoQ10 in a variety of stroke models, such as symptomatic vasospasm-triggered ischemic brain lesions [18]. Moreover, CoQ10 administration has been shown to ease venous ischemia/reperfusion injuries [19]. However, studies on the neuroprotective role of CoQ10 during ICH development and pathogenesis are scarce. Therefore, this research was designed to explore the neuroprotective impacts of CoQ10 against neurological deficits caused by ICH damage and the underlying molecular mechanism.

# Materials and methods

## Laboratory animals

Male C57BL/6 mice, with a weight range of 18.0–20.0 g, were acquired from Vital River Biotechnology Co., Ltd., China. All animal-related experiment operations had obtained the approval of Animal Care and Use Committee of Ruian People's Hospital, the Third Affiliated Hospital of Wenzhou Medical University, in full accordance with the ARRIVE guidelines. Mice were raised in individual cages under a 12-h light and dark cycle in controlled temperature conditions, and provided sufficient food and water.

## Experimental grouping

To examine the impacts of CoQ10 administration in an animal model of ICH, 36 C57 mice were arbitrarily allocated to six groups, consisting of a sham group (n = 6) and five ICH subgroups (n = 30, successful ICH mode number). The five subgroups that had been subjected to ICH injury were as follows (each n = 6): ICH group (no treatment), ICH + vehicle group (intragastric administration with phosphate-buffered saline at day 0 post ICH), ICH + lCoQ10 group (intragastric administration with low-dose CoQ10, 0.5 mg/g mouse weight at day 0 post ICH), ICH + mCoQ10 group (intragastric administration with medium-dose CoQ10, 5 mg/g mouse weight at day 0 post ICH), and ICH + hCoQ10 group (intragastric administration with high-dose CoQ10, 25 mg/g mouse weight at day 0 post ICH).

One mouse from each of the six groups was decapitated on day 1 following assessments of neurological function deficits caused by ICH. Subsequently, on day 5, one mouse from each of the six groups was used for neurological function deficit assessments, whereas the remaining mice were decapitated. Cerebral specimens were harvested from the sacrificed animals for biochemical examination.

## ICH model establishment

Following established protocols [20], the mice were given sodium pentobarbital for anesthesia and subsequently positioned in a stereotaxic frame. ICH model establishment was implemented in accordance with a previously described method [21]. In brief, through a 1 mm burr hole, infusion of a solution containing 0.5 U of collagenase VII was given to the right caudate nucleus at a rate of 0.4 μL/min, with the stereotaxic coordinates set at 1.0 mm posterior to the pons, 3.0 mm to the right, and 6.0 mm ventral to the skull. The sham group was subjected to identical operations except for the intracerebral injection. Upon awakening from the anesthesia, the mice were raised in cages and furnished sufficient water and food.

## RNA isolation and quantitative PCR analysis

Cerebral specimens, kept at −80°C, were processed to isolate total RNA using TRIzol reagent as the relevant instructions. The synthesis of cDNA was carried out utilizing a PrimeScript RT Master Mix (Takara, Dalian, China) as the relevant guidelines.

| Genes | Forward | Reverse |
|---|---|---|
| IL-1β | 5′-CCA CAG ACC TTC CAG GAG AAT G-3′ | 5′-GTG CAG TTC AGT GAT CGT ACA GG-3′ |
| IL-6 | 5′-AGA CAG CCA CTC ACC TCT TCA G-3′ | 5′-TTC TGC CAG TGC CTC TTT GCT G-3′ |
| TNF-α | 5′-CTC TTC TGC CTG CTG CAC TTT G-3′ | 5′-ATG GGC TAC AGG CTT GTC ACT C-3′ |
| GAPDH | 5′-GCA CCG TCA AGG CTG AGA A-3′ | 5′-TGG TGA AGA CGC CAG TGG A-3′ |
| Bcl-2 | 5′-CAT TTC CAC GTC AAC AGA ATT G-3′ | 5′-AGC ACA GGA TTG GAT ATT CCA T-3′ |
| Bax | 5′-AGC TGA GCG AGT GTC TCA AG-3′ | 5′-GTC CAA TGT CCA GCC CAT GA-3′ |

qRT-PCR (model 7500 Real-Time PCR System; Applied Biosystems) was implemented utilizing the SYBR Green kit (Takara, Dalian, China) as the relevant guidelines. The glyceraldehyde 3-phosphate dehydrogenase (GAPDH) gene served as a reference for data normalization. To quantify the expression of target mRNA relative to GAPDH in each sample, the cycle threshold (Ct) was utilized in the equation: expression = 2e−ΔCt, with ΔCt representing the deference between $Ct_{target}$ and $Ct_{GAPDH}$. The sequences of primers applied in qPCR were detailed below:

## Neurological deficit tests and determination of brain tissue water content

Corner and limb placement tests, components of neurological deficit tests (NDTs), were performed on day 5 after ICH induction, using previously described methods [22]. The NDTs were conducted by a technician unaware of mouse grouping.

An electronic balance was employed for measuring ipsilateral cerebral hemisphere wet weight. The brains were dried at 100°C for 1 day, after which their dry weight was determined. The formula applied for water content calculation: (wet weight – dry weight)/wet weight × 100%.

## Determination of neurological severity score

The mice underwent evaluation utilizing the modified neurological severity score (mNSS) test [23] which is similar to human contralateral neglect test and includes balance, movement, reflex, and sensory evaluations. The results were graded on a point scale of 0–18.

## Hematoxylin and eosin staining

Transcardial perfusion of the mice with saline, followed by 4% paraformaldehyde, was conducted 5 days after inducing ICH. Subsequently, the brain was separated, post-fixed overnight, immersed in sucrose solutions (15% and 30%, 1 day each) at 4°C, and then frozen. Slices of the frozen tissue, each 8 μm thick, were prepared. Hematoxylin and eosin (H&E) staining was implemented as the relevant guidelines.

## ELISA

The pro-inflammatory cytokines (IL-1beta, IL-6, and TNF-alpha) levels in culture supernatants and cerebral tissue homogenates (for 10 mg cerebral tissue, add 1 mL of ice-cold lysis buffer and homogenize using electric homogenizer and stored in −80°C) were measured utilizing ELISA kits (BMS224-2, EH2IL6, and BMS2034, Invitrogen) in accordance with the manufacturer guidelines.

## TUNEL assay

The TUNEL assay was utilized to assess cell death. In brief, the frozen brain tissue was defrosted at ambient temperature and underwent a 0.5-h fixation using 4%paraformaldehyde. Next, the slides were soaked for 5 min in Triton X-100 (0.1%) and subjected to 60-min incubation at 37°C using TUNEL reaction mixture.

## Western blot assay

Whole-cell lysates were obtained utilizing RIPA buffer (pH 8.0) added protease inhibitor cocktail, and their protein concentrations were determined utilizing BCA kit. Using SDS-PAGE, the proteins were separated and subsequently transferred to PVDF membranes. After the vacant sites on each membrane had been blocked, it was subjected to overnight incubation at 4°C utilizing primary antibodies. Then, following a wash with Tween-containing Tris-buffered saline (TBST), the membranes were exposed to secondary antibodies for 1-h incubation at room temperature. Finally, after rinsing with TBST several times, the protein bands were revealed using a Maximum Sensitivity Substrate Kit (Thermo Fisher Scientific, Waltham, MA, United States). The information for used antibodies (all from Abcam) is displayed here: Caspase-3 antibody (1:2000, ab4051),

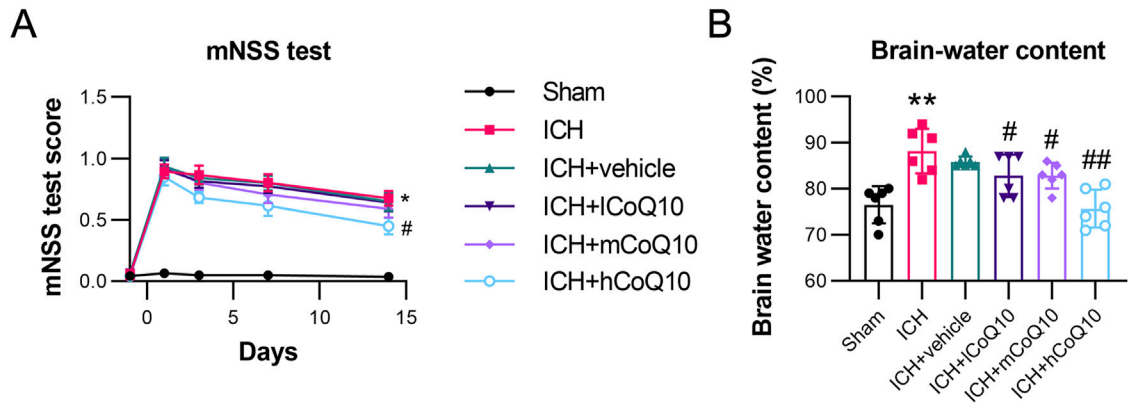


FIGURE 1
Neurobehavioral test results and brain water content of intracerebral hemorrhage (ICH)-injured mice. **(A)** The mNSS test of CoQ10-treated mice was conducted on days −1, 1, 3, 7, and 14 after ICH induction. **(B)** Brain water content was determined at day 5 after intracerebral hemorrhage induction. *P < 0.05, **P < 0.01 vs. Sham; #P < 0.05, ##P < 0.01 vs. ICH.

cleaved Caspase-3 antibody (1:500, ab2302), Caspase-9 antibody (1:2000, ab25758), cleaved Caspase-9 antibody (1:500, ab2324), Bax antibody (1:5000, ab53154), Bcl-2 antibody (1:5000, ab59348), GAPDH antibody (1:5000, ab8245), p-NF-kappaB antibody (1:1000, ab16502), p-STAT3 antibody (1:500, ab30647), p-p38 antibody (1:500, ab4822), p-p52 antibody (1:1000, ab227078).

### Statistical analysis

The data are reported in the format of the mean ± SD. The distinctions among different groups and between two groups were examined utilizing one-way ANOVA and t-test, respectively. $P < 0.05$ meant noticeable differences.

## Results

### CoQ10 administration restored neurological functions and reduced the brain water content in the ICH-injured animals

To verify the functional outcome of CoQ10-mediated neuroprotection in ICH, the mice in the ICH groups were exposed to different doses of CoQ10, and a series of neurobehavioral tests were performed. Neurological alterations were detected 1 day prior to ICH induction and at intervals of 1, 3, 7, and 14 days thereafter. CoQ10 (0.5, 5, and 25 mg/g) was injected 60 min following ICH induction. The high-dose CoQ10 group demonstrated lower mNSSs compared with the ICH + vehicle group at 7 and 14 days following ICH induction (Figure 1A). To assess the role of CoQ10 in brain lesions in the ICH-injured mice, water content in the brain was measured on day 5 after injury induction. In contrast to the sham group, the ICH model group demonstrated elevated brain water contents. However, medium and high doses of CoQ10 decreased the brain water contents in the ICH-injured mice (Figure 1B), attenuating the brain edema in a dose-dependent manner.

### CoQ10 treatment attenuated neurological function deficits and brain impairment in ICH-injured mice

Behavioral assessments were performed 5 days after ICH induction. The ICH group exhibited markedly elevated right-turn frequencies and decreased limb placement scores in contrast to the sham group results. By contrast, the different doses of CoQ10 restored the impaired neurological functions, especially at the high dose (Figures 2A, B).

Furthermore, according to the findings of H&E staining of the hematoma, histological differences existed between the ICH and sham groups. However, in the high-dose CoQ10-treated mice, the hematoma area was reduced than that in the ICH + vehicle mice (Figure 3A). The findings indicated that CoQ10 administration could ameliorate neurological dysfunction and brain impairment in ICH-injured mice.

### CoQ10 reduced the expression of pro-inflammatory cytokines in ICH-injured mice

To monitor the impact of CoQ10 on neuroinflammation in the ICH-injured mice, qPCR and ELISA were performed to examine the pro-inflammatory cytokine levels in the

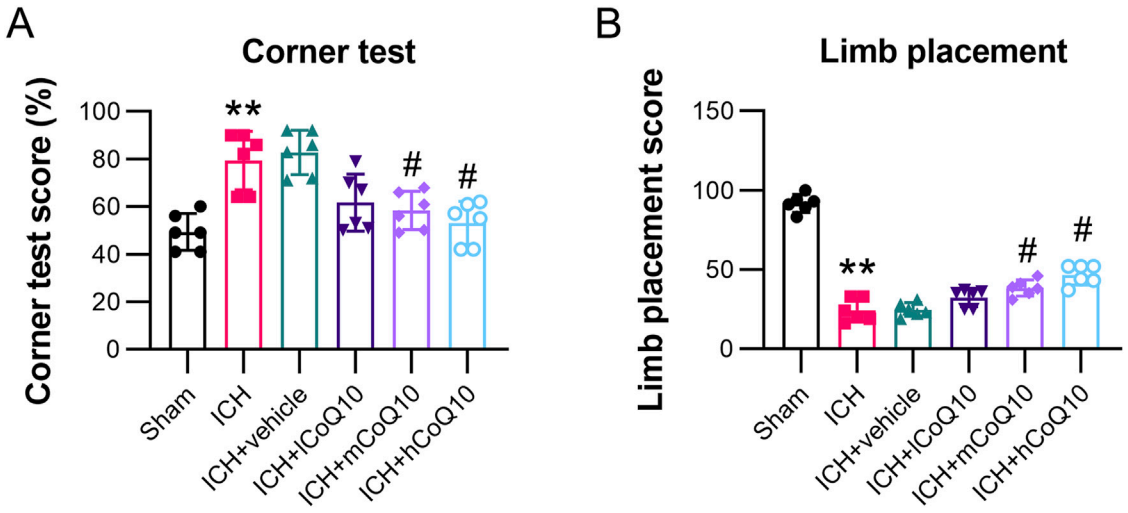


FIGURE 2
Administration of CoQ10 improved neurological function and eased cerebral impairment in intracerebral hemorrhage-injured mice. **(A, B)** Corner and forelimb placement tests were conducted at day 5 following intracerebral hemorrhage induction. **P < 0.01 vs. Sham; #P < 0.05 vs. ICH.

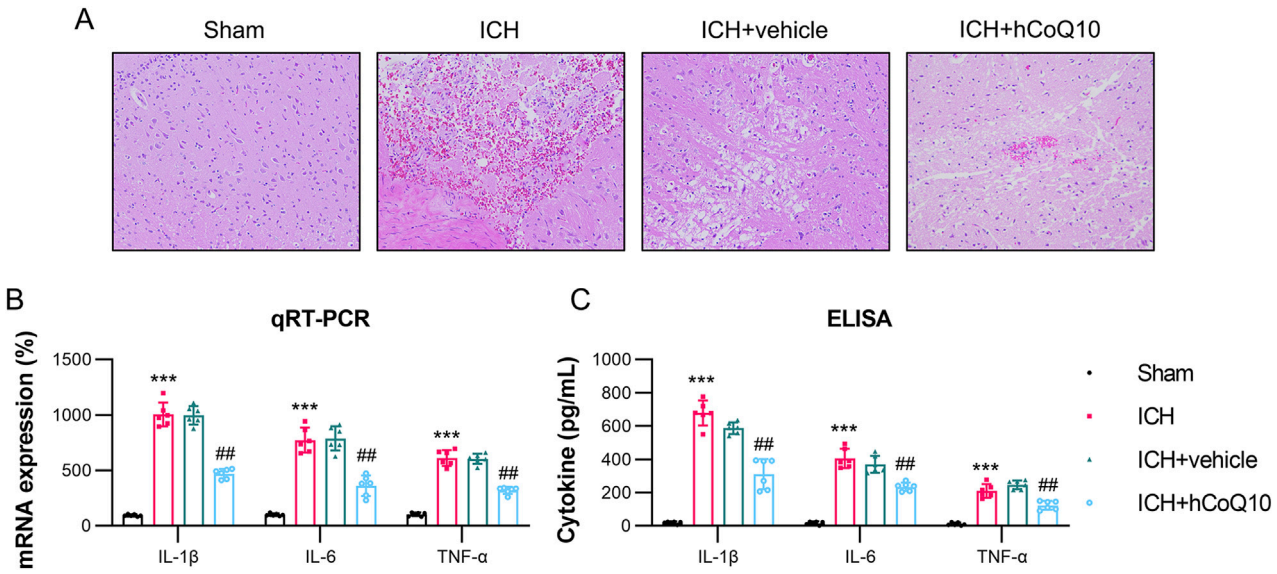


FIGURE 3
CoQ10 treatment attenuated pathological changes and neuroinflammation in intracerebral hemorrhage-injured mice. **(A)** H&E staining of the hematoma area at day 5 following intracerebral hemorrhage induction. **(B)** ELISA results of pro-inflammatory cytokine expression levels homogenate of the brain tissue. **(C)** qPCR results of pro-inflammatory cytokine mRNA expression in the homogenate of hematoma-affected brain tissue. ***P < 0.001 vs. Sham; ##P < 0.01 vs. ICH.

homogenate and supernatant of the brain tissue. As indicated by their increased levels in the tissue homogenate, ICH modeling markedly promoted the expression of cytokines, such as IL-1β, IL-6, and TNF-α, whereas treatment with CoQ10 reduced the expression of these three cytokines (Figure 3B). Furthermore, the ELISA data confirmed that the administration of CoQ10 could alleviate the inflammatory response in the ICH-injured mice (Figure 3C).

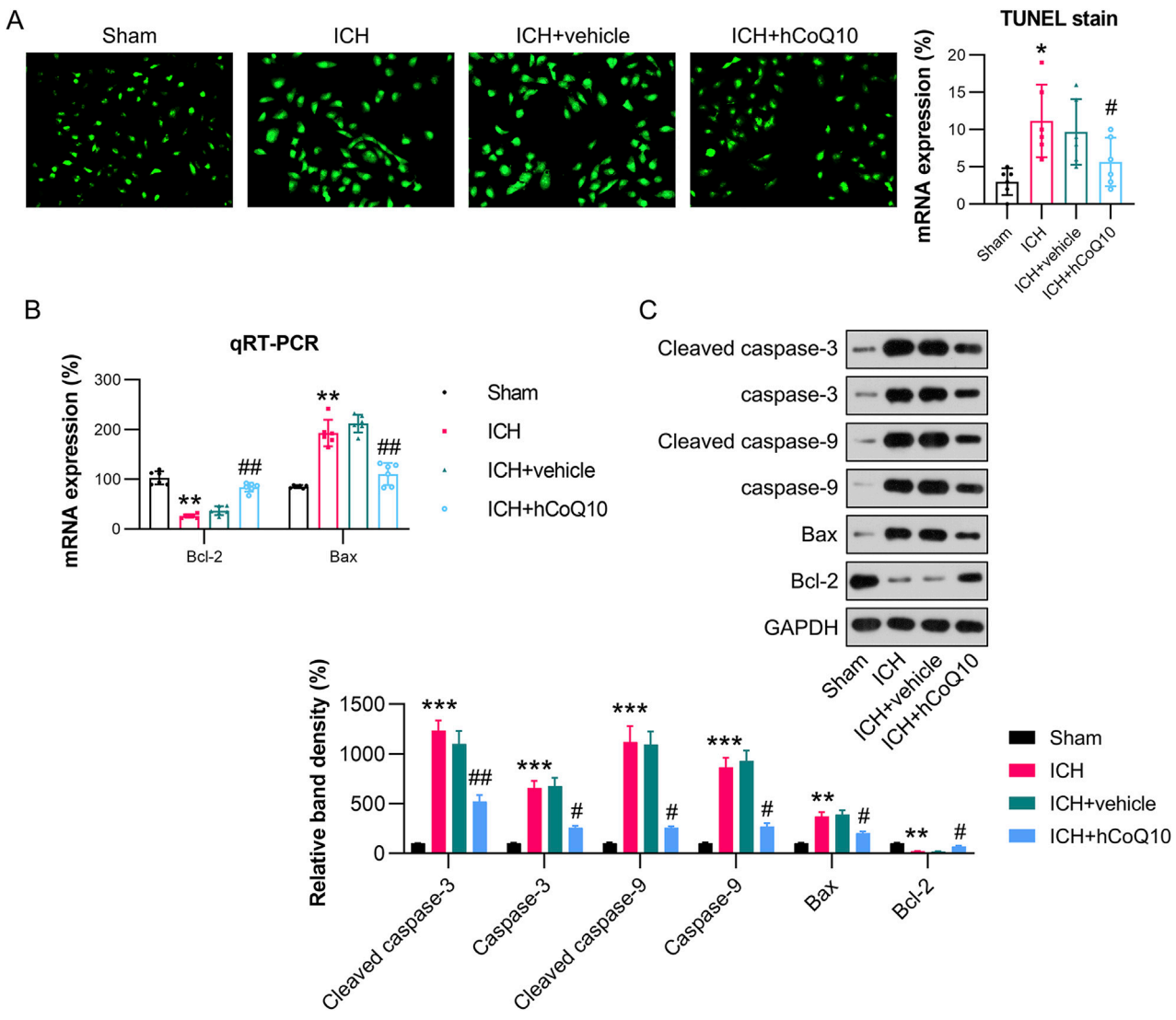


FIGURE 4
CoQ10 treatment inhibited neuronal apoptosis in intracerebral hemorrhage-injured mice. **(A)** TUNEL assay detection of apoptotic cells. **(B)** qPCR results of Bcl-2 and Bax mRNA expression levels in hematoma-affected brain tissue. **(C)** Western blot results of Bcl-2, Bax, cleaved caspase-3, and caspase-9 levels. *P < 0.05, **P < 0.01 vs. Sham; #P < 0.05, ##P < 0.01 vs. ICH.

## CoQ10 reduced the death of brain cells in ICH-injured mice

The levels of brain cell apoptosis in the ICH-injured mice were assessed utilizing TUNEL, qPCR, and western blot (WB) assays. Among them, TUNEL assay revealed that the ICH model group exhibited an elevated number of apoptotic cells, whereas the CoQ10-treated group showed a reduction (Figure 4A). The qPCR finding revealed that the mRNA level of Bcl-2 was reduced, whereas that of Bax was elevated, after ICH induction. However, CoQ10 treatment reversed these Bcl-2 and Bax levels (Figure 4B). WB analysis of expression of Bax, Bcl-2, cleaved caspase-3, and caspase-9 further confirmed that CoQ10 treatment reduced apoptosis in the perihematomal tissue of the ICH-injured animals (Figure 4C). These results indicate that CoQ10 alleviates ICH-induced neuronal cell apoptosis and neuroinflammation *in vivo*.

## CoQ10 suppressed p65 phosphorylation in the hematoma area of brain tissue in ICH-injured mice

Since NF-κB, STAT3, p38, and p52 sensors are responsible for inflammation, we examined whether these molecules are regulated by CoQ10. The western blot findings indicated that NF-κB, STAT3, p38, and p52 phosphorylation was promoted in

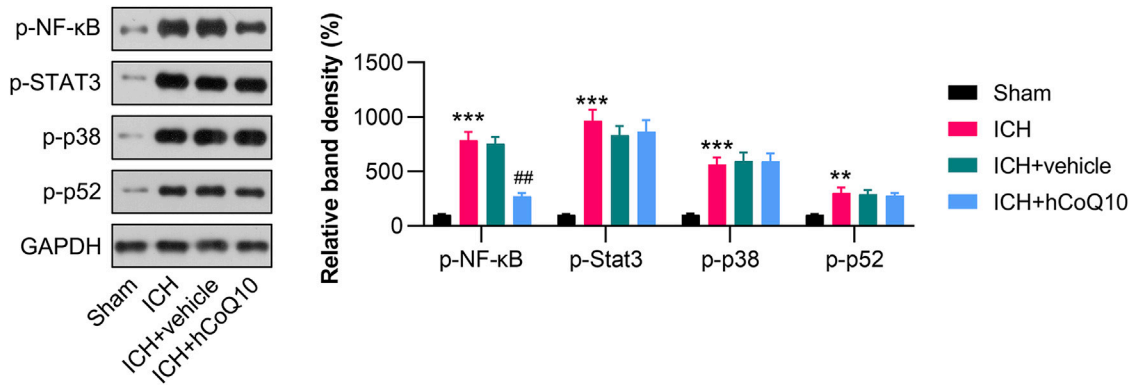


FIGURE 5
CoQ10 treatment inhibited the phosphorylation of p65 in the hematoma area of ICH-injured mice. Western blot results of the NF-κB, STAT3, p38, and p52 protein levels in the perihematomal brain area and in PCNs.

hematoma-affected tissue in response to ICH injury (Figure 5). CoQ10 treatment markedly reduced the phosphorylation of p65, but not that of STAT3, p38, and p52, suggesting that the neuroprotective function of CoQ10 is attributed to NF-κB deactivation.

## Discussion

ICH, a prevalent and destructive brain disorder, has higher incidence and mortality compared with those of ischemic stroke [24]. ICH injury can trigger cell death signaling, thereby causing a new stage of inflammation. The immune system is stimulated by a set of signals released by dead cells [25]. Although several investigations have demonstrated the neuroprotective impacts of CoQ10 on ICH [26], its definitive activity in protecting against this type of hemorrhagic injury remains unverified. This study is the first to confirm that CoQ10 can mitigate neuroinflammation and neuronal cell death in the perihematomal region as well as ameliorate neurological dysfunction following ICH injury. The results revealed that the inhibition of both pro-inflammatory cytokine secretion and neuronal death was associated with the neuroprotective effects of CoQ10 following experimental ICH injury.

In the mitochondrial respiratory chain, CoQ10 acquires electrons from complex I, transports protons through the inner mitochondrial membrane, and subsequently transfers the electrons to complex II. Furthermore, it facilitates ATP production, where it serves as a cofactor in a set of redox reactions associated with ATP synthesis in the electron transport chain [27]. CoQ10 deficiency is related to most neurodegenerative diseases like Alzheimer's, Huntington's, as well as Parkinson's diseases [28–30]. It can also stabilize membranes [31]. Several investigations have indicated that the drug may benefit patients with cardiovascular, neuromuscular, and neurodegenerative illnesses [31]. However, its effects on brain hemorrhage remains unclear [32]. CoQ10 deficiency in ICH can result in neuronal mitochondrial dysfunction and dysregulation of complexes I–III, which further leads to free radical production and oxidative stress [33], cell membrane injury caused by glutamate excitotoxicity [34], elevations of edema and blood–brain barrier permeability [35], neuroinflammation caused by glial cell overactivation [36], and neuronal apoptosis [37]. Therefore, we specifically assessed the impacts of CoQ10 on neuroinflammation and neuronal apoptosis in mouse brain tissue after ICH induction. Our data showed that a high dose of CoQ10 could alleviate neuroinflammation.

Inflammatory responses can worsen brain injury, which typically follows an ICH event. Pro-inflammatory reactions result in tissue injury, secondary edema, and eventual death of brain cells [24]. Inflammatory activation triggers hematoma enlargement, edema, and secondary neurological injury [25]. We provide the first evidence that CoQ10 can decrease pro-inflammatory cytokine levels 1 day after ICH, thereby protecting neurons from ICH-induced impairment. This research is also the first to indicate that the neuroprotective role of CoQ10 is mediated by anti-inflammatory reactions.

Given that apoptotic cell death is a dominant characteristic of neurotoxicity in perihematomal areas of the brain, inhibiting apoptosis would be a key strategy for reducing tissue damage and brain edema and improving functional outcomes in ICH [38, 39]. Nevertheless, no existing reports have explored the impacts of forkhead box protein M1 (*FoxM1*) gene knockdown or silencing on apoptosis during ICH. In the present research, TUNEL staining *in vivo* and flow cytometry *in vitro* were utilized to determine apoptotic cell death in the absence of FoxM1. The findings revealed marked decreases in the density of apoptotic cells in *FoxM1*-knockdown mice after ICH induction and in the proportion of apoptotic cells in *FoxM1*-silenced PCNs. Our data

also indicated that *FoxM1* depletion attenuated apoptosis via the upregulation of Bcl-2 and the downregulation of Bax expression. Both proteins are executive molecules in the common apoptotic pathway, playing essential roles in regulating both caspase-dependent and -independent apoptosis. Collectively, the findings demonstrate that FoxM1 plays an anti-apoptotic role by elevating Bcl-2 and decreasing Bax expression in the ICH model.

To sum up, our research verified the function of CoQ10 in protecting against ICH-induced brain injury and that its neuroprotective effect is in part due to its inhibition of pro-inflammatory cytokine secretion and neuronal death. Furthermore, we confirmed that the inhibition of pro-inflammatory cytokine secretion by CoQ10 was modulated through its inhibition of p65 phosphorylation.

## Author contributions

All authors participated in the design, interpretation of the studies and analysis of the data and review of the manuscript; XY, YZ, SY, LC, and YC conducted the experiments, XY and YZ wrote the manuscript. All authors contributed to the article and approved the submitted version.

## Data availability

The raw data supporting the conclusions of this article will be made available by the authors, without undue reservation.

## Ethics statement

All animal experiments were approved by the Animal Care and Use Committee of Ruian People's Hospital, the Third Affiliated Hospital of Wenzhou Medical University and conformed to ARRIVE guidelines. The study was conducted in accordance with the local legislation and institutional requirements.

## Funding

The author(s) declare that financial support was received for the research, authorship, and/or publication of this article. This study was supported by Wenzhou Science and Technology Bureau Project (Grant No.Y20240682).

## Conflict of interest

The author(s) declared no potential conflicts of interest with respect to the research, authorship, and/or publication of this article.

## Supplementary material

The Supplementary Material for this article can be found online at: https://www.ebm-journal.org/articles/10.3389/ebm.2025.10321/full#supplementary-material

## References

1. Min H, Jang YH, Cho I-H, Yu S-W, Lee SJ. Alternatively activated brain-infiltrating macrophages facilitate recovery from collagenase-induced intracerebral hemorrhage. *Mol Brain* (2016) **9**:42–10. doi:10.1186/s13041-016-0225-3

2. Zhu W, Gao Y, Chang C-F, Wan J-r, Zhu S-s, Wang J. Mouse models of intracerebral hemorrhage in ventricle, cortex, and hippocampus by injections of autologous blood or collagenase. *PLoS One* (2014) **9**:e97423. doi:10.1371/journal.pone.0097423

3. Lan X, Han X, Li Q, Yang Q-W, Wang J. Modulators of microglial activation and polarization after intracerebral haemorrhage. *Nat Rev Neurol* (2017) **13**: 420–33. doi:10.1038/nrneurol.2017.69

4. Keep RF, Hua Y, Xi G. Intracerebral haemorrhage: mechanisms of injury and therapeutic targets. *The Lancet Neurol* (2012) **11**:720–31. doi:10.1016/s1474-4422(12)70104-7

5. Urday S, Kimberly WT, Beslow LA, Vortmeyer AO, Selim MH, Rosand J, et al. Targeting secondary injury in intracerebral haemorrhage—perihaematomal oedema. *Nat Rev Neurol* (2015) **11**:111–22. doi:10.1038/nrneurol.2014.264

6. Lan X, Han X, Liu X, Wang J. Inflammatory responses after intracerebral hemorrhage: from cellular function to therapeutic targets. *J Cereb Blood Flow Metab* (2019) **39**:184–6. doi:10.1177/0271678x18805675

7. Yang X, Sun J, Kim TJ, Kim Y-J, Ko S-B, Kim CK, et al. Pretreatment with low-dose fimasartan ameliorates NLRP3 inflammasome-mediated neuroinflammation and brain injury after intracerebral hemorrhage. *Exp Neurol* (2018) **310**:22–32. doi:10.1016/j.expneurol.2018.08.013

8. Yang J, Li Q, Wang Z, Qi C, Han X, Lan X, et al. Multimodality MRI assessment of grey and white matter injury and blood-brain barrier disruption after intracerebral haemorrhage in mice. *Sci Rep* (2017) **7**:40358. doi:10.1038/srep40358

9. Han X, Lan X, Li Q, Gao Y, Zhu W, Cheng T, et al. Inhibition of prostaglandin E2 receptor EP3 mitigates thrombin-induced brain injury. *J Cereb Blood Flow Metab* (2016) **36**:1059–74. doi:10.1177/0271678x15606462

10. Han X, Zhao X, Lan X, Li Q, Gao Y, Liu X, et al. 20-HETE synthesis inhibition promotes cerebral protection after intracerebral hemorrhage without inhibiting angiogenesis. *J Cereb Blood Flow Metab* (2019) **39**:1531–43. doi:10.1177/0271678x18762645

11. Li Q, Weiland A, Chen X, Lan X, Han X, Durham F, et al. Ultrastructural characteristics of neuronal death and white matter injury in mouse brain tissues after intracerebral hemorrhage: coexistence of ferroptosis, autophagy, and necrosis. *Front Neurol* (2018) **9**:581. doi:10.3389/fneur.2018.00581

12. Weiland A, Wang Y, Wu W, Lan X, Han X, Li Q, et al. Ferroptosis and its role in diverse brain diseases. *Mol Neurobiol* (2019) **56**:4880–93. doi:10.1007/s12035-018-1403-3

13. Turunen M, Olsson J, Dallner G. Metabolism and function of coenzyme Q. *Biochim Biophys Acta (BBA)-Biomembranes* (2004) **1660**:171–99. doi:10.1016/j.bbamem.2003.11.012

14. Akbari A, Mobini GR, Agah S, Morvaridzadeh M, Omidi A, Potter E, et al. Coenzyme Q10 supplementation and oxidative stress parameters: a systematic review and meta-analysis of clinical trials. *Eur J Clin Pharmacol* (2020) **76**:1483–99. doi:10.1007/s00228-020-02919-8

15. Nagib MM, Tadros MG, Rahmo RM, Sabri NA, Khalifa AE, Masoud SI. Ameliorative effects of α-tocopherol and/or coenzyme Q10 on phenytoin-induced cognitive impairment in rats: role of VEGF and BDNF-TrkB-CREB pathway. *Neurotox Res* (2019) **35**:451–62. doi:10.1007/s12640-018-9971-6

16. Attia H, Albuhayri S, Alaraidh S, Alotaibi A, Yacoub H, Mohamad R, et al. Biotin, coenzyme Q10, and their combination ameliorate aluminium chloride-induced Alzheimer's disease via attenuating neuroinflammation and improving brain insulin signaling. *J Biochem Mol Toxicol* (2020) **34**:e22519. doi:10.1002/jbt.22519

17. Park HW, Park CG, Park M, Lee SH, Park HR, Lim J, et al. Intrastriatal administration of coenzyme Q10 enhances neuroprotection in a Parkinson's disease rat model. *Sci Rep* (2020) **10**:9572. doi:10.1038/s41598-020-66493-w

18. Grieb P, Ryba MS, Sawicki J, Chrapusta SJ. Oral coenzyme Q 10 administration prevents the development of ischemic brain lesions in a rabbit model of symptomatic vasospasm. *Acta Neuropathologica* (1997) **94**:363–8. doi:10.1007/s004010050720

19. Yi YY, Shin HJ, Choi SG, Kang JW, Song H-J, Kim SK, et al. Preventive effects of neuroprotective agents in a neonatal rat of photothrombotic stroke model. *Int J Mol Sci* (2020) **21**:3703. doi:10.3390/ijms21103703

20. Li F, Yang B, Li T, Gong X, Zhou F, Hu Z. HSPB8 over-expression prevents disruption of blood–brain barrier by promoting autophagic flux after cerebral ischemia/reperfusion injury. *J Neurochem* (2019) **148**:97–113. doi:10.1111/jnc.14626

21. Rosenberg GA, Mun-Bryce S, Wesley M, Kornfeld M. Collagenase-induced intracerebral hemorrhage in rats. *Stroke* (1990) **21**:801–7. doi:10.1161/01.str.21.5.801

22. Xi T, Jin F, Zhu Y, Wang J, Tang L, Wang Y, et al. miR-27a-3p protects against blood–brain barrier disruption and brain injury after intracerebral hemorrhage by targeting endothelial aquaporin-11. *J Biol Chem* (2018) **293**:20041–50. doi:10.1074/jbc.ra118.001858

23. Chen J, Li Y, Wang L, Zhang Z, Lu D, Lu M, et al. Therapeutic benefit of intravenous administration of bone marrow stromal cells after cerebral ischemia in rats. *Stroke* (2001) **32**:1005–11. doi:10.1161/01.str.32.4.1005

24. Wang J, Doré S. Inflammation after intracerebral hemorrhage. *J Cereb Blood Flow Metab* (2007) **27**:894–908. doi:10.1038/sj.jcbfm.9600403

25. Zhou Y, Wang Y, Wang J, Anne Stetler R, Yang Q-W. Inflammation in intracerebral hemorrhage: from mechanisms to clinical translation. *Prog Neurobiol* (2014) **115**:25–44. doi:10.1016/j.pneurobio.2013.11.003

26. Rajdev K, Mehan S. Neuroprotective methodologies of co-enzyme q10 mediated brain hemorrhagic treatment: clinical and pre-clinical findings. *CNS and Neurol Disorders-Drug Targets (Formerly Curr Drug Targets-CNS and Neurol Disorders)* (2019) **18**:446–65. doi:10.2174/1871527318666190610101144

27. Saini R. Coenzyme Q10: the essential nutrient. *J Pharm And Bioallied Sci* (2011) **3**:466–7. doi:10.4103/0975-7406.84471

28. Ferrante RJ, Andreassen OA, Dedeoglu A, Ferrante KL, Jenkins BG, Hersch SM, et al. Therapeutic effects of coenzyme Q10 and remacemide in transgenic mouse models of Huntington's disease. *J Neurosci* (2002) **22**:1592–9. doi:10.1523/jneurosci.22-05-01592.2002

29. Müller T, Büttner T, Gholipour A-F, Kuhn W. Coenzyme Q10 supplementation provides mild symptomatic benefit in patients with Parkinson's disease. *Neurosci Lett* (2003) **341**:201–4. doi:10.1016/s0304-3940(03)00185-x

30. Salama M, Yuan T-F, Machado S, Murillo-Rodríguez E, Vega J, Menéndez-González M, et al. Co-enzyme Q10 to treat neurological disorders: basic mechanisms, clinical outcomes, and future research direction. *CNS and Neurol Disorders-Drug Targets (Formerly Curr Drug Targets-CNS and Neurol Disorders)* (2013) **12**:641–64. doi:10.2174/18715273113129990071

31. Tawfik MK. Coenzyme Q10 enhances the anticonvulsant effect of phenytoin in pilocarpine-induced seizures in rats and ameliorates phenytoin-induced cognitive impairment and oxidative stress. *Epilepsy and Behav* (2011) **22**:671–7. doi:10.1016/j.yebeh.2011.09.018

32. Ely JT, Fudenberg HH, Bliznakov EG, Branch JD. Hemorrhagic stroke in human pretreated with coenzyme Q10: exceptional recovery as seen in animal models. *J orthomolecular Med* (1998) **13**:105–9.

33. Sanoobar M, Eghtesadi S, Azimi A, Khalili M, Jazayeri S, Reza Gohari M. Coenzyme Q10 supplementation reduces oxidative stress and increases antioxidant enzyme activity in patients with relapsing–remitting multiple sclerosis. *Int J Neurosci* (2013) **123**:776–82. doi:10.3109/00207454.2013.801844

34. Lee D, Shim MS, Kim K-Y, Noh YH, Kim H, Kim SY, et al. Coenzyme Q10 inhibits glutamate excitotoxicity and oxidative stress–mediated mitochondrial alteration in a mouse model of glaucoma. *Invest Ophthalmol Vis Sci* (2014) **55**:993–1005. doi:10.1167/iovs.13-12564

35. Doll DN, Hu H, Sun J, Lewis SE, Simpkins JW, Ren X. Mitochondrial crisis in cerebrovascular endothelial cells opens the blood–brain barrier. *Stroke* (2015) **46**:1681–9. doi:10.1161/strokeaha.115.009099

36. Rose J, Brian C, Woods J, Pappa A, Panayiotidis MI, Powers R, et al. Mitochondrial dysfunction in glial cells: implications for neuronal homeostasis and survival. *Toxicology* (2017) **391**:109–15. doi:10.1016/j.tox.2017.06.011

37. Singh A, Kumar A. Microglial inhibitory mechanism of coenzyme Q10 against aβ (1-42) induced cognitive dysfunctions: possible behavioral, biochemical, cellular, and histopathological alterations. *Front Pharmacol* (2015) **6**:268. doi:10.3389/fphar.2015.00268

38. Krafft PR, Altay O, Rolland WB, Duris K, Lekic T, Tang J, et al. α7 nicotinic acetylcholine receptor agonism confers neuroprotection through GSK-3β inhibition in a mouse model of intracerebral hemorrhage. *Stroke* (2012) **43**:844–50. doi:10.1161/strokeaha.111.639989

39. Matsushita K, Meng W, Wang X, Asahi M, Asahi K, Moskowitz MA, et al. Evidence for apoptosis after intracerebral hemorrhage in rat striatum. *J Cereb Blood Flow Metab* (2000) **20**:396–404. doi:10.1097/00004647-200002000-00022

EBM Experimental Biology and Medicine

TYPE Original Research
PUBLISHED 13 February 2025
DOI 10.3389/ebm.2025.10447



OPEN ACCESS

*CORRESPONDENCE
Li Liu,
amy2482863711@163.com
Xin Tian,
liontiger006342@163.com

†These authors have contributed equally to this work

RECEIVED 26 November 2024
ACCEPTED 28 January 2025
PUBLISHED 13 February 2025

CITATION
Wang Y, Wu P, Mao X, Jiang N, Huang Y, Zhang L, Liu L and Tian X (2025) Clinical characteristics and prognosis of ALL in children with CDKN2A/B gene deletion. *Exp. Biol. Med.* 250:10447. doi: 10.3389/ebm.2025.10447



# Clinical characteristics and prognosis of ALL in children with CDKN2A/B gene deletion

Yiyu Wang[1†], Peijing Wu[2†], Xiaoyan Mao[3], Nanjing Jiang[1], Yu Huang[1], Li Zhang[4], Li Liu[5*] and Xin Tian[1*]

[1]Department of Hematology, Sichuan Provincial Woman's and Children's Hospital/The Affiliated Women's and Children's Hospital of Chengdu Medical College, Chengdu, China, [2]Department of Pediatrics, Anning First People's Hospital, Kunming, China, [3]Department of Pediatrics, Children Hematological Oncology and Birth Defects Laboratory, Sichuan Clinical Research Center for Birth Defects, The Affiliated Hospital of Southwest Medical University, Luzhou, Sichuan, China, [4]Department of Pediatrics, Da Li University, Da Li, China, [5]Department of Pediatrics, Qujing Medical College, Qujing, China

## Abstract

This study aimed to explore the correlation between the deletion of the CDKN2A/B gene and the prognosis of pediatric acute lymphoblastic leukemia (ALL) patients. A total of 310 pediatric patients who were diagnosed with acute lymphoblastic leukemia at our hospital from January 2020 to September 2023 were included in this study. Among them, 78 patients with CDKN2A/B deletion were included in the final analysis. Additionally, 78 ALL patients without CDKN2A/B deletion, who were diagnosed during the same period, were randomly selected for comparison. A statistical analysis was conducted to compare the clinical characteristics and prognosis between the CDKN2A/B deletion group and the non-deletion group in ALL patients. The results showed that pediatric ALL patients with CDKN2A/B deletion had higher white blood cell counts and a greater proportion of immature cells in peripheral blood at diagnosis. The age at diagnosis was older in the deletion group, with a greater proportion in the >10-year-old group. CDKN2A/B deletion occurred more frequently in pediatric patients with T-ALL than in pediatric patients with B-ALL. Patients with CDKN2A/B deletion were more likely to have positive BCR-ABL1 expression combined with IKZF1 deletion. The overall survival (OS) rate was 89.7%, and the event-free survival (EFS) rate was 83.3% in the CDKN2A/B deletion group, which was lower than the OS rate of 97.4% and EFS rate of 93.6% in the non-deletion group. These results suggest that CDKN2A/B deletion may be one of the factors affecting poor prognosis. It provides a new perspective for clinical treatment, risk stratification, and prognostic assessment in pediatric ALL patients.

KEYWORDS

**CDKN2A/B gene, acute lymphoblastic leukemia, children, survival analysis, clinical characteristics**

## Impact statement

Research indicates that the CDKN2A/B gene is correlated with the occurrence, development, and prognosis of some tumors. However, there is no consensus or definitive conclusion regarding the clinical characteristics, biological manifestations, and prognosis of pediatric ALL patients with CDKN2A/B deletion. Further analysis and discussion are needed based on a large number of clinical samples and precise experimental data to elucidate the significance of CDKN2A/B deletion in the prognosis of pediatric ALL patients. This study aimed to explore the association between CDKN2A/B deletion and prognosis in pediatric ALL patients, with the goal of providing a new perspective for clinical treatment, risk stratification and prognostic assessment in pediatric ALL patients.

## Introduction

Acute lymphoblastic leukemia (ALL) is the most common malignant tumor disease in children [1]. While the majority of children with ALL can achieve a cure with conventional chemotherapy, 20% of these children still experience leukemia relapse. Relapsed ALL remains a leading cause of cancer-related death in children [2, 3]. The current first-line treatment is chemotherapy stratified by risk factors. With the development of genetic sequencing technology, an increasing number of risk factors associated with pediatric ALL have been identified to guide the risk stratification and treatment of ALL. Next-generation sequencing (NGS) technology is capable of detecting deeper levels of single nucleotide variations (SNVs), small insertions and deletions, and copy number variations (CNVs) [4]. The application of NGS in pediatric leukemia is becoming increasingly widespread [5]. When applied to leukemia diagnosis, certain meaningful gene mutations related to treatment, disease progression, prognosis, and risk factors of relapse and refractory can be detected earlier and more comprehensively than traditional gene detection methods [6]. This, in turn, provides better and timelier strategies and precision treatment for pediatric ALL patients, with the expectation of improving the therapeutic outcomes and prognosis of children with ALL.

With the application of NGS detection technology, numerous studies are being conducted to explore the correlation between copy number variations and the prognosis of pediatric ALL patients.

The cyclin-dependent kinase inhibitor 2A (CDKN2A) gene and the cyclin-dependent kinase inhibitor 2B (CDKN2B) gene are two adjacent tumor suppressor genes that are collectively referred to as the CDKN2A/B. The CDKN2A/B is located on the short arm, region 2, band 1 of chromosome 9 (9p21). The CDKN2A encodes two proteins, $p16^{INK4a}$ (p16) and $p14^{ARF}$ (p14), whereas the CDKN2B encodes $p15^{INK4b}$ (p15) [7, 8]. By encoding these three proteins, they play crucial roles in the pathogenesis of leukemia, regulation of the cell cycle, chemosensitivity, and apoptosis. The presence of CDKN2A/B deletion (biallelic or monoallelic) is associated with a lower EFS rate [9]. The CDKN2A often accompanies the CDKN2B with copy number abnormalities, most commonly deletions [10].

Research indicates that the CDKN2A is correlated with the occurrence, development, and prognosis of some tumors, such as ovarian cancer, pancreatic cancer, lung cancer, melanoma, lymphoma, and malignant glioma, and has certain guiding significance for the clinical prognosis and selection of clinical medications for these tumors. In leukemia, studies by Wang et al. [11] demonstrated that deletion of the CDKN2A was associated with poor prognosis in adult ALL patients. Kim et al. [12] found that homozygous deletions of the CDKN2A (p16, p14) and the CDKN2B (p15) was a factor indicating poor prognosis in adult ALL patients, but it did not have a significant impact on prognosis in pediatric ALL patients. Onizuka et al. [13] demonstrated that copy number variations of the CDKN2A/B was a prognostic factor associated with posttransplant relapse in Philadelphia chromosome-positive ALL (ph + ALL). Feng et al. [14] found that deletion of the CDKN2A/B was highly prevalent in pediatric ALL patients and had a detrimental effect on the prognosis of pediatric B-ALL patients, serving as an independent risk factor for poor prognosis.

In summary, the current study [15–18] reveals that there is no fully unified understanding or definitive conclusion regarding the clinical characteristics, biological manifestations, and prognosis of pediatric ALL patients with CDKN2A/B deletion. Therefore, a substantial number of clinical samples and precise experimental data are still needed to analyze the significance of CDKN2A/B deletion in the prognosis of pediatric ALL patients. The aim of this study was to discuss the occurrence and clinical characteristics of CDKN2A/B deletion in pediatric ALL patients, explore whether CDKN2A/B deletion is related to the prognosis of pediatric ALL patients, and provide a new insight for the clinical treatment and prognostic assessment of pediatric ALL patients.

## Materials and methods

Between January 2020 and September 2023, data were collected from 310 pediatric patients diagnosed with ALL at our hospital and treated according to the CCLG-ALL2018 protocol. Among them, 78 patients with CDKN2A/B deletion were ultimately included in the analysis. Additionally, 78 ALL patients without CDKN2A/B deletion, who were diagnosed during the same period, were randomly selected for comparison. The basic data (age, gender, ethnicity), basic

TABLE 1 Simplified overview of the CCLG-B-ALL2018 protocol.

| Treatment plan | Low risk (PEG × 4) | Intermediate risk (PEG × 8) | High risk (PEG × 13) |
|---|---|---|---|
| Remission Induction | VDLP (DNR × 2)<br>(PEG-ASP × 2) | VDLP (DNR × 4)<br>(PEG-ASP × 2) | VDLP (DNR × 4)<br>(PEG-ASP × 2) |
| | 1 × CAM | 2 × CAML (PEG-ASP × 2) | 2 × CAML (PEG-ASP × 2) |
| Consolidation | Randomized Control<br>4 × [HD-MTX 2 g/m$^2$+6-MP]<br>4 × [HD-MTX 2 g/m$^2$+VD] | Randomized Control<br>4 × [HD-MTX 5 g/m$^2$+6-MP]<br>4 × [HD-MTX 5 g/m$^2$+VD] | 2 × (HR-1′, HR-2′, HR- 3′)<br>(PEG-ASP × 6) |
| Intensification | VDLP (DNR × 3)<br>(PEG-ASP × 2) | VDLP (DNR × 4)<br>(PEG-ASP × 2) | VDLP (DNR × 3)<br>(PEG-ASP × 2) |
| | 1 × CAM | 2 × CAML (PEG-ASP × 2) | 1 × CAML (PEG-ASP × 1) |
| Maintenance | 6-MP/MTX + VD (4-week Cycle) | 6-MP/MTX + VD (4-week Cycle) | 6-MP/MTX + VD (4-week Cycle) |
| Total Treatment Course | Both Males and Females for 2 Years | Females for 2 Years, Males for 2.5 Years | Both Males and Females for 2.5 Years |

TABLE 2 Basic clinical information and immunophenotype.

| Category | Group | CDKN2A/B deletion (N = 78) | Non-deletion of CDKN2A/B (N = 78) | $\chi 2$ | *P* |
|---|---|---|---|---|---|
| Age (year) | — | 6.75 (3.23, 11.17) | 4.8 (2.92, 6.21) | −2.636 | 0.008* |
| Age (year) | <1 year | 2 (2.6%) | 3 (3.8%) | 7.170 | 0.022* |
| | 1–10 years | 51 (65.4%) | 64 (82.1%) | | |
| | >10 years | 25 (32.1%) | 11 (14.1%) | | |
| Sex | Male | 50 (64.1%) | 41 (52.6%) | 2.136 | 0.144 |
| | Female | 28 (35.9%) | 37 (47.4%) | | |
| Nationality | Han | 45 (57.7%) | 52 (66.7%) | 1.336 | 0.248 |
| | Non-Han | 33 (42.3%) | 26 (33.3%) | | |
| White Blood Cell (×10$^9$/L) | — | 43.56 (13.51, 131.22) | 6.61 (3.58, 25.63) | −5.238 | <0.001* |
| Hemoglobin (g/L)[a] | — | 89.55 ± 27.376 | 80.79 ± 24.491 | 2.105 | 0.037* |
| Platelet (×10$^9$/L) | — | 57.50 (28.00, 87.00) | 43.50 (22.75, 137.75) | −0.399 | 0.690 |
| Peripheral Blood Immature Cell Proportion (%) | — | 61.00 (21.50, 78.25) | 30.00 (5.75, 56.50) | −3.999 | <0.001* |
| Immunophenotype | B | 47 (60.3%) | 74 (94.9%) | 26.853 | <0.001* |
| | T | 31 (39.7%) | 4 (5.1%) | | |

[a]Compliance with a normal distribution, represented by mean ± standard deviation.
*: $P < 0.05$, statistically significant difference.

clinical information (immunophenotyping, risk stratification, peripheral blood white blood cell count, hemoglobin, platelet count, peripheral blood immature cell proportion), and molecular biological data (chromosome karyotype, combined abnormal genes) at diagnosis were collected. The detailed results of MRD in bone marrow on day 15 and day 33 of induction remission therapy were collected. The prognosis and survival status of both groups of patients were investigated. The cutoff date for follow-up was February 2024, and the total duration ranged from 2 to 48 months. The corresponding statistical methods were used to compare the clinical characteristics, OS and EFS rates between the CDKN2A/B deletion group and the non-deletion group.

## Statistical analysis

SPSS 26.0 and GraphPad Prism 9.0 software were used for statistical analysis. Independent sample *t*-test was used for data that met the normal distribution, and non-parametric rank sum test was used for data that did not meet the normal distribution. Count data were expressed as n (%) and analyzed using Pearson's

TABLE 3 Risk stratification and MRD positivity.

| Category | Group | CDKN2A/B deletion (N = 78) | Non-deletion of CDKN2A/B (N = 78) | χ2 | *P* |
|---|---|---|---|---|---|
| Risk Stratification | Low | 1 (1.3%) | 4 (5.1%) | 1.880 | 0.409 |
| | Intermediate | 55 (70.5%) | 55 (70.5%) | | |
| | High | 22 (28.2%) | 19 (24.4%) | | |
| Day 15 MRD | Positive | 12 (15.4%) | 10 (12.8%) | 0.212 | 0.645 |
| | Negative | 66 (84.6%) | 68 (87.2%) | | |
| Day 33 MRD | Positive | 1 (1.3%) | 2 (2.6%) | △ | 1.000 |
| | Negative | 77 (98.7%) | 76 (97.4%) | | |

△Fisher's exact test.

TABLE 4 Molecular biological characteristics.

| Category | Group | CDKN2A/B deletion (N = 78) | Non-deletion of CDKN2A/B (N = 78) | χ2 | *P* |
|---|---|---|---|---|---|
| Karyotype | Normal Chromosomes | 45 (57.7%) | 32 (41.0%) | 10.605 | 0.005* |
| | Numerical Abnormalities | 6 (7.7%) | 21 (26.9%) | | |
| | Structural Abnormalities | 27 (34.6%) | 25 (32.1%) | | |
| Concurrent Gene Abnormalities | No Other Gene Abnormalities | 10 (12.8%) | 14 (17.9%) | 4.065 | 0.254 |
| | With a Favorable Prognosis | 7 (9.0%) | 13 (16.7%) | | |
| | With a Poor Prognosis | 41 (52.6%) | 38 (48.7%) | | |
| | With Unclear Prognostic Impact | 20 (25.6%) | 13 (16.7%) | | |
| Several Common Genes | TEL-AML1 | 7 (9.0%) | 10 (12.8%) | 0.594 | 0.441 |
| | E2A-PBX1 | 4 (5.1%) | 4 (5.1%) | 0.000 | 1.000 |
| | BCR-ABL1 | 11 (14.1%) | 4 (5.1%) | 3.614 | 0.057 |
| | Ph Like | 26 (33.3%) | 29 (37.2%) | 0.253 | 0.615 |
| | SIL-TAL1 | 2 (2.6%) | 0 (0%) | △ | 0.477 |
| | BCR-ABL1 Positivity Combined with IKZF1 Deletion | 8 (10.3%) | 0 (0%) | △ | 0.011* |

△Fisher's exact test.
*$P < 0.05$, statistically significant difference.

chi-square test or Fisher's exact test when necessary. Measurement data with normal distribution were expressed as mean ± standard deviation, and non-normal distribution were expressed as M (P25, P75). *P* value <0.05 was considered statistically significant. For survival analysis, the Kaplan–Meier method was used to analyze the overall survival (OS) and event-free survival (EFS) of each group, and the corresponding survival curves were plotted. For prognostic analysis, log-rank univariate regression analysis was first used to screen for factors affecting the prognosis of each group. Factors with $P < 0.05$ were included in the multivariate Cox regression analysis. Ultimately, factors with $P < 0.05$ were considered to have statistically significant differences and were identified as prognostic risk factors.

## Inclusion criteria

(1) Meeting the diagnostic criteria for ALL, patients met the WHO 2016 bone marrow morphology standard, with primitive and immature lymphocytes in the bone marrow accounting for ≥20%, and were diagnosed with ALL based on morphological-immunological-cyto-genetic-molecular (MICM) classification.
(2) Received standardized chemotherapy according to the CCLG-ALL2018 protocol.
(3) Pediatric ALL patients who were identified as CDKN2A/B deletion through high-throughput sequencing for multigene mutation detection in lymphoid tumors.

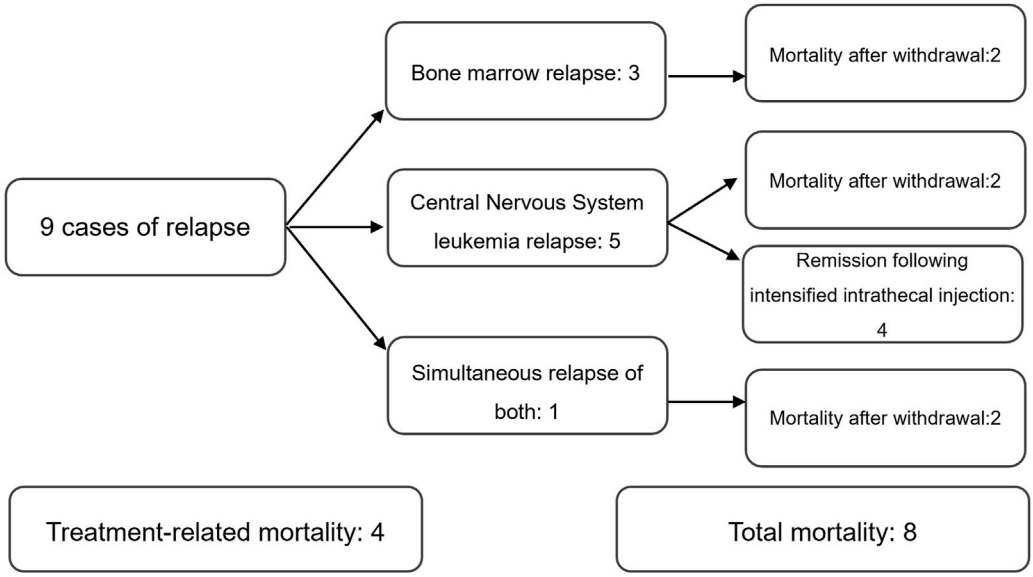


FIGURE 1
Relapse and mortality status.

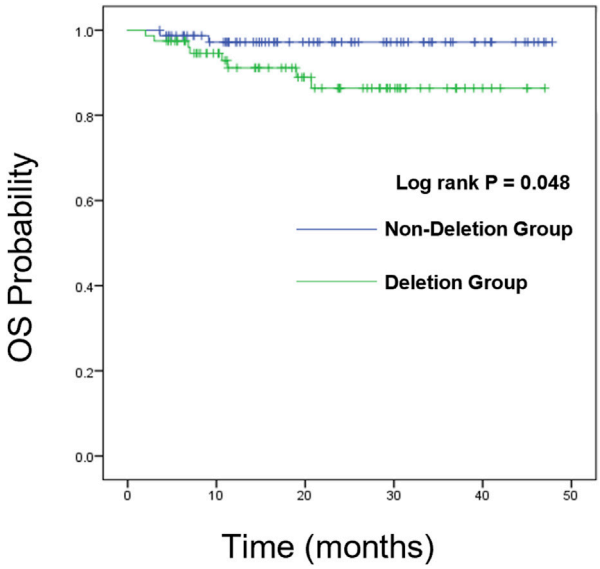


FIGURE 2
Kaplan-Meier survival curves of OS.

## Exclusion criteria

(1) Patients who had incomplete MICM classification information at diagnosis or who chose to forgo chemotherapy after diagnosis.
(2) Patients diagnosed with acute mixed lineage leukemia.
(3) Patients who did not receive standardized chemotherapy after diagnosis or were lost to follow-up.
(4) Patients whose complete genetic testing did not detect deletion of the CDKN2A/B.

## Chemotherapy regimen

Chemotherapy was conducted according to the CCLG-ALL2018 (Chinese Children Leukemia Group-ALL2018) treatment protocol. During the chemotherapy process, bone marrow cell morphology and bone marrow minimal residual disease (MRD) were dynamically monitored to assist in assessing the efficacy of chemotherapy and the status of bone marrow remission. Triple intrathecal injections (methotrexate-cytarabine-dexamethasone) were used during the chemotherapy process for the prevention and treatment of central nervous system leukemia (For details, see Table 1).

# Results

## Basic clinical information and immunophenotype at diagnosis

A total of 310 pediatric patients diagnosed with ALL who were treated at our hospital under the CCLG-ALL2018 protocol from January 2020 to September 2023 were included. Among them, 78 patients had CDKN2A/B deletion, accounting for 25.2%

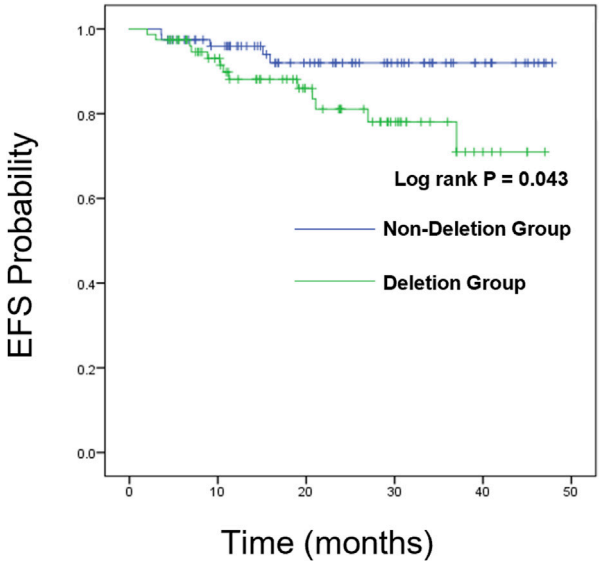


FIGURE 3
Kaplan-Meier survival curves of EFS.

(78/310) of the total. Additionally, clinical data from 78 pediatric patients diagnosed during the same period without detected CDKN2A/B deletion were randomly selected for comparison. The details are as follows: (These data are summarized in Table 2).

## Sex

CDKN2A/B deletion group: 50 male patients (64.1%, 50/78) and 28 female patients (35.9%, 28/78), with a male-to-female ratio of 1.8:1. CDKN2A/B non-deletion group: 41 male patients (52.6%, 41/78) and 37 female patients (47.4%, 37/78), with a male-to-female ratio of 1.1:1.

## Age

CDKN2A/B deletion group: the median age was 6.75 years (range, 3.23–11.17 years). CDKN2A/B non-deletion group: the median age of the was 4.8 years (range, 2.92–6.21 years).

## Nationality

CDKN2A/B deletion group: 45 Han individuals (57.7%, 45/78) and 33 non-Han individuals (42.3%, 33/78), with a ratio of Han to non-Han individuals of 1.4:1. CDKN2A/B non-deletion group: 52 Han individuals (66.7%, 52/78) and 26 non-Han individuals (33.3%, 26/78), with a ratio of Han to non-Han individuals of 2:1.

## Peripheral blood routine

CDKN2A/B deletion group: the median white blood cell count: 43.56 × $10^9$/L (range, 13.51–131.22) × $10^9$/L; the median platelet count: 57.50 × $10^9$/L (range, 28.00–87.00) × $10^9$/L; the mean hemoglobin level: 89.55 ± 27.376 g/L; the median proportion of peripheral blood immature cells: 61.00% (range, 21.50–78.25%). CDKN2A/B non-deletion group: the median white blood cell count: 6.61 × $10^9$/L (range, 3.58–25.63) × $10^9$/L; the median platelet count: 43.50 × $10^9$/L (range, 22.75–137.75) × $10^9$/L; the mean hemoglobin level: 80.79 ± 24.491 g/L; the median proportion of peripheral blood immature cells: 30.00% (range, 5.75–56.50%).

## Immunophenotype

CDKN2A/B deletion group: 31 T-ALL patients, accounting for 39.7%, and 47 B-ALL patients, accounting for 60.3%.

TABLE 5 Comparison of OS and EFS rates.

| Category | CDKN2A/B deletion (N = 78) | Non-deletion of CDKN2A/B (N = 78) | $\chi 2$ | *P* |
|---|---|---|---|---|
| OS rate | 70 (89.7%) | 76 (97.4%) | 3.924 | 0.048* |
| 1-year OS rate | 72 (92.3%) | 76 (97.4%) | 2.188 | 0.139 |
| 2-year OS rate | 70 (89.7%) | 76 (97.4%) | 3.924 | 0.048* |
| 3-year OS rate | 70 (89.7%) | 76 (97.4%) | 3.924 | 0.048* |
| EFS rate | 65 (83.3%) | 73 (93.6%) | 4.095 | 0.043* |
| 1-year EFS rate | 70 (89.7%) | 75 (96.2%) | 2.517 | 0.113 |
| 2-year EFS rate | 70 (89.7%) | 75 (96.2%) | 2.517 | 0.113 |
| 3-year EFS rate | 66 (84.6%) | 73 (93.6%) | 3.309 | 0.069 |

*$P < 0.05$, statistically significant difference.

TABLE 6 OS rates for several factors in the CDKN2A/B deletion group.

| Category | Group | Total number of cases | Number of events | OS rate | $\chi 2$ | *P* |
|---|---|---|---|---|---|---|
| Total | — | 78 | 8 | 89.7% | — | — |
| Age (year) | <1 year | 2 | 0 | 100.00% | 1.226 | 0.542 |
| | 1–10 years | 51 | 4 | 92.16% | | |
| | >10 years | 25 | 4 | 84.00% | | |
| Sex | Male | 50 | 4 | 92.00% | 0.673 | 0.412 |
| | Female | 28 | 4 | 85.71% | | |
| Nationality | Han | 45 | 6 | 86.67% | 1.038 | 0.308 |
| | Non-Han | 33 | 2 | 93.94% | | |
| Immunophenotype | B | 47 | 5 | 89.36% | 0.047 | 0.829 |
| | T | 31 | 3 | 90.32% | | |
| Risk Stratification | Low | 1 | 0 | 100.00% | 7.197 | 0.027* |
| | Intermediate | 55 | 3 | 94.55% | | |
| | High | 22 | 5 | 77.27% | | |
| Central Nervous System Infiltration | Yes | 3 | 1 | 66.67% | 0.914 | 0.339 |
| | No | 75 | 7 | 90.67% | | |
| White Blood Cell ( $\times 10^9$/L) | <4 | 7 | 0 | 100.00% | 2.215 | 0.330 |
| | 4–50 | 39 | 6 | 84.62% | | |
| | >50 | 32 | 2 | 93.75% | | |
| Hemoglobin (g/L) | <30 | 1 | 0 | 100.00% | 5.301 | 0.151 |
| | 30–60 | 7 | 2 | 71.43% | | |
| | 60–90 | 35 | 5 | 85.71% | | |
| | >90 | 35 | 1 | 97.14% | | |
| Platelet ($\times 10^9$/L) | <50 | 33 | 4 | 87.88% | 0.857 | 0.651 |
| | 50–99 | 27 | 3 | 88.89% | | |
| | 100–300 | 18 | 1 | 94.44% | | |
| | >300 | — | — | — | | |
| Karyotype | Normal | 45 | 5 | 88.89% | 0.583 | 0.747 |
| | Numerical Abnormalities | 6 | 0 | 100.00% | | |
| | Structural Abnormalities | 27 | 3 | 88.89% | | |
| Day 15 MRD | Positive | 66 | 7 | 89.39% | 0.010 | 0.919 |
| | Negative | 12 | 1 | 91.67% | | |
| Day 33 MRD | Positive | 77 | 8 | 89.61% | 0.148 | 0.700 |
| | Negative | 1 | 0 | 100.00% | | |
| Concurrent Gene Abnormalities | No Other Gene Abnormalities | 10 | 1 | 90.00% | 0.930 | 0.818 |
| | With a Favorable Prognosis | 7 | 0 | 100.00% | | |

(Continued on following page)

TABLE 6 (*Continued*) OS rates for several factors in the CDKN2A/B deletion group.

| Category | Group | Total number of cases | Number of events | OS rate | $\chi 2$ | *P* |
|---|---|---|---|---|---|---|
| | With a Poor Prognosis | 41 | 4 | 90.24% | | |
| | With Unclear Prognostic Impact | 20 | 3 | 85.00% | | |
| Concurrent TEL-AML1 Abnormalities | Yes | 7 | 0 | 100.00% | 0.798 | 0.372 |
| | No | 71 | 8 | 88.73% | | |
| Concurrent E2A-PBX1 Abnormalities | Yes | 4 | 1 | 75.00% | 0.564 | 0.453 |
| | No | 74 | 7 | 90.54% | | |
| Concurrent BCR-ABL1 Abnormalities | Yes | 11 | 2 | 81.82% | 0.776 | 0.378 |
| | No | 67 | 6 | 91.04% | | |
| Ph Like | Yes | 26 | 3 | 88.46% | 0.012 | 0.914 |
| | No | 52 | 5 | 90.38% | | |
| Concurrent SIT-TALL Abnormalities | Yes | 2 | 1 | 50.00% | 3.271 | 0.071 |
| | No | 76 | 7 | 90.79% | | |
| Concurrent BCR-ABL1 Positive Combined with IKZF1 Deletion | Yes | 8 | 1 | 87.50% | 0.054 | 0.816 |
| | No | 70 | 7 | 90.00% | | |

*$P < 0.05$, statistically significant difference.

CDKN2A/B non-deletion group: 4 T-ALL patients, accounting for 5.1%, and 74 B-ALL patients, accounting for 94.9%.

Rank sum test was used to compare the differences in age, white blood cell count, hemoglobin levels, platelet count, and the proportion of peripheral blood immature cells between the two groups. The results revealed no statistically significant difference in the platelet count at diagnosis ($P = 0.690$), but statistically significant differences were observed in age ($P = 0.008$), white blood cell count ($P < 0.001$), hemoglobin level ($P = 0.037$), and the proportion of peripheral blood immature cells ($P < 0.001$). And the results indicated that the age of onset in the CDKN2A/B deletion group was greater than that in the non-deletion group. Both the white blood cell count and the proportion of peripheral blood immature cells at diagnosis were greater in the CDKN2A/B deletion group than in the non-deletion group, suggesting that pediatric patients with CDKN2A/B deletion had a greater tumor burden at diagnosis. The hemoglobin level at diagnosis was slightly greater in the CDKN2A/B deletion group than in the non-deletion group, indicating that the degree of anemia in these patients was milder than that in the non-deletion group.

The Pearson's chi-squared test was used to compare the basic information of age, sex, and nationality at diagnosis between the two groups. The results revealed no statistically significant differences in sex ($P = 0.144$) or nationality ($P = 0.248$), but there was a statistically significant difference in age ($P = 0.022$). These findings showed that the proportion of patients in the CDKN2A/B deletion group was lower in the 1–10-year-old age group, but was significantly greater in the >10-year-old age group than in the non-deletion group.

The Pearson's chi-squared test was used to compare the immunophenotype distribution between the two groups, and the results indicated a statistically significant difference ($P < 0.001$). The proportion of T-ALL patients in the CDKN2A/B deletion group was significantly greater than that in the non-deletion group, suggesting that CDKN2A/B deletion occurred more frequently in T-ALL patients than in B-ALL patients.

## Risk stratification and MRD positivity

The CKDN2A/B deletion and the non-deletion groups of pediatric ALL patients were monitored for MRD status and risk stratification during the induction therapy phase on days 15 and 33. MRD positivity was defined as MRD $>1 \times 10^{-1}$ on day 15 or MRD $>1 \times 10^{-2}$ on day 33. Pearson's chi-squared test or Fisher's exact test was used to compare the risk stratification and positive rates of MRD on days 15 and 33 between the two groups. There was no statistically significant difference between the two groups ($P = 0.409$, $P = 0.645$, $P = 1.000$), suggesting that CDKN2A/B

TABLE 7 EFS rates for several factors in the CDKN2A/B deletion group.

| Category | Group | Total number of cases | Number of events | EFS rate | $\chi 2$ | *P* |
|---|---|---|---|---|---|---|
| Total | — | 78 | 13 | 83.3% | — | — |
| Age (year) | <1 year | 2 | 1 | 50.00% | 1.190 | 0.552 |
| | 1–10 years | 51 | 7 | 86.27% | | |
| | >10 years | 25 | 5 | 80.00% | | |
| Sex | Male | 50 | 8 | 84.00% | 0.009 | 0.923 |
| | Female | 28 | 5 | 82.14% | | |
| Nationality | Han | 45 | 9 | 80.00% | 0.918 | 0.338 |
| | Non-Han | 33 | 4 | 87.88% | | |
| Immunophenotype | B | 47 | 6 | 87.23% | 1.235 | 0.267 |
| | T | 31 | 7 | 77.42% | | |
| Risk Stratification | Low | 1 | 0 | 100.00% | 9.164 | 0.010 |
| | Intermediate | 55 | 6 | 89.09% | | |
| | High | 22 | 7 | 68.18% | | |
| Central Nervous System Infiltration | Yes | 3 | 2 | 33.33% | 3.062 | 0.080 |
| | No | 75 | 11 | 85.33% | | |
| White Blood Cell ($\times 10^9$/L) | <4 | 7 | 1 | 85.71% | 0.129 | 0.937 |
| | 4–50 | 39 | 7 | 82.05% | | |
| | >50 | 32 | 5 | 84.38% | | |
| Hemoglobin (g/L) | <30 | 1 | 0 | 100.00% | 5.705 | 0.127 |
| | 30–60 | 7 | 3 | 57.14% | | |
| | 60–90 | 35 | 7 | 80.00% | | |
| | >90 | 35 | 3 | 91.43% | | |
| Platelet ($\times 10^9$/L) | <50 | 33 | 8 | 75.76% | 3.238 | 0.198 |
| | 50–99 | 27 | 4 | 85.19% | | |
| | 100–300 | 18 | 1 | 94.44% | | |
| | >300 | — | — | — | | |
| Karyotype | Normal | 45 | 9 | 80.00% | 2.654 | 0.265 |
| | Numerical Abnormalities | 6 | 0 | 100.00% | | |
| | Structural Abnormalities | 27 | 4 | 85.19% | | |
| Day 15 MRD | Positive | 66 | 12 | 81.82% | 0.325 | 0.569 |
| | Negative | 12 | 1 | 91.67% | | |
| Day 33 MRD | Positive | 77 | 13 | 83.12% | 0.350 | 0.554 |
| | Negative | 1 | 0 | 100.00% | | |
| Concurrent Gene Abnormalities | No Other Gene Abnormalities | 10 | 1 | 90.00% | 2.027 | 0.567 |
| | With a Favorable Prognosis | 7 | 0 | 100.00% | | |

(Continued on following page)

TABLE 7 (*Continued*) EFS rates for several factors in the CDKN2A/B deletion group.

| Category | Group | Total number of cases | Number of events | EFS rate | χ2 | *P* |
|---|---|---|---|---|---|---|
| | With a Poor Prognosis | 41 | 7 | 82.93% | | |
| | With Unclear Prognostic Impact | 20 | 5 | 75.00% | | |
| Concurrent TEL-AML1 Abnormalities | Yes | 7 | 0 | 100.00% | 1.507 | 0.220 |
| | No | 71 | 13 | 81.69% | | |
| Concurrent E2A-PBX1 Abnormalities | Yes | 4 | 1 | 75.00% | 0.112 | 0.737 |
| | No | 74 | 12 | 83.78% | | |
| Concurrent BCR-ABL1 Abnormalities | Yes | 11 | 2 | 81.82% | 0.000 | 0.986 |
| | No | 67 | 11 | 83.58% | | |
| Ph Like | Yes | 26 | 3 | 88.46% | 1.213 | 0.271 |
| | No | 52 | 10 | 80.77% | | |
| Concurrent SIT-TALL Abnormalities | Yes | 2 | 1 | 50.00% | 1.674 | 0.196 |
| | No | 76 | 12 | 84.21% | | |
| Concurrent BCR-ABL1 Positive Combined with IKZF1 Deletion | Yes | 8 | 1 | 87.50% | 0.105 | 0.746 |
| | No | 70 | 12 | 82.86% | | |

*$P < 0.05$, statistically significant difference.

deletion could not be considered to be associated with risk stratification or the positive rate of day 15 MRD or day 33 MRD (These data are summarized in Table 3).

## Central nervous system involvement during chemotherapy

Cerebrospinal fluid (CSF) pathological results throughout the chemotherapy process were collected for both groups, with the presence of leukemic cells in the CSF considered central nervous system infiltration (CNS) by leukemia. CDKN2A/B deletion group: 3 patients CNS infiltration (3.8%, 3/78). CDKN2A/B non-deletion group: 2 patients CNS infiltration (2.6%, 2/78). Fisher's exact test was used for comparison, and the results revealed no statistically significant difference in the incidence of CNS infiltration by leukemia during chemotherapy between the two groups ($P = 1.000$), indicating that there was no association between CDKN2A/B deletion and CNS infiltration.

## Molecular biological characteristics at diagnosis

78 pediatric patients with CDKN2A/B deletion were assessed for bone marrow karyotype and concurrent gene abnormalities at diagnosis. Notably, because patients with chromosomal number abnormalities in the CDKN2A/B deletion group were relatively rare, they were not further classified into subgroups of hypodiploid and hyperdiploid patients for comparison. Instead, they were categorized into three groups based on their bone marrow karyotype: normal chromosomes, numerical abnormalities, and structural abnormalities. Given the vast array of gene detection methods and the increased positive rate of gene abnormalities in the context of next-generation sequencing, numerous genes with unclear prognostic significance for pediatric ALL patients have been identified. Therefore, in this study, concurrent gene abnormalities were classified into four groups based on their prognostic impact: no other gene abnormalities aside from CDKN2A/B deletion, genes associated with a favorable prognosis, genes associated with a poor prognosis, and genes with unclear prognostic impact. For the convenience of the study, several common genes with a clear impact on prognosis were also singled out for individual research.

The Pearson's chi-squared test was used to compare the prognostic impact of different concurrent gene abnormalities between the two groups. There were no statistically significant differences in the classification of patients with TEL-AML1 ($P = 0.441$), E2A-PBX1 ($P = 1.000$), BCR-ABL1 ($P = 0.057$), or Ph-like-related genes ($P = 0.615$) or SIL-TAL1 gene abnormalities ($P = 0.477$) between the two groups. A statistically significant difference in bone marrow karyotype ($P = 0.005$) was detected between the two groups, and showed that the proportion of chromosomal number abnormalities in the CDKN2A/B deletion group was significantly lower than that in the non-deletion

TABLE 8 OS rates for several factors in the CDKN2A/B non-deletion group.

| Category | Group | Total number of cases | Number of events | OS rate | $\chi 2$ | *P* |
|---|---|---|---|---|---|---|
| Total | — | 78 | 2 | 97.4% | — | — |
| Age (year) | <1 year | 3 | 0 | 100.00% | 2.334 | 0.311 |
| | 1–10 years | 64 | 1 | 98.44% | | |
| | >10 years | 11 | 1 | 90.91% | | |
| Sex | Male | 41 | 0 | 100.00% | 2.319 | 0.128 |
| | Female | 37 | 2 | 94.59% | | |
| Nationality | Han | 52 | 2 | 96.15% | 1.057 | 0.304 |
| | Non-Han | 26 | 0 | 100.00% | | |
| Immunophenotype | B | 74 | 1 | 98.65% | 10.274 | 0.001* |
| | T | 4 | 1 | 75.00% | | |
| Risk Stratification | Low | 4 | 0 | 100.00% | 5.645 | 0.059 |
| | Intermediate | 55 | 0 | 100.00% | | |
| | High | 19 | 2 | 89.47% | | |
| Central Nervous System Infiltration | Yes | 2 | 0 | 100.00% | 0.042 | 0.837 |
| | No | 76 | 2 | 97.37% | | |
| White Blood Cell ( $\times 10^9$/L) | <4 | 9 | 1 | 88.89% | 4.346 | 0.114 |
| | 4–50 | 18 | 0 | 100.00% | | |
| | >50 | 51 | 1 | 98.04% | | |
| Hemoglobin (g/L) | <30 | 1 | 0 | 100.00% | 0.623 | 0.891 |
| | 30–60 | 14 | 0 | 100.00% | | |
| | 60–90 | 38 | 1 | 97.37% | | |
| | >90 | 25 | 1 | 96.00% | | |
| Platelet ($\times 10^9$/L) | <50 | 60 | 1 | 98.33% | 6.701 | 0.082 |
| | 50–99 | 6 | 1 | 83.33% | | |
| | 100–300 | 10 | 0 | 100.00% | | |
| | >300 | 2 | 0 | 100.00% | | |
| Karyotype | Normal | 32 | 0 | 100.00% | 3.773 | 0.152 |
| | Numerical Abnormalities | 21 | 0 | 100.00% | | |
| | Structural Abnormalities | 25 | 2 | 92.00% | | |
| Day 15 MRD | Positive | 68 | 1 | 98.53% | 2.110 | 0.146 |
| | Negative | 10 | 1 | 90.00% | | |
| Day 33 MRD | Positive | 76 | 1 | 98.68% | 16.141 | <0.001* |
| | Negative | 2 | 1 | 50.00% | | |
| Concurrent Gene Abnormalities | No Other Gene Abnormalities | 14 | 0 | 100.00% | 1.996 | 0.573 |
| | With a Favorable Prognosis | 13 | 0 | 100.00% | | |

(Continued on following page)

TABLE 8 (*Continued*) OS rates for several factors in the CDKN2A/B non-deletion group.

| Category | Group | Total number of cases | Number of events | OS rate | χ2 | *P* |
|---|---|---|---|---|---|---|
| | With a Poor Prognosis | 38 | 2 | 94.74% | | |
| | With Unclear Prognostic Impact | 13 | 0 | 100.00% | | |
| Concurrent TEL-AML1 Abnormalities | Yes | 10 | 0 | 100.00% | 0.310 | 0.578 |
| | No | 68 | 2 | 97.06% | | |
| Concurrent E2A-PBX1 Abnormalities | Yes | 4 | 0 | 100.00% | 0.103 | 0.748 |
| | No | 74 | 2 | 97.30% | | |
| Concurrent BCR-ABL1 Abnormalities | Yes | 4 | 0 | 100.00% | 0.103 | 0.748 |
| | No | 74 | 2 | 97.30% | | |
| Ph Like | Yes | 29 | 2 | 93.10% | 3.255 | 0.071 |
| | No | 49 | 0 | 100.00% | | |
| Concurrent SIT-TALL Abnormalities | No | 78 | 2 | 97.44% | — | — |
| Concurrent BCR-ABL1 Positive Combined with IKZF1 Deletion | No | 78 | 2 | 97.44% | — | — |

*: $P < 0.05$, statistically significant difference.

group. A statistically significant difference was also found in the occurrence of BCR-ABL1 positivity combined with IKZF1 deletion ($P = 0.011$) between the two groups, with 8 patients (10.3%) in the deletion group and none in the non-deletion group. These findings suggested that pediatric ALL patients with CDKN2A/B deletion were more likely to exhibit BCR-ABL1 positivity in conjunction with IKZF1 deletion, and all patients were BCR-ABL1 (p190 type) positivity combined with IKZF1 deletion (IK16 type) positive (These data are summarized in Table 4).

## Relapse and mortality status

Of 78 patients with CDKN2A/B deletion, 9 cases of relapse and 8 cases of mortality. 9 cases of relapse included:3 bone marrow relapses, 5 central nervous system leukemia relapses, and 1 simultaneous relapse of both. 8 cases of mortality included: 4 treatment-related mortalities and 4 mortalities following relapse (Figure 1).

Of 78 patients without CDKN2A/B deletion, 3 cases of relapse, and 2 cases of mortality, both of which were treatment-related mortalities. All 3 cases of relapse were bone marrow relapses.

The Pearson's chi-squared test was used to compare the relapse and mortality rates between the two groups. The results revealed no statistically significant differences (relapse: $P = 0.071$, mortality: $P = 0.050$), suggesting that CDKN2A/B deletion could not be considered to be related to relapse or mortality in pediatric ALL patients.

## Survival analysis

We further analyzed the overall survival (OS) and event-free survival (EFS) of the two groups. For overall survival analysis, the median time of follow-up in the CDKN2A/B deletion group and non-deletion group was 21 months, 23 months respectively. For event-free survival analysis, the median time of follow-up in the CDKN2A/B deletion group and non-deletion group was 24 months, 23 months respectively. Kaplan-Meier analysis was used to plot the survival curves (see Figures 2, 3).

We compared the OS and EFS rates between the two groups. The Log-rank test showed significant differences in overall OS rate (89.7% vs. 97.4%, $P = 0.048$), 2-year OS rate (89.7% vs. 97.4%, $P = 0.048$), and 3-year OS rate (89.7% vs. 97.4%, $P = 0.048$) between the two groups, indicating that the OS rate of CDKN2A/B deletion group was lower than that of the non-deletion group (These data are summarized in Table 5). Kaplan-Meier analysis was used to plot the survival curves (see Figure 2).

The Log-rank test showed no statistically significant differences between the two groups in 1-year, 2-year, and 3-year EFS rates ($P > 0.05$). However, a statistically significant difference was observed in the total EFS rate (83.3% vs. 93.6%, $P = 0.043$), indicating that the total EFS rate of the CDKN2A/B deletion group was lower than that of the non-deletion group

TABLE 9 EFS rates for several factors in the CDKN2A/B non-deletion group.

| Category | Group | Total number of cases | Number of events | EFS rate | $\chi 2$ | *P* |
|---|---|---|---|---|---|---|
| Total | — | 78 | 5 | 93.6% | — | — |
| Age (year) | <1 year | 3 | 0 | 100.00% | 3.267 | 0.195 |
| | 1–10 years | 64 | 3 | 95.31% | | |
| | >10 years | 11 | 2 | 81.82% | | |
| Sex | Male | 41 | 3 | 92.68% | 0.104 | 0.747 |
| | Female | 37 | 2 | 94.59% | | |
| Nationality | Han | 52 | 4 | 92.31% | 0.525 | 0.469 |
| | Non-Han | 26 | 1 | 96.15% | | |
| Immunophenotype | B | 74 | 3 | 95.95% | 15.091 | <0.001* |
| | T | 4 | 2 | 50.00% | | |
| Risk Stratification | Low | 4 | 0 | 100.00% | 3.030 | 0.220 |
| | Intermediate | 55 | 2 | 96.36% | | |
| | High | 19 | 3 | 84.21% | | |
| Central Nervous System Infiltration | Yes | 2 | 0 | 100.00% | 0.111 | 0.739 |
| | No | 76 | 5 | 93.42% | | |
| White Blood Cell ($\times 10^9$/L) | <4 | 9 | 1 | 88.89% | 2.557 | 0.278 |
| | 4–50 | 18 | 0 | 100.00% | | |
| | >50 | 51 | 4 | 92.16% | | |
| Hemoglobin (g/L) | <30 | 1 | 0 | 100.00% | 1.528 | 0.676 |
| | 30–60 | 14 | 0 | 100.00% | | |
| | 60–90 | 38 | 3 | 92.11% | | |
| | >90 | 25 | 2 | 92.00% | | |
| Platelet ($\times 10^9$/L) | <50 | 60 | 4 | 93.33% | 2.279 | 0.517 |
| | 50–99 | 6 | 1 | 83.33% | | |
| | 100–300 | 10 | 0 | 100.00% | | |
| | >300 | 2 | 0 | 100.00% | | |
| Karyotype | Normal | 32 | 1 | 96.88% | 1.191 | 0.551 |
| | Numerical Abnormalities | 21 | 1 | 95.24% | | |
| | Structural Abnormalities | 25 | 3 | 88.00% | | |
| Day 15 MRD | Positive | 68 | 4 | 94.12% | 0.266 | 0.606 |
| | Negative | 10 | 1 | 90.00% | | |
| Day 33 MRD | Positive | 76 | 4 | 94.74% | 6.345 | 0.012* |
| | Negative | 2 | 1 | 50.00% | | |
| Concurrent Gene Abnormalities | No Other Gene Abnormalities | 14 | 0 | 100.00% | 2.411 | 0.492 |
| | With a Favorable Prognosis | 13 | 0 | 100.00% | | |

(Continued on following page)

TABLE 9 (*Continued*) EFS rates for several factors in the CDKN2A/B non-deletion group.

| Category | Group | Total number of cases | Number of events | EFS rate | χ2 | *P* |
|---|---|---|---|---|---|---|
| | With a Poor Prognosis | 38 | 4 | 89.47% | | |
| | With Unclear Prognostic Impact | 13 | 1 | 92.31% | | |
| Concurrent TEL-AML1 Abnormalities | Yes | 10 | 0 | 100.00% | 0.857 | 0.355 |
| | No | 68 | 5 | 92.65% | | |
| Concurrent E2A-PBX1 Abnormalities | Yes | 4 | 0 | 100.00% | 0.267 | 0.605 |
| | No | 74 | 5 | 93.24% | | |
| Concurrent BCR-ABL1 Abnormalities | Yes | 4 | 0 | 100.00% | 0.157 | 0.692 |
| | No | 74 | 5 | 93.24% | | |
| Ph Like | Yes | 29 | 3 | 89.66% | 0.937 | 0.333 |
| | No | 49 | 2 | 95.92% | | |
| Concurrent SIT-TALL Abnormalities | No | 78 | 5 | 93.60% | — | — |
| Concurrent BCR-ABL1 Positive Combined with IKZF1 Deletion | No | 78 | 5 | 93.60% | — | — |

*$P < 0.05$, statistically significant difference.

(These data are summarized in Table 5). Kaplan-Meier analysis was used to plot the survival curves (see Figure 3).

## Prognostic factor analysis

### In the CDKN2A/B deletion group

The statistical results of the OS rates for several factors in the CDKN2A/B deletion group (shown in Table 6) indicated that risk stratification ($P = 0.027$) was a factor affecting the OS rates in pediatric patients with CDKN2A/B deletion. Risk stratification was included in the Cox regression analysis. The results of the Cox regression analysis indicated that risk stratification (95%CI: 1.356~24.091, $P = 0.018$) was a significant factor affecting the OS rate in pediatric patients with CDKN2A/B deletion.

The statistical results of EFS rates for several factors in the CDKN2A/B deletion group (shown in Table 7) indicated that risk stratification was a factor affecting the EFS rates in pediatric patients with CDKN2A/B gene deletion ($P = 0.010$). Risk stratification was included in the Cox regression analysis. The results of the Cox regression analysis indicated that risk stratification (95%CI: 1.567~14.290, $P = 0.006$) was a significant factor affecting the EFS rate in pediatric patients with CDKN2A/B gene deletion.

These findings suggested that the greater the risk stratification of pediatric patients with CDKN2A/B gene deletion, the greater the possibility of relapse or death.

### In the CDKN2A/B non-deletion group

The statistical results of OS rates for several factors in the CDKN2A/B non-deletion Group (shown in Table 8) indicated that the immunophenotype ($P = 0.001$) and the positivity rate of MRD on day 33 ($P < 0.001$) were factors affecting the OS rates in pediatric patients without CDKN2A/B gene deletion. The immunophenotype and positivity rate of MRD on day 33 were included in the multivariate Cox regression analysis. The results of the Cox regression analysis indicated that neither the immunophenotype ($P = 0.977$) nor the positivity rate of MRD on day 33 ($P = 0.965$) were significant factors affecting the OS rates in pediatric patients without CDKN2A/B gene deletion.

The statistical results related to EFS rates for several factors in the CDKN2A/B non-deletion Group (shown in Table 9) indicated that the immunophenotype ($P < 0.001$) and the positivity rate of MRD on day 33 ($P = 0.012$) were factors affecting the EFS rates in pediatric patients without CDKN2A/B gene deletion. The immunophenotype and positivity rate of MRD on day 33 were included in the multivariate Cox regression analysis. The results of the Cox regression analysis indicated that the T-cell immunophenotype (95%CI: 1.728~162.834, $P = 0.015$) was a significant factor affecting the EFS rate in pediatric patients without CDKN2A/B deletion. These findings suggested that pediatric patients without CDKN2A/B deletion had a greater possibility of relapse or death when they were diagnosed with T-ALL.

# Discussion

## CDKN2A/B deletion rate and clinical characteristics

In this study, the male-to-female ratio among pediatric ALL patients was 1.8:1, slightly higher than the overall male-to-female ratio of 1.5:1 reported in epidemiological studies of ALL in China. Overseas studies indicated that the rate of CDKN2A/B deletion in pediatric ALL patients is between 15% and 35% [16]. Several studies have also reported a 44% overall frequency of CDKN2A/B deletion in pediatric ALL patients [19]. In the study by Steeghs et al., the rate of CDKN2A/B deletion was 33% [20]. In this study of 310 pediatric ALL patients, 78 patients with CDKN2A/B deletion were detected, accounting for 25.2%, slightly lower than the rates reported in the studies mentioned above. This discrepancy may be related to the smaller sample size or racial differences between countries, and further research with an expanded sample size is needed for confirmation. In this study, statistical analysis revealed a significant difference in the occurrence of CDKN2A/B deletion between the two groups in terms of immunophenotype ($P < 0.001$), with a greater proportion of T-ALL patients in the CDKN2A/B deletion group than in the non-deletion group. The proportion of patients with CDKN2A/B deletion in T-ALL patients was greater than that in B-ALL patients. This was consistent with the findings of studies by Agarwal et al. [21] and Sulong [22]. In terms of age at diagnosis, the proportion of CDKN2A/B deletion group was higher in the age >10 years than that in the non-deletion group ($P = 0.022$), which was consistent with the findings of Agarwal et al. [21] that deletion was more likely to occur in older children. Additionally, the white blood cell count and the proportion of peripheral blood immature cells at diagnosis were greater in the deletion group than in the non-deletion group. This finding was similar to the results of Kathiravan et al. [19], suggesting that pediatric patients with CDKN2A/B deletion had a greater tumor burden at diagnosis. In summary, this study revealed that pediatric patients with CDKN2A/B deletion generally present with the following clinical characteristics: a greater proportion of T-ALL patients, a higher median white blood cell count at diagnosis, and a greater proportion in the age >10 years. T-ALL, a white blood cell count of $\geq 50 \times 10^9$/L, age ≥1 year was classified as intermediate risk according to the risk stratification of the CCLG-ALL2018 protocol. In this study, there was a statistically significant difference in bone marrow karyotype between the two groups, indicating that the proportion of chromosomal number abnormalities in the CDKN2A/B deletion group was significantly lower than that in the non-deletion group. This finding was not consistent with the study by González-Gil [16], which reported a relatively low frequency of CDKN2A/B deletion in patients with a hyperdiploid karyotype, which was associated with a favorable prognosis. Furthermore, statistical analysis revealed that the CDKN2A/B deletion group was prone to BCR-ABL1 positivity concurrent with IKZF1 deletion, and all the patients were BCR-ABL1 (p190 type) positivity concurrently with IKZF1 deletion (IK16 type) positive. No cases of BCR-ABL1 positivity concurrent with IKZF1 deletion were found in the non-deletion group. This finding was not entirely consistent with the study by González-Gil [16], which suggested that CDKN2A/B deletion was more frequently observed in high-risk pediatric patients, especially those with BCR-ABL1 positivity. However, both BCR-ABL1 positivity and IKZF1 deletion are markers of poor prognosis. A larger sample size is needed to further investigate whether CDKN2A/B deletion is associated with BCR-ABL1 positivity combined with IKZF1 deletion and how the coexistence of the three affects the prognosis of pediatric ALL patients. Research by Williams et al. [23] indicated that in the treatment of BCR-ABL1 positive B-ALL with imatinib, the presence of ARF deletion at the p14 locus encoded by the CDKN2A can affect sensitivity to imatinib, leading to drug resistance and poorer treatment outcomes. However, the mechanism remains unclear. The use of imatinib in combination with a JAK kinase inhibitor may be beneficial for the treatment of B-ALL patients with BCR-ABL1 positivity combined with ARF locus deletion. Iacobucci et al. [24] have shown that the presence of IKZF1 deletion combined with deletion of the ARF locus encoded by the CDKN2A was associated with poorer prognosis and higher risk of relapse and can lead to resistance to TKIs targeted therapy in adults with BCR-ABL1 positive B-ALL. In pediatric ALL, more samples and relevant experimental data are needed to explore whether deletion of the CDKN2A/B or the encoded locus is related to resistance to TKIs in BCR-ABL1-positive patients, and may be able to guide the selection of targeted therapies for BCR-ABL1 positive pediatric ALL patients.

## Survival analysis and prognostic factor analysis

Under the CCLG-ALL2008 protocol in China, the 5-year OS and EFS rates for pediatric ALL patients were reported to be 85.3% and 79.9%, respectively [25]. In this study, the overall OS and EFS rates were 89.7%, and 83.3%, respectively. The 1-year OS and EFS rates were 92.3% and 89.7%, respectively. The 2-year OS and EFS rates were 89.7% and 89.7%, respectively. The 3-year OS and EFS rates were 89.7% and 84.6%, respectively. These rates were lower than those of the non-deletion group (For details see Table 5). Statistical analysis revealed significant differences in the overall OS rates, 2-year OS rates, 3-year OS rates, and overall EFS rates between the two groups of pediatric ALL patients ($P < 0.05$), indicating that CDKN2A/B deletion was associated with lower OS and EFS rates. These findings were generally consistent with the results of studies by Agarwal [21] and Kathiravan [19], which revealed that pediatric ALL patients with CDKN2A/B deletion had a greater risk and lower event-free survival rate. Owing to the relatively short follow-up period in this study, further analyses with more samples and extended follow-up time are needed. Statistical analysis of prognostic factors revealed that risk stratification was a significant factor affecting the OS and EFS rates in pediatric patients

with CDKN2A/B deletion ($P = 0.018$, $P = 0.06$). For patients with CDKN2A/B deletion, the higher the risk stratification level was, the greater the possibility of relapse or death.

Currently, there is still variability in the prognosis of pediatric ALL patients related to the CDKN2A/B, which may be due to the deletion of the CDKN2A/B being associated with specific genetics, with the frequency of CDKN2A/B deletion varying significantly depending on combination of other genes [22]. In this study, CDKN2A/B deletion combined with a number of risk stratification factors for intermediate risk, and it was easy to combine BCR-ABL1 positivity and IKZF1 deletion, but there was no statistical significance in risk stratification, which may be related to the small sample size of this study. With the progress of gene research in the field of leukemia and the further expansion of sample size, CDKN2A/B deletion may be included as a criterion for intermediate risk in the stratification of pediatric ALL patients.

## Conclusion

At diagnosis, pediatric patients with CDKN2A/B deletion had higher peripheral blood white blood cell counts and proportions of immature cells in the peripheral blood. The age at diagnosis was older in the deletion group, with a greater proportion in the age group over 10 years old.

Compared with that in pediatric patients with B-ALL, deletion of the CDKN2A/B occurred more frequently in pediatric patients with T-ALL.

CDKN2A/B deletion was more likely to result in BCR-ABL1 positivity combined with IKZF1 deletion.

Pediatric patients with CDKN2A/B deletion had lower OS and EFS rates, indicating that CDKN2A/B deletion was one of the factors influencing poor prognosis.

## Author contributions

Concept and design: YW and XT; data collection and analysis: XM, NJ, YH, and LZ; drafting of the article: YW and PW; critical revision of the article for important intellectual content: LL and XT; study supervision: XT and LL. All authors contributed to the article and approved the submitted version.

## Data availability

The original contributions presented in the study are included in the article, further inquiries can be directed to the corresponding authors.

## Ethics statement

This study was conducted in accordance with the Declaration of Helsinki and approved by Ethics Committee of Sichuan Provincial Woman's and Children's Hospital (approval no. 20241031-427). Written informed consent was obtained from all participants or their legal guardians.

## Funding

The author(s) declare that financial support was received for the research, authorship, and/or publication of this article. This work was supported by the funding of Sichuan Science and Technology Program (Grant Nos. 2022YFS0622, 2022YFS0622-B4).

## Conflict of interest

The author(s) declared no potential conflicts of interest with respect to the research, authorship, and/or publication of this article.

## Generative AI statement

The author(s) declare that no Generative AI was used in the creation of this manuscript.

## References

1. Hunger SP, Mullighan CG. Acute lymphoblastic leukemia in children. *New Engl J Med* (2015) **373**:1541–52. doi:10.1056/nejmra1400972

2. Pui CH, Campana D, Evans WE. Childhood acute lymphoblastic leukaemia--current status and future perspectives. *The Lancet Oncol* (2001) **2**:597–607. doi:10.1016/s1470-2045(01)00516-2

3. Cazzaniga G, Biondi A. Molecular monitoring of childhood acute lymphoblastic leukemia using antigen receptor gene rearrangements and quantitative polymerase chain reaction technology. *Haematologica* (2005) **90**:382–90.

4. Ishida H, Iguchi A, Aoe M, Takahashi T, Tamefusa K, Kanamitsu K, et al. Panel-based next-generation sequencing identifies prognostic and actionable genes in childhood acute lymphoblastic leukemia and is suitable for clinical sequencing. *Ann Hematol* (2019) **98**:657–68. doi:10.1007/s00277-018-3554-8

5. Coccaro N, Anelli L, Zagaria A, Specchia G, Albano F. Next-generation sequencing in acute lymphoblastic leukemia. *Int J Mol Sci* (2019) **20**:2929. doi:10.3390/ijms20122929

6. Kamps R, Brandão RD, Bosch BJ, Paulussen AD, Xanthoulea S, Blok MJ, et al. Next-generation sequencing in oncology: genetic diagnosis, risk prediction and cancer classification. *Int J Mol Sci* (2017) **18**:308. doi:10.3390/ijms18020308

7. Zhao R, Choi BY, Lee MH, Bode AM, Dong Z. Implications of genetic and epigenetic alterations of CDKN2A (p16(INK4a)) in cancer. *EBioMedicine* (2016) **8**:30–9. doi:10.1016/j.ebiom.2016.04.017

8. Spiliopoulou P, Yang SC, Bruce JP, Wang BX, Berman HK, Pugh TJ, et al. All is not lost: learning from 9p21 loss in cancer. *Trends Immunology* (2022) **43**:379–90. doi:10.1016/j.it.2022.03.003

9. Ampatzidou M, Papadhimitriou SI, Paisiou A, Paterakis G, Tzanoudaki M, Papadakis V, et al. The prognostic effect of CDKN2A/2B gene deletions in pediatric acute lymphoblastic leukemia (ALL): independent prognostic significance in BFM-based protocols. *Diagnostics (Basel, Switzerland)* (2023) **13**:1589. doi:10.3390/diagnostics13091589

10. Otsuki T, Clark HM, Wellmann A, Jaffe ES, Raffeld M. Involvement of CDKN2 (p16INK4A/MTS1) and p15INK4B/MTS2 in human leukemias and lymphomas. *Cancer Res* (1995) **55**:1436–40.

11. Wang HP, Zhou YL, Huang X, Zhang Y, Qian JJ, Li JH, et al. *CDKN2A* deletions are associated with poor outcomes in 101 adults with T-cell acute lymphoblastic leukemia. *Am J Hematol* (2021) **96**:312–9. doi:10.1002/ajh.26069

12. Kim M, Yim SH, Cho NS, Kang SH, Ko DH, Oh B, et al. Homozygous deletion of CDKN2A (p16, p14) and CDKN2B (p15) genes is a poor prognostic factor in adult but not in childhood B-lineage acute lymphoblastic leukemia: a comparative deletion and hypermethylation study. *Cancer Genet Cytogenet* (2009) **195**:59–65. doi:10.1016/j.cancergencyto.2009.06.013

13. Onizuka M, Kikkawa E, Machida S, Toyosaki M, Suzuki R, Ogiya D, et al. Association of CDKN2A/2B deletion with relapse after hematopoietic stem cell transplantation for acute lymphoblastic leukemia. *Blood Cel Ther* (2023) **6**:80–6. doi:10.31547/bct-2023-004

14. Feng J, Guo Y, Yang W, Zou Y, Zhang L, Chen Y, et al. Childhood acute B-lineage lymphoblastic leukemia with CDKN2A/B deletion is a distinct entity with adverse genetic features and poor clinical outcomes. *Front Oncol* (2022) **12**:878098. doi:10.3389/fonc.2022.878098

15. Mirebeau D, Acquaviva C, Suciu S, Bertin R, Dastugue N, Robert A, et al. The prognostic significance of CDKN2A, CDKN2B and MTAP inactivation in B-lineage acute lymphoblastic leukemia of childhood. Results of the EORTC studies 58881 and 58951. *Haematologica* (2006) **91**:881–5.

16. González-Gil C, Ribera J, Ribera JM, Genescà E. The Yin and Yang-like clinical implications of the CDKN2A/ARF/CDKN2B gene cluster in acute lymphoblastic leukemia. *Genes* (2021) **12**:79. doi:10.3390/genes12010079

17. Genescà E, Lazarenkov A, Morgades M, Berbis G, Ruíz-Xivillé N, Gómez-Marzo P, et al. Frequency and clinical impact of CDKN2A/ARF/CDKN2B gene deletions as assessed by in-depth genetic analyses in adult T cell acute lymphoblastic leukemia. *J Hematol and Oncol* (2018) **11**:96. doi:10.1186/s13045-018-0639-8

18. Jang W, Park J, Kwon A, Choi H, Kim J, Lee GD, et al. CDKN2B downregulation and other genetic characteristics in T-acute lymphoblastic leukemia. *Exp and Mol Med* (2019) **51**:1–15. doi:10.1038/s12276-018-0195-x

19. Kathiravan M, Singh M, Bhatia P, Trehan A, Varma N, Sachdeva MS, et al. Deletion of CDKN2A/B is associated with inferior relapse free survival in pediatric B cell acute lymphoblastic leukemia. *Leuk and Lymphoma* (2019) **60**:433–41. doi:10.1080/10428194.2018.1482542

20. Steeghs EMP, Boer JM, Hoogkamer AQ, Boeree A, de Haas V, de Groot-Kruseman HA, et al. Copy number alterations in B-cell development genes, drug resistance, and clinical outcome in pediatric B-cell precursor acute lymphoblastic leukemia. *Scientific Rep* (2019) **9**:4634. doi:10.1038/s41598-019-41078-4

21. Agarwal M, Bakhshi S, Dwivedi SN, Kabra M, Shukla R, Seth R. Cyclin dependent kinase inhibitor 2A/B gene deletions are markers of poor prognosis in Indian children with acute lymphoblastic leukemia. *Pediatr Blood and Cancer* (2018) **65**:e27001. doi:10.1002/pbc.27001

22. Sulong S, Moorman AV, Irving JA, Strefford JC, Konn ZJ, Case MC, et al. A comprehensive analysis of the CDKN2A gene in childhood acute lymphoblastic leukemia reveals genomic deletion, copy number neutral loss of heterozygosity, and association with specific cytogenetic subgroups. *Blood* (2009) **113**:100–7. doi:10.1182/blood-2008-07-166801

23. Williams RT, Roussel MF, Sherr CJ. Arf gene loss enhances oncogenicity and limits imatinib response in mouse models of Bcr-Abl-induced acute lymphoblastic leukemia. *Proc Natl Acad Sci* (2006) **103**:6688–93. doi:10.1073/pnas.0602030103

24. Iacobucci I, Ferrari A, Lonetti A, Papayannidis C, Paoloni F, Trino S, et al. CDKN2A/B alterations impair prognosis in adult BCR-ABL1-positive acute lymphoblastic leukemia patients. *Clin Cancer Res* (2011) **17**:7413–23. doi:10.1158/1078-0432.ccr-11-1227

25. Cui L, Li ZG, Chai YH, Yu J, Gao J, Zhu XF, et al. Outcome of children with newly diagnosed acute lymphoblastic leukemia treated with CCLG-ALL 2008: the first nation-wide prospective multicenter study in China. *Am J Hematol* (2018) **93**:913–20. doi:10.1002/ajh.25124

EBM Experimental Biology and Medicine

TYPE Original Research
PUBLISHED 08 January 2025
DOI 10.3389/ebm.2024.10401



OPEN ACCESS

*CORRESPONDENCE
Sulev Kõks,
sulev.koks@murdoch.edu.au

RECEIVED 08 October 2024
ACCEPTED 19 December 2024
PUBLISHED 08 January 2025

CITATION
Kõks S, Rallmann K, Muldmaa M, Price J, Pfaff AL and Taba P (2025) Whole blood transcriptome profile identifies motor neurone disease RNA biomarker signatures.
*Exp. Biol. Med.* 249:10401.
doi: 10.3389/ebm.2024.10401



# Whole blood transcriptome profile identifies motor neurone disease RNA biomarker signatures

Sulev Kõks[1,2]*, Karin Rallmann[3], Mari Muldmaa[4,5], Jack Price[2], Abigail L. Pfaff[1,2] and Pille Taba[5]

[1]Centre for Molecular Medicine and Innovative Therapeutics, Murdoch University, Perth, WA, Australia, [2]Perron Institute for Neurological and Translational Science, Perth, WA, Australia, [3]Department of Neurology, Tartu University Hospital, Tartu, Estonia, [4]Department of Neurology, North Estonia Medical Center, Tallinn, Estonia, [5]Institute of Clinical Medicine, University Tartu, Tartu, Estonia

## Abstract

Blood-based biomarkers for motor neuron disease are needed for better diagnosis, progression prediction, and clinical trial monitoring. We used whole blood-derived total RNA and performed whole transcriptome analysis to compare the gene expression profiles in (motor neurone disease) MND patients to the control subjects. We compared 42 MND patients to 42 aged and sex-matched healthy controls and described the whole transcriptome profile characteristic for MND. In addition to the formal differential analysis, we performed functional annotation of the genomics data and identified the molecular pathways that are differentially regulated in MND patients. We identified 12,972 genes differentially expressed in the blood of MND patients compared to age and sex-matched controls. Functional genomic annotation identified activation of the pathways related to neurodegeneration, RNA transcription, RNA splicing and extracellular matrix reorganisation. Blood-based whole transcriptomic analysis can reliably differentiate MND patients from controls and can provide useful information for the clinical management of the disease and clinical trials.

KEYWORDS

**motor neuron disease, amyotrophic lateral sclerosis, RNA-seq, whole transcriptome, gene expression profiling**

## Impact statement

The present study analysed the gene expression on the whole transcriptome scale in the blood of motor neuron disease (MND) patients. We demonstrated that MND patients have highly specific gene expression patterns or fingerprints, and many genes are differentially expressed in the blood of MND patients. This finding significantly impacts our understanding of the role of the differentially expressed genes in the

pathogenesis of MND. These findings present the utility of RNA-base blood biomarkers for neurological diseases and in precision clinical management.

## Introduction

Motor neurone disease (MND) is a group of chronic sporadic and familial disorders characterised by progressive degeneration of motor neurons [1]. The disease is caused by the degeneration of the upper, lower, or both motor neurones. The prognosis of MND depends upon the age at onset and the area of the central nervous system affected [2]. Based on the site of origin and the severity of neurological involvement, four main subtypes of MND have been described: amyotrophic lateral sclerosis (ALS), progressive bulbar palsy (PBP), progressive muscular atrophy (PMA), and primary lateral sclerosis (PLS) [3].

ALS is the most common form of MND. ALS and MND are commonly used interchangeably or as synonyms. ALS is also known as Lou Gehrig's disease or Charcot disease [1]. ALS is an adult-onset, progressive, neurodegenerative disorder involving the large motor neurons of the brain and the spinal cord. It produces a characteristic clinical picture with weakness and wasting of the limbs and bulbar muscles, leading to death from respiratory failure within 5 years.

The degeneration of motor neurons is irreversible, and apparently, it starts many years before the clinical features emerge. Therefore, reliable biomarkers from easily accessible tissues are needed for earlier diagnosis and better prediction of the progression of the disease. The molecular pathology underlying MND relies on genetic variants described in at least 100 different genes to date and on the overlay of the transcriptomic changes [4, 5]. The pathogenesis of the disease involves oxidative stress, inflammation, ER stress with protein aggregation, autophagy and aberrant RNA processing [5, 6]. Familial and sporadic forms of MND can be distinguished based on the evidence of genetic variants and family history [7]. However, only about 20% of MND cases can be explained by known genetic variations [8].

In addition to the well-known genes and their variants, we recently described an unexpectedly large number of exonisation of SINE-VNTR-Alu repeats (SVAs) in the motor cortex [9]. SVAs are known to alter splicing, and several of these elements have been associated with disease through such mechanisms [10, 11]. This indicates the significant role that noncoding or dark genomes can play in the pathogenesis of complex diseases. Moreover, analysis of the whole transcriptome gives an excellent functional opportunity to explore the molecular changes at different stages of diseases, making it a suitable tool for biomarkers [10]. Indeed, transcriptomic analysis can be performed from any biological material, like blood or cerebrospinal fluid and can be used for different conditions [5, 12, 13]. Transcriptomic analysis helps to understand the effect of DNA variants, especially for the splicing-altering variants.

Post-mortem tissue analysis for chronic diseases is always an option to identify molecular patterns in the affected tissues, and this can help to classify the different pathogenic mechanisms [6]. However, using peripheral tissues, like blood, skin, or saliva, allows molecular profiling during the disease's progression and real-life monitoring of pathogenic changes [12, 14, 15]. In the case of MND, several previous studies have been performed to analyse the transcriptomic profile of the blood [16, 17]. In one example, whole blood-derived RNA (PAXgene tubes) was used for microarray analysis; in another, PBMC-derived RNA was used for RNA sequencing. These studies have their limitations. In the case of the microarray analysis, only a certain number of genes that are printed in the microarray can be analysed, and while the number is high (29,830 unique and suitable probes), the

TABLE 1 General characteristics of the study cohort.

| Group | Motor neurone disease (MND) | Healthy controls (HC) |
|---|---|---|
| Total, n[a] | 42 | 42 |
| Male, n | 13 | 13 |
| Female, n | 29 | 29 |
| Total mean age, y (sd) | 65.6 (9.3) | 65.7 (9.4) |
| Male mean age, y (sd) | 64.6 (11.6) | 64.3 (11.4) |
| Female mean age, y (sd) | 66.2 (8.4) | 66.2 (8.4) |
| MND duration, m (sd) | 18.2 (19.2) | — |
| Male duration, m (sd) | 16.6 (24.5) | — |
| Female duration, m (sd) | 19.0 (16.8) | — |

[a]n, number of subjects; y, years; m, months; sd, standard deviation.

TABLE 2 Differentially expressed genes in the blood of MND patients compared to healthy controls. The top 30 genes are shown sorted by the FDR-adjusted *p*-value.

| Ensembl ID | logFC | p-adj | Gene name | Gene symbol |
|---|---|---|---|---|
| ENSG00000202354 | 6.49 | 1.25E-136 | RNA, Ro60-associated Y3 | RNY3 |
| ENSG00000201098 | 7.26 | 4.63E-119 | RNA, Ro60-associated Y1 | RNY1 |
| ENSG00000282885 | 3.29 | 3.44E-111 | novel transcript | lnc-NEMF-1 |
| ENSG00000091986 | −6.81 | 4.27E-101 | coiled-coil domain containing 80 | CCDC80 |
| ENSG00000011465 | −7.48 | 9.56E-99 | decorin | DCN |
| ENSG00000118523 | −4.88 | 5.04E-97 | cellular communication network factor 2 | CCN2 |
| ENSG00000164692 | −7.26 | 1.58E-95 | collagen type I alpha 2 chain | COL1A2 |
| ENSG00000108821 | −6.43 | 1.04E-93 | collagen type I alpha 1 chain | COL1A1 |
| ENSG00000128591 | −5.83 | 8.20E-93 | filamin C | FLNC |
| ENSG00000138131 | −5.55 | 1.70E-87 | lysyl oxidase like 4 | LOXL4 |
| ENSG00000113739 | −7.73 | 2.01E-86 | stanniocalcin 2 | STC2 |
| ENSG00000199568 | 9.05 | 1.07E-80 | RNA, U5A small nuclear 1 | RNU5A-1 |
| ENSG00000248527 | 3.20 | 6.12E-80 | MT-ATP6 pseudogene 1 | MTATP6P1 |
| ENSG00000087245 | −6.83 | 6.87E-80 | matrix metallopeptidase 2 | MMP2 |
| ENSG00000186340 | −7.55 | 2.94E-79 | thrombospondin 2 | THBS2 |
| ENSG00000115414 | −5.71 | 1.45E-78 | fibronectin 1 | FN1 |
| ENSG00000150459 | −0.79 | 3.01E-77 | Sin3A associated protein 18 | SAP18 |
| ENSG00000212283 | 5.02 | 4.23E-77 | small nucleolar RNA, C/D box 89 | SNORD89 |
| ENSG00000111799 | −6.88 | 1.03E-75 | collagen type XII alpha 1 chain | COL12A1 |
| ENSG00000199631 | 7.52 | 2.52E-73 | small nucleolar RNA, C/D box 33 | SNORD33 |
| ENSG00000144810 | −6.44 | 3.84E-73 | collagen type VIII alpha 1 chain | COL8A1 |
| ENSG00000164761 | −6.80 | 1.42E-72 | TNF receptor superfamily member 11b | TNFRSF11B |
| ENSG00000115963 | −6.65 | 2.38E-70 | Rho family GTPase 3 | RND3 |
| ENSG00000115461 | −7.69 | 9.88E-70 | insulin like growth factor binding protein 5 | IGFBP5 |
| ENSG00000126214 | 0.95 | 1.05E-63 | kinesin light chain 1 | KLC1 |
| ENSG00000186660 | −0.54 | 1.50E-63 | ZFP91 zinc finger protein, E3 ubiquitin ligase | ZFP91 |
| ENSG00000142156 | −2.90 | 1.73E-62 | collagen type VI alpha 1 chain | COL6A1 |
| ENSG00000238961 | 5.94 | 3.17E-62 | small nucleolar RNA, H/ACA box 47 | SNORA47 |
| ENSG00000166923 | −7.07 | 2.09E-61 | gremlin 1, DAN family BMP antagonist | GREM1 |
| ENSG00000281501 | 1.98 | 5.08E-61 | SEPSECS antisense RNA 1 | SEPSECS-AS1 |

whole transcriptome sequencing gives information entire transcriptome (60,230 elements) [17]. Moreover, RNA-seq has a better dynamic range in detecting gene expression therefore the power to detect differential expression is better. PBMC-derived samples only include monocytes and do not contain neutrophils, basophils, and eosinophils. While basophils and eosinophils are only a small subset of all immune cells (0–2% and 1–7%, respectively), neutrophils make up a majority of circulating nucleated blood cells (45–75%) [18]. Therefore, analysing PBMC samples will give only partial information about the RNA changes in the blood and this has been shown in many studies [18–20]. The present study aimed to perform whole transcriptome analysis from the whole-blood (Tempus tubes) derived RNA and to identify the

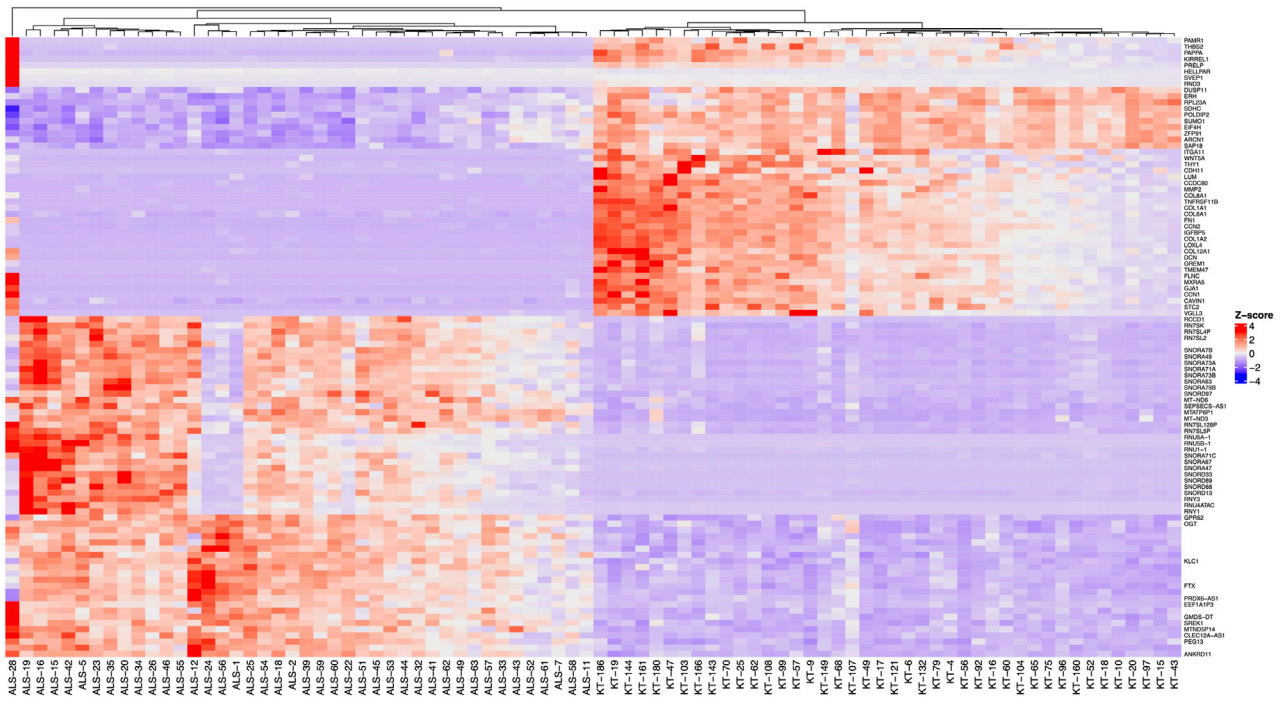


FIGURE 1
Heatmap of the 100 differentially expressed genes (FDR < 0.05, logFC > |0.07|) with the highest statistical significance. Before clustering, z-scores of the normalised expression data were calculated and a complete method for hierarchical clustering using Euclidean distance. Samples with "ALS" designate the MND group, and "KT" designate healthy controls.

whole blood transcriptomic profile by comparing MND patients to the age and sex-matched healthy controls.

## Materials and methods

### Study cohort

Between 2013 and 2018, a total of 84 participants (42 MND patients and 42 healthy control patients without any chronic diseases) were enrolled in the study and signed written informed consent. Inclusion criteria for MND patients were the diagnosis of probable or definitive MND based on El Escorial Criteria and the absence of a positive family history.

For the healthy controls, we excluded patients with any chronic diseases, especially any neurologic, rheumatological, haematological, or oncological conditions. In addition, treatment with biologics or chemotherapy was also excluded. A white blood cell (WBC) count and C-reactive protein (CRP) were measured in every health control to exclude any underlying inflammatory condition.

The blood samples were collected into Tempus Blood RNA tubes and stored according to the manufacturer's instructions. The research was conducted with the approval of the University of Tartu Research Ethics Committee, and all participants provided written informed consent. The comprehensive patient selection process leveraged hospital records, neurologist consultations, and the Estonian Health Insurance Fund's national health data repository.

The whole blood was collected from 42 MND patients and 42 healthy controls using Tempus Blood RNA collection tubes (Thermo Fisher Scientific). Neurologists recruited MND patients, and the subtype of the MND was confirmed. Healthy controls were recruited among the visitors referred to the blood analysis who did not have chronic diseases. The control samples were ideal controls without any neurological condition or major chronic illness and were age- and sex-matched to the MND group (complete information is given in Supplementary Table S1).

### Whole transcriptome analysis and functional annotation

The RNA was isolated from whole blood using a Tempus Spin Isolation Kit (Thermo Fisher Scientific). After initial quality control and quantification (A260/280 ratio, RIN number). RNA was used for the total RNA sequencing necessary for the whole transcriptome analysis.

Total RNA sequencing was performed in all 84 samples at the Genomics Core Facility at Murdoch University, Perth, WA. Illumina paired-end 2 × 100bp read length using NovaSeq 6000.

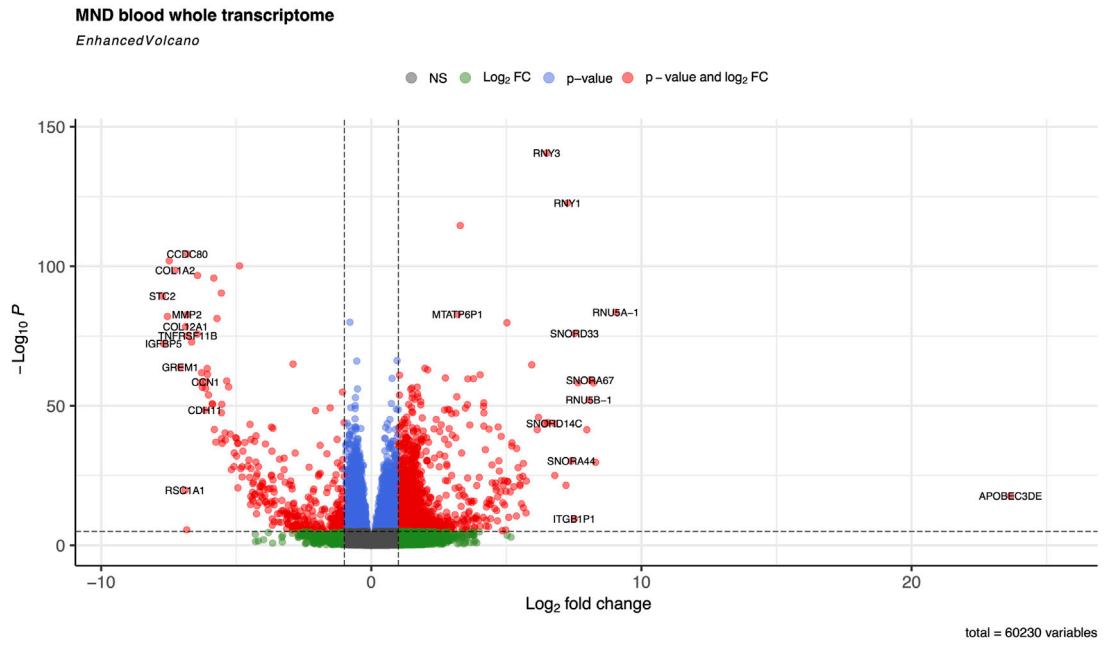


FIGURE 2
Volcano plot of the whole transcriptome data from the blood on controls and MND patients The default cut-off for log2FC is >|2|, and the default for *P*-value is 10e-6. Dashed lines represent these values. Red dots represent genes meeting both cut-off criteria; green dots meet only the log2FC cut-off, and blue dots indicate genes meeting only the *P*-value cut-off.

The NovaSeq Control Software v1.7.5 and Real-Time Analysis (RTA) v3.4.4 performed real-time image analysis. RTA performs real-time base calling on the NovaSeq instrument computer. The Illumina DRAGEN BCL Convert 07.021.624.3.10.8 pipeline generated the sequence data. The FASTQ files were analysed using salmon 1.10.3 by using the reference genome GRCh38 [21]. Salmon counts were imported to the R studio using the *tximeta* package [22]. Differential whole transcriptome analysis was performed with the *DESeq2* package [23]. No fold-change filtering was initially applied, but the False Discovery Rate (FDR) was set at 0.05 to adjust for multiple testing, and this corresponds to the 1.05 fold change threshold in our experiment.

The functional annotation of the differential gene expression was performed with the packages *ReactomePA*, *clusterProfiler* and *DOSE* [24–26]. Principal component analysis was performed by using *pcaExplorer* and *factoextra* packages. The heatmap clustering was performed with the *ComplexHeatmap* package based on the z-scores of the normalised expression data and using Euclidean distance for complete linkage agglomerative clustering.

## Pair-wise analysis

To perform a pair-wise analysis of individual genes between MND and healthy controls, we applied the two-tailed Wilcoxon rank-sum test implemented in the function compare_means() of the package *ggpubr* [27]. We generated a list of all known MND genes using the OMIM catalogue and identified 97 genes that are directly connected to the MND or its subtypes. This list extracted normalised counts from the salmon quant files and made boxplots with pairwise comparisons. Plots were generated using *ggplot2* version 3.5.1 and *ggpubr* version 0.6.0 packages. Statistical analysis was performed with R software version 4.4.0 and RStudio Version 2023.06.0 + 421.

# Results

## Description of the study cohort

The general characteristics of the population are reported in Table 1. The median age was 65.6 (standard deviation 9.3) years, and most subjects were female (69%). No patient reported a positive family history of MND; therefore, all the participants had sporadic forms, and all patients received standard MND therapy with riluzole. The most frequent clinical subtype was the classic ALS (86%). Spinal symptoms were present the most commonly (60%).

### Whole blood RNA sequencing

RNA sequencing resulted in at least 50 million paired 150 bp reads per sample, and all reads had Phred score higher than 30.

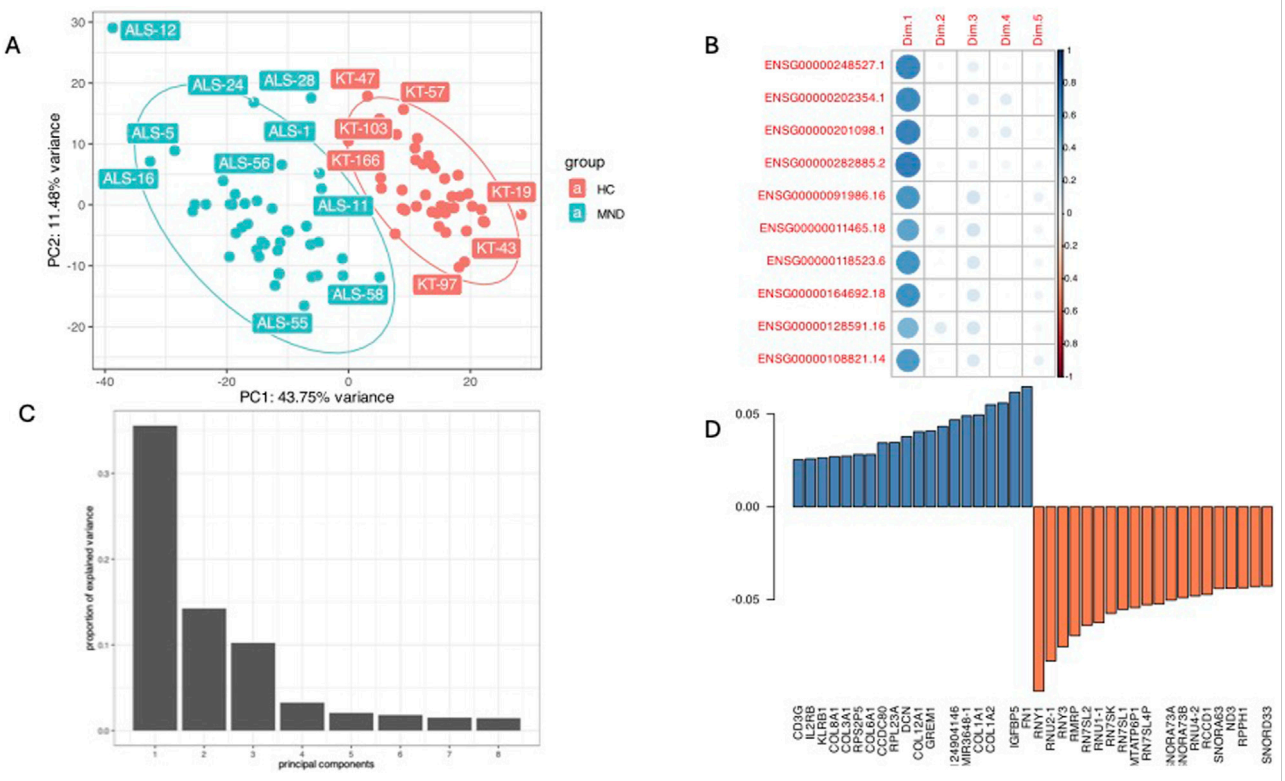


FIGURE 3
A combined plot of principal component analysis. Panel **(A)** is the PC1 and PC2 plot showing good separation of study cohort by PC1 and the highest impact of disease status (43.75% of variance). Panel **(B)** is a correlation plot of the expression of the top significant genes with PC1 (Dim.1), these genes all are correlated with the MND/control status. Panel **(C)** is a scree-plot showing that in our study three components (PC1, PC2, and PC3) were responsible for almost all the variance. Panel **(D)** shows the loading of different genes in the PC1.

Salmon was used to quantify transcript abundances from fastq files. *Tximeta* was used to import the resulting quant files, and gene-level summarisation was used for the *DESeq2* workflow. Healthy controls were compared to the MND RNA-seq results, and we identified 12,972 genes differentially expressed (FDR < 0.05) in the blood of MND patients. The top 30 differentially regulated genes are shown in Table 2. Out of these 12,972 genes, 8,008 were upregulated, and 4,964 were down-regulated (Supplementary Table S2, sheet 1). A heat map with all 12,972 genes is shown as Supplementary Figure S1, and it shows a clear separation of MND patients from the healthy controls. A smaller heatmap with the top 100 genes is shown in Figure 1, and a volcano plot is shown in Figure 2. The heatmap with 100 genes shows a consistent and clear separation of the MND from the healthy controls. This remarkable finding shows that a disease highly specific to the central nervous system can be differentiated from controls by the blood transcriptome profile.

When we used the FDR 0.05 filtering threshold, we detected the genes Log2 FC 0.07 threshold, which transforms to an expression difference of 1.05-fold change ($2^{0.07}$). We then applied an additional fold change threshold to filter the dataset further. When we applied FC threshold of 1.1 (log2 FC 0.13), we got 12,839 differentially expressed genes (DEGs, Supplementary Table S2, sheet 2). With the FC threshold of 1.5 (log2 FC 0.59), we got 6,403 DEGs (Supplementary Table S2, sheet 3), and finally, applying the threshold of FC 2.0 (log2 FC 1.0), we got 3,286 DEGs (Supplementary Table S2, sheet 4).

The principal component analysis identified that disease status, PC1 was responsible for 43.75% of the variance and gene expression profiles clearly separated MND patients from healthy controls (Figure 3A). The genes with the highest differential expression (the lowest FDR values) had a very high correlation with the PC1 (Figure 3B, "Dim.1" is PC1) and the scree plot (Figure 3C) verified that most of the variation in our study cohort is explained by three principal components, PC1, PC2 and PC3. PC1 is disease status, and we were not able to identify the essence of the PC2 and PC3. These are neither the sex (Supplementary Figure S2, Panels A) nor age (Supplementary Figure S2, Panels B and C) of the patients, nor the type of the disease (Supplementary Figure S2, Panels D and E). It could be that PC2 and PC3 are some other factors reflecting the heterogeneity of the pathophysiology of the MND.

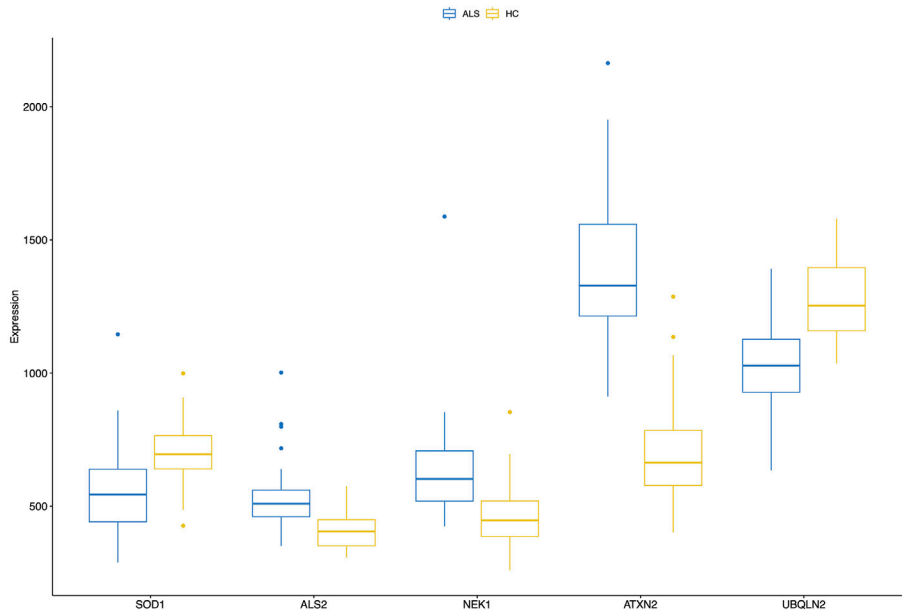


FIGURE 4
A combined boxplot of five MND-related genes and their expression levels in the blood of MND patients and controls gives comparative blood expression levels for these selected genes. Pairwise statistical comparisons are shown in Figure 5 and in Supplementary Figure S3.

## Pairwise analysis of known MND genes

In addition to the whole transcriptome analysis, we performed a pairwise (MND versus healthy controls) study of 97 known MND genes (a list of the genes is provided in Supplementary Table S3) and 30 top-regulated genes from the DESeq2 analysis. All results are shown in Supplementary Figure S3, and partial results are in Figures 4, 5. Interestingly, some MND-related genes are upregulated (*ALS2*, *NEK1*, *ATXN2*), while others are downregulated (*SOD1*, *UBQLN2* aka *ALS15*) in patients. In addition, *FUS* and *ANXA11* were upregulated, and *ANG* was downregulated in patients (Figures 5A–F). Moreover, the DESeq2 top genes *RNY3*, *RNY1*, and *ENSG0000282885* were highly upregulated in patients with almost no expression in control subjects (Figures 5G–I). At the same time, other DESeq2 top genes, *CCDC80*, *DCN*, and *CCN2*, were highly expressed in controls, and their expression was almost missing in patients' blood (Figures 5J–L). These examples indicate that there are many high fold-change difference genes with almost no expression in one group and very high expression in another, and these genes have very high potential to be a transcriptional biomarker for the MND.

The pairwise analysis of all 97 MND genes indicated that some well-known MND genes weren't differentially expressed in the blood (boxplots are in Supplementary Figure S3). Out of all 97 genes, 38 (39%) of them *AMFR, AR, ATX3, BICD2, C9orf72, CHRNA3, DAO, DCTN1, DNAJC7, ERBB4, HNRNPA2B1, IGFALS, KIF5A, LGALSL, LRP12, MAPT, MOBP, NEFH, OPTN, PAH, PON1, PON2, PON3, PRPH, PSEN1, SARM1, SCYL1, SETX, SLC1A2, SLC52A3, SMN1, SMN2, SQSTM1, TARDBP, TRPM7, TUBA4A, VRK1, VSX1*, were not differentially expressed between patients and controls. Fourteen genes of these 38 genes were not expressed in blood. Most of these genes that were not differentially expressed had excellent expression levels in the blood. *AMFR* has an expression level of 1,800 normalised counts, *C9orf72* has 1,500 normalised counts, *PSEN1* has an expression at 2,500 normalised counts, *TARDBP* has an average gene expression of 1,600 normalised counts, *SQSTM1* has an expression level of 3,100 normalised counts. Therefore, all these genes are highly expressed in the whole blood, but their expression level is not dependent on the disease status.

## Functional annotation of differentially expressed genes

Functional annotation of differentially expressed genes indicated statistically significant activation of several human disease pathways (Table 3, full version provided in Supplementary Table S4). Remarkably, three neurodegenerative diseases were at the top of the table of the KEGG pathways: Parkinson's disease, prion disease, and amyotrophic lateral sclerosis (Figure 6). In addition, several pathways involved in the pathogenesis of neurodegeneration were also activated. These included protein processing in the endoplasmic reticulum, proteasome, lysosome and ubiquitin-mediated proteolysis.

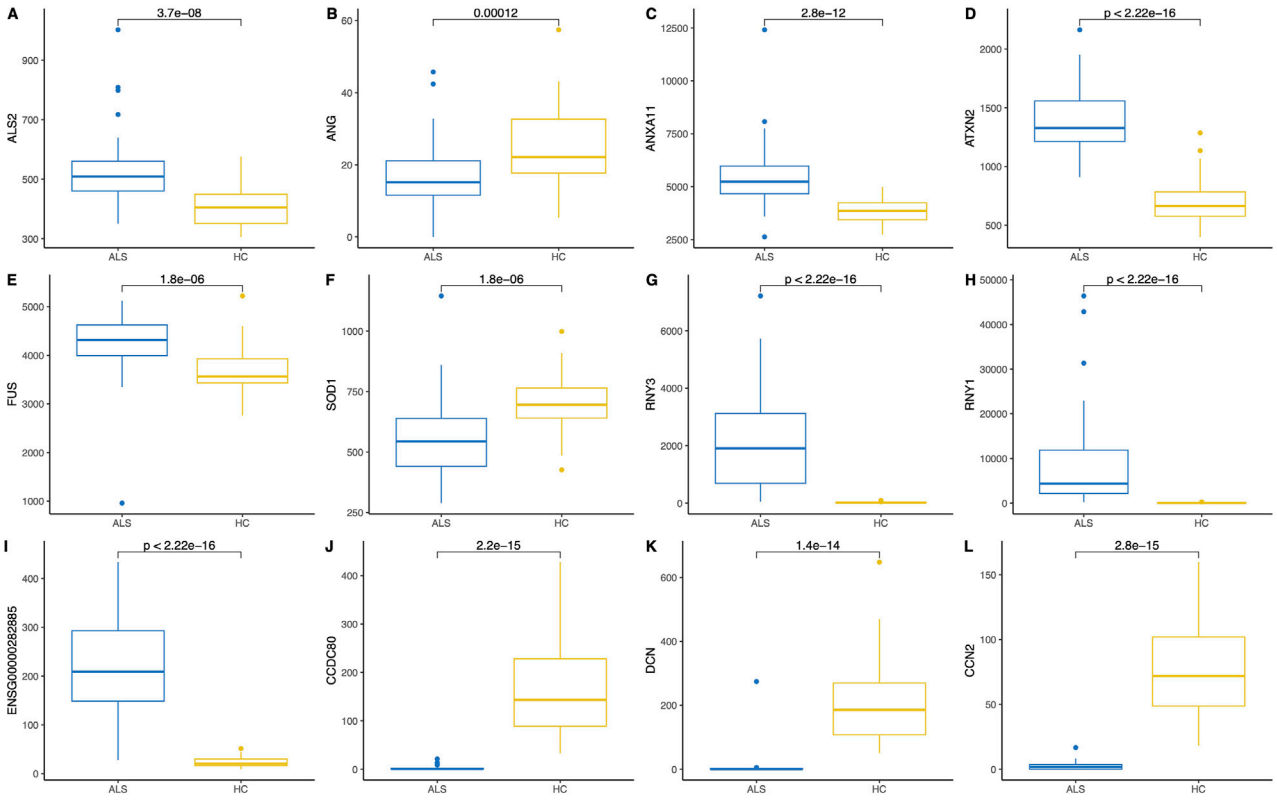


FIGURE 5
Pairwise comparison (Wilcoxon rank-sum test) and boxplots of six MND-related genes **(A–F)** and six of the most significant differentially expressed genes **(G–L)** in the blood of MND patients and controls. The Y-axis shows gene expression in normalised counts.

Reactome and GSEA analyses use more canonical pathways (Supplementary Tables S5, S6). Reactome identified statistically significant enrichment of the mRNA splicing and transcription-related pathways in combination with cellular energetics pathways (mitochondria and respiratory electron transport) to be affected (Figure 7). GSEA analysis (Figure 8) identified statistically significant enrichment of sensory perception, olfactory signalling and many pathways related to the extracellular matrix reorganisation (collagen degradation, elastic fibre formation, assembly of collagen fibres).

In summary, KEGG pathway analysis found statistically significant activation of the ALS pathway together with other neurodegeneration pathways. The findings from Reactome and GSEA added more details to the KEGG finding and identified several cellular pathways that can give a mechanistic understanding of the pathogenesis of MND.

## Discussion

The current study presented a whole transcriptome analysis of the whole blood RNA from MND patients compared to age and sex-matched healthy controls (Figure 9). As a main finding, we identified 12,972 genes differentially expressed; 8,008 were upregulated, and 4,964 were downregulated in the blood of MND patients. Most remarkably, the heatmap based on these 12,972 genes was highly specific and separated MND from healthy controls. Therefore, we can conclude that the identified differentially expressed genes are specific for the MND status. This doesn't mean that all of these genes are directly related to the pathogenesis of MND but instead reflects the complexity of the disease, where pathogenic changes are mixed with compensatory changes. However, this still shows that MND, while a CNS-specific disease, has remarkable changes in the blood transcriptomics, and blood could be a perfect source for the diagnostic biomarkers for MND.

The number of differentially expressed genes seems to be unreasonably high, but van Rheenen et al., used Illumina bead chips with only 29,830 unique and suitable probes, and they also identified 7,038 genes to be differentially expressed [17]. This number is very close to the one that we identified if we take into account that in our study, we used RNA-seq that analysed the expression of 60,230 genes, and our sample is perfect sex and age-matched, which means more power. In addition, in our own previous study, we identified

TABLE 3 KEGG pathways that are enriched in the blood transcriptome of MND patients.

| Category | Subcategory | ID | Description | Gene ratio | Bg ratio | *P*-adjusted |
|---|---|---|---|---|---|---|
| Human Diseases | Neurodegenerative disease | hsa05012 | Parkinson disease | 165/3,781 | 271/8,843 | 2.36E-07 |
| Human Diseases | Cardiovascular disease | hsa05415 | Diabetic cardiomyopathy | 130/3,781 | 205/8,843 | 2.36E-07 |
| Human Diseases | Neurodegenerative disease | hsa05020 | Prion disease | 167/3,781 | 278/8,843 | 3.14E-07 |
| Human Diseases | Neurodegenerative disease | hsa05014 | Amyotrophic lateral sclerosis | 212/3,781 | 371/8,843 | 5.97E-07 |
| Metabolism | Energy metabolism | hsa00190 | Oxidative phosphorylation | 92/3,781 | 138/8,843 | 5.97E-07 |
| Organismal Systems | Environmental adaptation | hsa04714 | Thermogenesis | 143/3,781 | 235/8,843 | 5.97E-07 |
| Genetic Information Processing | Folding, sorting and degradation | hsa04141 | Protein processing in endoplasmic reticulum | 109/3,781 | 170/8,843 | 5.97E-07 |
| Human Diseases | Neurodegenerative disease | hsa05022 | Pathways of neurodegeneration - multiple diseases | 265/3,781 | 483/8,843 | 1.07E-06 |
| Human Diseases | Cancer: overview | hsa05208 | Chemical carcinogenesis - reactive oxygen species | 136/3,781 | 226/8,843 | 2.72E-06 |
| Human Diseases | Neurodegenerative disease | hsa05010 | Alzheimer disease | 217/3,781 | 391/8,843 | 5.09E-06 |
| Human Diseases | Neurodegenerative disease | hsa05016 | Huntington disease | 177/3,781 | 311/8,843 | 7.00E-06 |
| Genetic Information Processing | Translation | hsa03013 | Nucleocytoplasmic transport | 72/3,781 | 108/8,843 | 1.14E-05 |
| Genetic Information Processing | Folding, sorting and degradation | hsa03050 | Proteasome | 36/3,781 | 46/8,843 | 2.46E-05 |
| Cellular Processes | Transport and catabolism | hsa04142 | Lysosome | 82/3,781 | 132/8,843 | 0.0001 |
| Genetic Information Processing | Folding, sorting and degradation | hsa04120 | Ubiquitin mediated proteolysis | 87/3,781 | 142/8,843 | 0.0001 |
| Genetic Information Processing | Translation | hsa03010 | Ribosome | 102/3,781 | 172/8,843 | 0.0002 |
| Genetic Information Processing | Chromosome | hsa03082 | ATP-dependent chromatin remodeling | 73/3,781 | 117/8,843 | 0.0003 |
| Cellular Processes | Cell growth and death | hsa04110 | Cell cycle | 94/3,781 | 158/8,843 | 0.0003 |
| Genetic Information Processing | Replication and repair | hsa03030 | DNA replication | 28/3,781 | 36/8,843 | 0.0004 |
| Human Diseases | Infectious disease: bacterial | hsa05132 | *Salmonella* infection | 138/3,781 | 251/8,843 | 0.0009 |
| Metabolism | Glycan biosynthesis and metabolism | hsa00510 | N-Glycan biosynthesis | 37/3,781 | 53/8,843 | 0.0010 |
| Human Disease | Neurodegenerative disease | hsa05017 | Spinocerebellar ataxia | 84/3,781 | 144/8,843 | 0.0016 |

Bg, background.

4,824 differentially expressed genes in the CSF of MND patients [5]. Therefore, the number of differentially expressed genes between MND patients and healthy controls seems to be high, but also other studies have found a similarly high number of differentially expressed genes.

In addition, the number of differentially expressed genes remains high even after applying different filtering criteria. While we initially did not use any specific fold-change filtering, the statistically significant FDR only detected genes with at least a 1.05 fold change difference. When we applied more stringent FC filtering thresholds, the number of differentially expressed genes reduced, but it was still remarkable, with 6,403 genes for FC 1.5 and 3,286 genes with the threshold of FC 2.0. This indicates a robustly specific gene expression profile in the blood of MND patients, making it a reliable source for potential RNA-based biomarkers.

The genes that we identified differentially expressed correlate quite well with the results of the previously published similar studies. We identified all the genes found

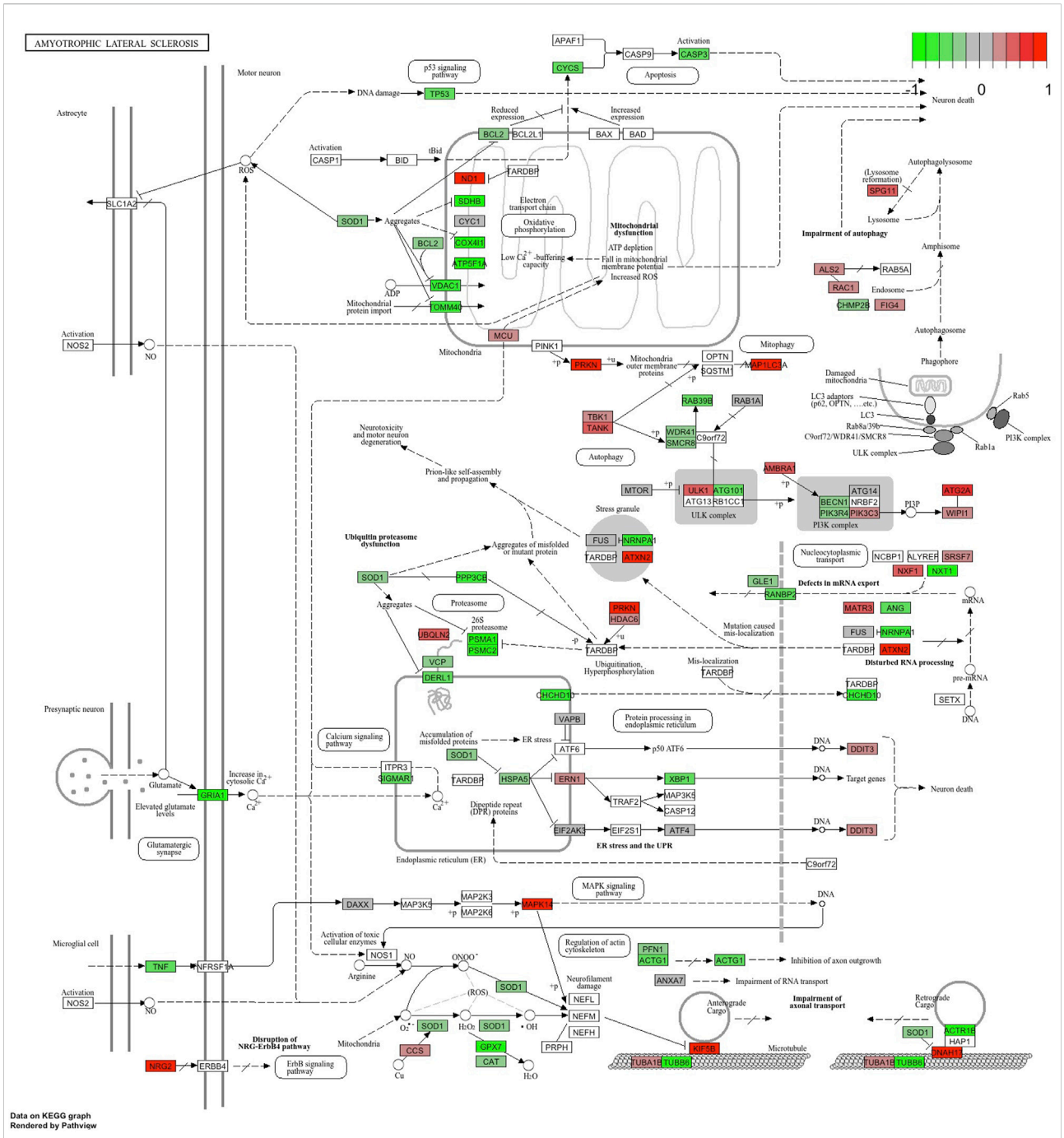


FIGURE 6
KEGG pathway "Amyotrophic Lateral Sclerosis" with the blood RNA gene expression data. Genes in green are downregulated, and genes in red are upregulated.

in the paper by Garau et al, Table 5 [28]. In addition, we also compared our genes to the study of van Rheenen et al and found that many genes overlapped between these studies [17]. Therefore, our results are generally in very good concordance with previously published studies.

Not all MND-specific genes were differentially expressed. *C9orf72* is a gene with the highest genetic impact in MND, but it was not differentially expressed. *C9orf72* is highly expressed in the blood with an average normalised count of 1,500. Therefore, the low expression level cannot explain the lack

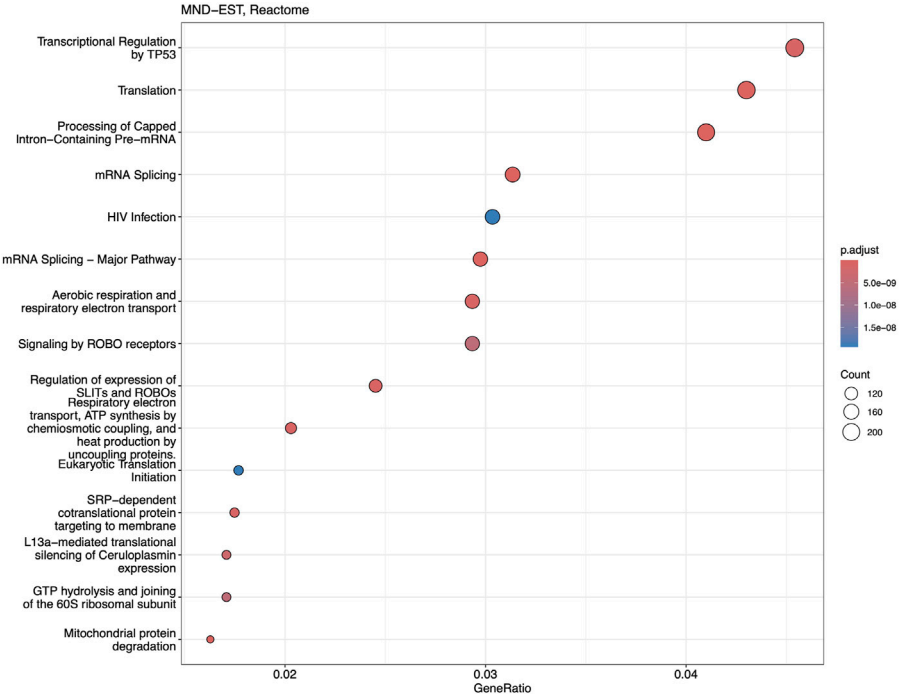


FIGURE 7
Dotplot of Reactome analysis based on the fold-change expression differences in the blood of MND patients. Top 15 the most significantly upregulated pathways are shown.

of significant differences. A similar observation is true for the *SQSTM1*, *TARDBP*, *OPTN* and *PSEN1*, all genes with high expression in the blood, but no difference in expression between MND and controls (Supplementary Figure S2). It is hard to understand why these genes did not show differential expression, but these genes have a mutation-specific effect, and in our cohort, we may not have mutations in these genes. This might be unlikely, as we have identified pathogenic repeat polymorphism for *C9orf72* in one patient who has 1,000 repeats with a length of over 6,000 bp.

We saw significant differences in many MND-related genes. For instance, *SOD1* was downregulated in MND patients. Similarly, *ANG* and *ACSL5* were significantly downregulated in MND patients compared to controls. It is somewhat surprising that *SOD1* is downregulated in MND patients as it is also assumed to form aggregates in sporadic patients [29–31]. At the same time, we couldn't find a significant difference for the *OPTN* gene, another gene that has clear implications in MND pathology and had a very high expression level in blood. It is remarkable that while its aggregates are common for familial and sporadic MND forms, we could not detect significant differences in the expression of *OPTN* [32].

Our study is certainly not the first to analyse MND patients' transcriptomes. One study analysed gene chips from whole blood RNA, finding 2,943 genes differentially expressed [17]. These authors did not find *SOD1, C9orf72, SQSTM1, TARDBP*, or *OPTN* to be differentially expressed; this study got similar results to ours. Other published studies have used selected cell fractions, like PBMCs or lymphoblastoid cells [16, 28, 33, 34]. The cell fractionation studies identified a much smaller number of differentially expressed genes, and their results are difficult to compare to our results as the approaches are quite different. However, one recent study used a machine learning approach to compare brain and blood transcriptomic data and identified three distinct clusters of the MND subtypes with potentially different pathological mechanisms [6]. These three pathogenic subtypes didn't describe any particular MND mutation but rather the biological pathways that involved particular differentially expressed genes. The present study is based on blood transcriptome, and we have identified similar differentially expressed genes. While we couldn't identify three distinctive subtypes, the heatmap of the 12,972 differentially expressed genes separated MND patients from controls. Moreover, for MND patients, we saw at least two clusters with specific gene expression profiles. Therefore, our study results seem to match the results of the study by Marriott et al [6]. The main finding is that gene expression profiles and RNA analysis could be

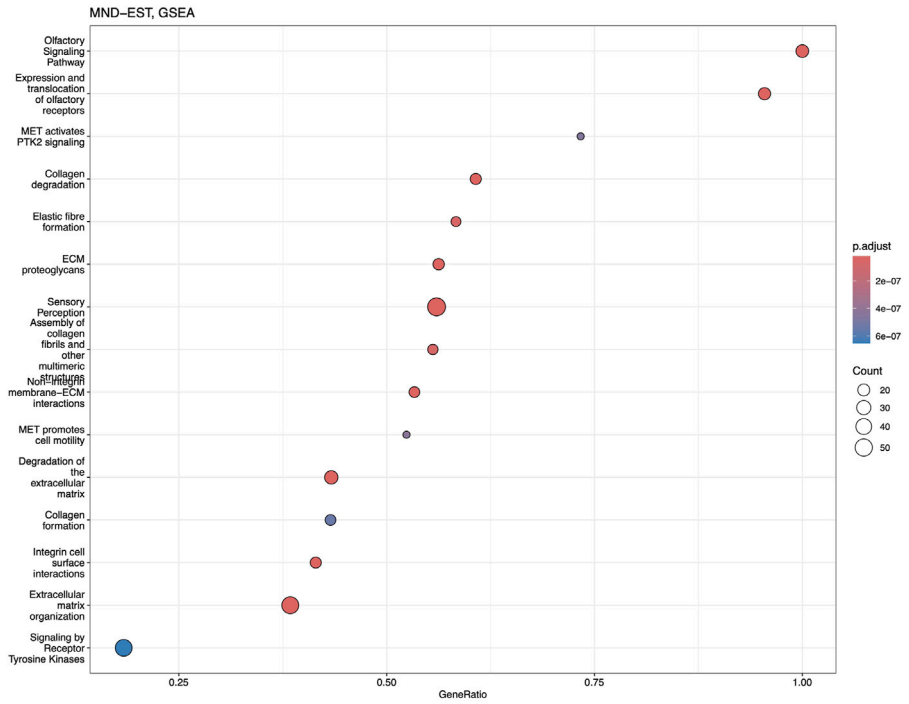


FIGURE 8
Dotplot of GSEA analysis based on the fold-change expression differences in the blood of MND patients. Top 15 the most significantly upregulated pathways are shown.

used as a source for biomarkers and can have clinical utility in differentiating patients with distinctive pathogenetic mechanisms.

We identified that the most up-regulated gene, with logFC 23, in MND blood is the *APOBEC3DE* gene (Volcano plot in Figure 2). *APOBEC3DE* is located at 22q13.1 and is a cytidine deaminase gene family member. This gene is one of the APOBEC cluster family on chromosome 22 [35, 36]. APOBEC proteins are part of innate immunity, and they inhibit retroviruses by deaminating cytosine residues in retroviral cDNA [37]. Interestingly, *APOBEC3DE* also inhibits retrotransposition of the long interspersed element-1 (LINE-1) by interacting with ORF1p, a protein encoded by LINE-1 [38]. LINE-1 has been implicated in the pathogenesis of MND, and therefore, *APOBEC3DE* finding seems very relevant as they suppress LINE1 activity [39]. In addition, *APOBEC* proteins can induce somatic mutations into genomic DNA and promote the development of different diseases [40]. *APOBEC* proteins are also involved in the clearance of foreign DNA from human cells, implicating their role in the cellular defence system against mutations that make them very plausible in connection with the MND [41, 42]. Loss of the nuclear *TDP-43* due to the cytoplasmic aggregation of the *TDP-43* is associated with decondensation of the chromatin around LINE1 elements and increased activation or LINE1 with their retrotransposition. Upregulation of the *APOBEC3DE* might be an endogenous defence mechanism as it is a part of the innate response to retroviral activation [43].

Many differentially expressed genes are involved in splicing and RNA processing: *RNU5A-1*, *RNU1-1*, *RNY3*, and *RNY1*, to name some. Interestingly, these RNA synthesis and splicing-related genes are all upregulated in MND samples and not expressed in the blood of control samples at all. These are genes that have a high potential to become a blood biomarker for MND or help to predict the progression of the disease. While it is not clear how these genes participate in the pathogenesis of MND, splicing mutations and genes participating in splicing involvement in MND have been shown in many previous studies [44–46]. The results from blood transcriptomics were very uniform and showed the upregulation of several genes related to RNA synthesis and splicing, as also indicated in Figure 6.

The function of downregulated genes is more diverse, with possible common denominators being the extracellular matrix (ECM) organisation and remodelling (Figure 7). Reduced expression of *CCDC80*, *COL1A1*, *COL1A2*, *MMP2*, and *TNFRSF11B* indicates the ECM reorganisation also found in GSEA enrichment analysis (Figure 2). The expression of these genes was very low in MND samples and very high in the blood of controls, showing a highly significant logFC for these genes. Similarly, *IGFBP5* almost lacked expression in the MND group and had very high expression in the blood of

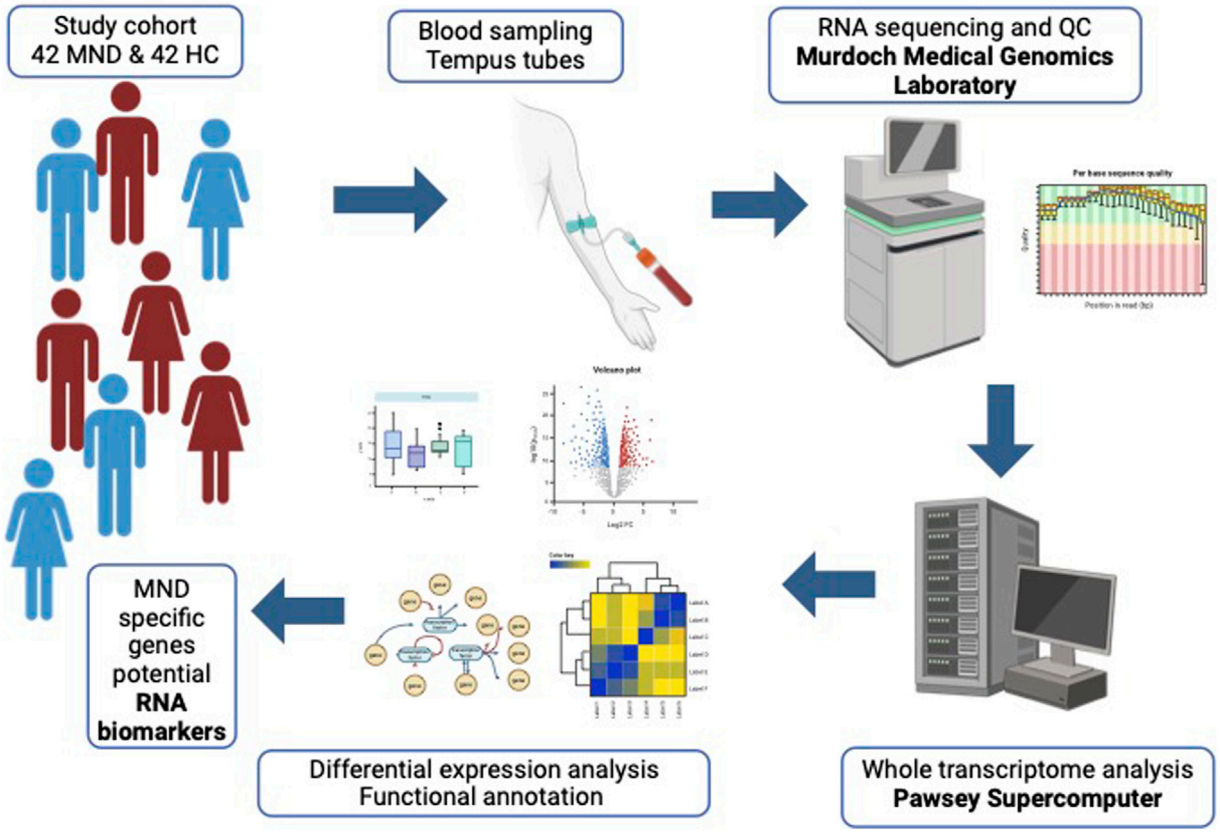


FIGURE 9
Graphical abstract of the study.

control subjects. Overexpression of the *IGFBP5* in mice has induced axonopathy and sensory deficits similar to those seen in diabetic neuropathy [47]. The motor axon degeneration in these mice resembled the pathology seen in MND [47]. *IGFBP5* has been shown to promote neuronal apoptosis in the experimental models and also in patients with spinal muscular atrophy and ALS [48–50].

When discussing these results, we have to consider the effect of MND itself on gene expression and not only the effect of genes on the disease. Most likely, the genes that are significantly downregulated and have very low expression levels in MND patients are the genes that are affected by the MND condition. The cluster of ECM organisation genes indicates the degeneration of the neurones and are the genes directly impacted by the MND. Stanniocalcin 2 (*STC2*) and thrombospondin 2 (*THBS2*) are genes that are related to organogenesis and tissue differentiation [51–53]. Interestingly, the proposed function of these genes is related to collagen genes and MMPs. Therefore, it seems that MND affects tissue reorganisation, and the genes that are required for tissue plasticity are downregulated. We can speculate that genes are not causative for the disease but are affected by the chronic disease condition and lead to enhanced degeneration of neurones.

## Conclusion

We performed whole transcriptome analysis from the whole blood RNA and identified 12,972 genes differentially expressed between MND patients and controls. These gene expression changes have the potential to be used as biomarkers to diagnose MND and possibly to evaluate the progression of the disease and drug responsiveness in clinical trials. RNA-based biomarkers have excellent potential as they are quickly responding biomarkers and can be analysed by standardised methods. In conclusion, we were able to identify the characteristic blood gene expression profile of MND patients.

## Author contributions

Conceptualization, SK and PT; methodology, SK, KR, MM, and JP; software, SK; validation, SK and AP; formal analysis, SK; investigation, KR, MM, and JP; resources, SK and PT; data curation, SK; writing—original draft preparation, SK; writing—review and editing, SK, KR, MM, JP, AP, and PT;

visualization, SK; supervision, SK; project administration, SK; funding acquisition, SK and PT. All authors contributed to the article and approved the submitted version.

## Data availability

The datasets presented in this study can be found in online repositories. The names of the repository/repositories and accession number(s) can be found below: https://www.ncbi.nlm.nih.gov/geo/, GSE277709.

## Ethics statement

The studies involving humans were approved by Institutional Review Board of the University of Tartu. The studies were conducted in accordance with the local legislation and institutional requirements. The participants provided their written informed consent to participate in this study.

## Funding

The author(s) declare that financial support was received for the research, authorship, and/or publication of this article. This research was funded by MSWA, Perron Institute, Grant PRG2736 of the Estonian Research Council, and the SA EUS 100a Fund.

## Acknowledgments

The technical support from the Genomics Core Facility of Mudoch University is appreciated.

## Conflict of interest

The author(s) declared no potential conflicts of interest with respect to the research, authorship, and/or publication of this article.

## Generative AI statement

The author(s) declare that no Generative AI was used in the creation of this manuscript.

## Supplementary material

The Supplementary Material for this article can be found online at: https://www.ebm-journal.org/articles/10.3389/ebm.2024.10401/full#supplementary-material

**SUPPLEMENTARY FIGURE S1**
HeatmapMNDEST12972genesBloodRNAseq.

**SUPPLEMENTARY FIGURE S2**
AllBoxplots.

**SUPPLEMENTARY TABLE S1**
DescriptionofTheCohort.

**SUPPLEMENTARY TABLE S2**
Differentially expressed genes.

**SUPPLEMENTARY TABLE S3**
CompleteListofMNDGENES.

**SUPPLEMENTARY TABLE S4**
FC_MNDEST_KEGG.

**SUPPLEMENTARY TABLE S5**
FC_MNDEST_Reactome.

**SUPPLEMENTARY TABLE S6**
FC_MNDEST_GSEA.

## References

1. Siddique T, Deng HX, Ajroud-Driss S. Chapter 132 - motor neuron disease. In: Rimoin D, Pyeritz R, Korf B, editors. *Emery and rimoin's principles and practice of medical genetics*. 6th ed. Oxford: Academic Press (2013). p. 1–22.

2. Brown RH, Al-Chalabi A. Amyotrophic lateral sclerosis. *N Engl J Med* (2017) **377**:162–72. doi:10.1056/nejmra1603471

3. Statland JM, Barohn RJ, McVey AL, Katz JS, Dimachkie MM. Patterns of weakness, classification of motor neuron disease, and clinical diagnosis of sporadic amyotrophic lateral sclerosis. *Neurol Clin* (2015) **33**:735–48. doi:10.1016/j.ncl.2015.07.006

4. Shatunov A, Al-Chalabi A. The genetic architecture of ALS. *Neurobiol Dis* (2021) **147**:105156. doi:10.1016/j.nbd.2020.105156

5. Frohlich A, Pfaff AL, Bubb VJ, Quinn JP, Koks S. Transcriptomic profiling of cerebrospinal fluid identifies ALS pathway enrichment and RNA biomarkers in MND individuals. *Exp Biol Med (Maywood)* (2023) **248**:2325–31. doi:10.1177/15353702231209427

6. Marriott H, Kabiljo R, Hunt GP, Khleifat AA, Jones A, Troakes C, et al. Unsupervised machine learning identifies distinct ALS molecular subtypes in post-mortem motor cortex and blood expression data. *Acta Neuropathol Commun* (2023) **11**:208. doi:10.1186/s40478-023-01686-8

7. Byrne S, Bede P, Elamin M, Kenna K, Lynch C, McLaughlin R, et al. Proposed criteria for familial amyotrophic lateral sclerosis. *Amyotroph Lateral Scler* (2011) **12**:157–9. doi:10.3109/17482968.2010.545420

8. Veldink JH. ALS genetic epidemiology "How simplex is the genetic epidemiology of ALS?" *J Neurol Neurosurg Psychiatry* (2017) **88**:537. doi:10.1136/jnnp-2016-315469

9. Pfaff AL, Bubb VJ, Quinn JP, Koks S. A genome-wide screen for the exonisation of reference SINE-VNTR-alus and their expression in CNS tissues of individuals with amyotrophic lateral sclerosis. *Int J Mol Sci* (2023) **24**:11548. doi:10.3390/ijms241411548

10. Koks G, Pfaff AL, Bubb VJ, Quinn JP, Koks S. At the dawn of the transcriptomic medicine. *Exp Biol Med (Maywood)* (2021) **246**:286–92. doi:10.1177/1535370220954788

11. Pfaff AL, Singleton LM, Kõks S. Mechanisms of disease-associated SINE-VNTR-Alus. *Exp Biol Med (Maywood)* (2022) **247**:756–64. doi:10.1177/15353702221082612

12. Lill M, Koks S, Soomets U, Schalkwyk LC, Fernandes C, Lutsar I, et al. Peripheral blood RNA gene expression profiling in patients with bacterial meningitis. *Front Neurosci* (2013) **7**:33. doi:10.3389/fnins.2013.00033

13. Koks G, Uudelepp ML, Limbach M, Peterson P, Reimann E, Koks S. Smoking-induced expression of the GPR15 gene indicates its potential role in chronic inflammatory pathologies. *The Am J Pathol* (2015) **185**:2898–906. doi:10.1016/j.ajpath.2015.07.006

14. Billingsley KJ, Lättekivi F, Planken A, Reimann E, Kurvits L, Kadastik-Eerme L, et al. Analysis of repetitive element expression in the blood and skin of patients with Parkinson's disease identifies differential expression of satellite elements. *Sci Rep* (2019) **9**:4369. doi:10.1038/s41598-019-40869-z

15. Planken A, Kurvits L, Reimann E, Kadastik-Eerme L, Kingo K, Koks S, et al. Looking beyond the brain to improve the pathogenic understanding of Parkinson's disease: implications of whole transcriptome profiling of Patients' skin. *BMC Neurol* (2017) **17**:6. doi:10.1186/s12883-016-0784-z

16. Zucca S, Gagliardi S, Pandini C, Diamanti L, Bordoni M, Sproviero D, et al. RNA-Seq profiling in peripheral blood mononuclear cells of amyotrophic lateral sclerosis patients and controls. *Sci Data* (2019) **6**:190006. doi:10.1038/sdata.2019.6

17. van Rheenen W, Diekstra FP, Harschnitz O, Westeneng HJ, van Eijk KR, Saris CGJ, et al. Whole blood transcriptome analysis in amyotrophic lateral sclerosis: a biomarker study. *PLoS One* (2018) **13**:e0198874. doi:10.1371/journal.pone.0198874

18. He D, Yang CX, Sahin B, Singh A, Shannon CP, Oliveria JP, et al. Whole blood vs PBMC: compartmental differences in gene expression profiling exemplified in asthma. *Allergy Asthma Clin Immunol* (2019) **15**:67. doi:10.1186/s13223-019-0382-x

19. Moris P, Bellanger A, Ofori-Anyinam O, Jongert E, Yarzabal Rodriguez JP, Janssens M. Whole blood can be used as an alternative to isolated peripheral blood mononuclear cells to measure *in vitro* specific T-cell responses in human samples. *J Immunological Methods* (2021) **492**:112940. doi:10.1016/j.jim.2020.112940

20. Gautam A, Donohue D, Hoke A, Miller SA, Srinivasan S, Sowe B, et al. Investigating gene expression profiles of whole blood and peripheral blood mononuclear cells using multiple collection and processing methods. *PLoS One* (2019) **14**:e0225137. doi:10.1371/journal.pone.0225137

21. Patro R, Duggal G, Love MI, Irizarry RA, Kingsford C. Salmon provides fast and bias-aware quantification of transcript expression. *Nat Methods* (2017) **14**:417–9. doi:10.1038/nmeth.4197

22. Love MI, Soneson C, Hickey PF, Johnson LK, Pierce NT, Shepherd L, et al. Tximeta: reference sequence checksums for provenance identification in RNA-seq. *Plos Comput Biol* (2020) **16**:e1007664. doi:10.1371/journal.pcbi.1007664

23. Love MI, Huber W, Anders S. Moderated estimation of fold change and dispersion for RNA-seq data with DESeq2. *Genome Biol* (2014) **15**:550. doi:10.1186/s13059-014-0550-8

24. Yu G, He QY. ReactomePA: an R/Bioconductor package for reactome pathway analysis and visualization. *Mol Biosyst* (2016) **12**:477–9. doi:10.1039/c5mb00663e

25. Yu G, Wang LG, Yan GR, He QY. DOSE: an R/Bioconductor package for disease ontology semantic and enrichment analysis. *Bioinformatics* (2015) **31**:608–9. doi:10.1093/bioinformatics/btu684

26. Yu G, Wang LG, Han Y, He QY. clusterProfiler: an R package for comparing biological themes among gene clusters. *OMICS: A J Integr Biol* (2012) **16**:284–7. doi:10.1089/omi.2011.0118

27. Kassambra A. Ggpubr: "ggplot2" based publication ready plots (2023).

28. Garau J, Garofalo M, Dragoni F, Scarian E, Di Gerlando R, Diamanti L, et al. RNA expression profiling in lymphoblastoid cell lines from mutated and non-mutated amyotrophic lateral sclerosis patients. *The J Gene Med* (2024) **26**:e3711. doi:10.1002/jgm.3711

29. Mielke JK, Klingeborn M, Schultz EP, Markham EL, Reese ED, Alam P, et al. Seeding activity of human superoxide dismutase 1 aggregates in familial and sporadic amyotrophic lateral sclerosis postmortem neural tissues by real-time quaking-induced conversion. *Acta Neuropathol* (2024) **147**:100. doi:10.1007/s00401-024-02752-8

30. Pokrishevsky E, DuVal MG, McAlary L, Louadi S, Pozzi S, Roman A, et al. Tryptophan residues in TDP-43 and SOD1 modulate the cross-seeding and toxicity of SOD1. *J Biol Chem* (2024) **300**:107207. doi:10.1016/j.jbc.2024.107207

31. Monteiro Neto JR, Ribeiro GD, Magalhães RSS, Follmer C, Outeiro TF, Eleutherio ECA. Glycation modulates superoxide dismutase 1 aggregation and toxicity in models of sporadic amyotrophic lateral sclerosis. *Biochim Biophys Acta (BBA) - Mol Basis Dis* (2023) **1869**:166835. doi:10.1016/j.bbadis.2023.166835

32. Zhao S, Chen R, Gao Y, Lu Y, Bai X, Zhang J. Fundamental roles of the optineurin gene in the molecular pathology of amyotrophic lateral sclerosis. *Front Neurosci* (2023) **17**:1319706. doi:10.3389/fnins.2023.1319706

33. Garofalo M, Pandini C, Bordoni M, Jacchetti E, Diamanti L, Carelli S, et al. RNA molecular signature profiling in PBMCs of sporadic ALS patients: HSP70 overexpression is associated with nuclear SOD1. *Cells* (2022) **11**:293. doi:10.3390/cells11020293

34. Garofalo M, Pandini C, Bordoni M, Pansarasa O, Rey F, Costa A, et al. Alzheimer's, Parkinson's disease and amyotrophic lateral sclerosis gene expression patterns divergence reveals different grade of RNA metabolism involvement. *Int J Mol Sci* (2020) **21**:9500. doi:10.3390/ijms21249500

35. Zhou T, Han Y, Dang Y, Wang X, Zheng YH. A novel HIV-1 restriction factor that is biologically distinct from APOBEC3 cytidine deaminases in a human T cell line CEM.NKR. *Retrovirology* (2009) **6**:31. doi:10.1186/1742-4690-6-31

36. Dang Y, Wang X, Esselman WJ, Zheng YH. Identification of APOBEC3DE as another antiretroviral factor from the human APOBEC family. *J Virol* (2006) **80**:10522–33. doi:10.1128/jvi.01123-06

37. Harris RS, Liddament MT. Retroviral restriction by APOBEC proteins. *Nat Rev Immunol* (2004) **4**:868–77. doi:10.1038/nri1489

38. Liang W, Xu J, Yuan W, Song X, Zhang J, Wei W, et al. APOBEC3DE inhibits LINE-1 retrotransposition by interacting with ORF1p and influencing LINE reverse transcriptase activity. *PLoS One* (2016) **11**:e0157220. doi:10.1371/journal.pone.0157220

39. Pfaff AL, Bubb VJ, Quinn JP, Koks S. Locus specific reduction of L1 expression in the cortices of individuals with amyotrophic lateral sclerosis. *Mol Brain* (2022) **15**:25. doi:10.1186/s13041-022-00914-x

40. Takei H, Fukuda H, Pan G, Yamazaki H, Matsumoto T, Kazuma Y, et al. Alternative splicing of APOBEC3D generates functional diversity and its role as a DNA mutator. *Int J Hematol* (2020) **112**:395–408. doi:10.1007/s12185-020-02904-y

41. Stenglein MD, Burns MB, Li M, Lengyel J, Harris RS. APOBEC3 proteins mediate the clearance of foreign DNA from human cells. *Nat Struct Mol Biol* (2010) **17**:222–9. doi:10.1038/nsmb.1744

42. Stenglein MD, Harris RS. APOBEC3B and APOBEC3F inhibit L1 retrotransposition by a DNA deamination-independent mechanism. *J Biol Chem* (2006) **281**:16837–41. doi:10.1074/jbc.m602367200

43. Liu EY, Russ J, Cali CP, Phan JM, Amlie-Wolf A, Lee EB. Loss of nuclear TDP-43 is associated with decondensation of LINE retrotransposons. *Cel Rep* (2019) **27**:1409–21.e6. doi:10.1016/j.celrep.2019.04.003

44. Irwin KE, Jasin P, Braunstein KE, Sinha IR, Garret MA, Bowden KD, et al. A fluid biomarker reveals loss of TDP-43 splicing repression in presymptomatic ALS-FTD. *Nat Med* (2024) **30**:382–93. doi:10.1038/s41591-023-02788-5

45. La Cognata V, Gentile G, Aronica E, Cavallaro S. Splicing players are differently expressed in sporadic amyotrophic lateral sclerosis molecular clusters and brain regions. *Cells* (2020) **9**:159. doi:10.3390/cells9010159

46. Kletzl H, Marquet A, Günther A, Tang W, Heuberger J, Groeneveld GJ, et al. The oral splicing modifier RG7800 increases full length survival of motor neuron 2 mRNA and survival of motor neuron protein: results from trials in healthy adults and patients with spinal muscular atrophy. *Neuromuscul Disord* (2019) **29**:21–9. doi:10.1016/j.nmd.2018.10.001

47. Rauskolb S, Dombert B, Sendtner M. Insulin-like growth factor 1 in diabetic neuropathy and amyotrophic lateral sclerosis. *Neurobiol Dis* (2017) **97**:103–13. doi:10.1016/j.nbd.2016.04.007

48. Wilczak N, de Vos RA, De Keyser J. Free insulin-like growth factor (IGF)-I and IGF binding proteins 2, 5, and 6 in spinal motor neurons in amyotrophic lateral sclerosis. *Lancet* (2003) **361**:1007–11. doi:10.1016/s0140-6736(03)12828-0

49. Kaymaz AY, Bal SK, Bora G, Talim B, Ozon A, Alikasifoglu A, et al. Alterations in insulin-like growth factor system in spinal muscular atrophy. *Muscle Nerve* (2022) **66**:631–8. doi:10.1002/mus.27715

50. Guo S, Lei Q, Yang Q, Chen R. IGFBP5 promotes neuronal apoptosis in a 6-OHDA-toxicant model of Parkinson's disease by inhibiting the sonic hedgehog signaling pathway. *Med Princ Pract* (2024) **33**:269–80. doi:10.1159/000538467

51. Qu HL, Hasen GW, Hou YY, Zhang CX. THBS2 promotes cell migration and invasion in colorectal cancer via modulating Wnt/β-catenin signaling pathway. *The Kaohsiung J Med Sci* (2022) **38**:469–78. doi:10.1002/kjm2.12528

52. Lai R, Ji L, Zhang X, Xu Y, Zhong Y, Chen L, et al. Stanniocalcin2 inhibits the epithelial-mesenchymal transition and invasion of trophoblasts via activation of autophagy under high-glucose conditions. *Mol Cell Endocrinol* (2022) **547**:111598. doi:10.1016/j.mce.2022.111598

53. Zhou J, Li Y, Yang L, Wu Y, Zhou Y, Cui Y, et al. Stanniocalcin 2 improved osteoblast differentiation via phosphorylation of ERK. *Mol Med Rep* (2016) **14**:5653–9. doi:10.3892/mmr.2016.5951

EBM Experimental Biology and Medicine

TYPE Review
PUBLISHED 11 February 2025
DOI 10.3389/ebm.2025.10235



OPEN ACCESS

*CORRESPONDENCE
Wenjun Liu,
wenjun_liu@swmu.edu.cn

RECEIVED 11 May 2024
ACCEPTED 23 January 2025
PUBLISHED 11 February 2025

CITATION
Zhang M, Yang Y, Liu J, Guo L, Guo Q and Liu W (2025) Bone marrow immune cells and drug resistance in acute myeloid leukemia.
*Exp. Biol. Med.* 250:10235.
doi: 10.3389/ebm.2025.10235



# Bone marrow immune cells and drug resistance in acute myeloid leukemia

Miao Zhang[1,2], You Yang[1,2], Jing Liu[1,2], Ling Guo[1,2], Qulian Guo[1,2] and Wenjun Liu[1,2]*

[1]Department of Pediatrics (Hematological Oncology), Children Hematological Oncology and Birth Defects Laboratory, The Affiliated Hospital of Southwest Medical University, Luzhou, Sichuan, China, [2]Sichuan Clinical Research Center for Birth Defects, The Affiliated Hospital of Southwest Medical University, Luzhou, Sichuan, China

## Abstract

In recent years, the relationship between the immunosuppressive niche of the bone marrow and therapy resistance in acute myeloid leukemia (AML) has become a research focus. The abnormal number and function of immunosuppressive cells, including regulatory T cells (Tregs) and myeloid-derived suppressor cells (MDSCs), along with the dysfunction and exhaustion of immunological effector cells, including cytotoxic T lymphocytes (CTLs), dendritic cells (DCs) and natural killer cells (NKs), can induce immune escape of leukemia cells and are closely linked to therapy resistance in leukemia. This article reviews the research progress on the relationship between immune cells in the marrow microenvironment and chemoresistance in AML, aiming to provide new ideas for the immunotherapy of AML.

KEYWORDS

**leukemia, immune cells, drug resistance, bone marrow, immunosuppressive microenvironment**

## Impact statement

Over the past few years, tolerance to chemical therapy in leukemia has become a significant challenge in treatment. The development of the leukemia immune niche significantly contributes to resistance in leukemia. Our article discusses the key roles of several immune cells in the immune microenvironment of AML in the development of resistance. Abnormalities in the number and function of immune cells in the AML immune microenvironment are vital in leukemia resistance. Therefore, immunotherapy is an important strategy to combat acute myeloid leukemia resistance and improve patient prognosis.

## Introduction

AML represents the most prevalent form of leukemia in adults and ranks as the second most frequently diagnosed leukemia in children. Currently, under conventional intensive chemotherapy, the complete remission (CR) rate ranges from 60% to 85% in adults younger than 60 years, while it decreases to 40%–60% in elderly patients aged 60 years or older [1]. Nevertheless, the overall survival (OS) rate over 5 years is only approximately 27% among patients with AML [2]. Although the CR rate of children with AML is high at approximately 90% compared with that of adults, the 3-year event-free survival (EFS) rate remains suboptimal at 45%, with the OS rate also being only at 65%, and nearly half of the children are resistant to relapse [3]. Therefore, relapse with drug resistance continues to be a significant factor contributing to poor prognosis among AML patients. The development for drug resistance in AML patients may be associated with leukemia cells evading immune responses and the progression of the minimal residual disease (MRD) in the bone marrow (BM) [4]. With the continuous proliferation of tumor cells, changes in immunogenicity, the recruitment of inhibitory immune cells, and the dysfunction and depletion of effector immune cells induce the immune evasion of leukemia cells. Among them, the strengthening of inhibitory immune cells and the weakening of effector immune cells could serve as a key contributor to the development of tumor cell resistance. Our review summarizes the role of immune cells in the bone marrow microenvironment of drug-resistant AML, helping to identify new therapeutic targets, optimize chemotherapy regimens, and improve the prognosis for AML patients.

## Tregs and drug resistance in AML

Tregs, a specialized subset of T cells with immunosuppressive properties, are essential for preserving immune tolerance and facilitating the immune evasion of tumor cells. Tregs can be divided into two categories based on their origin and function: natural Tregs (nTregs) and induced Tregs (iTregs). nTregs, characterized by the markers $CD4^+CD25+Foxp3+$, originate and mature in the thymus and possess intrinsic immunosuppressive functions, primarily maintaining self-tolerance and immune homeostasis by regulating effector immune responses. Unlike nTregs, iTregs are induced from $CD4^+$ T cells through external signals in peripheral blood (PB). Based on cellular phenotype and function, iTregs are divided into Foxp3+ Treg, T helper 3 cell (Th3), and Type 1 regulatory T cell (Tr1). According to their immunophenotypes, Tregs can be categorized into three types, including $CD4^+$ Tregs, $CD8^+$ Tregs and double-negative Tregs (DN Tregs, $CD4^-CD8^-$ Tregs). There were slight differences in the functions of Tregs with different phenotypes and their specific roles in AML, as shown in Table 1. Additionally, DN Tregs possess unique immunoregulatory capabilities that can induce the functional inactivation of effector T lymphocytes (Teffs) while also suppressing the immune response of NKs via the secretion of perforin [11]. McIver et al. suggested that DN Tregs are essential for immune tolerance after allogeneic hematopoietic stem cell transplantation (allo-HSCT) by regulating the diversity of the TCR repertoire and suppressing the excessive proliferation of immune-reactive T cells, which is especially critical for preventing graft-versus-host disease (GVHD) [12]. Ford et al. revealed that LPS-activated allogeneic antigen-presenting Cells (APCs) can promote the expansion of DN Tregs, which in turn enhances their immune-regulatory function by killing B cells through a perforin-dependent pathway [13]. Studies have shown that re-infusion of human DN Treg cells, after *ex vivo* expansion, can effectively inhibits the growth of autologous T and B lymphocytes and alleviate GVHD [14]. Additionally, pretreatment with rapamycin (an mTOR inhibitor) further enhances their immunoregulatory function, highlighting the potential clinical application of DN Treg cells in therapeutic settings [14]. However, the role of DN Tregs in AML is still in the early stages, requiring further investigation.

## Cytokines secreted by Tregs are involved in drug resistance in AML

A high frequency of $CD4^+CD25+Foxp3+$ Tregs is closely associated with immune tolerance and chemoresistance relapse in AML. The transcription factor Foxp3, when highly expressed in the nucleus, plays a vital role in triggering suppressive activity of Tregs and stabilizes of their phenotype and functional properties. [15], and its mechanism may be related to DNA methyltransferases at the Foxp3 locus [16]. Foxp3+ Tregs maintain immune tolerance by suppressing immune responses through the secretion of inhibitory cytokines, including IL-10, TGF-β, and IL-35, as well as the expression of immune regulatory molecules [17, 18]. These molecules interact with receptors on immune cells to exert potent immunosuppressive effects, making Tregs key factors in facilitating immune evasion of tumors. Studies have shown that the elevated levels of IL-35 are linked to unfavorable outcomes in AML [19, 20]. TGF-β can cooperate with IL-2 to upregulate the production of Foxp3 and promote the transformation of naive $CD4^+$ T lymphocytes to Tregs [21] (Figure 1). IL-35 plays a dual role by suppressing the proliferation of $CD4^+CD25^-$ effector T cells while simultaneously promoting the growth and preventing the apoptosis of AML cells [22] (Figure 1). Compared with healthy individuals, AML patients present significantly elevated levels of Tregs in the PB and BM, which are positively correlated with IL-35 expression [18, 23]. Conversely, the proportions of cytotoxic lymphocytes and

TABLE 1 Phenotype and function of Tregs.

| Type | | Origin | Immunophenotype | Main function | Role in AML |
|---|---|---|---|---|---|
| CD4+Tregs | Natural Tregs (nTregs) | Thymus | CD4+, CD25+, Foxp3+ Tregs | Suppress autoreactive T cells through contact-dependent mechanisms and inhibitory cytokines to maintain self-tolerance | Promote immune escape by inhibiting CD8+ T cells, DCs and NKs. High levels in AML correlate with poor prognosis. |
| | Induced Tregs (iTregs) | Peripheral tissues | Tr1 (CD4+, IL-10high) | Secrete elevated amounts of IL-10 and TGF-β, with minimal Foxp3 expression, and release granzyme B and perforin to mediate cytotoxicity [5] | Regulate the tumor microenvironment through IL-10 and TGF-β, induce the increase of Tregs, and indirectly promote tumor immune escape while suppressing the immune response |
| | | | Th3 (CD4+, TGF-βhigh) | Primarily secrete TGF-β, induce the differentiation of CD4+ T cells into Tregs, and upregulate Foxp3 expression [6] | |
| | | | CD4+, Foxp3+ Tregs | Differentiated from CD4+T cells under the induction of TGF-β and IL-2, inhibit effector T-cell function, maintain peripheral tolerance, and inhibit autoimmune responses [7] | |
| CD8+ Tregs | | Thymus or Peripheral tissues | CD8+ T cells, partially expressing Foxp3 | Secrete IL-10 and TGF-β to inhibits the activity of CD4+ T cells and B cells, reduce the release of inflammatory cytokines through the CTLA-4 and PD-1 pathways, directly induce target cells death via the Fas/Fasl and perforin/granzyme B pathways,thereby enhancing the anti-tumor effect [8] | CD8+ Tregs exert their unique therapeutic potential and advantages by secreting immunosuppressive factors and specifically regulating immune responses, thereby alleviating GVHD while maintaining the GVL effect. However, research on CD8+ Tregs in AML is limited |
| CD4-CD8- Tregs | | Thymus and peripheral tissues [9] | Double negative T cells,CD4-, CD8- | Express IFN-γ, TNF-α, Ly6A, FcRγ, and CXCR5; acquire MHC-peptide complexes from antigen-presenting cells; and exert immunosuppression through Fas/Fas ligand interactions [10] | mechanisms include suppression of effector cells and promotion of a tolerogenic microenvironment |

B cells are relatively low [24]. It is closely related to recurrence and drug resistance in AML. Elevated IL-10 levels and reduced IL-6 levels are linked to OS rates in AML patients and could act as potential biomarkers for predicting disease progression in AML patients [25]. Furthermore, studies have shown that a high-frequency single-nucleotide polymorphism (SNP) at position −819 of IL-10 has been identified as a factor that raises the risk of AML [26]. In AML patients, high expression of TGF-β1 may inhibit the immune function of NKs by phosphorylating SMAD and downregulating Natural Killer Group 2 Member D Receptor (NKG2DR) expression [27]. In addition, studies have demonstrated that TGF-β1 can suppress the antitumor immunity of NK cells through enhancing the SMAD3 signaling to induce CD96 expression on NK cells, thereby reducing IFN-γ production [28]. Importantly, transcriptomic analysis of HL60 cells (M3 subtype) revealed that TGF-β/activin signaling represents a promising target to overcome drug resistance in AML [29]. Studies indicate that relapse after allogeneic hematopoietic stem cell transplantation (allo-HSCT) may be linked to increased levels of TGF-β1, which strongly suppress mTORC1 activity, mitochondrial oxidative phosphorylation, cell proliferation, and cytotoxic functions of NKs in the BM, leading to their functional impairment [30]. In addition, Tregs promote the polarization of macrophages into M2-type tumor-associated macrophages (M2-TAMs) by secreting IL-10 and TGF-β. M2-TAMs exhibit tumor-promoting functions, such as degrading the tumor extracellular matrix, promoting angiogenesis, and recruiting immunosuppressive cells, thereby facilitating tumor progression and distant metastasis [31]. Research has demonstrated that AML blasts recruit M2-TAMs and Tregs, resulting in their high infiltration into the BM, which is linked to poor prognosis [32]. To conclude, the inhibitory cytokines secreted by Tregs can enhance immune tolerance and immune escape by directly inhibiting the function of effector immune cells, promoting differentiation and function of Tregs, and regulating immune microenvironment.

Moreover, $CD4^+CD25^+$ Tregs possess high-affinity IL-2 receptor (CD25), which depletes IL-2, thereby suppressing the proliferation of Teff cells and promoting their apoptosis (Figure 1). IL-2 can stimulate the growth of NKs, however, when Tregs and NKs are cocultured, Tregs can inhibit the proliferation of NKs by competing with IL-2 [33, 34], indicating that the affinity between Tregs and IL-2 may be dominant, which can weaken the immune ability and facilitate the escape of tumor cells (Figure 1). CD8+Foxp3- Tregs can inhibit the function of Teffs through intercellular contact and the release of suppressive cytokines like IL-10 and TGF-β [35].

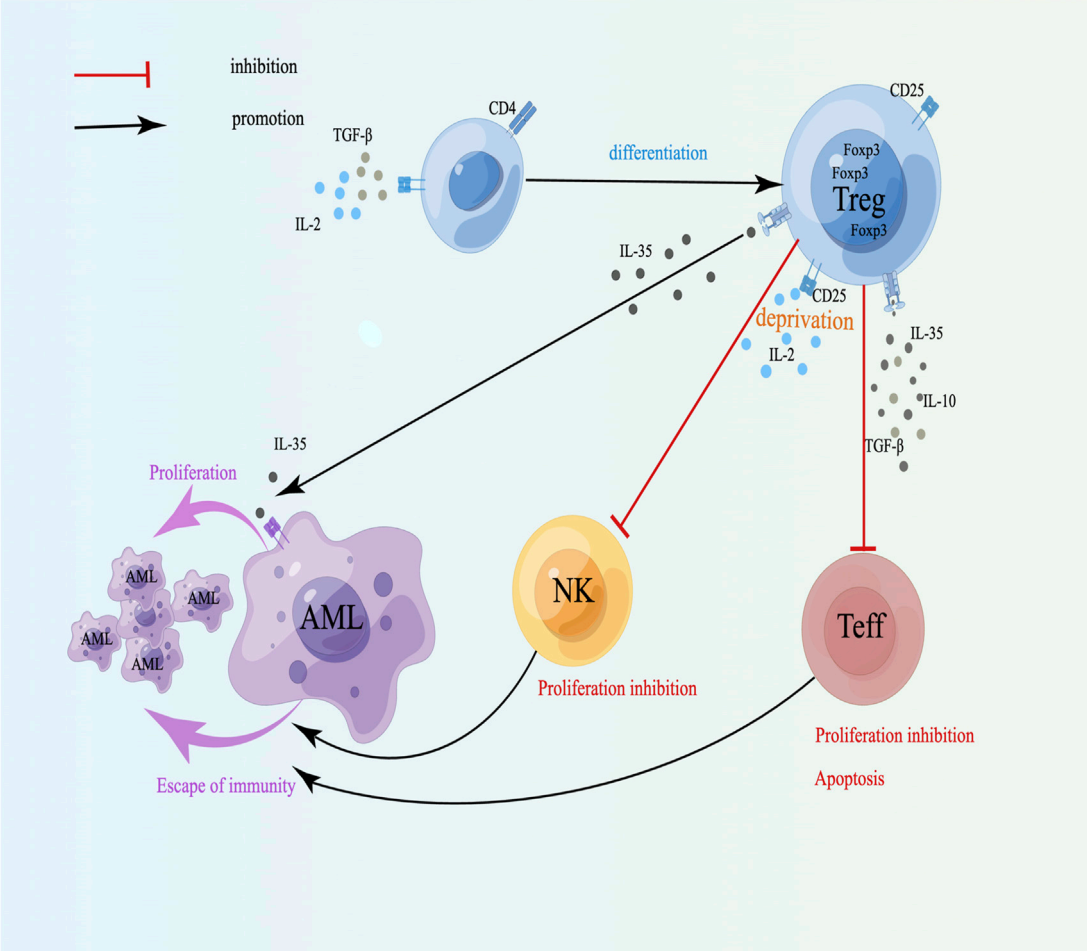


FIGURE 1
Cytokines secreted by Tregs and drug resistance in AML. TGF-β can cooperate with IL-2 to induce naive T lymphocytes to differentiate into Tregs; $CD25^+$ Tregs inhibit NK and Teff proliferation and induce apoptosis through competitive binding to IL-2; IL-35 can directly promote the proliferation of leukemia cells. A schematic diagram is created by Figdraw (www.figdraw.com).

Therefore, Tregs mainly downregulate the quantity and activity of Teffs by secreting different soluble negative immune molecules and suppress the growth of Teffs and NKs by competing with and depleting IL-2, which can cause immune escape of tumor cells and induce drug resistance in AML.

## Surface molecules of Tregs and drug resistance in AML

A variety of coinhibitory receptors (CIRs), including cytotoxic T lymphocyte-associated protein 4 (CTLA-4), T-cell immunoglobulin and mucin domain 3 (TIM-3), programmed cell death protein 1 (PD-1), lymphocyte activation 3 (LAG-3, CD223) and T-cell immunoglobulin and immunoreceptor tyrosine-based inhibitory motif domains (TIGIT), expressed on the surface of Tregs are critical for their immunosuppressive activity. Studies have shown that the highly expressed coinhibitory molecule CTLA-4 on Tregs competes with CD28 on Teff cells to attach to CD80/86 on the surface of APCs, resulting in the inhibition of Teffs and APCs activation and increased apoptosis, thereby weakening the immune killing effect of Teffs on tumor cells [36]. Compared with those of healthy controls, AML patients exhibit significantly higher levels of CTLA-4 and LAG-3, which is closely related to poor prognosis [37, 38]. Interestingly, the CTLA-4 expression level in individuals with APL is markedly higher compared to those with non-M3 subtypes [39]. Research conducted by Davids demonstrated that CTLA-4-specific antibody ipilimumab in treating AML patients who relapsed following allo-HSCT can promote the infiltration of cytotoxic $CD8^+$ T lymphocytes and the expansion of Teff subsets, suggesting that ipilimumab is feasible for managing drug-resistant relapsed patients [40].

Studies have shown that the combination of PD-L1 highly expressed on AML cells and PD-1 on the surface of T lymphocytes can induce them to differentiate and expand into Tregs that highly express Foxp3 and PD-1, and these Tregs release suppressive cytokines, including IL-10 and IL-35, enabling tumor cell immune escape [41]. Moreover, PD-1 on T lymphocytes interacts with PD-L1 on tumor cells, which can also induce T lymphocyte apoptosis [42]. Chen et al. analyzed The Cancer Genome Atlas (TCGA) database and verified 62 AML bone marrow samples and indicated that the combined high expression of PD1, PD-L1, PD-L2 and CTLA-4 was linked to reduce OS rates [43]. In patients with a high AML cell burden, the bone marrow shows a significant increase in PD-1+ Tregs and PD-1+ TIGIT+ Tregs. Interestingly, the elevated PD-1 is closely linked to lactate secretion by AML blasts [44]. TIGIT is expressed only on lymphocytes, especially nTregs, which can promote the differentiation of Tregs and combine with CD112 and CD155 [45]. TIGIT+ Tregs mainly inhibit the differentiation and proliferation of Th1 cells and Th17 cells via a mechanism dependent on fibrinogen-like protein 2 (FGL2) [45]. Thus, TIGIT may be an important immunosuppressive molecule related to the immunosuppressive function of Tregs, which are involved in tumor immune escape and resistance. Relapse, the primary cause of mortality in AML patients following allo-HSCT, is strongly linked to elevated TIGIT expression on $CD4^+$ T cells [44]. LAG-3 shares high homology with CD4 [46], is highly expressed on Tregs [47], and has a high affinity for major histocompatibility complex class II (MHC II). The combination of LAG-3 and MHC II on $CD4^+$ T cells induces an inhibitory pathway mediated by the activation of immune body tyrosine kinase [48], inhibits the immunity of T cells so that targeting the LAG-3/MHC II signaling pathway helps to promote the immune effect of $CD4^+$ T cells against tumors, indicating that LAG-3 is critical for Treg-mediated immunosuppression and may serve as a novel therapeutic strategy in AML. Research has indicated that LAG3 not only can bind to MHC II [49] but can also interact with soluble liver-secreted fibrinogen-like protein 1 (FGL-1), thereby inhibiting both autoimmune and antitumor immunity [50]. Additionally, Tregs in AML patients express high levels of LAG3, which can reduce the activation of $CD8^+$ T cells and is linked to poor outcomes [51]. *In vitro* experiments have confirmed that anti-LAG3 antibodies can downregulate Tregs, increase their cytotoxic activity against $CD8^+$ T cells, reduce IFN-γ secretion, and modulate the immune tolerance of AML cells. Research has demonstrated that TIM3+ Treg cells exhibit elevated expression of inhibitory molecules, including LAG-3, PD-1, and CTLA-4, resulting in increased inhibitory function via releasing more IL-10, granzymes and perforin [52]. Dama et al. found that the high frequency of TIM-3+Tregs and Gal9+CD34- leukemic cells in the BM can promote T-cell exhaustion and induce immune escape in AML [53]. Therefore, targeting the Gal9/Tim-3 axis may improve AML patient prognosis. Additionally, research has indicated that functional single nucleotide polymorphisms (SNPs) of TIM-3 are connected to the risk prediction of AML [54]. The above studies revealed that high expression of coinhibitory molecules on Tregs can cause the dysfunction in APCs and effector T cells, promote their own differentiation and expansion, and are crucial for promoting immune escape and drug resistance in tumor cells (Figure 2). In summary, monitoring these immune-related biomarkers can help identify the immunosuppressive state in AML patients, predict treatment response, and provide guidance for personalized immunotherapy regimens.

Recently, the application of immune checkpoint inhibitors (ICIs) that target Tregs has provided new therapeutic directions and hope for overcoming resistance in AML. Widely studied and considered potential therapeutic targets include PD-1, TIM-3, LAG-3, and TIGIT. The clinical efficacy of ICIs is determined by factors, including the targeted pathway, disease stage, and combination with conventional therapies. Clinical studies have shown that when nivolumab or pembrolizumab is combined with azacitidine, the overall response rates (ORRs) are 33% and 55%, respectively, among individuals with relapsed/refractory (R/R) AML. Especially, patients who had not previously received hypomethylating agents (HMAs) had even higher ORRs [55–57], which may be related to the ability of HMA to increase the levels of PD-1/PD-L1 [58]. The combination of pembrolizumab with high-dose cytarabine or decitabine demonstrated efficacy, which was consistent with previous studies [59]. Other studies have shown that nonresponders to the combination of nivolumab and azacitidine primarily exhibit increased CTLA-4 expression on T lymphocytes [55]. The combination of ipilimumab with azacitidine and nivolumab for treating R/R AML demonstrated superior efficacy compared with the combination of nivolumab and azacitidine alone, along with an improvement in overall survival [60]. Research suggests that dual immunotherapy holds promising potential for clinical application. Additionally, research indicates that the application of ICIs targeting PD-1 (nivolumab) or CTLA-4 (ipilimumab) before stem cell transplantation (SCT) can enhance the progression-free survival (PFS) of AML/MDS patients post-transplant [61]. Clinical studies on the utilization of PD-L1 inhibitors for treating R/R AML have shown suboptimal therapeutic efficacy. For example, the combination of avelumab with decitabine has not yielded promising results [62]. The combination of atezolizumab with azacitidine has also shown limited therapeutic efficacy for treating R/R AML [63]. An earlier study showed that an anti-CTLA-4 mAb (MDX-010) induced the expansion of Teffs by enhancing the activity of DCs [64]. Research have demonstrated that the anti-TIGIT mAb TGTB227 is capable of suppressing the immunosuppressive function of Tregs by reducing the expression of Foxp3 in Tregs. This mechanism may be associated with the CD25/IL-2 signaling pathway [65]. Furthermore, an elevation in the frequency of TIGIT+ $CD8^+$ T cells is associated with R/R AML and post-HSCT relapse. This effect is mediated

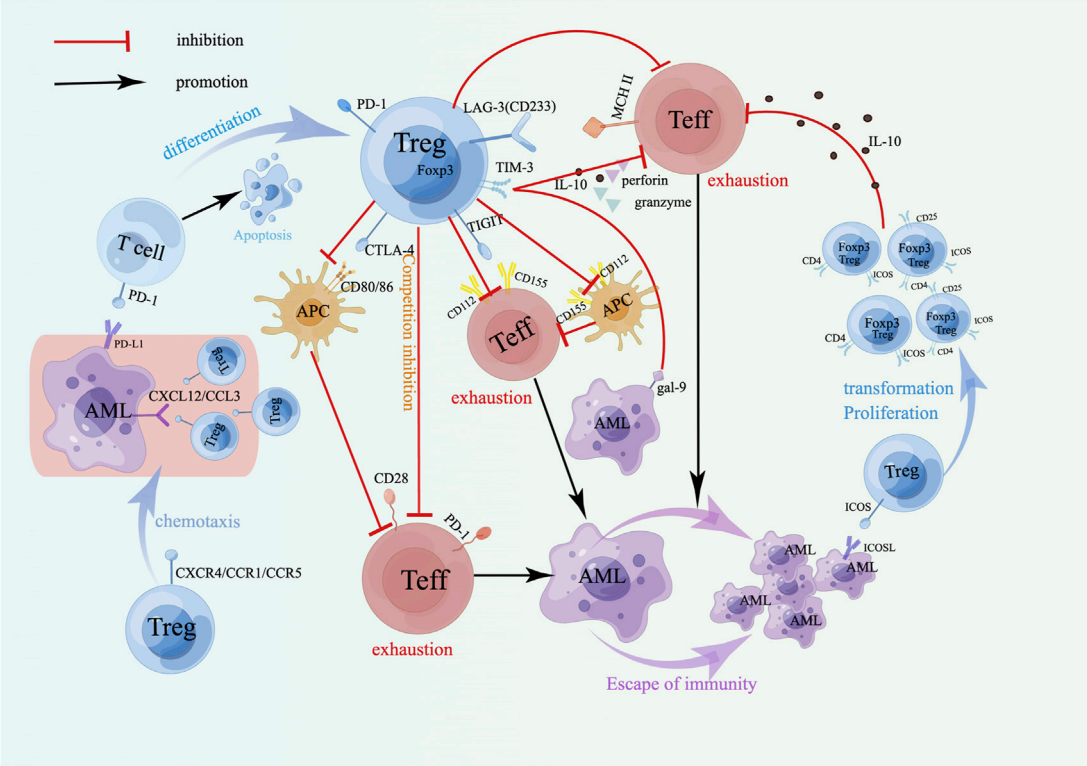


FIGURE 2
Surface molecules of Tregs and drug resistance in AML. The coinhibitory receptor on Tregs mainly induces immune escape of AML cells by inhibiting APCs and depleting Teffs. The combination of the costimulatory receptor ICOS on Tregs and ICOSL on AML cells can induce the transformation and proliferation of Tregs, produce more IL-10, and play a stronger immunosuppressive role. Treg-expressed chemokine receptors promote their accumulation at the tumor site to exert an immunosuppressive effect. A schematic diagram is created by Figdraw (www.figdraw.com).

primarily through the dysfunction of $CD8^+$ T cells and diminished cytokine production. Moreover, knockdown of TIGIT can reverse the immunosuppressive effects induced by its high expression [66]. Tiragolumab, a novel anti-TIGIT monoclonal antibody, has demonstrated promising efficacy in studies on solid tumors when combined with the immune checkpoint inhibitor atezolizumab to overcome immunosuppression and restore immune responses [67]. Research on its use in malignant hematological tumors is limited. However, clinical studies on TIGIT inhibitors for R/R AML are relatively rare, although TIGIT inhibitors represent potential therapeutic targets for overcoming AML resistance. Sabatolimab (MBG453), a monoclonal antibody targeting TIM-3, has demonstrated the ability to enhance immune responses against leukemia cells *in vitro* [68]. We hypothesize that inhibiting the immune checkpoint TIM-3 may help alleviate the immunosuppressive effects of Treg cells and restore the antitumor immune activity of Teffs, making it a promising therapeutic approach for R/R AML. Currently, a study is underway to investigate whether sabatolimab, either as a monotherapy or combined with azacitidine, can amplify the graft-versus-leukemia (GvL) response in patients who achieve complete remission and are MRD positive following allogeneic stem cell transplantation (allo-SCT) [NCT04623216]. Relatlimab (BMS-986016), a human IgG4 anti-LAG-3 mAb, is a LAG-3-targeting drug that can enhance antitumor immune responses [69]. The combination of relatlimab with azacitidine in immune therapy for AML is currently under investigation [NCT04913922]. While LAG-3 inhibitors appear to be effective immunotherapeutic targets for treating R/R AML, further research is needed to increase their clinical applicability.

Tregs also express inducible T-cell costimulatory molecules (ICOSs) on their surface. Its binding to inducible T-cell costimulatory ligand (ICOSL) on AML cells can maintain overexpression of Foxp3 and CD25 and promote the transformation and proliferation of Tregs [70] (Figure 2). Moreover, the upregulation of IL-10 secretion by $CD4^+CD25+ICOS+$ Tregs indicated that the expansion of Tregs in AML could be achieved through the ICOS/ICOSL pathway, which enhances the body's immunosuppressive ability and induces leukemia cells to immune escape and drug resistance (Figure 2). Experiments have demonstrated that

ICOS+ Tregs exhibit an increased suppressive effect on $CD4^+CD25^-$ effector T cells. Treatment of AML mice with anti-ICOSL mAb can decrease the number of Tregs, thereby slowing the progression of AML [70]. Thus, the strategy targeting the ICOS/ICOSL signaling pathways is expected to become new targets in drug-resistant AML. Elevated ICOS expression is linked to reduced OS rates in AML patients, and the coexpression of ICOS with PD-1 in non-M3 patients predicts even lower OS rates. Additionally, ICOS/PD-1 has emerged as an independent predictor of poor outcomes in AML [71]. Studies by Wan et al. have demonstrated that the proportion of Tregs in the BM of AML patients is greater than that observed in normal individuals, mainly because regulatory B cells (Bregs) induce $CD4^+$CD25-T cells to transform into Tregs, and the chemokine receptor CXCR4 highly expressed on Tregs facilitates the strong migration and aggregation to the BM [72] (Figure 2). In addition, other chemokines, CCR1 and CCR5, expressed by Tregs can also cause Tregs to accumulate at the tumor site to mediate immunosuppression, promote immune evasion by cancer cells, and promote drug resistance recurrence. Animal experiments have confirmed that blocking the CXCL12-CXCR4 and CCL3-CCR1/CCR5 axes can inhibit the recruitment of Tregs in the bone marrow microenvironment and delay the progression of leukemia [73] (Figure 2), therefore, targeting the CXCL12-CXCR4 and CCL3-CCR1/CCR5 signaling pathways may become targets of leukemia immunotherapy. Moreover, AML cells can also effectively recruit Tregs by expressing CCL2, which binds to CCR2 receptors on Tregs [74]. These interactions help create an immunosuppressive microenvironment that enhances the survival and drug resistance of AML cells. Studies have shown that ICOSL, which is overexpressed on AML cells, interacts with ICOS+ Tregs, which enhances their ability to secrete IL-10, potentially inducing AML cell proliferation by triggering the Akt, Erk1/2, p38, and STAT3 signaling cascades. Additionally, it directly promotes the expansion of Tregs [70]. The upregulation of hypoxia-inducible factor (HIF) expression triggered by hypoxia in the AML microenvironment is associated with resistance to doxorubicin, possibly because HIF-1α enhances the expression of the YAP gene in AML cells, which stabilizes the binding of HIF-1α to its target genes [75]. Regulating the glycolytic pathway is associated with promoting Treg proliferation [76], further assisting in the evasion of immune surveillance by AML cells. Early studies have shown that leukemia-derived microvesicles (MVs) in AML patients suppress NKs cytotoxicity through TGF-β1, and this inhibition is mediated via the SMAD signaling pathway [27]. AML cell-derived extracellular vesicles (EVs) inhibit the activity of $CD4^+$ T cells by carrying immune suppressive factors, such as PD-L1, TGF-β1 or miRNA, thereby promoting immune evasion in leukemia [77]. Research reported that leukemia cell-derived exosomes can stimulate bone marrow stromal cells (BMSCs) to secrete IL-8. IL-8 not only enhances the drug resistance of AML cells (e.g., etoposide) and promotes the survival of leukemia cells [78], but also interacts with the CXCR1 and CXCR2 on Tregs, facilitating the migration of Tregs to the tumor site and thereby suppressing effector T cells in the immune microenvironment. Hong et al.'s research indicated that EVs isolated from patients with relapsed/refractory AML can inhibit the antileukemic cytotoxicity of NK-92 cells [79]. These findings suggest that leukemia cells can induce the accumulation of Tregs at the tumor site and inhibit the antitumor immune response by changing the tumor immune microenvironment, thus affecting the outcome of chemotherapy and leading to drug resistance.

Over the past few years, substantial advancements have been achieved in AML immunotherapy, with the identification of multiple critical immune targets on AML cells that have been utilized for drug development. Among these, CD33 is a widely studied target, and its antibody–drug conjugate, gemtuzumab ozogamicin, was approved in 2017 for use in treating newly diagnosed and relapsed or refractory CD33-positive AML patients [80, 81]. CD123, a marker of leukemia stem cells, has been targeted by drugs such as flotetuzumab (a CD123/CD3 bispecific antibody) and IMGN632 (an antibody–drug conjugate), both of which have demonstrated therapeutic potential in R/R AML patients [82, 83]. The SIRPα-αCD123 fusion antibody targets both CD123 and CD47, with a specific focus on AML leukemia stem cells (LSCs). This dual-targeting approach significantly enhances immune clearance while reducing off-target toxicity, offering a novel strategy for achieving long-term remission and improved survival in AML patients [84]. These studies not only provide new strategies for the treatment of AML but also offer hope for improving patient survival rates and quality of life in the future.

## Other immune cells and drug resistance in AML

### Dendritic cells (DCs)

DCs originate from hematopoietic stem cells (HSCs) in the BM and are the most powerful APCs in the body. DCs are mainly categorized into conventional DCs (cDCs) and plasmacytoid DCs (pDCs). Mature cDCs, characterized by high expression of MHC II, the costimulatory molecules CD80/86 and CD40, and intercellular adhesion molecule 1 (ICAM-1), effectively present antigens, stimulate T cells, trigger adaptive immune responses, and fight tumors. pDCs also have the ability to process and present antigens, but their main function is to generate substantial amounts of type I interferon (IFN-I) and other proinflammatory factors, contribute to the antiviral innate immune response, and participate in the initiation and progression of tumors. Research have suggested that the expansion of pDCs is closely associated with the progression of AML [85]. The drug Tagraxofusp, which targets the pDC surface marker CD123, has shown significant efficacy in clearing pDCs

[86]. Research by Wenbin et al. reported that the frequent occurrence of RUNX1 mutations is crucial for the differentiation and expansion of pDCs [86]. Therefore, CD123-targeted immunotherapy may represent a potential therapeutic approach for RUNX1-mutated AML. Importantly, Zhu et al. reported that patients with pDC infiltration in AML-M4/M5 patients had lower chemotherapy sensitivity and longer durations of CR and OS than those without pDC infiltration did, indicating that pDCs can be used for AML-M4/M5 risk stratification and to guide treatment [87]. Ocadlikova et al. reported that doxorubicin and cytarabine can induce the upregulation of CD39 or CD73 on DCs. The large amounts of ATP released by AML cells during exhaustion can be broken down by CD39 and CD73 into adenosine, which stabilizes the immune activity of Tregs, promoting the formation of an immunosuppressive microenvironment and inducing resistance [88]. ATP can bind to the P2X7 receptor on DCs to induce the upregulation of IDO1, depleting tryptophan and promoting the production of kynurenine, which inhibits T-cell proliferation and function [88–91]. Furthermore, Tregs release IL-10 and TGF-β, driving DCs and macrophages to adopt an immune-tolerant or protumor phenotype, further dampening the immune response [92, 93]. Other research has revealed that differentiation and proliferation of DCs rely on the FLT3/FLT3L signaling pathway, with FLT3 mutations being the most common in AML [94], and approximately 25% of patients harbor FLT3 mutations, which is linked to an unfavorable prognosis [95]. In recent years, with the development of tumor immunotherapy, DCs presenting tumor-specific antigens have been developed as vaccines, through which DCs present tumor antigens to T cells to induce adaptive immune responses to fight tumors and prevent drug resistance recurrence. However, the effectiveness of DC vaccination in inducing the anti-tumor response of immune system is relatively limited [96], and combined treatment with chemotherapy and radiotherapy may enhance the anti-tumor effect [97, 98]. Pepeldjiyska et al. reported that the increase in the frequency of leukemia-derived DCs (DCleu) derived from bone marrow primitive leukemia cells in AML patients can downregulate Tregs and activate specific T cells and NKs, promoting anti-tumor immune response [99], thus, the heightened frequency of induced DCleu helps to increase the body's antitumor immunity and reverse tumor resistance.

## Natural killer cells (NKs)

NKs are lymphoid innate immune cells and are the key effector cells in immunotherapy [100], which are related to the occurrence, progression and recurrence of AML [101]. The killer cell immunoglobulin-like receptor (KIR) expressed on the surface of NKs can be divided into two types, inhibitory and activating [102], which can specifically recognize and bind target cell surface molecules and play important antitumor roles [103]. NKs express different immunophenotypes at the immature, mature, and hypermature stages and can migrate, release cytokines, and destroy target cells [104]. A study reported that the ratio of NK cells in the BM of newly diagnosed AML patients may forecast patient outcomes. In comparison to healthy individuals, the proportion of NKs in the BM of R/R patients is the lowest [105], and their function is impaired, suggesting that a reduced NK cell ratio correlates with a worse prognosis in AML patients [106, 107]. NK-based immunotherapy can significantly improve the outcomes of patients with advanced or high-risk AML [108]. Studies have shown that the overexpression of heme oxygenase 1 (HO1) in AML patients induces NK dysfunction [109], thus, targeting HO1 to restore NK cell function may be a promising anti-AML immunotherapy strategy. Dai et al. reported that the myeloid cell leukemia-1 (MCL1) is negatively correlated with that of NKs and that the combined action of MCL1 inhibitors and NKs can significantly exhaust primary AML cells and cell lines. Interestingly, the proportion of NKs in the BM can affect the effect of MCL1 inhibitors [105], indicating that the proportion and abnormal function of NKs play important roles in the drug resistance of AML leukemia cells. Chajuwan et al. observed that elevated TIM-3 expression in NKs correlated with CR status after induction therapy, indicating that TIM-3 in NKs may be a prognostic marker for AML [110]. Bou-Tayeh et al. reported that NKs from mice with leukemia express IL-15/mTOR signaling, and this pathway can induce NK metabolism and functional failure in leukemic mice [111]. Compared with that in healthy controls, AML patients showed reduced levels of the NK-activating receptors NKG2D, NKp46, and NKp30 in their peripheral blood, while there was an upregulation in the expression of inhibitory receptors such as TIM-3, ILT-4, ILT-5, and PD-1. At the same time, the expression of Siglec-7 in NK cells was notably reduced in AML patients [101], suggesting that Siglec7 is an indicator of NK cell function and could potentially be targeted to improve NK cell activity, thereby boosting the antitumor immune response. Disruption of the NKG2D/NKG2DL pathway, which is crucial for NK cell-mediated tumor cell killing, can lead to immune escape in AML, resulting in drug resistance [112]. Furthermore, NKs can release cytokines like IFN-γ and perforin/granzyme, and express TNF-related apoptosis-inducing ligand (TRAIL) and Fas Ligand (FasL) to activate apoptotic pathways in tumor cells [113]. The loss of these functions may represent a key mechanism through which tumors escape killing mediated by NK cells. The immunosuppressive tumor microenvironment created by TAMs, MDSCs, and Tregs is a major obstacle to NK cell-mediated antitumor activity. They drive NKs exhaustion and facilitate tumor immune escape by depleting activation factors like IL-2, releasing immunosuppressive molecules such as TGF-β and IL-10, and activating inhibitory receptors on NK cells, including PD-1 and TIGIT. Studies have shown that NK cells recognize ligands like PDL1, Gal-9, and CD112/CD155 on AML cells through their surface receptors PD-1, TIM3, and TIGIT, triggering inhibitory

signaling pathways. This activation affects NK cell function via the PI3K, ERK, and PKCθ pathways, thereby facilitating tumor immune evasion [114, 115]. Moreover, the high expression of CD200 on leukemia cells, through binding to CD200R, inhibits the cytotoxicity of NK cells, inducing immune evasion of leukemia cells, which is associated with the recurrence and progression of AML [116, 117]. NKs exhibit strong anti-tumor activity. Restoring the antitumor properties of NK cells may represent a promising approach for treating relapse. Notably, AML cells can evade the immune recognition of NKs via gene mutation, fusion and epigenetic modification, though the exact mechanism remains uncertain [118]. Research has shown that the hypomethylation agent (HMA) decitabine can upregulate the level of ICAM-1(CD54) and CD48 on AML cells, thereby activating NKs to kill leukemia cells while reversing immune evasion by leukemia cells [118, 119]. This suggests that the combination of HMA and NK cells infusion may serve as a promising new approach for AML treatment.

The immune exhaustion of effector immune cells poses a critical challenge in cancer treatment. Current strategies to reverse T cells and NKs exhaustion primarily include ICIs, activation receptor enhancement, and the application of genetically engineered CAR-T/CAR-NK cells. ICIs target molecules such as PD-1, CTLA-4, TIM-3, TIGIT, and LAG-3, blocking the interaction of checkpoint molecules to relieve the inhibition of effector immune cells, enhance their activity, reverse immune exhaustion, and overcome immune resistance. IL-2 and IL-15 are critical cytokines that promote the growth and activation of T cells and NK cells [120, 121]. Local or systemic administration of recombinant IL-2 or IL-15 can enhance the proliferation and function of immune cells, thereby reversing immune exhaustion. Additionally, a study on CD33-targeted CAR-T-cell therapy for AML demonstrated a transient reduction in $CD33^+$ leukemic blasts (lasting only 7 days), accompanied by adverse effects such as leukopenia [122]. CD123-targeted CAR-T-cell therapy can achieve CR in AML patients, but it is linked to notable adverse effects [123, 124]. NKG2D is a type II transmembrane receptor, and its signaling induces cytolytic effector functions [125]. In a study involving 22 AML patients, repeated infusions of NKG2D CAR-T cells resulted in a 4.5% probability of achieving a morphologic leukemia-free state (MLFS) [126]. CAR-T-cell therapy for AML remains under study but has demonstrated significant potential. Owing to the potent antitumor properties of NK cells, CAR-NK cells can also specifically target tumor cells [127], and CAR-NK cells offer several advantages, including immediate availability, inducible proliferation, and a longer lifespan [128]. However, when donor-derived NKs are used, GVHD may occur [129].

## Cytotoxic T lymphocytes (CTLs)

$CD8^+$ T cells are activated, proliferate, and differentiate into CTLs in peripheral immune organs and can accumulate at tumor sites under the action of chemokines. The surface of $CD8^+$ T cells highly expresses lymphocyte function-associated antigen-1 (LFA-1) and CD2, which can interact with the expression of ICAM-1. LFA-3 binds to target cells and kills target cells efficiently. Early research has demonstrated that the accumulation of Tregs in the AML progression model can suppress the expansion of CTLs [130], potentially through the secretion of the inhibitory cytokines IL-10 and TNF-β. Leukemic progenitor cells and leukemic stem cells (LPCs/LSCs) are currently believed to be responsible for disease relapse after intensive therapy, and targeting LPCs/LSCs through specific CTLs may be an option to prevent AML relapse [131]. The application of anti-PD-1 antibody (nivolumab) in AML significantly increases T-cell-directed immune response targeting leukemia-associated antigen (LAA), particularly in the context of targeting LPCs [131], thus, the nivolumab could a candidate immunotherapy for those who are resistant. However, Rakova reported that ICIs targeting PD-1 and CTLA4 exhibit limited clinical effectiveness in AML [132]. In AML with TP53 gene mutations, TIM-3 expression is significantly increased, and CTLs exhibit characteristics of exhaustion/dysfunction, indicating that the antitumor immune response of TP53-mutated AML is insufficient, which presents a new strategy for overcoming drug resistance in AML [133]. Studies have suggested that IFN-I can promote the recruitment of tumor-specific CTLs; therefore, stimulator of interferon genes (STING) agonists have a killing effect on AML leukemia cells [134]. In conclusion, CTLs specifically kill target cells, and immunotherapy to restore and enhance the cytotoxic function of CTLs is an effective treatment to combat tumor drug resistance.

A clinical study demonstrated progress in treating relapsed AML patients with tumor-associated antigen-specific cytotoxic T lymphocytes (TAA-CTLs), showing that some patients achieved MRD negativity with a reduced incidence of relapse [135], but the study involved a limited sample size, leading to lack statistical significance and reliability. However, some studies have revealed that immunotherapeutic approaches with TAA-CTLs are less reliable at eradicating the disease, potentially because of the immunosuppressive tumor microenvironment [136]. Studies indicate that LAA-CTLs (such as CG1-CTLs or PR1-CTLs) combined with pembrolizumab are more effective in eliminating AML cells than LAA-CTLs alone without increasing toxic side effects or the risk of GVHD [136, 137]. Chapuis et al. used adoptive transfer of WT1-specific allogeneic TCR-T cells in a clinical trial to treat high-risk AML patients, achieving good therapeutic outcomes and helping to prevent disease relapse (NCT01640301) [138]. In addition, an additional clinical study of autologous WT1-specific TCR-T cells aimed to evaluate their therapeutic effects on high-risk bone marrow malignancies, which showed significant efficacy and excellent safety (NCT02550535) [139].

## T helper 17 (Th17) cells

The primary function of Th17 cells is to induce neutrophils to phagocytose and kill pathogens, primarily by secreting IL-17, IL-

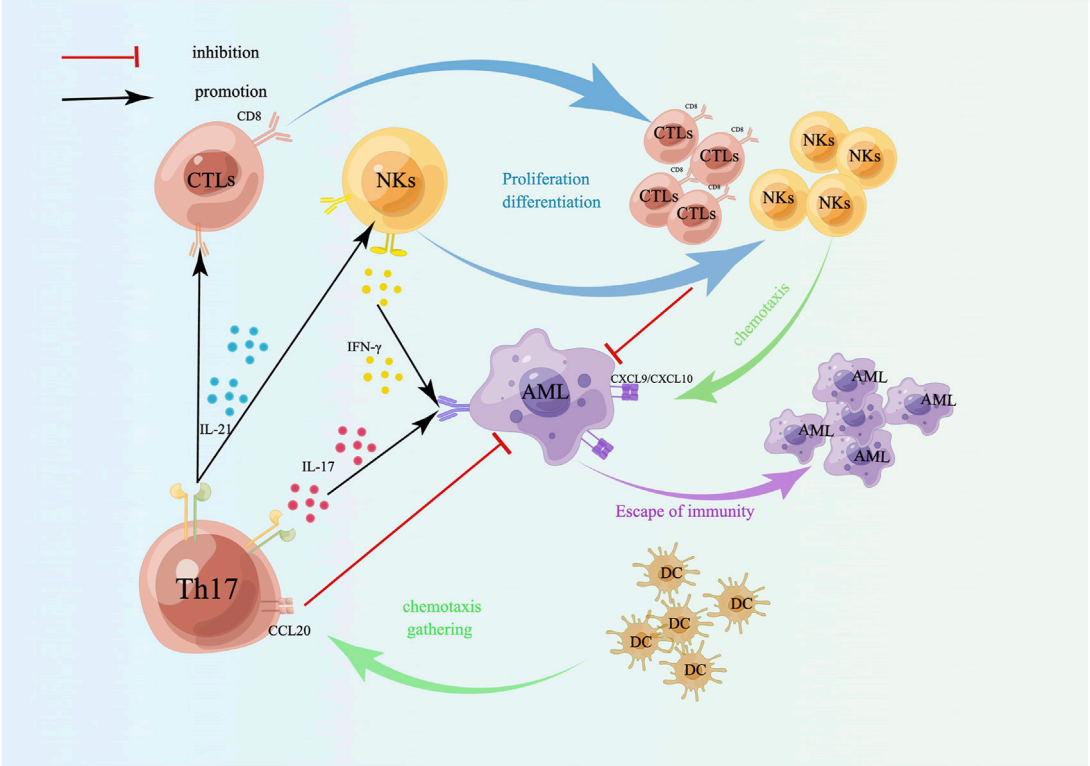


FIGURE 3
Targeting effect of Th17 cells on AML cells. Th17 cells induce the differentiation and proliferation of CTLs and NKs by secreting IL-21; IL-17 secreted by Th17 cells and IFN-γ secreted by NKs act on AML cells together, which can induce tumor cells to secrete CXCL9/CXCL10, accumulate NKs and CTLs, and kill tumor cells. Th17 cells also recruit DCs by releasing CCL20 to enhance the immune response at the tumor site. A schematic diagram is created by Figdraw (www.figdraw.com).

21, and IL-22 to exert their immune effects. Among these cytokines, IL-21 can amplify Th17 function through autocrine signaling, stimulate $CD8^+$ T-cell and NK proliferation and differentiation, and have antitumor immune effects (Figure 3). IL-17 has both tumor-promoting and antitumor effects. The tumor-promoting properties of AML are mediated mainly by angiogenesis, which stimulates endothelial cells to release chemokines (CXCL1, CXCL2) and growth factors (GM-CSF) to recruit neutrophils, and induces epithelial cells and fibroblasts to release monocyte chemoattractant protein 1 (MCP-1) to recruit monocytes to tumor sites to differentiate into TAMs [140], whereas TAMs lose their antitumor immune properties and are linked to unfavorable outcomes [141] (Figure 4). The antitumor effect of IL-17 is synergistic with that of IFN-γ, which stimulates tumor cells to release the chemokines CXCL9 and CXCL10 to recruit NKs and CTLs into tumor sites [140, 142] (Figure 3). In addition, Th17 cells can also recruit DCs by releasing CCL20, which may enhance the immune response at the tumor site [140] (Figure 3). Studies have confirmed that the proportion of Th17 cells and the concentration of IL-17 in the bone marrow of patients with newly diagnosed and relapsed AML are significantly increased and that there is no notable distinction between these patients and healthy controls in the CR and disease-free survival (DFS) stages [143]. Ren et al. reported that the overexpression of beta-1,4-galactosyltransferase 1 (B4GALT1) in AML may be linked to poor patient outcomes, and the proportion of Th17 cells shows a positive correlation with B4GALT1 levels [144]. In newly diagnosed AML patients, peripheral blood $CD4^+$ T cells (mainly Th17 cells) secrete abundant TNF-α, which binds to TNFR2 on the surface of Tregs, inducing Treg expansion and enhancing their function [145]. An *in vitro* study confirmed that IL-1β, IL-6 and IL-23 can promote naive $CD4^+$ T cells to differentiate into Th17 cells. High levels of Th17 cells can promote the proliferation and poor prognosis of AML patients through IL-17-mediated activation of the PI3K/AKT and JAK/STAT3 pathways. In addition, high levels of Th17 cells can inhibit Th1 cell and IFN-γ production through the secretion of IL-17 and IL-22 [146]. Another clinical study indicated that the cytokines IL-23 and IL-17 secreted by Th17 cells are also positively correlated with poor clinical outcomes in AML [147].

This novel epigenetic therapy shows safety and efficacy in managing early relapse in non-APL AML patients following transplantation, with Th1/Th17 ratio modulation offering both immunological benefits and potential as a biomarker for relapse

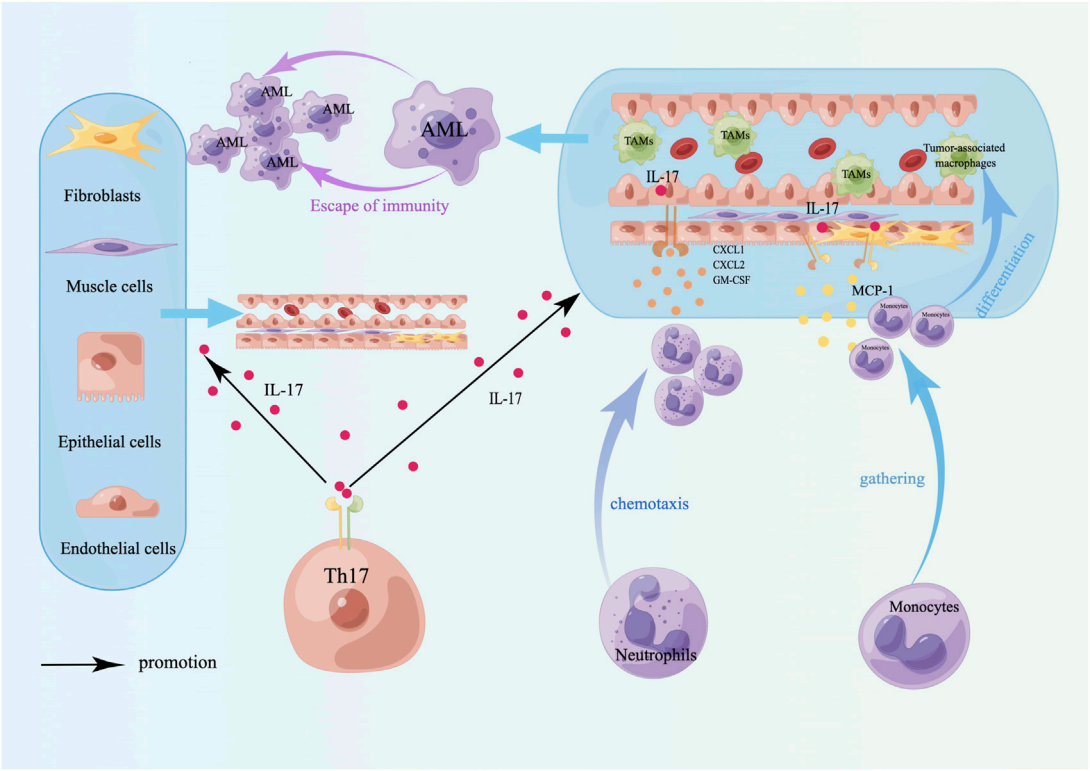


FIGURE 4
Tumor-promoting effects of Th17 cells. The tumor-promoting effect of Th17 cells is mainly to induce angiogenesis and TAM differentiation. TAMs lose their antitumor properties, have immunosuppressive effects, induce immune escape of tumor cells, and are linked to a poor prognosis in AML. A schematic diagram is created by Figdraw (www.figdraw.com).

monitoring [148]. The traditional stimulator of interferon genes pathway can effectively improve antitumor immunity. However, owing to its easy degradation and membrane transport difficulties, its antitumor effect is blocked. Emerging bioinspired nanomedicines can enhance the STING pathway to target AML cells systemically, and the mechanism may be related to the increased proportion of Th1/Th17 cells, the concentration of IFN-I and proinflammatory cytokines, and the decreased proportion of Th2 cells [149]. Elevated expression of the immunoregulatory transcription factor ZEB1 is related to poor overall survival, and the underlying mechanism may involve the promotion of Th17 cell development, increasing the secretion of IL-17 and TGF-β, and the expression of suppressor of cytokine signaling 2 (SOCS2) [150]. Therefore, ZEB1 may be a promising therapeutic target for AML.

## Myeloid-derived suppressor cells (MDSCs)

MDSCs are composed mainly of granulocyte myeloid-derived suppressor cells (G-MDSCs, CD66b+CD15+HLA-DR- cells), monocyte MDSCs (M-MDSCs, $CD14^{+}$CD11b+CD33+HLA-DR-/lo cells) and immature myeloid cells (IMCs, CD11b+$CD33^{+}$CD14-HLA-DR-$CD34^{+}$ cells) [151]. An increase in the number of MDSCs in myeloid malignancies results in a significant immunosuppressive effect, which may induce immune escape of tumor cells and promote tumor development [152]. MDSCs can inhibit Teffs by releasing arginase 1 (Arg1), nitric oxide synthase 2 (NOS2), reactive oxygen species (ROS), cyclooxygenase 2 (COX2), TGF-β, etc. [153–155], thereby promoting the progression of various cancers. In addition, MDSCs can indirectly upregulate Tregs [156]. In AML, MDSCs can suppress potent antitumor immune responses [157] and can suppress the function of $CD8^{+}$ T cells via high expression of Arg1 and indoleamine-2,3-dioxygenase 1 (IDO) [158]. Among them, IDO1 can decompose tryptophan, and a decrease in tryptophan and the accumulation of its metabolites can suppress the proliferation of antigen-specific T cells and trigger their apoptosis [159]. Arginase II induces T-cell apoptosis and autophagy by depriving T cells of the ability to metabolize the essential amino acid arginine [160], thereby reducing the immune effect of T cells on cancer cells. MDSCs and Tregs are complex, as they can enhance their interactions through soluble mediators (such as IL-10 and TGF-β), metabolic cooperation (such as Arg-1, iNOS, and CD73), and intercellular communication (such as PD-L1/PD-1, CD80/

CTLA-4, and CD40/CD40L), establishing a complex immunosuppressive feedback mechanism [161]. Ren et al. reported that high levels of M-MDSCs, which possess potent immunosuppressive capabilities, can predict poor prognosis in AML patients [162]. In addition, Tohumeken et al. reported that AML-derived EVs can induce conventional monocytes to differentiate into MDSCs, obtain a CD14+HLADRlow phenotype, and upregulate IDO to inhibit effector T-cell immunity. The Akt/mTOR pathway plays a critical factor in the phenotype and functional transformation of monocytes induced by AML-released EVs [163], and MDSCs also significantly inhibit the proliferation of NKs [164], indicating that an increase in MDSCs facilitates tumor cell immune escape. Research by Bai et al. revealed that the mechanism of AraC-induced AML resistance may involve the amplification of TNF-α, which activates the IL-6/STAT3 and NF-KB pathways, enhancing the function and survival of MDSCs and thereby mediating the immune evasion by tumors and drug resistance [165], suggesting that chemotherapy combined with TNF-α-targeting therapy may be an effective strategy to inhibit MDSC-induced immune escape. Additionally, Pyzer et al. reported that AML induces the release of the c-Myc protein through MUC1-C signaling, which inhibits the expression of miR34a, driving the proliferation of MDSCs, the levels of PD-L1, and immunosuppressive functions [166]. These findings highlight the potential of targeting the MUC1-C/c-Myc pathway as an approach for AML immunotherapy. Au et al. reported that the accumulation of immunosuppressive cells, including Tregs, MDSCs (mainly G-MDSCs) and TAMs, in the BM of AML patients is connected to $CD34^+$ AML progenitor cells [32], which promotes the immune evasion of AML blasts. Research has demonstrated that MDSC-like progenitor cells can induce Tregs expansion and cause CTLs dysfunction and exhaustion [158, 167], further reinforcing the tumor-suppressive microenvironment, which is closely associated with relapse following allo-HSCT in AML [168]. VISTA inhibits the activity of $CD8^+$ T cells via high expression on MDSCs from AML patients, and its synergistic effect with PD-1 suggests that combined inhibition of VISTA and PD-1 pathways may be a new strategy to enhance AML immunotherapy [169]. *In vitro* studies have shown that an IDO1 inhibitor (INCB024360) can induce the proliferation of CTLs, reduce Tregs, and decrease the immunosuppressive activity of MDSCs [170]. However, a phase II trial in MDS patients revealed that INCB024360 had no significant therapeutic effect [171]. Currently, research on INCB024360 (epacadostat) in AML is relatively limited. Research conducted by Masahiro et al. showed that DC vaccines loaded with Wilms' tumor 1 (WT1) enhance immune surveillance by reducing the number of MDSCs and downregulating their immunosuppressive functions, particularly the arginase 1 and IDO pathways, offering new hope for immunotherapy in AML [172]. Miner et al.'s study revealed that myeloid leukemia cells (including AML and MDS cells) can inhibit T-cell function through the STAT3 and arginase pathways [173]. These findings suggest that therapeutic strategies targeting STAT3 and arginase inhibitors may increase the effectiveness of leukemia immunotherapy and improve immune evasion mechanisms.

## Summary

We conducted a detailed exploration of the immune mechanisms responsible for resistance to treatment in AML, with an emphasis on immune cells in the bone marrow microenvironment. Research indicates that Tregs contribute significantly to immune evasion and chemoresistance by releasing inhibitory cytokines and expressing immune checkpoint molecules, with elevated Treg levels being associated with poor prognosis. AML cells further promote tumor survival and evade immune surveillance by releasing immunosuppressive molecules and altering the bone marrow microenvironment. DCs, NKs, and CTLs also contribute significantly to immune regulation in AML, with impaired DC function, suppressed NK activity, and reduced CTL antitumor capacity closely linked to drug resistance. Moreover, myeloid-derived suppressor cells exacerbate immune suppression by secreting metabolic inhibitory molecules and increasing Treg activity. We also summarize recent advances in immunotherapy, including ICIs, CAR-T and CAR-NK cell therapies, and treatments targeting AML-specific antigens, all of which have potential in enhancing immune function and overcoming drug resistance. We emphasize the need for future research to optimize immunotherapy protocols, integrate chemotherapy and other treatments, improve patient outcomes and increase survival rates.

## Author contributions

MZ and WJL designed, wrote, illustrated, and revised the manuscript. YY and JL contributed to the revision of the graphics, while LG and QLG collected and sorted the data. All authors contributed to the article and approved the submitted version.

## Funding

The author(s) declare financial support was received for the research, authorship, and/or publication of this article. This work received support from the Sichuan Science and Technology Program (2024YFFK0271), Luzhou Science and Technology Bureau (2024LZXNYDJ102), Southwest Medical University (2024LCYXZX10).

## Conflict of interest

The author(s) declared no potential conflicts of interest with respect to the research, authorship, and/or publication of this article.

# References


1. Niu J, Peng D, Liu L. Drug resistance mechanisms of acute myeloid leukemia stem cells. *Front Oncol* (2022) **12**:896426. doi:10.3389/fonc.2022.896426

2. Shapoorian H, Zalpoor H, Ganjalikhani-Hakemi M. The correlation between Flt3-ITD mutation in dendritic cells with TIM-3 expression in acute myeloid leukemia. *Blood Science Baltimore, Md* (2021) **3**(4):132–5. doi:10.1097/bs9.0000000000000092

3. Conneely SE, Stevens AM. Acute myeloid leukemia in children: emerging paradigms in genetics and new approaches to therapy. *Curr Oncol Rep* (2021) **23**(2):16. doi:10.1007/s11912-020-01009-3

4. Buckley SA, Kirtane K, Walter RB, Lee SJ, Lyman GH. Patient-reported outcomes in acute myeloid leukemia: where are we now? *Blood Rev* (2018) **32**(1):81–7. doi:10.1016/j.blre.2017.08.010

5. Song Y, Wang N, Chen L, Fang L. Tr1 cells as a key regulator for maintaining immune homeostasis in transplantation. *Front Immunol* (2021) **12**:671579. doi:10.3389/fimmu.2021.671579

6. Carrier Y, Yuan J, Kuchroo VK, Weiner HL. Th3 cells in peripheral tolerance. I. Induction of foxp3-positive regulatory T cells by Th3 cells derived from TGF-β T cell-transgenic mice. *The J Immunol* (2007) **178**(1):179–85. doi:10.4049/jimmunol.178.1.179

7. Davidson TS, DiPaolo RJ, Andersson J, Shevach EM. Cutting edge: IL-2 is essential for TGF-β-mediated induction of Foxp3+ T regulatory cells. *The J Immunol* (2007) **178**(7):4022–6. doi:10.4049/jimmunol.178.7.4022

8. Wang W, Hong T, Wang X, Wang R, Du Y, Gao Q, et al. Newly found peacekeeper: potential of CD8+ Tregs for graft-versus-host disease. *Front Immunol* (2021) **12**:764786. doi:10.3389/fimmu.2021.764786

9. Ford MS, Zhang ZX, Chen W, Zhang L. Double-negative T regulatory cells can develop outside the thymus and do not mature from CD8+ T cell precursors. *The J Immunol* (2006) **177**(5):2803–9. doi:10.4049/jimmunol.177.5.2803

10. Thomson CW, Lee BP, Zhang L. Double-negative regulatory T cells: non-conventional regulators. *Immunologic Res* (2006) **35**(1-2):163–78. doi:10.1385/ir:35:1:163

11. Su Y, Huang X, Wang S, Min WP, Yin Z, Jevnikar AM, et al. Double negative Treg cells promote nonmyeloablative bone marrow chimerism by inducing T-cell clonal deletion and suppressing NK cell function. *Eur J Immunol* (2012) **42**(5):1216–25. doi:10.1002/eji.201141808

12. McIver Z, Wlodarski M, Powers J, O'Keefe C, Jin T, Sobecks R, et al. Double negative T cells influence TCR VB variablity to induce allotolerance. *Blood* (2006) **108**(11):759–9. doi:10.1182/blood.v108.11.759.759

13. Ford McIntyre MS, Gao JF, Li X, Naeini BM, Zhang L. Consequences of double negative regulatory T cell and antigen presenting cell interaction on immune response suppression. *Int immunopharmacology* (2011) **11**(5):597–603. doi:10.1016/j.intimp.2010.11.015

14. Achita P, Dervovic D, Ly D, Lee JB, Haug T, Joe B, et al. Infusion of *ex-vivo* expanded human TCR-αβ+ double-negative regulatory T cells delays onset of xenogeneic graft-versus-host disease. *Clin Exp Immunol* (2018) **193**(3):386–99. doi:10.1111/cei.13145

15. Ono M. Control of regulatory T-cell differentiation and function by T-cell receptor signalling and Foxp3 transcription factor complexes. *Immunology* (2020) **160**(1):24–37. doi:10.1111/imm.13178

16. Zhang Y, Maksimovic J, Naselli G, Qian J, Chopin M, Blewitt ME, et al. Genome-wide DNA methylation analysis identifies hypomethylated genes regulated by FOXP3 in human regulatory T cells. *Blood* (2013) **122**(16):2823–36. doi:10.1182/blood-2013-02-481788

17. Szczepanski MJ, Szajnik M, Czystowska M, Mandapathil M, Strauss L, Welsh A, et al. Increased frequency and suppression by regulatory T cells in patients with acute myelogenous leukemia. *Clin Cancer Res* (2009) **15**(10):3325–32. doi:10.1158/1078-0432.ccr-08-3010

18. Yang PX, Wang P, Fang L, Wang Q. Expression of Tregs and IL-35 in peripheral blood of patients with newly diagnosed acute myeloid leukemia. *Zhongguo shi yan xue ye xue za zhi* (2022) **30**(6):1688–92. doi:10.19746/j.cnki.issn.1009-2137.2022.06.010

19. Ahmed HA, Maklad AM, Khaled SA, Elyamany A. Interleukin-27 and interleukin-35 in *de novo* acute myeloid leukemia: expression and significance as biological markers. *J Blood Med* (2019) **10**:341–9. doi:10.2147/jbm.s221301

20. Wang J, Tao Q, Wang H, Wang Z, Wu F, Pan Y, et al. Elevated IL-35 in bone marrow of the patients with acute myeloid leukemia. *Hum Immunol* (2015) **76**(9):681–6. doi:10.1016/j.humimm.2015.09.020

21. Chen W, Jin W, Hardegen N, Lei KJ, Li L, Marinos N, et al. Conversion of peripheral CD4+CD25− naive T cells to CD4+CD25+ regulatory T cells by TGF-β induction of transcription factor *Foxp3*. *The J Exp Med* (2003) **198**(12):1875–86. doi:10.1084/jem.20030152

22. Tao Q, Pan Y, Wang Y, Wang H, Xiong S, Li Q, et al. Regulatory T cells-derived IL-35 promotes the growth of adult acute myeloid leukemia blasts. *Int J Cancer* (2015) **137**(10):2384–93. doi:10.1002/ijc.29563

23. Shenghui Z, Yixiang H, Jianbo W, Kang Y, Laixi B, Yan Z, et al. Elevated frequencies of $CD4^+CD25^+CD127^{lo}$ regulatory T cells is associated to poor prognosis in patients with acute myeloid leukemia. *Int J Cancer* (2011) **129**(6):1373–81. doi:10.1002/ijc.25791

24. Tan J, Chen S, Xu L, Lu S, Zhang Y, Chen J, et al. Increasing frequency of T cell immunosuppressive receptor expression in CD4+ and CD8+ T cells may related to T cell exhaustion and immunosuppression in patients with AML. *Blood* (2016) **128**(22):5166–6. doi:10.1182/blood.v128.22.5166.5166

25. Sanchez-Correa B, Bergua JM, Campos C, Gayoso I, Arcos MJ, Bañas H, et al. Cytokine profiles in acute myeloid leukemia patients at diagnosis: survival is inversely correlated with IL-6 and directly correlated with IL-10 levels. *Cytokine* (2013) **61**(3):885–91. doi:10.1016/j.cyto.2012.12.023

26. Rashed R, Shafik RE, Shafik NF, Shafik HE. Associations of interleukin-10 gene polymorphisms with acute myeloid leukemia in human (Egypt). *J Cancer Res Ther* (2018) **14**(5):1083–6. doi:10.4103/0973-1482.187367

27. Boyiadzis M, Szczepanski M, Whiteside T. Membrane associated TGF-β1 on leukemia blast-derived microvesicles in sera of acute myeloid leukemia patients suppresses NK cell function. *Blood* (2010) **116**(21):502–2. doi:10.1182/blood.v116.21.502.502

28. Zhang Q, Huang T, Li X, Liu G, Xian L, Mao X, et al. Prognostic impact of enhanced CD96 expression on NK cells by TGF-β1 in AML. *Int immunopharmacology* (2024) **141**:112958. doi:10.1016/j.intimp.2024.112958

29. Reichelt P, Bernhart S, Wilke F, Schwind S, Cross M, Platzbecker U, et al. MicroRNA expression patterns reveal a role of the TGF-β family signaling in AML chemo-resistance. *Cancers* (2023) **15**(20):5086. doi:10.3390/cancers15205086

30. Wang D, Sun Z, Zhu X, Zheng X, Zhou Y, Lu Y, et al. GARP-mediated active TGF-β1 induces bone marrow NK cell dysfunction in AML patients with early relapse post–allo-HSCT. *Blood* (2022) **140**(26):2788–804. doi:10.1182/blood.2022015474

31. Han S, Wang W, Wang S, Yang T, Zhang G, Wang D, et al. Tumor microenvironment remodeling and tumor therapy based on M2-like tumor associated macrophage-targeting nano-complexes. *Theranostics* (2021) **11**(6):2892–916. doi:10.7150/thno.50928

32. Au Q, Hanifi A, Parnell E, Kuo J, Leones E, Sahafi F, et al. Phenotypic characterization of the immune landscape in the bone marrow of patients with acute myeloid leukemia (AML) using MultiOmyxTM hyperplexed immunofluorescence assay. *Blood* (2019) **134**(Suppl. 1):1455–5. doi:10.1182/blood-2019-122206

33. Bachanova V, Cooley S, Defor TE, Verneris MR, Zhang B, McKenna DH, et al. Clearance of acute myeloid leukemia by haploidentical natural killer cells is improved using IL-2 diphtheria toxin fusion protein. *Blood* (2014) **123**(25):3855–63. doi:10.1182/blood-2013-10-532531

34. Cooley S, Bachanova V, Geller M, Verneris M, Zhang B, McCullar V, et al. IL-2 stimulated treg inhibit *in vitro* expansion of haploidentical natural killer (NK) cells, which is partially overcome with an IL-2-diphtheria toxin fusion protein *in vivo*. *Blood* (2011) **118**(21):3611–1. doi:10.1182/blood.v118.21.3611.3611

35. Frimpong-Boateng K, van Rooijen N, Geiben-Lynn R. Regulatory T cells suppress natural killer cells during plasmid DNA vaccination in mice, blunting the CD8+ T cell immune response by the cytokine TGFβ. *PloS one* (2010) **5**(8):e12281. doi:10.1371/journal.pone.0012281

36. Qureshi OS, Zheng Y, Nakamura K, Attridge K, Manzotti C, Schmidt EM, et al. Trans-endocytosis of CD80 and CD86: a molecular basis for the cell-extrinsic function of CTLA-4. *Science* (2011) **332**(6029):600–3. doi:10.1126/science.1202947

37. Radwan SM, Elleboudy NS, Nabih NA, Kamal AM. The immune checkpoints Cytotoxic T lymphocyte antigen-4 and Lymphocyte activation gene-3 expression is up-regulated in acute myeloid leukemia. *Hla* (2020) **96**(1):3–12. doi:10.1111/tan.13872

38. El Dosoky W, Aref S, El Menshawy N, Ramez A, Abou Zaid T, Aref M, et al. Prognostic effect of CTLA4/LAG3 expression by T-cells subsets on acute myeloid leukemia patients. *Asian Pac J Cancer Prev* (2024) **25**(5):1777–85. doi:10.31557/apjcp.2024.25.5.1777

39. Ramzi M, Iravani Saadi M, Yaghobi R, Arandi N. Dysregulated expression of CD28 and CTLA-4 molecules in patients with acute myeloid leukemia and possible association with development of graft versus host disease after hematopoietic stem cell transplantation. *Int J Organ Transplant Med* (2019) **10**(2):84–90.

40. Davids MS, Kim HT, Bachireddy P, Costello C, Liguori R, Savell A, et al. Ipilimumab for patients with relapse after allogeneic transplantation. *New Engl J Med* (2016) **375**(2):143–53. doi:10.1056/nejmoa1601202

41. Dong Y, Han Y, Huang Y, Jiang S, Huang Z, Chen R, et al. PD-L1 is expressed and promotes the expansion of regulatory T cells in acute myeloid leukemia. *Front Immunol* (2020) **11**:1710. doi:10.3389/fimmu.2020.01710

42. Davis KL, Agarwal AM, Verma AR. Checkpoint inhibition in pediatric hematologic malignancies. *Pediatr Hematol Oncol* (2017) **34**(6-7):379–94. doi:10.1080/08880018.2017.1383542

43. Chen C, Liang C, Wang S, Chio CL, Zhang Y, Zeng C, et al. Expression patterns of immune checkpoints in acute myeloid leukemia. *J Hematol and Oncol* (2020) **13**(1):28. doi:10.1186/s13045-020-00853-x

44. Zhang Y, Huang Y, Hong Y, Lin Z, Zha J, Zhu Y, et al. Lactate acid promotes PD-1+ Tregs accumulation in the bone marrow with high tumor burden of Acute myeloid leukemia. *Int immunopharmacology* (2024) **130**:111765. doi:10.1016/j.intimp.2024.111765

45. Joller N, Lozano E, Burkett PR, Patel B, Xiao S, Zhu C, et al. Treg cells expressing the coinhibitory molecule TIGIT selectively inhibit proinflammatory Th1 and Th17 cell responses. *Immunity* (2014) **40**(4):569–81. doi:10.1016/j.immuni.2014.02.012

46. Triebel F, Jitsukawa S, Baixeras E, Roman-Roman S, Genevee C, Viegas-Pequignot E, et al. LAG-3, a novel lymphocyte activation gene closely related to CD4. *The J Exp Med* (1990) **171**(5):1393–405. doi:10.1084/jem.171.5.1393

47. Anderson AC, Joller N, Kuchroo VK. Lag-3, tim-3, and TIGIT: Co-inhibitory receptors with specialized functions in immune regulation. *Immunity* (2016) **44**(5):989–1004. doi:10.1016/j.immuni.2016.05.001

48. Liang B, Workman C, Lee J, Chew C, Dale BM, Colonna L, et al. Regulatory T cells inhibit dendritic cells by lymphocyte activation gene-3 engagement of MHC class II. *The J Immunol* (2008) **180**(9):5916–26. doi:10.4049/jimmunol.180.9.5916

49. Maruhashi T, Sugiura D, Okazaki IM, Shimizu K, Maeda TK, Ikubo J, et al. Binding of LAG-3 to stable peptide-MHC class II limits T cell function and suppresses autoimmunity and anti-cancer immunity. *Immunity* (2022) **55**(5):912–24.e8. doi:10.1016/j.immuni.2022.03.013

50. Wang J, Sanmamed MF, Datar I, Su TT, Ji L, Sun J, et al. Fibrinogen-like protein 1 is a major immune inhibitory ligand of LAG-3. *Cell* (2019) **176**(1-2):334–47.e12. doi:10.1016/j.cell.2018.11.010

51. Abdelhakim H, Dunavin N, Li M, Braun M, Elkhanany A, Lin T, et al. LAG3 promotes acute myeloid leukemia-induced immune suppression. *Blood* (2018) **132**(Suppl. 1):2414–4. doi:10.1182/blood-2018-99-117784

52. Gautron AS, Dominguez-Villar M, de Marcken M, Hafler DA. Enhanced suppressor function of TIM-3+ FoxP3+ regulatory T cells. *Eur J Immunol* (2014) **44**(9):2703–11. doi:10.1002/eji.201344392

53. Dama P, Tang M, Fulton N, Kline J, Liu H. Gal9/Tim-3 expression level is higher in AML patients who fail chemotherapy. *J Immunother Cancer* (2019) **7**(1):175. doi:10.1186/s40425-019-0611-3

54. Alqahtani M, Aljuaimlani A, Al-Tamimi J, Alomar S, Mansour L. TIM3 and CTLA4 immune checkpoint polymorphisms are associated with acute myeloid leukemia in Saudi Arabia. *Hematology* (2024) **29**(1):2329024. doi:10.1080/16078454.2024.2329024

55. Daver N, Garcia-Manero G, Basu S, Boddu PC, Alfayez M, Cortes JE, et al. Efficacy, safety, and biomarkers of response to azacitidine and nivolumab in relapsed/refractory acute myeloid leukemia: a nonrandomized, open-label, phase II study. *Cancer Discov* (2019) **9**(3):370–83. doi:10.1158/2159-8290.cd-18-0774

56. Gojo I, Stuart R, Webster J, Blackford A, Varela J, Morrow J, et al. Multi-center phase 2 study of pembroluzimab (pembro) and azacitidine (AZA) in patients with relapsed/refractory acute myeloid leukemia (AML) and in newly diagnosed (≥65 Years) AML patients. *Blood* (2019) **134**(Suppl. 1):832–2. doi:10.1182/blood-2019-127345

57. Chien KS, Kim K, Nogueras-Gonzalez GM, Borthakur G, Naqvi K, Daver NG, et al. Phase II study of azacitidine with pembrolizumab in patients with intermediate-1 or higher-risk myelodysplastic syndrome. *Br J Haematol* (2021) **195**(3):378–87. doi:10.1111/bjh.17689

58. Yang H, Bueso-Ramos C, DiNardo C, Estecio MR, Davanlou M, Geng QR, et al. Expression of PD-L1, PD-L2, PD-1 and CTLA4 in myelodysplastic syndromes is enhanced by treatment with hypomethylating agents. *Leukemia* (2014) **28**(6):1280–8. doi:10.1038/leu.2013.355

59. Zeidner JF, Vincent BG, Ivanova A, Moore D, McKinnon KP, Wilkinson AD, et al. Phase II trial of pembrolizumab after high-dose cytarabine in relapsed/refractory acute myeloid leukemia. *Blood Cancer Discov* (2021) **2**(6):616–29. doi:10.1158/2643-3230.bcd-21-0070

60. Daver N, Garcia-Manero G, Konopleva M, Alfayez M, Pemmaraju N, Kadia T, et al. Azacitidine (aza) with nivolumab (nivo), and aza with nivo + ipilimumab (ipi) in relapsed/refractory acute myeloid leukemia: a non-randomized, prospective, phase 2 study. *Blood* (2019) **134**(Suppl. 1):830–0. doi:10.1182/blood-2019-131494

61. Oran B, Garcia-Manero G, Saliba R, Alatrash G, Jabbour E, Popat U, et al. Post allogeneic stem cell transplant (SCT) cyclophosphamide improves progression free survival (PFS) in pts with AML/MDS treated with CTLA-4 or PD-1 blockade prior to SCT. *Blood* (2018) **132**(Suppl. 1):483–3. doi:10.1182/blood-2018-99-115382

62. Zheng H, Mineishi S, Claxton D, Zhu J, Zhao C, Jia B, et al. A phase I clinical trial of avelumab in combination with decitabine as first line treatment of unfit patients with acute myeloid leukemia. *Am J Hematol* (2021) **96**(2):E46–e50. doi:10.1002/ajh.26043

63. Gerds AT, Scott BL, Greenberg P, Lin TL, Pollyea DA, Verma A, et al. Atezolizumab alone or in combination did not demonstrate a favorable risk-benefit profile in myelodysplastic syndrome. *Blood Adv* (2022) **6**(4):1152–61. doi:10.1182/bloodadvances.2021005240

64. Zhong RK, Loken M, Lane TA, Ball ED. CTLA-4 blockade by a human MAb enhances the capacity of AML-derived DC to induce T-cell responses against AML cells in an autologous culture system. *Cytotherapy* (2006) **8**(1):3–12. doi:10.1080/14653240500499507

65. Jones B, Liu C, Swiecki M, Strake B, Chi E, Bansal-Pakala P. An agonist TIGIT mab suppresses regulatory T cell activity via an IL-2-mediated mechanism. *The J Immunol* (2019) **202**(1_Suppl. e):57.9. doi:10.4049/jimmunol.202.supp.57.9

66. Kong Y, Zhu L, Schell TD, Zhang J, Claxton DF, Ehmann WC, et al. T-cell immunoglobulin and ITIM domain (TIGIT) associates with CD8+ T-cell exhaustion and poor clinical outcome in AML patients. *Clin Cancer Res* (2016) **22**(12):3057–66. doi:10.1158/1078-0432.ccr-15-2626

67. Yamamoto N, Koyama T, Sato J, Yoshida T, Sudo K, Iwasa S, et al. Phase I study of the anti-TIGIT antibody tiragolumab in combination with atezolizumab in Japanese patients with advanced or metastatic solid tumors. *Cancer Chemother Pharmacol* (2024) **94**(1):109–15. doi:10.1007/s00280-023-04627-3

68. Schwartz S, Patel N, Longmire T, Jayaraman P, Jiang X, Lu H, et al. Characterization of sabatolimab, a novel immunotherapy with immuno-myeloid activity directed against TIM-3 receptor. *Immunother Adv* (2022) **2**(1):ltac019. doi:10.1093/immadv/ltac019

69. Sordo-Bahamonde C, Lorenzo-Herrero S, González-Rodríguez AP, Payer Á, González-García E, López-Soto A, et al. LAG-3 blockade with relatlimab (BMS-986016) restores anti-leukemic responses in chronic lymphocytic leukemia. *Cancers* (2021) **13**(9):2112. doi:10.3390/cancers13092112

70. Han Y, Dong Y, Yang Q, Xu W, Jiang S, Yu Z, et al. Acute myeloid leukemia cells express ICOS ligand to promote the expansion of regulatory T cells. *Front Immunol* (2018) **9**:2227. doi:10.3389/fimmu.2018.02227

71. Pan S, Cai Q, Wei Y, Tang H, Zhang Y, Zhou W, et al. Increased co-expression of ICOS and PD-1 predicts poor overall survival in patients with acute myeloid leukemia. *Immunobiology* (2024) **229**(3):152804. doi:10.1016/j.imbio.2024.152804

72. Wan Y, Zhang C, Xu Y, Wang M, Rao Q, Xing H, et al. Hyperfunction of CD4 CD25 regulatory T cells in *de novo* acute myeloid leukemia. *BMC cancer* (2020) **20**(1):472. doi:10.1186/s12885-020-06961-8

73. Wang R, Feng W, Wang H, Wang L, Yang X, Yang F, et al. Blocking migration of regulatory T cells to leukemic hematopoietic microenvironment delays disease progression in mouse leukemia model. *Cancer Lett* (2020) **469**:151–61. doi:10.1016/j.canlet.2019.10.032

74. Modak RV, de Oliveira Rebola KG, McClatchy J, Mohammadhosseini M, Damnernsawad A, Kurtz SE, et al. Targeting CCL2/CCR2 signaling overcomes MEK inhibitor resistance in acute myeloid leukemia. *Clin Cancer Res* (2024) **30**(10):2245–59. doi:10.1158/1078-0432.ccr-23-2654

75. Zhu B, Pan S, Liu J, Wang S, Ni Y, Xiao L, et al. HIF-1α forms regulatory loop with YAP to coordinate hypoxia-induced adriamycin resistance in acute myeloid leukemia cells. *Cell Biol Int* (2020) **44**(2):456–66. doi:10.1002/cbin.11246

76. Miska J, Lee-Chang C, Rashidi A, Muroski ME, Chang AL, Lopez-Rosas A, et al. HIF-1α is a metabolic switch between glycolytic-driven migration and oxidative phosphorylation-driven immunosuppression of Tregs in glioblastoma. *Cell Rep* (2022) **39**(10):110934. doi:10.1016/j.celrep.2022.110934

77. Amin AH, Sharifi LMA, Kakhharov AJ, Opulencia MJC, Alsaikhan F, Bokov DO, et al. Role of Acute Myeloid Leukemia (AML)-Derived exosomes in tumor progression and survival. *Biomed and Pharmacother* (2022) **150**:113009. doi:10.1016/j.biopha.2022.113009

78. Chen T, Zhang G, Kong L, Xu S, Wang Y, Dong M. Leukemia-derived exosomes induced IL-8 production in bone marrow stromal cells to protect the leukemia cells against chemotherapy. *Life Sci* (2019) **221**:187–95. doi:10.1016/j.lfs.2019.02.003

79. Hong CS, Sharma P, Yerneni SS, Simms P, Jackson EK, Whiteside TL, et al. Circulating exosomes carrying an immunosuppressive cargo interfere with cellular immunotherapy in acute myeloid leukemia. *Scientific Rep* (2017) **7**(1):14684. doi:10.1038/s41598-017-14661-w

80. Norsworthy KJ, Ko CW, Lee JE, Liu J, John CS, Przepiorka D, et al. FDA approval summary: mylotarg for treatment of patients with relapsed or refractory CD33-positive acute myeloid leukemia. *The Oncologist* (2018) **23**(9):1103–8. doi:10.1634/theoncologist.2017-0604

81. Jen EY, Ko CW, Lee JE, Del Valle PL, Aydanian A, Jewell C, et al. FDA approval: gemtuzumab ozogamicin for the treatment of adults with newly diagnosed CD33-positive acute myeloid leukemia. *Clin Cancer Res* (2018) **24**(14):3242–6. doi:10.1158/1078-0432.ccr-17-3179

82. Wei A, Fong C, Montesinos P, Calbacho M, Gil J, Perez De Oteyza J, et al. A phase 1 study of flotetuzumab, a CD123 x CD3 DART® protein, combined with MGA012, an anti-PD-1 antibody, in patients with relapsed or refractory acute myeloid leukemia. *Blood* (2019) **134**(Suppl. 1):2662–2. doi:10.1182/blood-2019-125966

83. Daver N, Montesinos P, DeAngelo D, Wang E, Todisco E, Tarella C, et al. A phase I/II study of IMGN632, a novel CD123-targeting antibody-drug conjugate, in patients with relapsed/refractory acute myeloid leukemia, blastic plasmacytoid dendritic cell neoplasm, and other CD123-positive hematologic malignancies. *J Clin Oncol* (2020) **38**(15_Suppl. l):Tps7563–tps63. doi:10.1200/jco.2020.38.15_suppl.tps7563

84. Tahk S, Vick B, Hiller B, Schmitt S, Marcinek A, Perini ED, et al. SIRPα-αCD123 fusion antibodies targeting CD123 in conjunction with CD47 blockade enhance the clearance of AML-initiating cells. *J Hematol and Oncol* (2021) **14**(1):155. doi:10.1186/s13045-021-01163-6

85. Wilson NR, Bover L, Konopleva M, Han L, Neelapu S, Pemmaraju N. CD303 (BDCA-2) - a potential novel target for therapy in hematologic malignancies. *Leuk and Lymphoma* (2022) **63**(1):19–30. doi:10.1080/10428194.2021.1975192

86. Xiao W, Chan A, Waarts MR, Mishra T, Liu Y, Cai SF, et al. Plasmacytoid dendritic cell expansion defines a distinct subset of RUNX1-mutated acute myeloid leukemia. *Blood* (2021) **137**(10):1377–91. doi:10.1182/blood.2020007897

87. Zhu L, Wang P, Zhang W, Li Q, Xiong J, Li J, et al. Plasmacytoid dendritic cell infiltration in acute myeloid leukemia. *Cancer Manag Res* (2020) **12**:11411–9. doi:10.2147/cmar.s260825

88. Ocadlikova D, Casella S, Pintao I, Adinolfi E, Sangaletti S, De Marchi E, et al. Mechanisms of tolerance induction through T regulatory cells during chemotherapy-mediated immunogenic cell death in acute myeloid leukemia. *Blood* (2019) **134**(Suppl. 1):2332–2. doi:10.1182/blood-2019-126478

89. Parisi S, Trabanelli S, Ocadlikova D, Paolini S, Papayannidis C, Ottaviani E, et al. Indoleamine 2,3-dioxygenase (Ido) is associated with high incidence of chemorefractory disease in acute myeloid leukemia (AML) patients. *Blood* (2012) **120**(21):4787–7. doi:10.1182/blood.v120.21.4787.4787

90. Sarangi P. Role of indoleamine 2, 3-dioxygenase 1 in immunosuppression of breast cancer. *Cancer Pathogenesis Ther* (2024) **2**(4):246–55. doi:10.1016/j.cpt.2023.11.001

91. Chamuleau ME, van de Loosdrecht AA, Hess CJ, Janssen JJ, Zevenbergen A, Delwel R, et al. High INDO (indoleamine 2,3-dioxygenase) mRNA level in blasts of acute myeloid leukemic patients predicts poor clinical outcome. *Haematologica* (2008) **93**(12):1894–8. doi:10.3324/haematol.13113

92. Schmidt A, Oberle N, Krammer PH. Molecular mechanisms of treg-mediated T cell suppression. *Front Immunol* (2012) **3**:51. doi:10.3389/fimmu.2012.00051

93. Onishi Y, Fehervari Z, Yamaguchi T, Sakaguchi S. Foxp3+ natural regulatory T cells preferentially form aggregates on dendritic cells *in vitro* and actively inhibit their maturation. *Proc Natl Acad Sci* (2008) **105**(29):10113–8. doi:10.1073/pnas.0711106105

94. Wilson KR, Villadangos JA, Mintern JD. Dendritic cell Flt3 - regulation, roles and repercussions for immunotherapy. *Immunol and Cell Biol* (2021) **99**(9):962–71. doi:10.1111/imcb.12484

95. Yamamoto Y, Kiyoi H, Nakano Y, Suzuki R, Kodera Y, Miyawaki S, et al. Activating mutation of D835 within the activation loop of FLT3 in human hematologic malignancies. *Blood* (2001) **97**(8):2434–9. doi:10.1182/blood.v97.8.2434

96. Vacchelli E, Vitale I, Eggermont A, Fridman WH, Fučíková J, Cremer I, et al. Trial watch: dendritic cell-based interventions for cancer therapy. *Oncoimmunology* (2013) **2**(10):e25771. doi:10.4161/onci.25771

97. Zhang L, Xu Y, Shen J, He F, Zhang D, Chen Z, et al. Feasibility study of DCs/CIKs combined with thoracic radiotherapy for patients with locally advanced or metastatic non-small-cell lung cancer. *Radiat Oncol (London, England)* (2016) **11**:60. doi:10.1186/s13014-016-0635-5

98. Yanagisawa R, Koizumi T, Koya T, Sano K, Koido S, Nagai K, et al. WT1-pulsed dendritic cell vaccine combined with chemotherapy for resected pancreatic cancer in a phase I study. *Anticancer Res* (2018) **38**(4):2217–25. doi:10.21873/anticanres.12464

99. Pepeldjiyska E, Li L, Gao J, Seidel CL, Blasi C, Özkaya E, et al. Leukemia derived dendritic cell (DCleu) mediated immune response goes along with reduced (leukemia-specific) regulatory T-cells. *Immunobiology* (2022) **227**(4):152237. doi:10.1016/j.imbio.2022.152237

100. Huntington ND, Cursons J, Rautela J. The cancer-natural killer cell immunity cycle. *Nat Rev Cancer* (2020) **20**(8):437–54. doi:10.1038/s41568-020-0272-z

101. Yang L, Feng Y, Wang S, Jiang S, Tao L, Li J, et al. Siglec-7 is an indicator of natural killer cell function in acute myeloid leukemia. *Int immunopharmacology* (2021) **99**:107965. doi:10.1016/j.intimp.2021.107965

102. Djaoud Z, Parham P. HLAs, TCRs, and KIRs, a triumvirate of human cell-mediated immunity. *Annu Rev Biochem* (2020) **89**:717–39. doi:10.1146/annurev-biochem-011520-102754

103. Schetelig J, Baldauf H, Heidenreich F, Massalski C, Frank S, Sauter J, et al. External validation of models for KIR2DS1/KIR3DL1-informed selection of hematopoietic cell donors fails. *Blood* (2020) **135**(16):1386–95. doi:10.1182/blood.2019002887

104. Cianga VA, Campos Catafal L, Cianga P, Pavel Tanasa M, Cherry M, Collet P, et al. Natural killer cell subpopulations and inhibitory receptor dynamics in myelodysplastic syndromes and acute myeloid leukemia. *Front Immunol* (2021) **12**:665541. doi:10.3389/fimmu.2021.665541

105. Dai YJ, He SY, Hu F, Li XP, Zhang JM, Chen SL, et al. Bone marrow infiltrated natural killer cells predicted the anti-leukemia activity of MCL1 or BCL2 inhibitors in acute myeloid leukemia. *Mol Cancer* (2021) **20**(1):8. doi:10.1186/s12943-020-01302-6

106. Liu L, Chen X, Jin HM, Zhao SS, Zhu Y, Qian SX, et al. The expression and function of NK cells in patients with acute myeloid leukemia. *Zhongguo shi yan xue ye xue za zhi* (2022) **30**(1):49–55. doi:10.19746/j.cnki.issn.1009-2137.2022.01.009

107. Russick J, Torset C, Hemery E, Cremer I. NK cells in the tumor microenvironment: prognostic and theranostic impact. Recent advances and trends. *Semin Immunol* (2020) **48**:101407. doi:10.1016/j.smim.2020.101407

108. Kaweme NM, Zhou F. Optimizing NK cell-based immunotherapy in myeloid leukemia: abrogating an immunosuppressive microenvironment. *Front Immunol* (2021) **12**:683381. doi:10.3389/fimmu.2021.683381

109. Zhang T, Fang Q, Liu P, Wang P, Feng C, Wang J. Heme oxygenase 1 overexpression induces immune evasion of acute myeloid leukemia against natural killer cells by inhibiting CD48. *J translational Med* (2022) **20**(1):394. doi:10.1186/s12967-022-03589-z

110. Chajuwan T, Kansuwan P, Kobbuaklee S, Chanswangphuwana C. Characteristics and clinical correlation of TIM-3 and PD-1/PD-L1 expressions in leukemic cells and tumor microenvironment in newly diagnosed acute myeloid leukemia. *Leuk and Lymphoma* (2022) **63**(2):450–6. doi:10.1080/10428194.2021.1984454

111. Bou-Tayeh B, Laletin V, Salem N, Just-Landi S, Fares J, Leblanc R, et al. Chronic IL-15 stimulation and impaired mTOR signaling and metabolism in natural killer cells during acute myeloid leukemia. *Front Immunol* (2021) **12**:730970. doi:10.3389/fimmu.2021.730970

112. Baragaño Raneros A, Martín-Palanco V, Fernandez AF, Rodriguez RM, Fraga MF, Lopez-Larrea C, et al. Methylation of NKG2D ligands contributes to immune system evasion in acute myeloid leukemia. *Genes Immun* (2015) **16**(1):71–82. doi:10.1038/gene.2014.58

113. Belizário JE, Neyra JM, Setúbal Destro Rodrigues MF. When and how NK cell-induced programmed cell death benefits immunological protection against intracellular pathogen infection. *Innate Immun* (2018) **24**(8):452–65. doi:10.1177/1753425918800200

114. Zhang Q, Bi J, Zheng X, Chen Y, Wang H, Wu W, et al. Blockade of the checkpoint receptor TIGIT prevents NK cell exhaustion and elicits potent anti-tumor immunity. *Nat Immunol* (2018) **19**(7):723–32. doi:10.1038/s41590-018-0132-0

115. Wang M, Bu J, Zhou M, Sido J, Lin Y, Liu G, et al. CD8+T cells expressing both PD-1 and TIGIT but not CD226 are dysfunctional in acute myeloid leukemia (AML) patients. *Clin Immunol* (2018) **190**:64–73. doi:10.1016/j.clim.2017.08.021

116. Coles SJ, Wang EC, Man S, Hills RK, Burnett AK, Tonks A, et al. CD200 expression suppresses natural killer cell function and directly inhibits patient anti-tumor response in acute myeloid leukemia. *Leukemia* (2011) **25**(5):792–9. doi:10.1038/leu.2011.1

117. Tonks A, Hills R, White P, Rosie B, Mills KI, Burnett AK, et al. CD200 as a prognostic factor in acute myeloid leukaemia. *Leukemia* (2007) **21**(3):566–8. doi:10.1038/sj.leu.2404559

118. Xiao Y, Chen J, Wang J, Guan W, Wang M, Zhang L, et al. Acute myeloid leukemia epigenetic immune escape from nature killer cells by ICAM-1. *Front Oncol* (2021) **11**:751834. doi:10.3389/fonc.2021.751834

119. Wang Z, Xiao Y, Guan W, Wang M, Chen J, Zhang L, et al. Acute myeloid leukemia immune escape by epigenetic CD48 silencing. *Clin Sci* (2020) **134**(2):261–71. doi:10.1042/cs20191170

120. Ewen EM, Pahl JHW, Miller M, Watzl C, Cerwenka A. KIR downregulation by IL-12/15/18 unleashes human NK cells from KIR/HLA-I inhibition and enhances killing of tumor cells. *Eur J Immunol* (2018) **48**(2):355–65. doi:10.1002/eji.201747128

121. Satwani P, van de Ven C, Ayello J, Cairo D, Simpson LL, Baxi L, et al. Interleukin (IL)-15 in combination with IL-2, fms-like tyrosine kinase-3 ligand and anti-CD3 significantly enhances umbilical cord blood natural killer (NK) cell and NK-cell subset expansion and NK function. *Cytotherapy* (2011) **13**(6):730–8. doi:10.3109/14653249.2011.563292

122. Wang QS, Wang Y, Lv HY, Han QW, Fan H, Guo B, et al. Treatment of CD33-directed chimeric antigen receptor-modified T cells in one patient with relapsed and refractory acute myeloid leukemia. *Mol Ther* (2015) **23**(1):184–91. doi:10.1038/mt.2014.164

123. Yao S, Jianlin C, Yarong L, Botao L, Qinghan W, Hongliang F, et al. Donor-derived cd123-targeted CAR T cell serves as a RIC regimen for haploidentical transplantation in a patient with FUS-ERG+ AML. *Front Oncol* (2019) **9**:1358. doi:10.3389/fonc.2019.01358

124. You L, Han Q, Zhu L, Zhu Y, Bao C, Yang C, et al. Decitabine-mediated epigenetic reprograming enhances anti-leukemia efficacy of cd123-targeted chimeric antigen receptor T-cells. *Front Immunol* (2020) **11**:1787. doi:10.3389/fimmu.2020.01787

125. Raulet DH, Gasser S, Gowen BG, Deng W, Jung H. Regulation of ligands for the NKG2D activating receptor. *Annu Rev Immunol* (2013) **31**:413–41. doi:10.1146/annurev-immunol-032712-095951

126. Sallman D, Al-Homsi A, Davila M, Kerre T, Moors I, Poire X, et al. Results from the phase I clinical studies evaluating cyad-01, a first-generation NKG2D CAR T-cell product in relapsed or refractory acute myeloid leukemia and myelodysplastic syndrome patients. *Blood* (2020) **136**(Suppl. 1):40–1. doi:10.1182/blood-2020-139609

127. Xie G, Dong H, Liang Y, Ham JD, Rizwan R, Chen J. CAR-NK cells: a promising cellular immunotherapy for cancer. *EBioMedicine* (2020) **59**:102975. doi:10.1016/j.ebiom.2020.102975

128. Marofi F, Saleh MM, Rahman HS, Suksatan W, Al-Gazally ME, Abdelbasset WK, et al. CAR-engineered NK cells; a promising therapeutic option for treatment of hematological malignancies. *Stem Cel Res and Ther* (2021) **12**(1):374. doi:10.1186/s13287-021-02462-y

129. Lu H, Zhao X, Li Z, Hu Y, Wang H. From CAR-T cells to CAR-NK cells: a developing immunotherapy method for hematological malignancies. *Front Oncol* (2021) **11**:720501. doi:10.3389/fonc.2021.720501

130. Zhou Q, Bucher C, Munger ME, Highfill SL, Tolar J, Munn DH, et al. Depletion of endogenous tumor-associated regulatory T cells improves the efficacy of adoptive cytotoxic T-cell immunotherapy in murine acute myeloid leukemia. *Blood* (2009) **114**(18):3793–802. doi:10.1182/blood-2009-03-208181

131. Greiner J, Götz M, Hofmann S, Schrezenmeier H, Wiesneth M, Bullinger L, et al. Specific T-cell immune responses against colony-forming cells including leukemic progenitor cells of AML patients were increased by immune checkpoint inhibition. *Cancer Immunol Immunother* (2020) **69**(4):629–40. doi:10.1007/s00262-020-02490-2

132. Rakova J, Truxova I, Holicek P, Salek C, Hensler M, Kasikova L, et al. TIM-3 levels correlate with enhanced NK cell cytotoxicity and improved clinical outcome in AML patients. *Oncoimmunology* (2021) **10**(1):1889822. doi:10.1080/2162402x.2021.1889822

133. Abolhalaj M, Sincic V, Lilljebjörn H, Sandén C, Aab A, Hägerbrand K, et al. Transcriptional profiling demonstrates altered characteristics of $CD8^+$ cytotoxic T-cells and regulatory T-cells in *TP53*mutated acute myeloid leukemia. *Cancer Med* (2022) **11**(15):3023–32. doi:10.1002/cam4.4661

134. Song X, Peng Y, Wang X, Chen Q, Lan X, Shi F. The stimulator of interferon genes (STING) agonists for treating acute myeloid leukemia (AML): current knowledge and future outlook. *Clin Translational Oncol* (2022) **25**:1545–53. doi:10.1007/s12094-022-03065-6

135. Xue L, Hu Y, Wang J, Liu X, Wang X. T cells targeting multiple tumor-associated antigens as a postremission treatment to prevent or delay relapse in acute myeloid leukemia. *Cancer Manag Res* (2019) **11**:6467–76. doi:10.2147/cmar.s205296

136. Zhang M, Sukhumalchandra P, Philips A, Qiao N, Kerros C, Molldrem JJ, et al. Pembrolizumab enhances the anti-leukemia activity of antigen specific cytotoxic T lymphocytes. *Blood* (2018) **132**(Suppl. 1):4542–2. doi:10.1182/blood-2018-99-114864

137. Gibson A, Zhang M, Sukhumalchandra P, Philips A, Qiao N, Perakis A, et al. Pembrolizumab in combination with antigen-specific cytotoxic T lymphocytes enhances killing of acute myeloid leukemia. *Blood* (2021) **138**(Suppl. 1):2775–5. doi:10.1182/blood-2021-149318

138. Chapuis AG, Egan DN, Bar M, Schmitt TM, McAfee MS, Paulson KG, et al. T cell receptor gene therapy targeting WT1 prevents acute myeloid leukemia relapse post-transplant. *Nat Med* (2019) **25**(7):1064–72. doi:10.1038/s41591-019-0472-9

139. Morris E, Tendeiro-Rego R, Richardson R, Fox T, Sillito F, Holler A, et al. A phase I study evaluating the safety and persistence of allorestricted WT1-TCR gene modified autologous T cells in patients with high-risk myeloid malignancies unsuitable for allogeneic stem cell transplantation. *Blood* (2019) **134**(Suppl. 1):1367–7. doi:10.1182/blood-2019-128044

140. Maniati E, Soper R, Hagemann T. Up for Mischief? IL-17/Th17 in the tumour microenvironment. *Oncogene* (2010) **29**(42):5653–62. doi:10.1038/onc.2010.367

141. Xu ZJ, Gu Y, Wang CZ, Jin Y, Wen XM, Ma JC, et al. The M2 macrophage marker CD206: a novel prognostic indicator for acute myeloid leukemia. *Oncoimmunology* (2020) **9**(1):1683347. doi:10.1080/2162402x.2019.1683347

142. Su X, Ye J, Hsueh EC, Zhang Y, Hoft DF, Peng G. Tumor microenvironments direct the recruitment and expansion of human Th17 cells. *The J Immunol* (2010) **184**(3):1630–41. doi:10.4049/jimmunol.0902813

143. Zhang GL, Pan M, Wang YZ, Huang JX, Gu GS, Wang Y, et al. Regulation effect of myeloid leukemia No.1 Chinese herb medicine prescription combined with chemotherapy on Th17 cells in bone marrow of patients with acute myeloid leukemia. *Zhongguo shi yan xue ye xue za zhi* (2021) **29**(2):328–32. doi:10.19746/j.cnki.issn.1009-2137.2021.02.004

144. Ren Z, Huang X, Lv Q, Lei Y, Shi H, Wang F, et al. High expression of B4GALT1 is associated with poor prognosis in acute myeloid leukemia. *Front Genet* (2022) **13**:882004. doi:10.3389/fgene.2022.882004

145. Wang M, Zhang C, Tian T, Zhang T, Wang R, Han F, et al. Increased regulatory T cells in peripheral blood of acute myeloid leukemia patients rely on tumor necrosis factor (TNF)-α-TNF receptor-2 pathway. *Front Immunol* (2018) **9**:1274. doi:10.3389/fimmu.2018.01274

146. Han Y, Ye A, Bi L, Wu J, Yu K, Zhang S. Th17 cells and interleukin-17 increase with poor prognosis in patients with acute myeloid leukemia. *Cancer Sci* (2014) **105**(8):933–42. doi:10.1111/cas.12459

147. Dhakal D, Kunwar L. Clinical expression of th17 related cytokinesin acute myeloid leukemia patients: a prospective descriptive study. *Int J Adv Res* (2022) **10**(03):34–9. doi:10.21474/ijar01/14359

148. Yang X, Zheng H, Dai J, Li C, Zhang R, Wang X, et al. Epigenetic therapy targets Th1/Th17 polarization to reversing immune evasion and treating leukemia relapse post allogeneic stem cell transplantation in non-APL AML patients. *Blood* (2018) **132**(Suppl. 1):3424–4. doi:10.1182/blood-2018-99-111671

149. Wang X, Huang R, Wu W, Xiong J, Wen Q, Zeng Y, et al. Amplifying STING activation by bioinspired nanomedicine for targeted chemo- and immunotherapy of acute myeloid leukemia. *Acta Biomater* (2023) **157**:381–94. doi:10.1016/j.actbio.2022.11.007

150. Bassani B, Simonetti G, Cancila V, Fiorino A, Ciciarello M, Piva A, et al. ZEB1 shapes AML immunological niches, suppressing CD8 T cell activity while fostering Th17 cell expansion. *Cell Rep* (2024) **43**(2):113794. doi:10.1016/j.celrep.2024.113794

151. Swatler J, Turos-Korgul L, Kozlowska E, Piwocka K. Immunosuppressive cell subsets and factors in myeloid leukemias. *Cancers* (2021) **13**(6):1203. doi:10.3390/cancers13061203

152. Kapor S, Santibanez JF. Myeloid-derived suppressor cells and mesenchymal stem/stromal cells in myeloid malignancies. *J Clin Med* (2021) **10**(13):2788. doi:10.3390/jcm10132788

153. Rodriguez PC, Hernandez CP, Quiceno D, Dubinett SM, Zabaleta J, Ochoa JB, et al. Arginase I in myeloid suppressor cells is induced by COX-2 in lung carcinoma. *The J Exp Med* (2005) **202**(7):931–9. doi:10.1084/jem.20050715

154. Corzo CA, Cotter MJ, Cheng P, Cheng F, Kusmartsev S, Sotomayor E, et al. Mechanism regulating reactive oxygen species in tumor-induced myeloid-derived suppressor cells. *The J Immunol* (2009) **182**(9):5693–701. doi:10.4049/jimmunol.0900092

155. Yang L, Huang J, Ren X, Gorska AE, Chytil A, Aakre M, et al. Abrogation of TGFβ signaling in mammary carcinomas recruits gr-1+CD11b+ myeloid cells that promote metastasis. *Cancer cell* (2008) **13**(1):23–35. doi:10.1016/j.ccr.2007.12.004

156. Giallongo C, Parrinello N, Brundo MV, Raccuia SA, Di Rosa M, La Cava P, et al. Myeloid derived suppressor cells in chronic myeloid leukemia. *Front Oncol* (2015) **5**:107. doi:10.3389/fonc.2015.00107

157. Braun LM, Zeiser R. Immunotherapy in myeloproliferative diseases. *Cells* (2020) **9**(6):1559. doi:10.3390/cells9061559

158. Hyun SY, Na EJ, Jang JE, Chung H, Kim SJ, Kim JS, et al. Immunosuppressive role of CD11b+ CD33+ HLA-DR- myeloid-derived suppressor cells-like blast subpopulation in acute myeloid leukemia. *Cancer Med* (2020) **9**(19):7007–17. doi:10.1002/cam4.3360

159. Folgiero V, Goffredo BM, Filippini P, Masetti R, Bonanno G, Caruso R, et al. Indoleamine 2,3-dioxygenase 1 (Ido1) activity in leukemia blasts correlates with poor outcome in childhood acute myeloid leukemia. *Oncotarget* (2014) **5**(8): 2052–64. doi:10.18632/oncotarget.1504

160. Mussai F, De Santo C, Abu-Dayyeh I, Booth S, Quek L, McEwen-Smith RM, et al. Acute myeloid leukemia creates an arginase-dependent immunosuppressive microenvironment. *Blood* (2013) **122**(5):749–58. doi:10.1182/blood-2013-01-480129

161. Haist M, Stege H, Grabbe S, Bros M. The functional crosstalk between myeloid-derived suppressor cells and regulatory T cells within the immunosuppressive tumor microenvironment. *Cancers* (2021) **13**(2):210. doi:10.3390/cancers13020210

162. Ren X, Tao Q, Wang H, Zhang Q, Zhou M, Liu L, et al. Monocytic myeloid-derived suppressor cells but not monocytes predict poor prognosis of acute myeloid leukemia. *Turkish J Hematol* (2022) **39**(4):230–6. doi:10.4274/tjh.galenos.2022.2022.0137

163. Tohumeken S, Baur R, Böttcher M, Stoll A, Loschinski R, Panagiotidis K, et al. Palmitoylated proteins on AML-derived extracellular vesicles promote myeloid-derived suppressor cell differentiation via TLR2/akt/mTOR signaling. *Cancer Res* (2020) **80**(17):3663–76. doi:10.1158/0008-5472.can-20-0024

164. Li X, Li Y, Yu Q, Xu L, Fu S, Wei C, et al. mTOR signaling regulates the development and therapeutic efficacy of PMN-MDSCs in acute GVHD. *Front Cel Dev Biol* (2021) **9**:741911. doi:10.3389/fcell.2021.741911

165. Bai H, Peng Y, Li Y, Duan J, Fu W, Liang X, et al. Cytarabine-induced TNFα promotes the expansion and suppressive functions of myeloid-derived suppressor cells in acute myeloid leukaemia. *Scand J Immunol* (2022) **95**(6):e13158. doi:10.1111/sji.13158

166. Pyzer A, Stroopinsky D, Rajabi H, Washington A, Cole L, Jain S, et al. Acute myeloid leukemia cells export c-myc in extracellular vesicles driving a proliferation of immune-suppressive myeloid-derived suppressor cells. *Blood* (2016) **128**(22): 703–3. doi:10.1182/blood.v128.22.703.703

167. Mehta R, Chen X, Antony J, Szabolcs P. Myeloid derived suppressor cells (MDSC)-like acute myeloid leukemia (AML) cells are associated with resistance to cytotoxic effects of autologous (auto) T-lymphocytes (CTLs). *Biol Blood Marrow Transplant* (2015) **21**(2):S191–S192. doi:10.1016/j.bbmt.2014.11.290

168. Notarantonio AB, Bertrand A, Piucco R, Fievet G, Sartelet H, Boulangé L, et al. Highly immunosuppressive myeloid cells correlate with early relapse after allogeneic stem cell transplantation. *Exp Hematol and Oncol* (2024) **13**(1):50. doi:10.1186/s40164-024-00516-4

169. Wang L, Jia B, Claxton DF, Ehmann WC, Rybka WB, Mineishi S, et al. VISTA is highly expressed on MDSCs and mediates an inhibition of T cell response in patients with AML. *Oncoimmunology* (2018) **7**(9):e1469594. doi:10.1080/2162402x.2018.1469594

170. Jochems C, Kwilas A, Kim Y, Brechbiel M, Hodge J, Newton R, et al. The Ido inhibitor INCB024360 to enhance dendritic cell immunogenicity and anti-tumor immunity *in vitro*. *J Clin Oncol* (2015) **33**(15_Suppl. l):e14012–e12. doi:10.1200/jco.2015.33.15_suppl.e14012

171. Komrokji RS, Wei S, Mailloux AW, Zhang L, Padron E, Sallman D, et al. A phase II study to determine the safety and efficacy of the oral inhibitor of indoleamine 2,3-dioxygenase (Ido) enzyme INCB024360 in patients with myelodysplastic syndromes. *Clin Lymphoma Myeloma Leuk* (2019) **19**(3): 157–61. doi:10.1016/j.clml.2018.12.005

172. Ogasawara M, Ota S. Dendritic cell vaccination in acute leukemia patients induces reduction of myeloid-derived suppressor cells: immunological analysis of a pilot study. *Blood* (2014) **124**(21):1113–3. doi:10.1182/blood.v124.21.1113.1113

173. Miner S, Ito S, Tanimoto K, Hensel N, Chinian F, Keyvanfar K, et al. Myeloid leukemias directly suppress T cell proliferation through STAT3 and arginase pathways. *Blood* (2013) **122**(21):3885–5. doi:10.1182/blood.v122.21.3885.3885

EBM Experimental Biology and Medicine

TYPE Original Research
PUBLISHED 21 February 2025
DOI 10.3389/ebm.2025.10254



OPEN ACCESS

*CORRESPONDENCE
Jia L. Stevens,
jialiu.stevens@nhs.net
Andrew J. Murray,
ajm267@cam.ac.uk

RECEIVED 22 May 2024
ACCEPTED 14 January 2025
PUBLISHED 21 February 2025

CITATION
Stevens JL, McKenna HT, Minnion M, Murray AJ, Feelisch M and Martin DS (2025) The effects of major abdominal surgery on skeletal muscle mitochondrial respiration in relation to systemic redox status and cardiopulmonary fitness.
*Exp. Biol. Med.* 250:10254.
doi: 10.3389/ebm.2025.10254



# The effects of major abdominal surgery on skeletal muscle mitochondrial respiration in relation to systemic redox status and cardiopulmonary fitness

Jia L. Stevens[1,2]*, Helen T. McKenna[3], Magdalena Minnion[4], Andrew J. Murray[5]*, Martin Feelisch[4] and Daniel S. Martin[3]

[1]Department of Anaesthesia, Royal Sussex County Hospital, University Hospital Sussex NHS Foundation Trust, Brighton and Hove, United Kingdom, [2]Division of Surgery and Interventional Science, Faculty of Medical Sciences University College London, London, United Kingdom, [3]Peninsula Medical School, Faculty of Medicine and Dentistry, University of Plymouth, Plymouth, United Kingdom, [4]Clinical and Experimental Sciences and Integrative Physiology and Critical Illness Group, Faculty of Medicine, Southampton General Hospital, University of Southampton, Southampton, United Kingdom, [5]Department of Physiology, Development and Neuroscience, Faculty of Biology, School of Biological Sciences, University of Cambridge, Cambridge, United Kingdom

## Abstract

More complex surgeries are being performed in increasingly sicker patients, resulting in a greater burden of postoperative morbidity. Delineating the metabolic and bioenergetic changes that occur in response to surgical stress may further our understanding about how humans respond to injury and aid the identification of resilient and frail phenotypes. Skeletal muscle biopsies were taken from patients undergoing hepato-pancreatico-biliary surgery at the beginning and end of the procedure to measure mitochondrial respiration and thiol status. Blood samples were taken at the same timepoints to measure markers of inflammation and systemic redox state. A sub-group of patients underwent cardiopulmonary exercise testing prior to surgery, and were assigned to two groups according to their oxygen consumption at anaerobic threshold (≤10 and >10 mL/kg/min) to determine whether redox phenotype was related to cardiorespiratory fitness. No change in mitochondrial oxidative phosphorylation capacity was detected. However, a 26.7% increase in LEAK (uncoupled) respiration was seen after surgery (P = 0.03). Free skeletal muscle cysteine also increased 27.0% (P = 0.003), while S-glutathionylation and other sulfur and nitrogen-based metabolite concentrations remained unchanged. The increase in LEAK was 200% greater in fit patients (P = 0.004). Baseline plasma inflammatory markers, including TNF-α and IL-6 were greater in unfit patients, 96.6% (P = 0.04) and 111.0% (P = 0.02) respectively, with a 58.7% lower skeletal muscle nitrite compared to fit patients. These data suggest that oxidative phosphorylation is preserved during the acute intraoperative period. Increase in free cysteine may demonstrate the muscle's response to surgical stress to maintain redox balance. The differences in tissue metabolism between fitness groups suggests underlying metabolic phenotypes of frail and resilient patients. For example,

increased LEAK in fitter patients may indicate mitochondrial adaptation to stress. Higher baseline measurements of inflammation and lower tissue nitrite in unfit patients, may reflect a state of frailty and susceptibility to postoperative demise.

KEYWORDS

**cardiopulmonary, mitochondrial respiration, redox, antioxidants, perioperative**

## Impact statement

Improved access to surgery has increased the global burden of postoperative pathology. Understanding the mechanisms that drive postoperative demise, and identifying at-risk patients are paramount to the advance of perioperative medicine. This study provides new insight into the body's responses to acute surgical stress, demonstrating that the initial response to injury does not solely release markers of cell/tissue damage, but also markers of adaptation, with evidence of mitochondrial bioenergetic alterations and the maintenance of sulfur and nitrogen-based metabolites. Our study also provides phenotypic profiles of patients representing perioperative resilience and frailty. The association of reduced baseline aerobic capacity with increased levels of cyclic guanosine monophosphate, inflammation, and intraoperative mitochondrial uncoupling, is indicative of a biochemical phenotype for deconditioned and frail patients. The identification of such responses to major surgery and their variability brings us closer to personalised and stratified medicine.

## Introduction

As surgical technology advances, we are performing more complex procedures in frailer and more multi-morbid patients than ever before, and the consequences of undergoing surgery can be life changing. Whilst the intention, particularly in cancer surgery, is to provide a cure, complications can occur, resulting in a proportion of these patients being left with deficits for months or years to come. Characterising the metabolic and bioenergetic changes that occur after acute surgical stress may further our understanding of how the human body responds to injury and how these responses differ between individuals. Identifying a physiological and biochemical phenotype that characterises resilience and protection is an important step for making progress in perioperative medicine.

The pivotal role that mitochondria play in cellular bioenergetics is well established, but their role in redox metabolism, including the production and scavenging of reactive oxygen species (ROS) and reactive nitrogen species (RNS) which can promote a state of oxidative and/or nitrosative stress, is being recognised only more recently. In addition, reactive sulfur species (e.g., hydrogen sulfide and per/polysulfides) and sulfur-containing compounds such as thiols have potent antioxidant capacity and can produce a wide array of oxidation products. When combined, these redox metabolic reactions can be conceptualised using the "reactive species interactome" framework [1].

Altered mitochondrial function, in conjunction with oxidative stress, has been linked to the pathogenesis of multiple chronic conditions and to the mechanisms that underlie frailty and physical fitness [2]. Physical fitness is associated with many health benefits, including reductions in occurrence of metabolic and cardiovascular diseases and cancer [3], increased longevity and a reduction in the development of age-related illnesses [4, 5]. Cardiopulmonary exercise testing (CPET) provides a direct measure of cardiorespiratory fitness where oxygen consumption ($VO_2$) and carbon dioxide production ($VCO_2$) in response to increasing levels of physical activity provide an indirect yet integrative measure of tissue respiration and hence mitochondrial function. Data from CPETs are used as predictor of a patient's physiological response to the stress of surgery. Lower levels of preoperative aerobic fitness [peak $VO_2$ and $VO_2$ at anaerobic threshold (AT)] have repeatedly been associated with postoperative morbidity [6, 7].

The contributions of altered mitochondrial respiratory function with oxidative stress in an acute surgical setting are less well established and described. They have been reported in one animal study and one human study (of skeletal muscle biopsies) to date [8, 9]. Both studies observed markers of altered mitochondrial respiration after surgery. In addition, greater release of ROS was associated with a loss of mitochondrial membrane potential [10]. In the perioperative setting, an AT of <11 mL/kg/min, has been associated with increased levels of preoperative markers of inflammation [11]. Peak $VO_2$ levels have been positively correlated with mitochondrial respiratory capacity, and in particular of oxidative phosphorylation [12]. However, the links between fitness, redox metabolism, mitochondrial respiration and the effects of surgery have not yet been addressed.

We conducted a single-centre, prospective exploratory study of patients undergoing major hepato-pancreatico-biliary (HPB) surgery at the Royal Free Hospital (London, UK). Results from the main study have been previously reported [13]. A subgroup of patients from the main study underwent additional investigations. We hypothesized that less fit patients would display a greater degree of perturbation to whole-body redox

balance with greater systemic oxidative stress and early changes in mitochondrial respiratory function in skeletal muscle following surgery. Specifically, we were interested to learn: 1) how major abdominal surgery affects mitochondrial respiration and redox status of skeletal muscle under conditions of systemically increased oxidative stress, and 2) whether those changes differ between fit and unfit individuals.

# Materials and methods

## Participants

Patients for this sub-study were selected from a larger study of the effects of major abdominal surgery on circulating redox markers [13]. All patients were approached up to 1 month prior to scheduled surgery to seek their agreement to participate. Inclusion criteria included: major (intra-cavity) inpatient surgery; age ≥18 years; planned general anaesthesia; calculated morbidity risk ≥40% (Portsmouth Physiological and Operative Severity Score for the enUmeration of Mortality and morbidity – P-POSSUM). Exclusion criteria included: mitochondrial disease; emergency surgery; lack of capacity; prisoners. In addition, patients in the sub-study were required to undergo skeletal muscle biopsies at the beginning and end of surgery and (if feasible) a cardiopulmonary exercise testing prior to their surgery (see Supplementary Figure S1 *CONSORT diagram*).

The study was designed and reported according to the Strengthening the Reporting of Observational Studies in Epidemiology (STROBE) Guidelines [14]. Ethical approval was obtained from the West London Research Ethics Committee and Human Research Authority [214019]. All patients provided written informed consent prior to surgery.

## Cardiopulmonary exercise testing

CPET took place on a cycle ergometer according to a local protocol, which followed the perioperative CPET consensus clinical guidelines [15]. Exercise was conducted on an electromagnetically braked cycle ergometer (Lode BV medical technology), following a protocol of: 3 minutes rest; 2 minutes of freewheel pedalling; ramped incremental cycling until the patient could no longer continue; and a 5-min recovery period of freewheel pedalling. Ventilation and gas exchange were measured through use of a metabolic cart (Metalyzer 3B, Cortex Biophysics GmbH) and the data was analysed using the Metasoft 3.9 software. The ramp gradient was set to 10–25 W/min based on the participant's self-reported level of activity. Resting flow-volume loops were used to derive measures of forced expiratory volume over one second. AT was estimated in the conventional manner, involving the use of the three-point discrimination technique (identification of excess $VCO_2$ relative to $VO_2$; identification of hyperventilation relative to oxygen; hyperventilation excluded relative to carbon dioxide). Two separate reviewers determined the AT values independently and the average of the measurements was taken as the final AT. When there was disagreement of >10%, a third reviewer was invited to be the final adjudicator, and the average of the two measurements within 10% was taken as the final AT. Peak $VO_2$ was averaged over the last 30 s of exercise.

## Anaesthetic and surgical techniques

For details of anaesthesic and surgical techniques the reader is referred to the methodology section of the main study published elsewhere [13] and the supplementary section of the present paper.

## Blood collection

Samples of venous blood were collected at baseline (after induction of anaesthesia but prior to the first surgical incision) and at the end of surgery (EoS) after wound closure. Samples were immediately placed on ice and centrifuged at 2000 × *g* for 15 min at 4°C. Plasma and serum samples were divided into aliquots for storage at −80°C.

## Blood analysis

The following markers were chosen on the basis of their relationship within the "reactive species interactome" framework to include lipid oxidation products such as malondialdehyde (MDA), 4-hydroxynonenal (4-HNE) and 8-iso-prostaglandin $F_{2\alpha}$ (8-isoprostanes); markers of total reducing capacity (TRC), total free thiols (TFTs) and ferric reducing ability of plasma (FRAP); as well as markers of NO production, metabolism and availability including cyclic guanosine monophosphate (cGMP), nitrite, nitrate and total nitroso-species (RXNO). Interleukin-6 (IL-6) and tumour necrosis factor alpha (TNF-α) were also measured to evaluate inflammation. Pristine (first thaw from −80°C) serum samples were used throughout; for details of method of analysis please refer to reference 13[13] and the Supplementary Material.

## Skeletal muscle biopsy

Vastus lateralis muscle was biopsied at two separate timepoints under general anaesthesia, which was coupled with blood sample extraction; at baseline and EoS, using previously described methods [16]. Biopsies were taken from the mid-thigh

using Tilley-Henckel forceps under local anaesthesia (1% lidocaine) of the skin and superficial muscle fascia. A 5 mm incision was made, and 100 mg wet-weight tissue was collected. The sample was divided, with 50 mg allocated for immediate respirometric analysis and the remainder snap frozen in liquid nitrogen and stored at −80°C until later analysis. The muscle sample was divided into aliquots, the sample for high-resolution respirometry (HRR) was immediately placed in ice-cold biopsy preservation medium (BIOPS): [$CaK_2EGTA$ (2.77 mM), $K_2EGTA$ (7.23 mM), $MgCl_2.6H_2O$ (6.56 mM), taurine (20 mM), PCr (15 mM), imidazole (20 mM), DTT (0.5 mM), MES (50 mM) and $Na_2ATP$ (5.77 mM) at pH 7.10], which was filtered and stored at −40°C until use to prevent bacterial growth. The aliquots for muscle metabolomics were snap frozen in liquid nitrogen and subsequently stored at −80°C for later analysis.

## Sample preparation and high resolution respirometry

Skeletal muscle fibre bundles were prepared from the respirometry-designated sample according to previously described methods [17]. After permeabilisation of the sarcolemmal membrane using saponin (50 µg/mL, in ice cold BIOPS, rocked for 20 min at 20 rpm), fibre bundles were rinsed in respiration medium (MiR05, outlined below) blotted on filter paper and weighed using a microbalance (Mettler-Toledo). Respiration of fibre bundles was then measured in mitochondrial respiration medium (MiR05) containing EGTA (0.5 mM), $MgCl_2.6H_2O$ (3 mM), K-lactobionate (60 mM), taurine (20 mM), $KH_2PO_4$ (10 mM), HEPES (20 mM), sucrose (110 mM) and defatted BSA (1g.L-1) at pH 7.4, using the substrate-uncoupler-inhibitor titration (SUIT) protocol described below. All assays were performed, in duplicate, using an Oxygraph O2K (Oroboros Instruments, Innsbruck), at 37°C with oxygen concentrations kept between 250 and 400 µM and constant stirring to prevent diffusion limitation of respiration. Respirometry was performed by the same operator throughout the study.

Oxygen consumption of permeabilised muscle fibres were measured using a fatty acid oxidation (FAO)-mediated SUIT protocol. In brief, mitochondrial respiratory states were recorded following stepwise titrations. Addition of malate and octanoylcarnitine supported LEAK respiration ($LEAK_{FAO}$), with oxygen consumption not coupled to oxidative phosphorylation (OXPHOS); addition of adenosine diphosphate (ADP) resulted in OXPHOS supported by fatty acid oxidation ($FAO_{OXPHOS}$); addition of pyruvate reconstituted the Krebs cycle ($MOP_{OXPHOS}$), and glutamate produced OXPHOS supported by complex I ($CI_{OXPHOS}$). Addition of succinate stimulated OXPHOS supported by complexes I and II, with a further titration of ADP to achieve maximum complex I and II-mediated OXPHOS (MAX OXPHOS). Titration of the protonophore, carbonyl cyanide p-trifluoro-methoxyphenyl hydrazone (FCCP), resulted in maximal electron transfer system (ETS) capacity, unlimited by the phosphorylation system (CI + $II_{ETS}$). The relative contribution of complex II was assessed by addition of the complex I inhibitor, rotenone ($CII_{ETS}$). For further information refer to Supplementary Table S1.

## Metabolomic analysis of skeletal muscle

Muscle biopsies were accurately weighed and mixed with 300 µL of homogenisation buffer (10 mM phosphate-buffered saline with 10 mM N-ethylmaleimide (NEM) and 2.5 mM EDTA) and homogenised by 8 up-and-down strokes under ice-cooling using a Kimble all-glass tissue grinder attached to a GlasCol GT Series stirrer. Tissue homogenates were then split and treated depending on the markers to be analysed, as detailed below. One 100 µL aliquot of the muscle homogenate was deproteinised by precipitation with ice-cold methanol (1:1, v:v) and centrifugation at 16,000 × *g* for 20 min. Clear supernatants were analysed for nitrite ($NO_2^-$) and nitrate ($NO_3^-$) using a dedicated high-performance liquid chromatography system for NOx analysis (ENO-30 with AS-700 autosampler, Eicom/Amuza), and data were processed using the Clarity software. The remainder of the muscle homogenates was utilised to evaluate thiol redox status using an ultra-high performance liquid chromatography tandem mass spectrometry (UPLC-MS/MS) method described in detail elsewhere [18]. A 100 µL supernatant of the muscle homogenates was mixed 1:1 with internal standards before centrifugation and injection onto the LC-MS/MS system (Aquity/XEVO-TQS, Waters). The method was used to separate and quantify biological aminothiols such as reduced and oxidized glutathione (GSH, GSSG), cysteine (Cys/cystine) and homocysteine (HCys/homocystine) as well as sulfide ($HS^-$). In addition to the free thiols, total thiol concentrations (free + protein-bound forms and disulfides) were determined after sample pre-processing with dithiothreitol (DTT). For this purpose, an additional 50 µL aliquot of muscle homogenate was subjected to reduction by DTT (50 mM, 1:1, v:v) followed by incubation for 30 min at room temperature before addition of 400 µL of 100 mM NEM for derivatization of liberated thiols. After 15 min incubation at room temperature, derivatized samples were spiked with internal standards, subjected to ultrafiltration for protein removal and injected onto the LC-MS/MS system.

## Clinical data collection and sample size determination

Clinical data were collected prospectively throughout the perioperative admission and entered into a database.

TABLE 1 Baseline patient data. Baseline patient demographics and co-morbidities with absolute numbers and percentages, unless otherwise stated and presented as median and IQR.

| Characteristics | |
|---|---|
| Age (years) | 67.0 (58.0–69.5) Median (IQR) |
| Gender (male: female) | 24:10 (70.6:29.4) |
| BMI (kg/m$^2$) | 24.3 (22.7–28.6) Median (IQR) |
| **Ethnicity [n (%)]** | |
| White | 32 (94.1) |
| Asian | 1 (2.9) |
| Black | 1 (2.9) |
| **Smoking status [n (%)]** | |
| Yes | 4 (11.8) |
| No | 19 (55.9) |
| Ex-smoker | 11 (32.4) |
| **Alcohol [n (%)]** | |
| Yes | 11 (32.4) |
| No | 23 (67.6) |
| Consumption (units per week) | 2 (2–6.5) |
| **ASA [n (%)]** | |
| I | 3 (8.8) |
| II | 19 (58.8) |
| III | 11 (32.4) |
| IV | 0 (0.0) |
| **Comorbidities [n (%)]** | |
| Cardiovascular | 19 (55.9) |
| Hypertension | 12 (35.3) |
| Ischaemic heart disease | 4 (11.8) |
| Heart failure | 0 (0.0) |
| Arrythmia | 3 (8.8) |
| Valvular heart disease | 0 (0.0) |
| Cerebral vascular disease | 1 (2.9) |
| Peripheral vascular disease | 2 (5.9) |
| Respiratory | 6 (17.6) |
| COPD | 3 (8.8) |
| Asthma | 2 (5.9) |
| OSA | 1 (2.9) |
| Other | 0 (0.0) |
| Endocrine and metabolic | 16 (44.4) |
| Diabetes | 9 (26.2) |
| Hypercholesterolaemia | 5 (14.7) |
| Other | 2 (5.9) |
| Renal disease | 0 (0.0) |
| Rheumatological | 4 (11.8) |
| Other systemic disease | 2 (5.9) |

(Continued in next column)

TABLE 1 (*Continued*) Baseline patient data. Baseline patient demographics and co-morbidities with absolute numbers and percentages, unless otherwise stated and presented as median and IQR.

| Characteristics | |
|---|---|
| **Diagnosis [n (%)]** | |
| Pancreatic cancer | 12 (35.3) |
| Liver metastasis | 10 (29.4) |
| Cholangiocarcinoma | 5 (14.7) |
| Hepatocellular carcinoma | 4 (11.8) |
| Neuroendocrine tumour | 1 (2.9) |
| Ampulla and duodenal cancer | 1 (2.9) |
| Other | 1 (2.9) |
| Neo-adjuvant chemoradiotherapy within the last year [n (%)] | 7 (20.6) |

## Statistical analysis

Data were assessed for normality by visual examination of histograms and using the Shapiro-Wilk test. Data were presented as median and interquartile range (IQR). Wilcoxon signed-rank sum was used for paired tests and Mann-Whitney U for two independent samples for non-normally distributed data. Changes in intraoperative concentrations of metabolic indices (calculated as EoS concentration – baseline concentration) was used to reflect intraoperative trajectory/dynamics of the metabolic profile. AT was chosen as a discriminatory measure of cardiopulmonary fitness. A cut-off point of 10 mL/kg/min was chosen to dichotomise the patients into two groups, labelled "fit" and "unfit." This threshold was chosen because it was found to be specifically associated with outcomes after HPB surgery [6]. The linear relationships between non-normally distributed continuous data were assessed using Pearson's correlation. Missing values were excluded from the analysis. All tests were two-tailed and $P < 0.05$ was selected as the threshold for statistical significance. In view of the exploratory nature of the study, a decision was made not to correct for multiplicity. Whilst this increased the risk of generation of a type-1 error, it simultaneously reduced the risk of generation of a type-2 error, which was considered important in work of this nature. Statistical analyses were carried out using IBM SPSS version 26 software and graphs were created using GraphPad Prism 8 software.

# Results

## Clinical data

37 patients underwent paired (baseline and EoS) muscle biopsies, 33 sets were used for HRR and 37 sets of samples

were used for metabolomic analyses. A sub-group of 23 patients underwent CPET prior to surgery.

Patient demographics and baseline preoperative data can be found in Table 1. For detailed intraoperative and postoperative clinical data refer to Supplementary Tables S2, S3. Of the 37 patients, 34.3% had pancreatic surgeries, 45.7% hepatic resections, and 20.0% palliative procedures. CPET measurements are summarised in Table 2. Participants had a median AT of 11.5 mL/kg/min and $VO_2$ peak of 16.5 mL/kg/min. The median number of days on ICU and in hospital were 2.7 (1–2.8) and 9.0 days (6.2–14.8) respectively.

## Changes in skeletal muscle mitochondrial respiratory capacity and redox metabolome between baseline and end of surgery

Skeletal muscle respiratory function measured by HRR revealed a 26.7% increase in $LEAK_{FAO}$ respiration from baseline to EoS (P = 0.03). No difference in any other measured respiratory state, including maximal oxidative phosphorylation capacity, was detected between these two timepoints (Figure 1). While the intramuscular concentrations of nitrite and nitrate as well as those of free and total thiols (aminothiols and sulfide) did not differ between baseline and end of surgery, a 27.0% increase in free cysteine content was observed after surgery (Figure 2).

## Perioperative differences in blood and skeletal muscle markers based on patients' cardiorespiratory fitness

Baseline levels of circulating antioxidant, lipid oxidation, NO and inflammation status were compared in the fit and unfit patient groups. No differences between the groups were detected in serum markers of antioxidant capacity (TRC) or lipid oxidation. Plasma cGMP was found to be 81.6% higher in the unfit group compared with the fit group (P = 0.006). Serum levels of inflammatory markers IL-6 and TNF-α were 111.0% and 96.6% higher in the unfit group compared with the fit group (P = 0.04 and P = 0.02 respectively). No significant differences were detected between these two groups in skeletal muscle mitochondrial respiration capacity or thiol status at baseline. However, muscle nitrite was 58.7% lower in unfit patients compared to fit patients (P = 0.003), with no baseline differences in nitrate (Table 3).

We then compared the magnitude of intraoperative *changes* (EoS-baseline) in the concentrations of circulating serum redox and inflammatory markers as well as skeletal muscle mitochondrial function and muscle metabolites between the fit and unfit groups to explore the effects of the surgery on these parameters. No differences were detected between groups in terms of intraoperative changes in serum TRC, lipid oxidation or nitrosative stress. The intraoperative reduction in serum TNF-α levels in the fit group was 65.2% less than that reported in the unfit group (P = 0.03). No between-groups difference was detected in terms of changes in IL-6 (Supplementary Table S4).

The increase in intraoperative skeletal muscle mitochondrial $LEAK_{FAO}$ was 200% higher in fit compared with unfit patients (P = 0.004). No other differences were observed between the two groups (Supplementary Table S4).

Peak $VO_2$ was found to correlate with baseline blood measurements of TNF-α (r = 0.491, P = 0.045, n = 17), baseline skeletal nitrite levels (r = 0.492, P = 0.045, n = 17) and with the degree of intraoperative changes in mitochondrial LEAK respiration (r = 0.730, P = 0.003, n = 14).

# Discussion

This sub-study aimed to improve our understanding of how major abdominal surgery affects mitochondrial respiration and redox status of skeletal muscle under conditions of systemically increased oxidative stress (results of main study reported elsewhere [13]), and whether these changes differ between fit and unfit individuals. The key findings include no intraoperative change in mitochondrial respiratory capacity, ($FAO_{OXPHOS}$, $CI_{OXPHOS}$ and MAX OXPHOS), suggesting that oxidative phosphorylation is preserved during this hyper-acute intraoperative period. However, an increase in respiration not coupled to oxidative phosphorylation ($LEAK_{FAO}$ respiration) was detected by the end of surgery, along with an increase in skeletal muscle free cysteine levels. These changes were related to the patient's cardiopulmonary fitness (as assessed by CPET): the intraoperative increase in LEAK respiration was greater in fit patients (and LEAK respiration also correlated positively with peak VO2?). In addition, baseline differences in inflammatory profile were detected in the fit and unfit groups, with plasma inflammatory markers (cGMP, IL-6 and TNF-α) found to be greater in less fit patients along with a lower level of skeletal muscle nitrite.

Our findings invite several plausible explanations that warrant further experimental investigation and, at this stage, are essentially hypothesis-generating. The increase in skeletal muscle $LEAK_{FAO}$ respiration may be a sign of mitochondrial adaptation to rising systemic oxidative/nitrosative stress; explanations for a potential underlying mechanism are discussed below. The flexibility of skeletal muscle to increase $LEAK_{FAO}$ respiration was also associated with increased physical fitness, where fitter patients demonstrated greater increases in $LEAK_{FAO}$ intraoperatively than those with lower ATs. Moreover, baseline measurements of cGMP, IL-6 and TNF-α were higher in unfit patients, who also had less nitrite in their skeletal muscle. The dichotomy in NO-related metabolites between skeletal

TABLE 2 Baseline CPET data. CPET data of the main test group, and divided into unfit and fit groups based on AT (cut-off ≤10 mL/kg/min).

| Fitness indices derived from CPET | Total Median (IQR) | Unfit (n = 6) Median (IQR) | Fit (n = 17) Median (IQR) |
|---|---|---|---|
| AT (mL/kg/min) | 11.5 (4.3) | 9.0 (2.0) | 13.5 (3.5) |
| $VO_2$ peak (mL/kg/min) | 16.5 (8.0) | 15 (1.5) | 22.9 (9.0) |
| $VE/VCO_2$ | 29.0 (4.3) | 31.4 (6.9) | 27.9 (3.4) |
| Peak HR (bpm) | 131 (39) | 142 (22) | 125 (21) |
| $O_2$ pulse at peak $VO_2$ (mL) | 10.5 (6.5) | 9 (1.9) | 11.6 (6.60) |
| Work ramp rate (W) | 15 (5) | 20 (5) | 15 (5) |
| Work rate at peak $VO_2$ (W/min) | 115.0 (94) | 105 (31) | 126 (69) |

muscle and circulating concentrations observed in the present study appears to be counter-intuitive insofar as the capacity to raise circulating nitrite concentrations (secondary to stimulation of endothelial NO synthase) in healthy individuals is typically a direct function of muscle mass and cardiorespiratory fitness [19]. However, whole-body regulation of these molecules in health is likely to differ from that in ill-health. Importantly, nitrite is not a passive oxidative breakdown product of NO but a reactive species and a signalling molecule in its own right [1, 20]. This includes the modulation of mitochondrial function [21] with complex interactions between endogenous NO production, dietary NOx intake and oral microbiome [22], cross-talk between nitrite and sulfide/persulfide-related (NO-independent) pathways [23, 24], oxygen-dependent tissue processing [25], and physical activity-dependent inter-organ exchange processes [20, 21]. Moreover, associated redox metabolism/signalling are subject to considerable alterations under inflammatory conditions [26, 27], making it difficult to predict the outcome of these interactions in the context of mitochondrial function and systemic inflammation. In any case, the differences in muscle nitrite observed in the present study may reflect either greater tissue utilization or leakage of nitrite from muscle into blood in frail patients. Why circulating cGMP levels were higher in less fit patients is similarly unclear but may be a reflection of higher iNOS expression and formation of peroxynitrite in either vasculature or circulating blood cells and linked to chronic inflammation.

Skeletal muscle free cysteine levels increased during the intraoperative period, with no change in glutathione concentrations. Since neither free cystine nor homocystine were detected (and levels of oxidized glutathione were vanishingly small), the differences between total and free thiol concentrations measured in skeletal muscle largely reflect the level of protein-bound thiols (i.e., the extent to which protein thiols are cysteinylated, homocysteinylated, glutathionylated and persulfidated). The differences in cysteine levels observed may be a sign of the muscle's ability to elevate this sulfur-containing amino acid to maintain levels of glutathione in this tissue, in particular under conditions of increased oxidative stress. Since glutathione is of importance for much more than cellular antioxidant protection including, for example, mitochondrial function [24] it is tempting to speculate that the observed differences in cysteine concentrations in skeletal muscle before and after surgery may be linked to the ability of skeletal muscle to withstand major stress, thus reflecting biological resilience.

Regardless of these considerations, our findings suggest that cardiopulmonary fitness correlates more closely with intrinsic inflammatory levels than with oxidative/nitrosative stress in this cohort of patients with cancer. The raised baseline inflammatory state may also be a reflection of the cancer burden [28, 29], and the reduction in cardiopulmonary fitness may be the phenotypic expression of a state of functional loss and cachexia in cancer patients. In addition, raised systemic baseline IL-6 and reduced nitrate was found in patients who went on to develop severe morbidity [13]. These metabolic observations may reflect the complexity of metabolic regulation and response to surgical stress at the whole-body level [30] but are consistent with clinical observations that unfit patients are more likely to develop greater postoperative morbidity, which may be secondary to increased baseline inflammation, greater ROS production and a consecutively reduced bioavailability of NO (a powerful antioxidant) [31]. Skeletal muscle plays a vital role in inter-organ exchange of building blocks, redox regulation and metabolic flexibility. Sarcopenia, which is a hallmark of ageing and a measure of frailty, has been associated with chronic exposure to oxidative stress, inflammation and reduction in antioxidant capacity [32–34]. Raised levels of IL-6, which is independent of body composition, have been associated with reduced physical activity and increasing frailty [35, 36]. These findings may form part of the notion that fitter individuals have a lower baseline inflammatory state, which renders them to be more resilient and better able to adapt to stresses intraoperatively through mitochondrial protective mechanisms.

LEAK respiration is the dissipative component of mitochondrial respiration, which is independent of oxidative phosphorylation. The main contributor to this is proton leak,

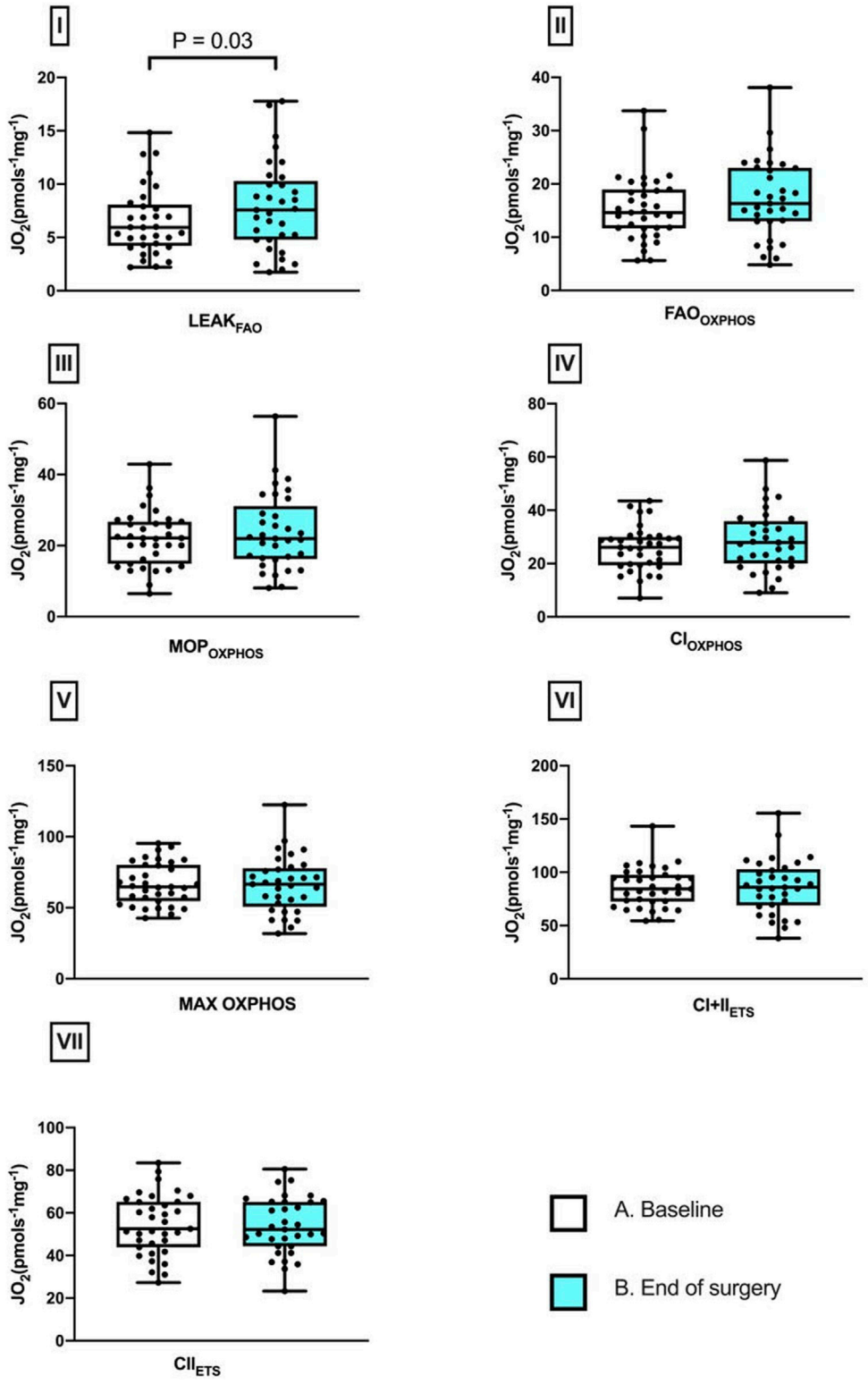


FIGURE 1
Perioperative changes in skeletal muscle mitochondrial respiratory states. Differences between baseline and after surgery in I, $LEAK_{FAO}$; II, $FAO_{OXPHOS}$; III, $MOP_{OXPHOS}$; IV, $CI_{OXPHOS}$; V, CI + $II_{OXPHOS}$; VI, CI + $II_{ETS}$; and VII, $CII_{ETS}$ (median and IQR). Pairwise comparisons were performed using the Wilcoxon signed ranks test (n = 33).

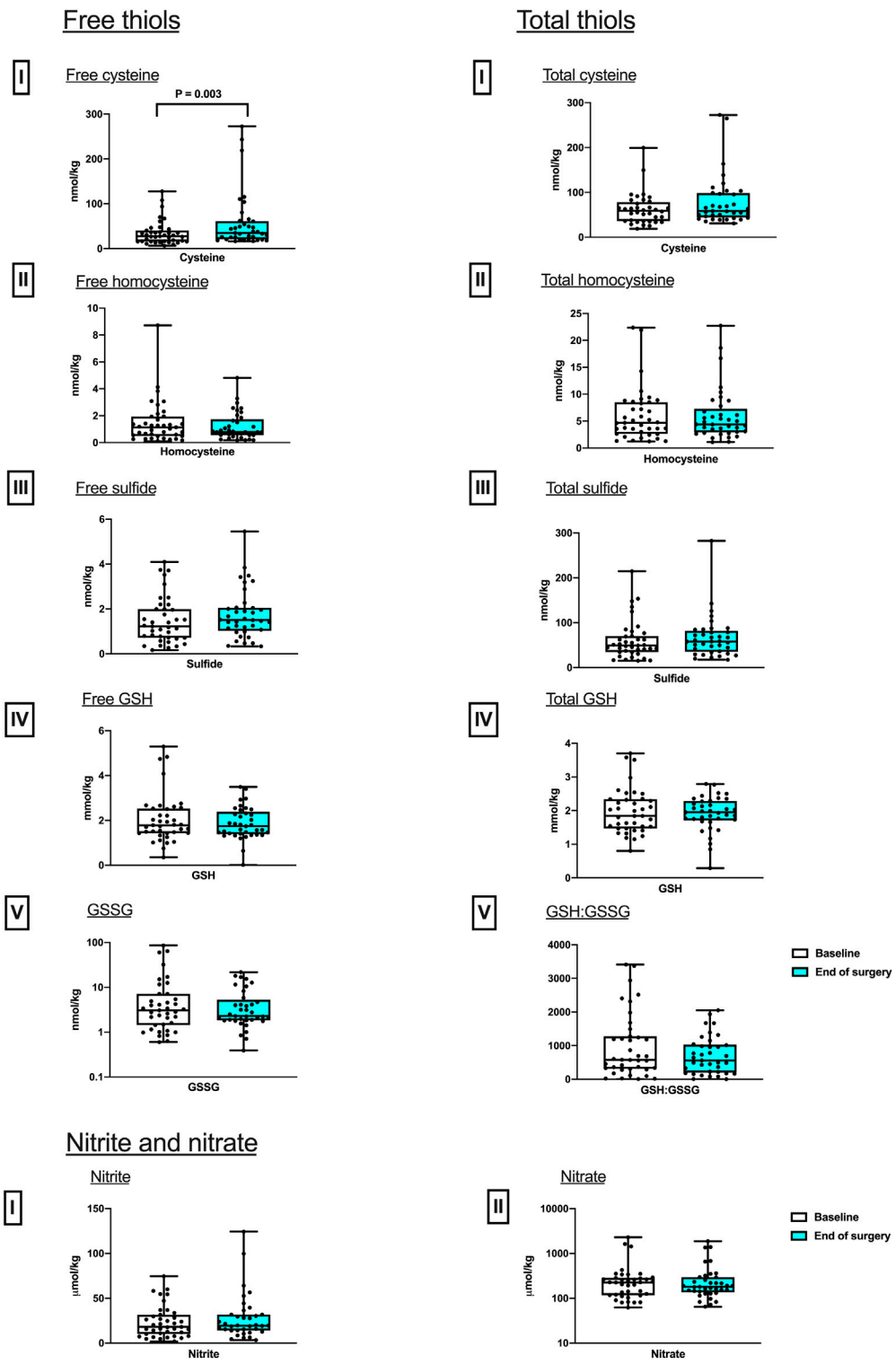


FIGURE 2
Perioperative changes in skeletal muscle sulfur (free and total thiols) and nitrogen-based metabolites. Differences in concentrations between baseline and after surgery in Free, I, Cysteine; II Homocysteine; III, Sulfide; IV, GSH; and V, GSSG; and total, I, Cysteine; II Homocysteine; III, Sulfide; IV, GSH; as well as V, the ratio of reduced over oxidized glutathione, GSH:GSSG. Nitrite and nitrate, I, Nitrite; II Nitrate. (median and IQR). Pairwise comparisons were performed using the Wilcoxon signed ranks test (n = 37).

TABLE 3 Baseline metabolic differences according fitness. A comparison of baseline serum oxidative/nitrosative markers, skeletal muscle mitochondrial respiratory capacity and redox-related tissue metabolites of unfit and fit patients.

| | Unfit median (IQR) | Fit median (IQR) | Sig. P value |
|---|---|---|---|
| **Baseline serum redox and inflammatory markers** | | | |
| Adjusted TFT (μmoles/g protein) | 4.21 (2.31) | 4.94 (0.90) | 0.30 |
| FRAP (μM) | 839.05 (726.17) | 869.70 (563.23) | 0.92 |
| TBARS (μM) | 7.50 (8.55) | 4.32 (3.49) | 0.11 |
| HNE (ng/mL) | 6.29 (5.74) | 10.02 (5.76) | 0.10 |
| Isoprostanes (pg/mL) | 251.31 (164.67) | 228.90 (127.27) | 0.41 |
| cGMP (pg/mL) | 154.49 (57.92) | 85.03 (39.22) | 0.006 |
| Nitrite (μM) | 0.17 (0.17) | 0.17 (0.21) | 0.45 |
| Nitrate (μM) | 33.25 (24.06) | 33.60 (23.81) | 0.92 |
| RxNO (nM) | 44.48 (90.01) | 27.48 (12.59) | 0.11 |
| IL-6 (pg/mL) | 4.77 (16.32) | 2.26 (2.76) | 0.04 |
| TNF-a (pg/mL) | 0.59 (0.56) | 0.30 (0.25) | 0.02 |
| **Baseline skeletal muscle mitochondrial respiratory capacity** | | | |
| $LEAK_{FAO}$ ($pmoles^{-1}$ $mg^{-1}$) | 10.21 (8.64) | 5.68 (4.41) | 0.25 |
| $FAO_{OXPHOS}$ ($pmoles^{-1}$ $mg^{-1}$) | 18.92 (15.57) | 14.68 (6.94) | 0.68 |
| $MOP_{OXPHOS}$ ($pmoles^{-1}$ $mg^{-1}$) | 26.66 (20.44) | 22.76 (5.05) | 0.86 |
| $CI_{OXPHOS}$ ($pmoles^{-1}$ $mg^{-1}$) | 28.55 (23.60) | 26.57 (7.84) | 0.95 |
| MAX OXPHOS ($pmoles^{-1}$ $mg^{-1}$) | 64.27 (43.73) | 72.04 (28.23) | 0.99 |
| CI + $II_{ETS}$ ($pmoles^{-1}$ $mg^{-1}$) | 79.81 (14.14) | 77.42 (30.86) | 0.76 |
| $CII_{ETS}$ ($pmoles^{-1}$ $mg^{-1}$) | 47.08 (23.00) | 59.35 (33.15) | 0.72 |
| **Baseline skeletal muscle metabolites free concentration** | | | |
| Cysteine (nmoles/kg) | 35.37 (15.45) | 35.47 (37.85) | 0.65 |
| Homocysteine (nmoles/kg) | 2.31 (5.69) | 1.40 (0.69) | 0.72 |
| Sulfide (nmoles/kg) | 1.22 (1.43) | 1.99 (2.22) | 0.27 |
| GSH (mmoles/kg) | 2.75 (3.30) | 2.55 (0.82) | 0.44 |
| GSSG (nmoles/kg) | 4.56 (47.48) | 2.19 (5.13) | 0.65 |
| **Baseline skeletal muscle metabolites total concentration** | | | |
| Cysteine (nmoles/kg) | 57.30 (33.14) | 66.33 (30.15) | 0.28 |
| Homocysteine (nmoles/kg) | 8.59 (14.48) | 7.74 (3.71) | 0.88 |
| Sulfide (nmoles/kg) | 62.11 (66.71) | 51.26 (39.13) | 0.80 |
| GSH (mmoles/kg) | 2.06 (1.99) | 1.82 (0.86) | 0.24 |
| GSH:GSSG | 1,159.00 (2069.10) | 1,233.00 (1,344.50) | 0.57 |
| **Skeletal muscle NO metabolites** | | | |
| Nitrite (μmoles/kg) | 11.95 (11.56) | 16.83 (12.90) | 0.19 |
| Nitrate (μmoles/kg) | 276.90 (1,028.30) | 260.80 (203.30) | 0.86 |

whereby a proportion of protons leak across the inner mitochondrial membrane through a route that is not coupled to formation of ATP, with this having both basal (i.e., unregulated) and inducible components [37]. The increased LEAK respiration observed here following surgery could therefore indicate increased proton leak, which might be mediated by protein-dependent or independent mechanisms. Mild uncoupling has been shown to lower ROS production in cellular models, at the expense of ATP production [38, 39]. In our study, the observation of increased LEAK respiration may therefore reflect an adaptive response to acute surgical stress at the muscular end-organ level.

In response to sepsis, upregulation of uncoupling protein 3 (UCP3) has been seen in mouse skeletal muscle [40, 41], whilst UCP3 expression is also elevated in human muscle in response to redox stress following shorter-term hypoxic exposure [16, 42]. Although the short timeframe of the intraoperative acute stress exposure in this study makes altered UCP expression unlikely, an alternative explanation could involve post-translational modification. For example, the glutathionylation of UCP3 has been shown to activate uncoupling [39]. Although we saw no change in overall GSH levels, our measure is reflective of skeletal muscle overall and not specifically the mitochondrial compartment. A UCP3-dependent mechanism might not, however, explain the greater increase in LEAK respiration seen in fit compared with less fit individuals in our study, since UCP3 expression (relative to mitochondrial content) is typically lower in the skeletal muscle of more trained individuals, in conjunction with enhanced mechanical efficiency [43]. Moreover, the physiological significance of any UCP3-mediated uncoupling is unclear, since in a mouse model of sepsis, survival rates were not different between wild-type and UCP3 knockout mice [41].

Instead, a non-UCP mediated mechanism might underpin our finding of a surgery-induced increase in LEAK; for example, in a hypoxic environment, NO can cause mild membrane depolarisation [44, 45]. Alternatively, the adenine nucleotide translocases (ANTs) have been proposed to be major fatty acid-inducible mediators of proton leak in many tissues, including skeletal muscle [46, 47]. Expression of the ANT1 isoform increased in human skeletal muscle in response to endurance training, and this was associated with greater sensitivity for fatty acid-mediated uncoupling [48]. This mechanism has been proposed to be protective against the development of insulin resistance in the event of fatty acid overload [48], but deserves further investigation in the contexts of redox stress, sepsis and surgical stress.

Comparison of the results of the present investigation to previous studies is challenging as the combinations of biological sampling sites, analytes and fitness measures using CPET in a surgical setting has not been undertaken before. Mitochondrial respiratory changes in skeletal muscle in a pig model after surgery have been investigated. Altered mitochondrial respiration was found when muscle fibres were biopsied 24 h apart and studied using HRR [8]. Increased fatty acid-mediated LEAK respiration was seen, which was directly comparable to our findings, along with evidence of no change in ADP-stimulated respiration with glutamate. Similarly, no reduction in ADP-stimulated respiration with pyruvate, was measured in our study. In a separate study, human skeletal muscle biopsies were taken before and after major abdominal surgery in patients with pancreatic cancer and benign disease. Muscle mitochondria were isolated and used to measure pyruvate dehydrogenase complex activity along with maximal ATP production, using bioluminescence. This study demonstrated reduced pyruvate dehydrogenase complex activity and a decreased rate of mitochondrial ATP production supported by palmitoyl-carnitine, and complex I and complex I&II-mediated substrates post-surgery [9]. Whilst we did not see a decreased capacity for $O_2$ consumption supported by octanoyl-carnitine, or complex I and complex I&II substrates in combination in the oxidative phosphorylation state, the lower ATP production reported by Atkins and colleagues, might be explained by greater uncoupling as a result of proton leak (i.e., less ATP production per $O_2$ consumed), and this would be in accordance with our findings and those of Hagve and colleagues in the porcine model.

Changes in tissue thiol levels have been observed previously, with skeletal muscle concentrations of cysteine and GSH remaining unchanged immediately after surgery, and GSH levels subsequently falling at 24 h [49], a timescale not measured in our study. Exercise and fitness-based studies, however, have demonstrated a positive correlation between levels of cGMP and fitness; physical training has been associated with increased circulating cGMP levels, for example, in hypertensive individuals [50]. The opposite was observed in this study, where less aerobically fit individuals demonstrated increased levels of cGMP. Evidence of increased inflammation and low CPET fitness has been previously reported in a study measuring preoperative CPET with neutrophil-leukocyte ratio as a measure of level of systemic inflammation, AT was found to be independently associated with neutrophil-leukocyte ratio [11]. In the context of our study of unfit patients with malignancy, multifactorial inflammatory mechanism may be contributing to the increased IL-6 and TNF-α observed.

This study highlights several areas for potential further investigation, particularly in phenotyping patients to better understand the biology of resilience under acute surgical stress. This includes exploring the role of increased mitochondrial LEAK in preoperative fitness, the mechanisms underlying this process, and the function of skeletal muscle cysteine—specifically whether its presence serves a protective role during surgical stress. While this study focused on the acute intraoperative period, examining later physiological responses (e.g., on days three, five, and seven)—when postoperative complications commonly arise—could provide additional

insights into protective metabolic responses and favorable characteristics for recovery.

### Study limitations

Our study was not initially designed to be powered to detect mitochondrial and metabolic changes in skeletal muscle. In addition, CPET was not part of the patients' routine preoperative work-up. The voluntary performance of CPET could be a major confounder in this study, since the sub-group of patients investigated may have been physically fitter than the main study cohort. The lack of difference in oxygen consumption (in absolute terms) between the respiratory states during the perioperative period may partly be attributable to the short time-frame between biopsy extractions, since protein translational responses may not have occurred. Secondly, the vastus lateralis is remote from the site of surgical injury, so the tissue exposure to inflammatory changes may not have been as exaggerated as that experienced intra-abdominally or within the circulation.

## Conclusion

This sub-study offers novel insights into mitochondrial, redox, metabolic and inflammatory changes at a systemic and end-organ level before and acutely after surgery. Higher preoperative systemic inflammation levels, reduced tissue nitrite and blunted intraoperative LEAK respiration in unfit individuals may be hallmarks of inferior resilience, with overall preservation of mitochondrial respiratory capacity and GSH in skeletal muscle reflecting the whole-body ability to withstand major surgical stress. The exemplary approach taken in the present study may be suited to phenotype patients into subgroups of lesser or greater resilience or susceptibility to postoperative complications.

## Author contributions

All authors contributed towards data interpretation, manuscript preparation and write up. JS and DM contributed towards study design, sample collection, data collection and sample analysis. HM and DM contributed towards study design and securing funding. MM and MF performed sample analysis. AM contributed towards study design. All authors contributed to the article and approved the submitted version.

## Data availability

The datasets presented in this study can be found in online repositories. The names of the repository/repositories and accession number(s) can be found in the article/ Supplementary Material.

## Ethics statement

The studies involving humans were approved by West London Research Ethics Committee and Human Research Authority. The studies were conducted in accordance with the local legislation and institutional requirements. The participants provided their written informed consent to participate in this study.

## Funding

The author(s) declare that financial support was received for the research, authorship, and/or publication of this article. National Institute of Academic Anaesthesia and British Journal of Anaesthesia/Royal College of Anaesthesia Project Grant (No. 537555) for the study *Characterising the impact of Oxidative Stress and Mitochondrial function on Outcomes following major Surgery* (COSMOS).

## Acknowledgments

We are grateful to Bernadette Fernandez, Laurie Lau and Monika Mikus-Lelinska for plasma/serum analysis of nitric oxide/oxidative stress metabolites, the National Institute of Academic Anaesthesia (NIAA) and the British Journal of Anaesthesia/Royal College of Anaesthesia for providing funding support, and the patients who took part in this study. This work is based on Stevens, Jia Liu; (2022) The roles of redox and bioenergetics in perioperative outcomes following major surgery. Doctoral thesis (Ph.D), UCL (University College London).

## Conflict of interest

The author(s) declared no potential conflicts of interest with respect to the research, authorship, and/or publication of this article.

## Supplementary material

The Supplementary Material for this article can be found online at: https://www.ebm-journal.org/articles/10.3389/ebm.2025.10254/full#supplementary-material

# References


1. Cortese-Krott MM, Koning A, Kuhnle GGC, Nagy P, Bianco CL, Pasch A, et al. The reactive species interactome: evolutionary emergence, biological significance, and opportunities for redox metabolomics and personalized medicine. *Antioxid and Redox signaling* (2017) **27**:684–712. doi:10.1089/ars.2017.7083

2. Soysal P, Isik AT, Carvalho AF, Fernandes BS, Solmi M, Schofield P, et al. Oxidative stress and frailty: a systematic review and synthesis of the best evidence. *Maturitas* (2017) **99**:66–72. doi:10.1016/j.maturitas.2017.01.006

3. McQueen MA. Exercise aspects of obesity treatment. *Ochsner J* (2009) **9**:140–3.

4. Finkel T, Holbrook NJO. Oxidants, oxidative stress and the biology of ageing. *Nature* (2000) **408**:239–47. doi:10.1038/35041687

5. Harman D. Aging: a theory based on free radical and radiation chemistry. *J Gerontol* (1956) **11**:298–300. doi:10.1093/geronj/11.3.298

6. Otto JM, Levett DZH, Grocott MPW. Cardiopulmonary exercise testing for preoperative evaluation: what does the future hold. *Curr Anesthesiology Rep* (2020) **10**:1–11. doi:10.1007/s40140-020-00373-x

7. Older P, Hall A, Hader R. Cardiopulmonary exercise testing as a screening test for perioperative management of major surgery in the elderly. *Chest* (1999) **116**:355–62. doi:10.1378/chest.116.2.355

8. Hagve M, Gjessing PF, Fuskevåg OM, Larsen TS, Irtun O. Skeletal muscle mitochondria exhibit decreased pyruvate oxidation capacity and increased ROS emission during surgery-induced acute insulin resistance. *Am J Physiology-Endocrinology Metab* (2015) **308**:E613–E620. doi:10.1152/ajpendo.00459.2014

9. Atkins R, Constantin-Teodosiu D, Varadhan KK, Constantin D, Lobo DN, Greenhaff PL. Major elective abdominal surgery acutely impairs lower limb muscle pyruvate dehydrogenase complex activity and mitochondrial function. *Clin Nutr* (2021) **40**:1046–51. doi:10.1016/j.clnu.2020.07.006

10. Delogu G, H S, Dh N, M B, Wa B, Jl V, et al. Mitochondrial perturbations and oxidant stress in lymphocytes from patients undergoing surgery and general anesthesia. *Arch Surg* (2001) **136**:1190. doi:10.1001/archsurg.136.10.1190

11. Sultan P, Edwards MR, Gutierrez del Arroyo A, Cain D, Sneyd JR, Struthers R, et al. Cardiopulmonary exercise capacity and preoperative markers of inflammation. *Mediators Inflamm* (2014) **2014**:727451–8. doi:10.1155/2014/72745.1

12. Gonzalez-Freire M, Scalzo P, D'Agostino J, Moore ZA, Diaz-Ruiz A, Fabbri E, et al. Skeletal muscle *ex vivo* mitochondrial respiration parallels decline *in vivo* oxidative capacity, cardiorespiratory fitness, and muscle strength: the Baltimore Longitudinal Study of Aging. *Aging cell* (2018) **17**:e12725. doi:10.1111/acel.12725

13. Stevens JL, McKenna HT, Filipe H, Lau L, Fernandez BO, Murray AJ, et al. Perioperative redox changes in patients undergoing hepato-pancreatico-biliary cancer surgery. *Perioper Med* (2023) **12**:35–11. doi:10.1186/s13741-023-00325-z

14. von ElmAltmanEgger EDGM, Pocock SJ, Gøtzsche PC, Vandenbroucke JP, STROBE Initiative. The Strengthening the Reporting of Observational Studies in Epidemiology (STROBE) statement: guidelines for reporting observational studies. *J Clin Epidemiol* (2008) **61**:344–9. doi:10.1016/j.jclinepi.2007.11.008

15. Levett DZH, Jack S, Swart M, Carlisle J, Wilson J, Snowden C, et al. Perioperative cardiopulmonary exercise testing (CPET): consensus clinical guidelines on indications, organization, conduct, and physiological interpretation. *Br J Anaesth* (2018) **120**:484–500. doi:10.1016/j.bja.2017.10.020

16. Horscroft JA, Kotwica AO, Laner V, West JA, Hennis PJ, Levett DZH, et al. Metabolic basis to Sherpa altitude adaptation. *Proc Natl Acad Sci* (2017) **114**:6382–7. doi:10.1073/pnas.1700527114

17. Kuznetsov AV, Veksler V, Gellerich FN, Saks V, Margreiter R, Kunz WS. Analysis of mitochondrial function *in situ* in permeabilized muscle fibers, tissues and cells. *Nat Protoc* (2008) **3**:965–76. doi:10.1038/nprot.2008.61

18. Sutton TR, Minnion M, Barbarino F, Koster G, Fernandez BO, Cumpstey AF, et al. A robust and versatile mass spectrometry platform for comprehensive assessment of the thiol redox metabolome. *Redox Biol* (2018) **16**:359–80. doi:10.1016/j.redox.2018.02.012

19. Rassaf T, Lauer T, Heiss C, Balzer J, Mangold S, Leyendecker T, et al. Nitric oxide synthase-derived plasma nitrite predicts exercise capacity. *Br J Sports Med* (2007) **41**:669–73. doi:10.1136/bjsm.2007.035758

20. Bryan NS, Fernandez BO, Bauer SM, Garcia-Saura MF, Milsom AB, Rassaf T, et al. Nitrite is a signaling molecule and regulator of gene expression in mammalian tissues. *Nat Chem Biol* (2005) **1**:290–7. doi:10.1038/nchembio734

21. Shiva S. Nitrite: a physiological store of nitric oxide and modulator of mitochondrial function. *Redox Biol* (2013) **1**:40–4. doi:10.1016/j.redox.2012.11.005

22. Black MI, Wylie LJ, Kadach S, Piknova B, Park JW, Stoyanov Z, et al. Effects of low and high dietary nitrate intake on human saliva, plasma and skeletal muscle nitrate and nitrite concentrations and their functional consequences. *Free Radic Biol Med* (2024) **225**:881–93. doi:10.1016/j.freeradbiomed.2024.10.282

23. Cortese-Krott MM, Fernandez BO, Kelm M, Butler AR, Feelisch M. On the chemical biology of the nitrite/sulfide interaction. *Nitric Oxide* (2015) **46**:14–24. doi:10.1016/j.niox.2014.12.009

24. Feelisch M, Akaike T, Griffiths K, Ida T, Prysyazhna O, Goodwin JJ, et al. Long-lasting blood pressure lowering effects of nitrite are NO-independent and mediated by hydrogen peroxide, persulfides, and oxidation of protein kinase G1α redox signalling. *Cardiovasc Res* (2020) **116**:51–62. doi:10.1093/cvr/cvz202

25. Feelisch M, Fernandez BO, Bryan NS, Garcia-Saura MF, Bauer S, Whitlock DR, et al. Tissue processing of nitrite in hypoxia: an intricate interplay of nitric oxide-generating and-scavenging systems. *J Biol Chem* (2008) **283**:33927–34. doi:10.1074/jbc.m806654200

26. Dyson A, Bryan NS, Fernandez BO, Garcia-Saura M-F, Saijo F, Mongardon N, et al. An integrated approach to assessing nitroso-redox balance in systemic inflammation. *Free Radic Biol Med* (2011) **51**:1137–45. doi:10.1016/j.freeradbiomed.2011.06.012

27. Saijo F, Milsom AB, Bryan NS, Bauer SM, Vowinkel T, Ivanovic M, et al. On the dynamics of nitrite, nitrate and other biomarkers of nitric oxide production in inflammatory bowel disease. *Nitric Oxide* (2010) **22**:155–67. doi:10.1016/j.niox.2009.11.009

28. Cohen PJ. Effect of anesthetics on mitochondrial function. *Anesthesiology* (1973) **39**:153–64. doi:10.1097/00000542-197308000-00007

29. Grimm M, Lazariotou M, Kircher S, Höfelmayr A, Germer CT, von Rahden BHA, et al. Tumor necrosis factor-α is associated with positive lymph node status in patients with recurrence of colorectal cancer—indications for anti-TNF-α agents in cancer treatment. *Cell Oncol* (2011) **34**:315–26. doi:10.1007/s13402-011-0027-7

30. Feelisch M, Cortese-Krott MM, Santolini J, Wootton SA, Jackson AA. Systems redox biology in health and disease. *EXCLI J* (2022) **21**:623–46. doi:10.17179/excli2022-4793

31. Wink DA, Miranda KM, Espey MG, Pluta RM, Hewett SJ, Colton C, et al. Mechanisms of the antioxidant effects of nitric oxide. *Antioxid and Redox Signaling* (2001) **3**:203–13. doi:10.1089/152308601300185179

32. Moylan JS, Reid MB. Oxidative stress, chronic disease, and muscle wasting. *Muscle and Nerve* (2007) **35**:411–29. doi:10.1002/mus.20743

33. Steinbacher P, Eckl P. Impact of oxidative stress on exercising skeletal muscle. *Biomolecules* (2015) **5**:356–77. doi:10.3390/biom5020356

34. Wandrag L, Siervo M, Riley HL, Khosravi M, Fernandez BO, Leckstrom CA, et al. Does hypoxia play a role in the development of sarcopenia in humans? Mechanistic insights from the Caudwell Xtreme Everest Expedition. *Redox Biol* (2017) **13**:60–8. doi:10.1016/j.redox.2017.05.004

35. Colbert LH, Visser M, Simonsick EM, Tracy RP, Newman AB, Kritchevsky SB, et al. Physical activity, exercise, and inflammatory markers in older adults: findings from the Health, Aging and Body Composition Study. *J Am Geriatr Soc* (2004) **52**:1098–104. doi:10.1111/j.1532-5415.2004.52307.x

36. Fischer CP, Berntsen A, Perstrup LB, Eskildsen P, Pedersen BK. Plasma levels of interleukin-6 and C-reactive protein are associated with physical inactivity independent of obesity. *Scand J Med and Sci Sports* (2007) **17**:580–7. doi:10.1111/j.1600-0838.2006.00602.x

37. Jastroch M, Divakaruni AS, Mookerjee S, Treberg JR, Brand MD. Mitochondrial proton and electron leaks. *Essays Biochem* (2010) **47**:53–67. doi:10.1042/bse0470053

38. Mailloux RJ, Harper M-E. Uncoupling proteins and the control of mitochondrial reactive oxygen species production. *Free Radic Biol Med* (2011) **51**:1106–15. doi:10.1016/j.freeradbiomed.2011.06.022

39. Toime LJ, Brand MD. Uncoupling protein-3 lowers reactive oxygen species production in isolated mitochondria. *Free Radic Biol Med* (2010) **49**:606–11. doi:10.1016/j.freeradbiomed.2010.05.010

40. Sun X, Wray C, Tian X, Hasselgren P-O, Lu J. Expression of uncoupling protein 3 is upregulated in skeletal muscle during sepsis. *Am J Physiology-Endocrinology Metab* (2003) **285**:E512–E520. doi:10.1152/ajpendo.00446.2002

41. Zolfaghari PS, Carré JE, Parker N, Curtin NA, Duchen MR, Singer M. Skeletal muscle dysfunction is associated with derangements in mitochondrial bioenergetics (but not UCP3) in a rodent model of sepsis. *Am J Physiology-Endocrinology Metab* (2015) **308**:E713–E725. doi:10.1152/ajpendo.00562.2014

42. Levett DZ, Radford EJ, Menassa DA, Graber EF, Morash AJ, Hoppeler H, et al. Acclimatization of skeletal muscle mitochondria to high-altitude hypoxia during an ascent of Everest. *The FASEB J* (2012) **26**:1431–41. doi:10.1096/fj.11-197772

43. Schrauwen P, Troost FJ, Xia J, Ravussin E, Saris WHM. Skeletal muscle UCP2 and UCP3 expression in trained and untrained male subjects. *Int J Obes* (1999) **23**:966–72. doi:10.1038/sj.ijo.0801026

44. Knauer. *HPLC Basics-Principles and parameters* (2025).

45. Schweizer M, Richter C. Nitric oxide potently and reversibly deenergizes mitochondria at low oxygen tension. *Biochem biophysical Res Commun* (1994) **204**: 169–75. doi:10.1006/bbrc.1994.2441

46. Bertholet AM, Chouchani ET, Kazak L, Angelin A, Fedorenko A, Long JZ, et al. H+ transport is an integral function of the mitochondrial ADP/ATP carrier. *Nature* (2019) **571**:515–20. doi:10.1038/s41586-019-1400-3

47. Bround MJ, Bers DM, Molkentin JD. A 20/20 view of ANT function in mitochondrial biology and necrotic cell death. *J Mol Cell Cardiol* (2020) **144**: A3–A13. doi:10.1016/j.yjmcc.2020.05.012

48. Sparks LM, Gemmink A, Phielix E, Bosma M, Schaart G, Moonen-Kornips E, et al. ANT1-mediated fatty acid-induced uncoupling as a target for improving myocellular insulin sensitivity. *Diabetologia* (2016) **59**:1030–9. doi:10.1007/s00125-016-3885-8

49. Luo J-L, Hammarqvist F, Andersson K, Wernerman J. Skeletal muscle glutathione after surgical trauma. *Ann Surg* (1996) **223**:420–7. doi:10.1097/00000658-199604000-00011

50. Novais IP, Jarrete AP, Puga GM, Araujo HN, Delbin MA, Zanesco A. Effect of aerobic exercise training on cGMP levels and blood pressure in treated hypertensive postmenopausal women. *Motriz: Revista de Educação Física* (2017) **23**:1–6. doi:10.1590/s1980-6574201700010001

## Scope

Experimental Biology and Medicine (EBM) is a global, peer-reviewed journal dedicated to the publication of multidisciplinary and interdisciplinary research in the biomedical sciences. The journal covers the spectrum of translational research from T0, basic research, to T4, population health. Articles in EBM represent cutting edge research at the overlapping junctions of the biological, physical and engineering sciences that impact upon the health and welfare of the world's population. EBM is particularly appropriate for publication of papers that are multidisciplinary in nature, are of potential interest to a wide audience, and represent experimental medicine in the broadest sense of the term. However, manuscripts reporting novel findings on any topic in the realm of experimental biology and medicine are most welcome.

**EBM publishes Research, Reviews, Mini Reviews, and Brief Communications in the following categories.**

- Anatomy/Pathology
- Artificial Intelligence/ Machine Learning Applications to Biomedical Research
- Biochemistry and Molecular Biology
- Bioimaging
- Biomedical Engineering
- Bionanoscience
- Cell and Developmental Biology
- Clinical Trials
- Endocrinology and Nutrition
- Environmental Health/Biomarkers/ Precision Medicine
- Genomics, Proteomics, and Bioinformatics
- Immunology/Microbiology/Virology
- Mechanisms of Aging
- Neuroscience
- Pharmacology and Toxicology
- Physiology and Pathophysiology
- Population Health
- Stem Cell Biology
- Structural Biology
- Synthetic Biology
- Systems Biology and Microphysiological Systems
- Translational Research

EBM Experimental Biology and Medicine

EBM is the official journal of the Society for Experimental Biology and Medicine

Led by Dr Steven Goodman, Experimental Biology and Medicine (EBM) is a global, peer-reviewed journal dedicated to the publication of multidisciplinary and interdisciplinary research in the biomedical sciences.

---

# Discover more of our Special Issues

See more →


Contact

development@ebm-journal.org

See more

ebm-journal.org

publishingpartnerships.frontiersin.org/our-partners